Quaternary Glaciations in the Lago Pueyrredón Valley, Argentina

Andrew S. Hein



PhD

The University of Edinburgh

School of Geosciences
College of Science and Engineering

2009

Declaration

This thesis is the result of four years work. The work presented herein is my own; where chapters have been published, the authorship and contributions have been noted accordingly. The thesis has not been submitted for any other degree or professional qualification.

Andrew S. Hein

Acknowledgements

I thank for financial support the UK Natural Environmental Research Council (NERC) for my studentship and for financing sample analysis via a NERC-CIAF beam-time grant; the Royal Geographic Society (with IBG) award funded by Rio Tinto plc; the Royal Scottish Geographic Society; the Carnegie Trust for the Universities of Scotland; and the Scottish Universities Environmental Research Centre (SUERC) performed and supported my sample analysis; at SUERC I thank Christoph Schnabel, Sheng Xu, Stewart Freeman and Fin Stuart.

This thesis benefited from discussions with and contributions from many people in a variety of ways to numerous to mention in entirety. I thank my supervisors and friends Nick Hulton and Tibor Dunai for their efforts, encouragement and continued support; my unofficial supervisors Mike Kaplan and David Sugden for their valuable input particularly in the final year of writing up; Chris Fogwill and David Sugden for employing me on their Shackleton Project; Jorge Rabassa, Andrea Coronato and others for discussions during an excellent field school in Tierra del Fuego; Oscar Martínez and Corina Risso for discussions and for essential logistical support in Argentina; Steve Binnie who taught me the chemistry and more; and Elaine McDougall for invaluable lab-work support. Special thanks to the Fortuny family: Susan, Pedro, Pablo and Luciana for making me feel welcome in their home in Lago Posadas. Mark Naylor, Pilar Alvarez, Anne-Sophie Meriaux, Chris Place, Anthony Newton, Simon Mudd, Mehmet Karatay, Steve Dowers, Isabel Hurtado de Mendoza, Kate Briggs, Rachel Walcott, Jake Boex, and Richard Phillips are amongst many others who helped in a variety of ways.

I thank my friends for adventures unrelated to this work which helped to keep my perspective; you know who you are. Special thanks to my parents, Jill and Clarence who, along with my brother and sister in law, Tim and Karrie, have been continually supportive and encouraging in every way since the beginning. Thanks to my mother

and father in law Avril and Richard Newton for their continued support of my studies.

I would especially like to thank my lovely wife Rachel for her love, patience, encouragement and reassurance throughout this period. She dealt with my ups and downs and my presence and absence. She has been incredibly supportive and a great mother to our beautiful son Francis, and for that I am forever grateful. Most of all, I thank my son Francis, who arrived during the second year of my study, and who has kept me laughing and smiling ever since. This is for you.

Quaternary Glaciations in the Lago Pueyrredón Valley, Argentina

Contents

Contents iv
List of figures vii
List of tables viii
Abstract ix
Resumen x
Chapter 1 Introduction 1
1.1 Aim 1
1.2 Background 1
1.3 Wider implications 13
1.4 Study area 15
1.5 Objectives 21
1.6 Thesis scope 21
Chapter 2 Methodology 24
2.1 Introduction 24
2.2 Geomorphic mapping 25
2.3 Cosmogenic-nuclide methodology 26
2.3.1 Cosmic radiation 27
2.3.2 Secondary cosmic rays 29
2.3.2.1 In-situ cosmogenic ^{10}Be and ^{26}Al production 31
2.3.3 Production rates and scaling factors 33
2.3.3.1 Scaling factors 34
Spatial 34
Topography and local obstructions 36
Sample thickness 37
Other factors 38
2.3.3.2 Production rates 39
2.3.3.3 ^{26}Al/^{10}Be ratio 41
2.3.4 Exposure ages 44
2.3.5 Sampling considerations and limitations 46
Chapter 3 The chronology of the Last Glacial Maximum and deglacial events in central Argentine Patagonia 49
Abstract 50
3.1 Introduction 51
3.1.1 LGM in southern South America 52
3.2 Regional setting 54
3.2.1 Geology 54
3.2.2 Geologic implications 55
3.2.3 Existing chronology 56
3.3 Materials and methods 59

3.3.1 Geomorphic mapping 59
3.3.1.1 Río Blanco and recessional moraines 59
3.3.1.2 Paleoshorelines 62
3.3.1.3 Inter-relationships 64
3.3.2 Surface exposure ages 66
3.3.2.1 Sampling strategy 67
3.3.2.2 Exposure age calculations and production rates 68
3.4 Results 71
3.5 Discussion 76
3.5.1 Río Blanco moraines – revised chronology 76
3.5.2 Regional significance of the new chronology 77
3.5.3 The evolution and diversion of paleolakes 80
3.5.4 Wider implications 84
3.6 Conclusions 87
3.7 Acknowledgements 88
Chapter 4 Middle Pleistocene glaciation in Patagonia dated by cosmogenic-nuclide measurements on outwash gravels 89
Abstract 90
4.1 Introduction 91
4.1.1 Patagonian glacial history and the age gap 92
4.1.2 Exposure ages of old moraines 92
4.1.3 Exposure ages of outwash terraces 94
4.2 The Lago Pueyrredón valley, 47.5º S, Argentina 95
4.2.1 Geology 95
4.2.2 Climate 97
4.2.3 Existing glacial chronology 98
4.3 Approach and methodology 99
4.3.1 Sampling 100
4.3.1.1 Sampling criteria and methods 100
4.3.1.2 Sample location 102
4.3.2 Depth-profile exposure model optimization 104
4.3.3 Exposure age calculations 107
4.4 Results 108
4.4.1 Río Blanco unit 112
4.4.2 Hatcher unit 112
4.4.2.1 Moraine samples 112
4.4.2.2 ^{10}Be concentration depth-profile 114
4.4.2.3 Outwash cobbles 116
4.5 Discussion 119
4.5.1 Nuclide inheritance 119
4.5.2 Age of the Hatcher unit 119
4.5.2.1 Discordant ages 121
4.5.3 Correlation to LBA record 124
4.6 Conclusions 125
4.7 Acknowledgements 127
Chapter 5 Cosmogenic-nuclide ages of Early and Middle Pleistocene glacial sequences in Patagonia 128
Abstract 129

5.1 Introduction 130
5.1.1 Underlying rationale 131
5.1.2 Geologic setting 132
5.1.3 Existing chronology 135
5.2 Approach and methodology 136
5.2.1 Intermediate moraines and outwash terraces 137
5.2.2 Outermost moraines and outwash terraces 141
5.2.3 Cosmogenic nuclide analysis 143
5.3 Results 146
5.3.1 Intermediate moraines and outwash terrace 147
5.3.2 Outermost outwash terrace 149
5.4 Discussion 149
5.4.1 Evaluation and interpretation of exposure ages 149
5.4.1.1 Intermediate Cañadón de Caracoles sequence 151
5.4.1.2 Outermost Gorra de Poivre sequence 154
5.4.2 Chronologic significance 156
5.5 Conclusions 159
5.6 Acknowledgements 160
Chapter 6 Synthesis and principal conclusions 161
6.1 Introduction 162
6.2 Exposure age dating utilizing cosmogenic nuclides 163
6.2.1 Approach 163
6.2.2 Sampling strategies 165
6.2.2.1 Sample location 166
6.2.2.2 Sampling 171
6.2.3 Summary 173
6.3 Glacial chronology 174
6.3.1 Comparison to other Patagonian records 179
6.3.2 Comparison to global glacier records 182
6.3.3 Comparison to marine and ice-core records 184
6.3.4 Potential non-climatic influences on ice extent 186
6.4 Southern hemisphere westerlies 189
6.5 Dust in Antarctica 195
6.6 Overall conclusions 199
6.7 Further considerations and future research 200
Thesis development 202
Appendix A Isotope extraction and measurement 207
A.1 Target preparation 207
A.1.1 Quartz extraction 207
A.1.1.1 Physical separation 207
A.1.1.2 Junk etch 208
A.1.1.3 Quartz etch 208
A.1.2 Isotope extraction 209
A.1.2.1 Aluminium test strips 209
A.1.2.2 Quartz dissolution 210
A.1.2.3 Perchloric fuming 212
A.1.2.4 Aluminium aliquot 212
A.1.2.5 Anion columns 213

A.1.2.6 Titanium precipitation 214
A.1.2.7 Cation columns 214
A.1.2.8 Final perchloric fume 215
A.1.2.9 Hydroxide precipitation 215
A.1.2.10 Firing and target pressing 216
A.2 AMS analysis 216
A.3 Calculating ^{10}Be and ^{26}Al concentrations 218
Appendix B Exposure age calculator 220
B.1 Input 220
B.1.1 Location 220
B.1.2 Sample thickness and density 221
B.1.3 Shielding correction 221
B.1.4 Erosion rate 222
B.1.5 Nuclide concentration 222
B.2 Reference production rates 223
B.3 Exposure age calculation 223
B.4 Output 225
Appendix C Chapter Four supplementary material 227
C.1 Production rates 227
C.2 Depth-profile production rate 228
Appendix D Raw chemistry and AMS data 229
References 235

List of figures

Figure 1.1. The Southern Andes location map 2
Figure 1.2. Erratic boulder and Caldenius 4
Figure 1.3. Caldenius' map of Patagonian glacial sequences 5
Figure 1.4. Pre-LGM glacial chronology 9
Figure 1.5. Geomorphic map of the Lago Pueyrredón valley 17
Figure 1.6. Photos of the Lago Pueyrredón valley 19
Figure 1.7. Landslides and lake levels 20
Figure 1.8. Cave paintings 20
Figure 2.1. Cosmic ray nuclear cascade 30
Figure 2.2. Production rate variation with altitude: Scaling model dependencies 36
Figure 2.3. ^{26}Al/^{10}Be production ratio plot 42
Figure 2.4. ^{10}Be/^{36}Cl production ratio plot 43
Figure 3.1. Context map 53
Figure 3.2. Geomorphic map of the Lago Pueyrredón valley 58
Figure 3.3. Photos of glacial features 60
Figure 3.4. Detailed geomorphic relationships 62
Figure 3.5. Paleoshoreline relationships 63
Figure 3.6. Photo of paleoshorelines 65
Figure 3.7. Photos of boulder samples 67
Figure 3.8. Geomorphic context of exposure ages 74
Figure 3.9. Synthesis of dated ice limits in Patagonia 79

Figure 3.10. Conceptual model for deglaciation 81
Figure 4.1. Context map 93
Figure 4.2. Ice limits and sample locations 96
Figure 4.3. Photos of samples and sample sites 101
Figure 4.4. Geomorphology of the Hatcher sequence and sample sites 103
Figure 4.5. Illustration of ^{10}Be exposure age results 113
Figure 4.6. Plot of $\Sigma\chi^2$ solution surface 115
Figure 4.7. Plots of measured & modeled ^{10}Be concentrations with depth 117
Figure 5.1. Context map 131
Figure 5.2. Ice limits and sample locations 134
Figure 5.3. Cañadón de Caracoles sample locations 138
Figure 5.4. Cañadón de Caracoles sample photos 140
Figure 5.5. Gorra de Poivre sample locations 141
Figure 5.6. Gorra de Poivre sample photos 144
Figure 5.7. Illustration of exposure age results 146
Figure 5.8. ^{26}Al/^{10}Be ratios 150
Figure 5.9. Glacier advances at Lago Pueyrredón against global records 157
Figure 6.1. Cartoon of moraine and outwash diffusion 165
Figure 6.2. Ventifacts on fluvial cobble 166
Figure 6.3. Dust pathway 167
Figure 6.4. Photo of soil inflation 169
Figure 6.5. Photo of Hatcher soil profile 169
Figure 6.6. Severe ventifacts on boulder 170
Figure 6.7. Sampling strategy and confidence 172
Figure 6.8. Ventifacts on surface cobble 173
Figure 6.9. Ice limits in the Lago Pueyrredón valley 177
Figure 6.10. Lago Pueyrredón chronology vs. marine and ice core records 178
Figure 6.11. Difference in summer precipitation 193
Figure 6.12. Difference in winter precipitation 193
Figure 6.13. Comparison of deuterium, sea-salt and benthic δ^{18}O 195
Figure 6.14. The timing of Antarctic dust peaks 197

List of tables

Table 2.1. Reference production rates 40
Table 3.1. ^{10}Be data for the Río Blanco moraines 72
Table 3.2. ^{10}Be exposure ages from the Río Blanco moraine system 73
Table 3.3. Recalculated ^{10}Be ages from LBA and the Strait of Magellan 75
Table 4.1. Hatcher depth-profile data 110
Table 4.2. Data for the Río Blanco and Hatcher glacial sequences 111
Table 4.3. Data from Moreno 1 moraine cobbles at LBA 125
Table 5.1. Cosmogenic nuclide data 148
Table 6.1. Summary of the glacial chronology at Lago Pueyrredón 176
Table D.1. Beryllium data 230
Table D.2. Aluminum data 233

Abstract

This thesis develops a better knowledge of the extent and timing of glaciations in southern Argentina throughout the Quaternary. It provides a detailed understanding of successive major glacial outlet lobes in the Lago Pueyrredón valley. The glacial and glaciofluvial deposits in the valley, as elsewhere in the region, are extremely well-preserved and reflect punctuated glacial advances between ~ 1.1 Ma and ~ 17 ka. Several intermediate glaciations are undated, constrained by the limited time frame of radiocarbon age dating, the limited potential volcanic sites for K-Ar or $^{40}Ar/^{39}Ar$ age dating, and erosion and exhumation problems associated with cosmogenic-nuclide surface exposure ages on moraines.

This thesis provides a new chronology for the mid-Quaternary glaciations based on methodological advances in cosmogenic-nuclide surface exposure age dating. This is done by deriving ages from glacial outwash terrace sediment and demonstrating their reliability. The work shows that for younger (i.e., last glacial) moraines, well-constrained ages can be derived from the common-practice of dating large boulders on the moraine surface. However, on older moraines, the ages so-derived become considerably scattered. This is interpreted to be caused primarily by boulder exhumation as a consequence of moraine erosion, resulting in shorter residence of some boulders at the surface relative to the moraine formation date. By contrast, glacial outwash surfaces in this area, if carefully chosen, can be shown to have undergone little aggradation or erosion, and thus have had long and consistent surface exposure since formation. Provided these surfaces can be stratigraphically linked with the glacial limits, they can provide good surface exposure ages. This has been convincingly confirmed in one location by a sequence of ages obtained from a ^{10}Be concentration depth-profile which demonstrate the surface stability and lack of inherited nuclides. Using these methods, cosmogenic ^{10}Be and ^{26}Al surface exposure ages indicate successive major advances occurred at ~ 1.2 Ma, ~ 600 ka, ~ 260 ka and ~27 – 17.5 ka. These are correlated with global marine and ice core records.

Resumen

Esta tesis pretende contribuir a un mejor conocimiento del alcance y la cronología de las glaciaciones en el sur de Argentina durante el Cuaternario. Se ofrece una interpretación detallada de importantes lóbulos glaciares sucesivos en la cuenca del Lago Pueyrredón. Los depósitos glaciares y glaciofluviales de la cuenca, al igual que los del resto de la región, se encuentran en un estado de conservación extraordinario y muestran avances glaciares pronunciados entre ~ 1,1 Ma y ~ 17 ka. Aún queda por fechar varias glaciaciones intermedias, debido a las dificultades que presenta el espectro tan limitado que abarca la datación mediante radiocarbono, los escasos emplazamientos volcánicos disponibles para la datación por K-Ar o $^{40}Ar/^{39}Ar$, y los problemas de erosión y exhumación relacionados con la datación cosmogénica de superficie en exposición de las morrenas.

Esta tesis ofrece una nueva cronología para las glaciaciones del Cuaternario Medio basada en los avances metodológicos de la datación cosmogénica de superficie en exposición. Las fechas se obtienen de los sedimentos de las terrazas de acarreos fluvioglaciares para más tarde demostrar su fiabilidad. Esta obra demuestra que para las morrenas más recientes (esto es, de la última glaciación), se pueden obtener fechas exactas a partir de la práctica común de la datación de bloques de grandes dimensiones en la superficie de las morrenas. No obstante, para las morrenas más antiguas, las fechas obtenidas mediante este método resultan considerablemente dispersas. Se cree que la razón principal es la exhumación de los bloques como consecuencia de la erosión de las morrenas, lo que provocó una menor permanencia en la superficie de algunos de los bloques en comparación con la fecha de formación de las morrenas. Por contraste, si se eligen cuidadosamente, se puede demostrar que las superficies de acarreos fluvioglaciares de esta zona, han sufrido una agradación o erosión menor y, consecuentemente, su exposición de superficie desde su formación ha sido más larga y consistente. Siempre que dichas superficies puedan relacionarse estratigráficamente con los límites glaciares, podrán ofrecer una buena datación por superficie en exposición. Este método se ha confirmado de manera convincente en un emplazamiento mediante una secuencia de fechas obtenidas con el perfil de

profundidad de la concentración de ^{10}Be, que demuestran la estabilidad de la superficie y la ausencia de núclidos heredados. Utilizando estos métodos, la datación cosmogénica de superficie en exposición ^{10}Be y ^{26}Al indica que en ~ 1.2 Ma, ~ 600 ka, ~ 260 ka y ~27 – 17.5 ka ocurrieron importantes avances sucesivos, los cuales están correlacionados con los registros globales del sondeo marino y de hielos.

Chapter 1 Introduction

1.1 Aim

The aim of this thesis is to understand the processes, mechanisms and timings of Quaternary glaciations in central Argentina. In particular, it aims to improve the dating of glacial sequences that pre-date the Last Glacial Maximum (LGM). The Quaternary moraines and outwash terraces in southernmost South America record more than one million years of glacier activity. In places, they have been described as 'probably the most complete and intact sequence of Quaternary moraines anywhere in the world' (Clapperton, 1993; p. 358). Such glacial geologic records are an important terrestrial proxy for past climates in the middle latitudes of southern South America. By developing a new sampling strategy, I aim to directly date the Quaternary glacial sequences using cosmogenic-nuclide surface exposure methods and thereby improve the chronologic base and achieve a better understanding of landscape evolution and long-term terrestrial climates in southern South America and in the southern hemisphere.

1.2 Background

Southern South America is the only continental landmass to extend through the middle latitudes of the southern hemisphere, and the Patagonian and Fuegian Andes are located on its western margin between latitudes 37º S and 56º S (Coronato et al., 2008). The Patagonian Andes form the only significant barrier to the precipitation

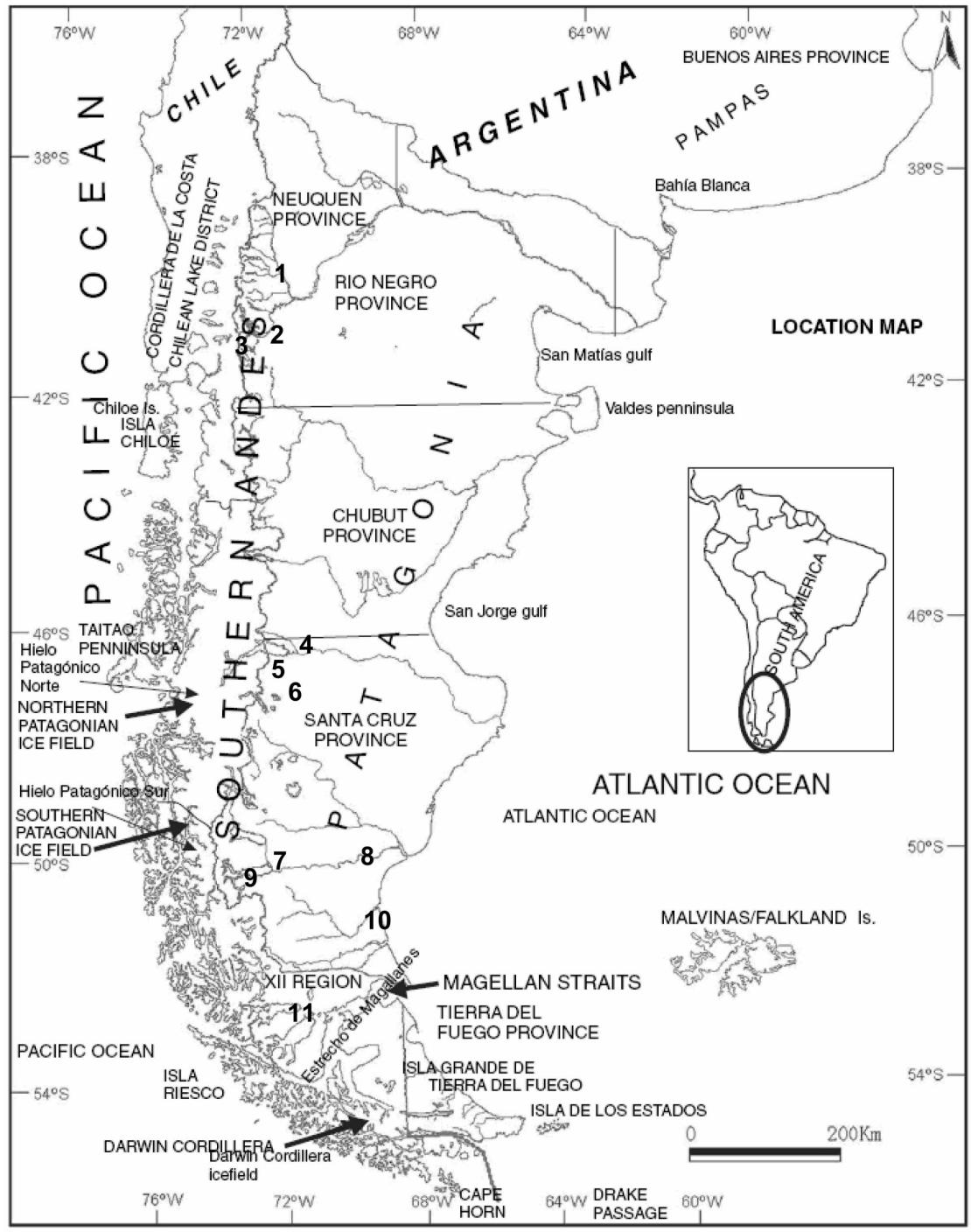

1. Malleo valley
2. Lago Nahuel Huapi
3. Cerro Tronador
4. Lago Buenos Aires
5. Meseta del Lago Buenos Aires
6. Lago Pueyrredón
7. Lago Argentino
8. Río Santa Cruz
9. Cerro del Fraile
10. Río Gallegos
11. Otway Sound

Figure 1.1. The Southern Andes location map

The southern Andes and the locations discussed in the text. The figure is modified after Rabassa (2008).

bearing southern westerly winds and to Southern Ocean circulation. They now host three large icefields, the Hielo Patagónico Norte (North Patagonian Icefield), the Hielo Patagónico Sur (South Patagonian Icefield) and the smaller Darwin Cordillera Icefield (Fig. 1.1). These icefields are the most significant in the southern hemisphere outside of Antarctica and they are the remnants of a much larger Late Pleistocene mountain ice sheet that covered the southern Andes (Rabassa, 2008). Precipitation on the west side of the Andes can locally exceed 8,000 mm a^{-1} [1], but rapidly diminishes to semi-arid levels (< 500 mm a^{-1}) to the east (Prohaska, 1976). The geology is of varied lithology, structure and age and includes Paleozoic metamorphic complexes, Mesozoic plutonics, Tertiary sediments and Miocene plateau lavas (Coronato et al., 2008; Gorring et al., 2003; Lagabrielle et al., 2004). The mountains have been repeatedly glaciated throughout the Pliocene and Quaternary periods; the associated glacial deposits are particularly well preserved in arid Argentine Patagonia (Rabassa, 2008).

There is a long history of exploration and geoscientific study in Patagonia (for a detailed review see Rabassa, 2008). It began in 1834 with the observations of Charles Darwin (1842) who, during his travels aboard H.M.S. Beagle, identified erratic boulders in the Río Santa Cruz valley (51º S) in southern Patagonia (Rabassa, 2008; Strelin and Malagnino, 2009). Ironically, over 170 years later, the genesis of some of these erratic boulders has yet to be fully resolved (Strelin and Malagnino, 2009). In 1899, several decades after Darwin's visit, the Swedish geologist and explorer Otto Nordenskjöld reported the first scientific investigations and detailed

[1] Dates are abbreviated as follows: Ma – million years; ka – thousand years; a – years.

mapping of the extent of Quaternary glaciations in southernmost Patagonia where he recognized the presence of multiple glacial sequences of different age (Rabassa, 2008). These initial scientific investigations were followed by perhaps the most significant contribution to the study of the Quaternary glacial sequences in Patagonian by the Swedish geologist Carl Caldenius in the late 1920s.

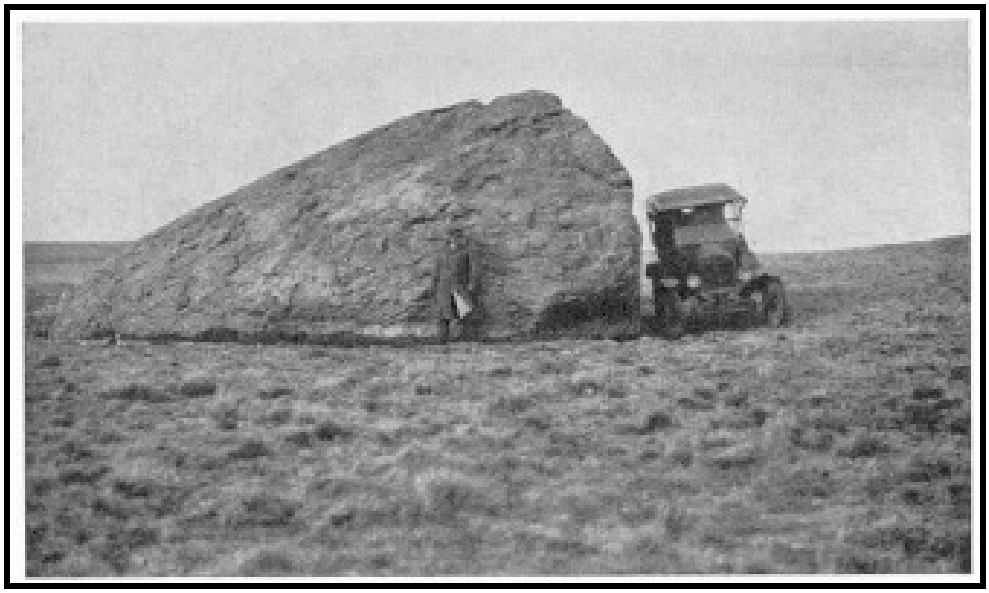

Figure 1.2. Erratic boulder and Caldenius

Large erratic boulder in southern Patagonia with vehicle for scale (Caldenius, 1932). The mapping was made difficult at the time by a lack of reliable roads and accurate maps.

Working between 1925 and 1931, Caldenius (1932) mapped the glacial deposits and landforms throughout Argentine Patagonia (Fig. 1.2). Caldenius' map (Fig. 1.3) covers over 1 M km^2, extending between Lago Nahuel Huapi (41° S) in northern Patagonia down to Cape Horn (56° S) in Tierra del Fuego, a distance of ~2,500 km (Rabassa, 2008). In his work, Caldenius identified the extents of four different glacial sequences throughout Argentine Patagonia. Based on his mapping and

teleconnection of glacial varve sequences in Patagonia to those of Sweden (e.g., de Geer, 1927), Caldenius adopted the Scandinavian glacial model for Patagonia. Thus,

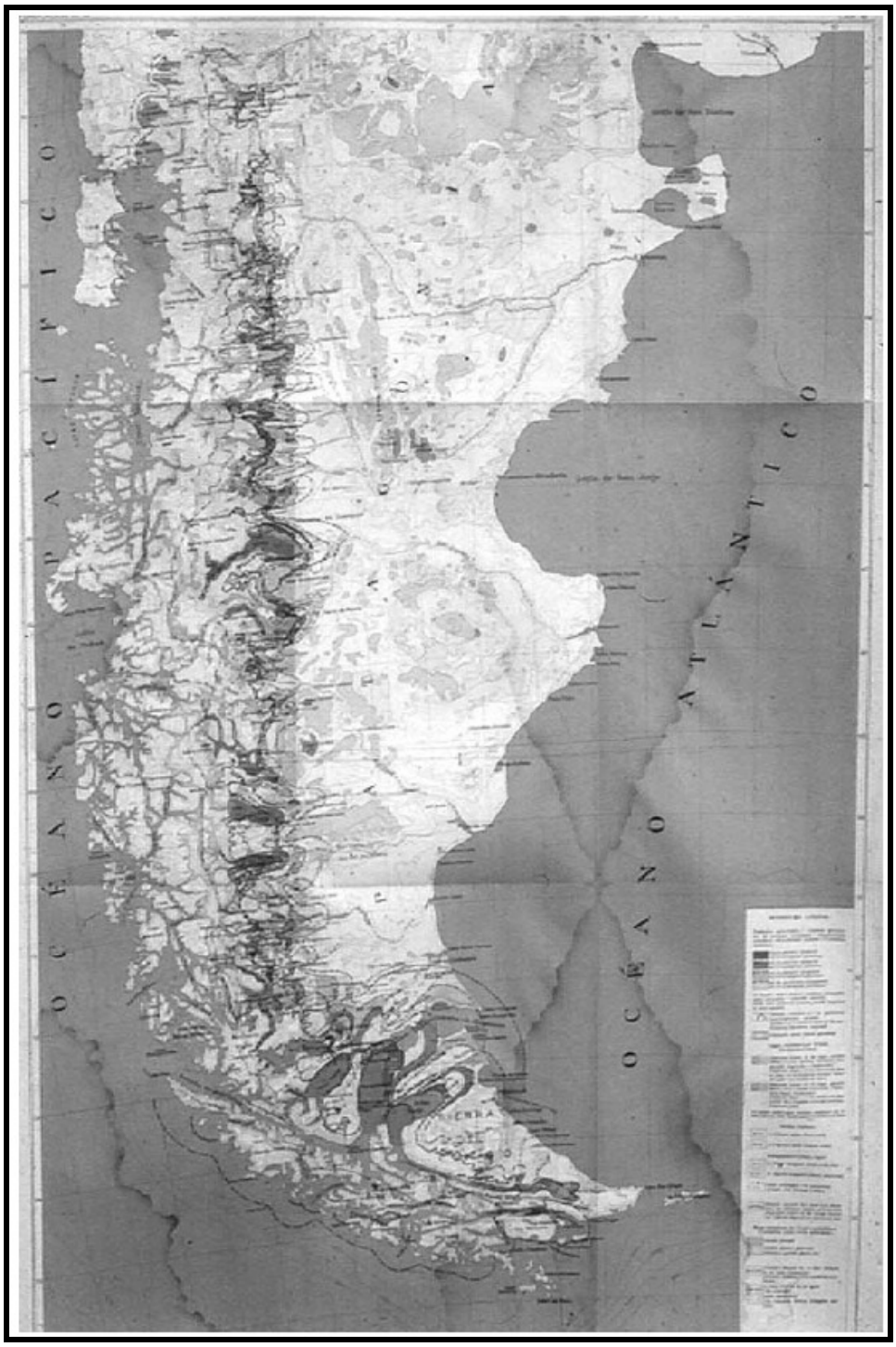

Figure 1.3. Caldenius' map of Patagonian glacial sequences

Caldenius' (1932) mapping of the Quaternary glacial sequences in Patagonia. The mapping was carried out in the late 1920's (Photo from Rabassa, 2008).

in decreasing relative age and ice-extent, the four glacial sequences were named the "Initioglacial", "Daniglacial", "Gotiglacial" and "Finiglacial", with a "Post-Finiglacial" sequence also identified at some locations. In keeping with the Scandinavian model, Caldenius considered all but the Initioglacial deposits to be from the Last Glaciation. It is now known that Caldenius underestimated the age of the older moraine sequences, but his stratigraphy is generally considered to be sound (Sugden et al., 2005). Subsequent researchers have improved the chronology and distinguished additional glacial sequences within each of the moraine groups identified in Caldenius' basic model. Thus, some of Caldenius' glacial sequences are in fact compound features that reflect multiple glaciations (e.g., Rabassa and Evenson, 1996), and therefore the basic model is not strictly valid. However, the nomenclature remains in use because it has a high value as unifying criteria for the different glacial events throughout the region (Rabassa, 2008).

Following Caldenius, a number of significant contributions were made to the study of the stratigraphy of glacial deposits, their relative ages, and to more detailed mapping of glacial deposits and their geomorphic associations. These important studies provided the foundation for later chronologic investigations. Major contributions were made, for example, by Feruglio (1950), who mapped the geology and glacial deposits in Argentine Patagonia at a regional scale, Flint and Fidalgo (1964; 1969) who mapped the glacial drift in northern Patagonia between 39º S and 43º S, and Fidalgo and Riggi (1965) who mapped the glacial deposits in and around Lago Buenos Aires (46.5º S). In the 1940s, some of the oldest glacial deposits in Patagonia were identified at Cerro del Fraile (51º S; Fig. 1.1). Feruglio (1944)

documented a sequence of tills interbedded with lava flows on the high meseta, to which he assigned a Pliocene age. This was the first identification of pre-Quaternary glaciations in Patagonia (Rabassa, 2008).

In the late 1960s, radiometric dating techniques (K-Ar, ^{14}C) allowed, for the first time, the absolute dating of the Patagonian glacial sequences. The fortuitous volcanism, particularly in central and southern Patagonia south of ~46º S, allowed several investigators to determine the great age of Patagonian glacial deposits. John Mercer dated the lavas at Cerro del Fraile and at other locations on high mesetas where lava flows are found interbedded with glacial till, for example, on the Meseta del Lago Buenos Aires (Mercer, 1969; Mercer, 1976; Mercer and Sutter, 1982). These K-Ar and paleomagnetic (Fleck et al., 1972) studies, together with later studies utilizing $^{40}Ar/^{39}Ar$ incremental heating methods (Singer et al., 2004; Ton-That et al., 1999), indicate that major glaciations in Patagonia had begun by 5 – 7 Ma, and regular fluctuations of the Patagonian ice sheet occurred after about 2 Ma. Several other researchers have found evidence of these earliest glaciations throughout Patagonia (e.g., Malagnino, 1995; Martínez and Coronato, 2008; Meglioli, 1992; Rabassa et al., 1986; Schlieder, 1989; Strelin, 1995; Strelin et al., 1999; Wenzens, 2000; Wenzens, 2006b).

The identification of basalts over- and underlying till in southern Patagonia (~51º S) allowed Mercer (1976) to determine the great age of the most *extensive* glacial moraine sequences in Patagonia by K-Ar methods at about 1.1 Ma. Mercer (1976) coined the name "Greatest Patagonian Glaciation" to distinguish the most extensive

glacial deposits corresponding to the Initioglacial moraine sequence of Caldenius (1932). Subsequently, the deposits have been re-dated by the $^{40}Ar/^{39}Ar$ total fusion (Meglioli, 1992) and incremental heating methods (Singer et al., 2004; Ton-That et al., 1999), and at different localities (e.g., Lago Buenos Aires, 47º S; Cerro Tronador, 41° S) these data have provided additional constraints on the timing of the most extensive glacial advance in Patagonian, which remains dated at ~ 1.1 Ma (Meglioli, 1992; Rabassa, 2008; Rabassa et al., 1986; Singer et al., 2004; Ton-That et al., 1999).

Subsequent to the Greatest Patagonian Glaciation, glacier moraine sequences are less extensive and the glaciers were entrenched within their valleys (Rabassa, 2008). The chronology for the pre-LGM glacial sequences (Gotiglacial, Daniglacial, Initioglacial) is available at some locations where geomorphic associations with limiting radiometric ages and/or paleomagnetic studies are available. Good reviews of the available age constraints are given by Rabassa and Clapperton (1990), Clapperton (1993) and more recently by Coronato et al. (2004), Rabassa (2008) and Rabassa and Coronato (in press); Fig. 1.4 summarizes the Quaternary glacial chronology. Limiting age constraints for pre-LGM glacial sequences are found in, for example, northern Argentine Patagonia (e.g., Rabassa et al., 2005; Schlieder, 1989), the Chilean Lake District and Isla Chiloe (e.g., Clapperton, 1993; Denton et al., 1999b; Porter, 1981) and in southernmost Patagonia and Tierra del Fuego (e.g., Bujalesky et al., 1997; Kaplan et al., 2007; Meglioli, 1992; Rabassa et al., 2000). Perhaps the best dated pre-LGM glacial sequence is at Lago Buenos Aires (46.5º S) where $^{40}Ar/^{39}Ar$ dating of associated lava flows (Singer et al., 2004; Ton-That et al., 1999) indicates at least six terminal moraines were deposited between 109 ka and

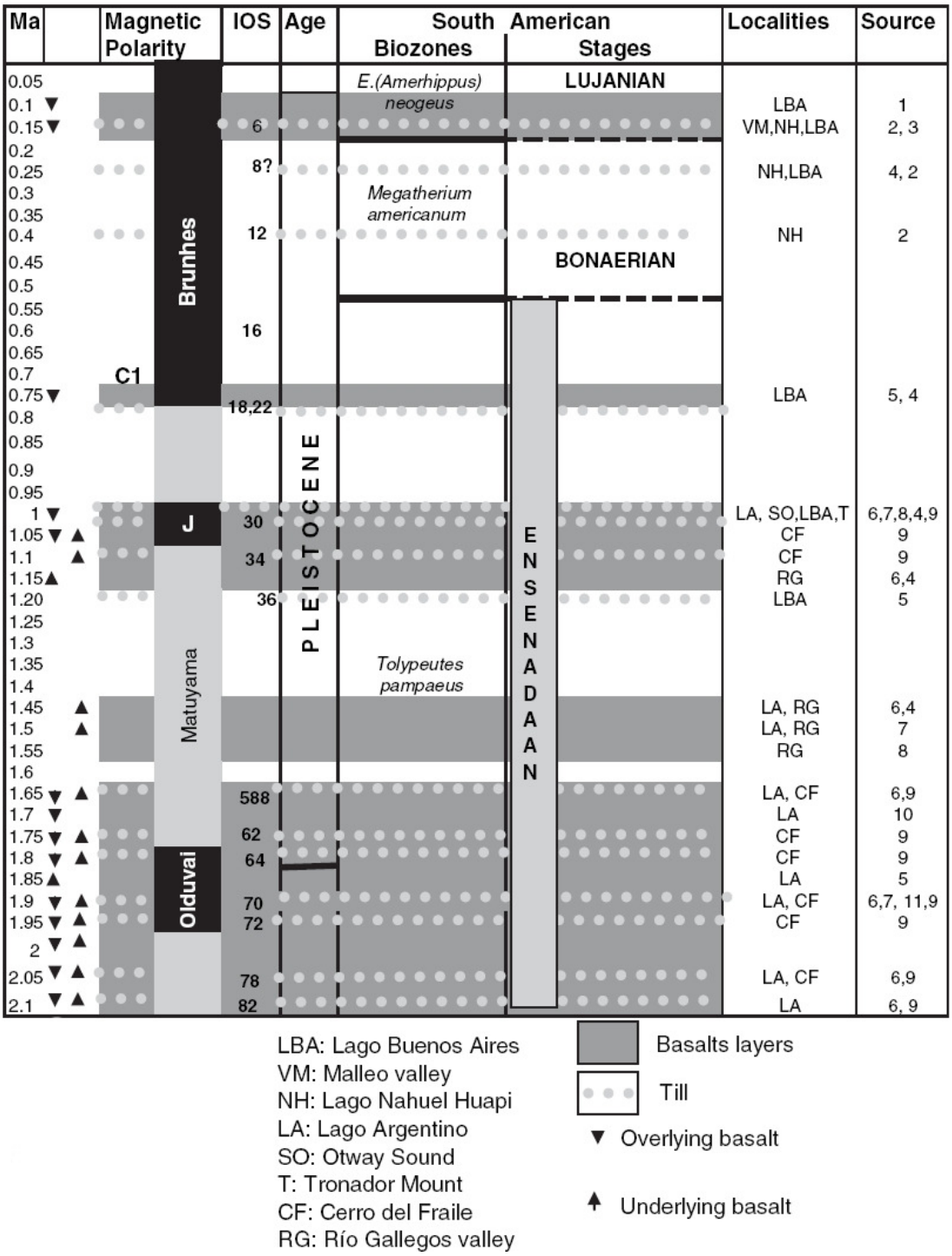

Figure 1.4. Pre-LGM glacial chronology

Summary of the pre-LGM (Quaternary) glacial chronology in Argentine Patagonia (from Rabassa et al., 2005). The IOS refers the the marine oxygen isotope stages and the locations are shown in Fig. 1.1. Sources are 1. (Guillou and Singer, 1997) 2. (Rabassa and Evenson, 1996) 3. (Mercer and Sutter, 1982) 4. (Ton-That et al., 1999) 5. (Sylwan, 1989) 6. (Mercer, 1976) 7. (Mercer, 1983) 8. (Meglioli, 1992) 9. (Rabassa, 1999) 10. (Mercer, 1969) 11. (Schellmann, 1998).

760 ka, and another six between 760 and 1,016 ka. The ages have been further constrained by paleomagnetic studies (Mörner and Sylwan, 1989) and by cosmogenic ^{10}Be, ^{26}Al, ^{3}He surface exposure ages on moraine surface boulders (Kaplan et al., 2005). In sum, several detailed studies have allowed researchers to obtain useful minimum or maximum age constraints, and in some cases to assign particular glacial sequences to the glacial stages evident in the marine isotope record. However, given that bracketing ages are often broad, spanning multiple glacial stages, it is possible that some of the deposits that have been assigned to a particular glacial stage, could in fact relate to another (Rabassa, 2008).

There is now a wealth of data pertaining to former ice extents and paleoclimates of the LGM (Finiglacial – post-Finiglacial) and Holocene periods. The glacial chronology is particularly well-defined in humid localities where glaciers terminated on land such as the Chilean Lake District (e.g., Bentley, 1997; Denton et al., 1999a; Denton et al., 1999b; Lowell et al., 1995; Mercer, 1976; Porter, 1981) and southern Patagonia (e.g., Clapperton et al., 1995; Marden and Clapperton, 1995; McCulloch et al., 2005; Meglioli, 1992; Mercer, 1976; Mercer, 1982; Strelin and Malagnino, 2000; Sugden et al., 2005; Wenzens, 1999) due mainly to extensive radiocarbon dating and more recently by cosmogenic-nuclide surface exposure methods (e.g., Ackert et al., 2008; Douglass et al., 2005; Douglass et al., 2006; Fogwill and Kubik, 2005; Glasser et al., 2006; Kaplan et al., 2004; Kaplan et al., 2007; Kaplan et al., 2008a; McCulloch et al., 2005; Moreno et al., 2009). The latter is of particular relevance to studies in arid Argentine Patagonia where little material is available for radiocarbon dating. For example, at Lago Buenos Aires in central Argentine Patagonia, the Last Glacial

chronology and Holocene moraine ages have been established based on cosmogenic ^{10}Be, ^{26}Al and ^{3}He surface exposure ages on moraine boulders (Douglass et al., 2005; Douglass et al., 2006; Kaplan et al., 2004). In addition to former ice extents, a great deal of paleoclimate information for the period during and after the LGM is available from paleoecological records (e.g., pollen analysis) at various locations in Patagonia. Thus, in general, the LGM glacial chronology and paleoclimate is comparatively well-constrained at key locations throughout Patagonia where records exist.

In summary, the present knowledge of glacial and glaciofluvial sequences in Patagonia is the result of several decades of research. The introduction of geochronometers such as K-Ar, ^{40}Ar/^{39}Ar, radiocarbon, and cosmogenic-nuclide surface exposure age dating has permitted the quantitative determination of the age of glacial sequences throughout Patagonia. However, each chronometer has its limitations. Radiocarbon dating of material associated with glacial deposits is restricted spatially to zones of high humidity, and temporally to the last glacial cycle given the short half-life of ^{14}C which limits the range of accurate dating to ca. 40 ka. K-Ar and ^{40}Ar/^{39}Ar methods can be highly accurate across the temporal range of glacial sequences in Patagonian (ca. 1.1 Ma), but are limited by the presence or absence of such lava flow associations. Other geochronometers such as Uranium-thorium disequilibria and Optically Stimulated Luminescence have proved useful in some Patagonian environments (e.g., Glasser et al., 2006; Phillips et al., 2006) but are normally limited temporally to less than ca. 500 ka. Thus, direct dating of the well-preserved ice-contact or associated glacial deposits in Patagonia by cosmogenic-nuclide surface exposure methods may be the most appropriate

geochronometer because it is, in theory, not limited spatially or temporally given the target mineral (normally quartz) is abundant in most Andean lithologies, and the age of the glacial sequences are within the dating range of cosmogenic nuclides such as ^{10}Be and ^{26}Al.

In practice, the method is limited by environmental conditions that can affect the continuous exposure of surface material and rock surface erosion rates. These can be highly variable and difficult to assess in the field, and they become increasingly problematic and limiting on older surfaces. For example, exposure ages from numerous boulders on moraines known to be 150 ka – 1,100 ka in Tierra del Fuego of southernmost South America (ca. 53º S), give ages of less than 100 ka in all cases; thus erosion or exhumation of the boulder surfaces has limited the applicability of these methods to the last glacial cycle in this area (Kaplan et al., 2007). In contrast, exposure ages from boulders on pre-LGM moraines at Lago Buenos Aires (46.5º S) give ages of ca. 150 ka that are consistent with minimum ages obtained from independently dated lava flows (Kaplan et al., 2005). These important initial studies indicate that central Patagonia is better situated to test a new approach aimed at extending the useful range of exposure dating in this environment. Thus overall, there remains much potential to better pinpoint the temporal sequence of glacial events in southern South America, and in doing so to better exploit an unparalleled continuous sequence of Quaternary moraines that indicates long-term terrestrial climate oscillations.

1.3 Wider implications

Even if I can determine the climate change, there are many different potential causes. Over Quaternary timescales, we have to consider the major factors linking globally forced events to local expression of phenomena such as glacier change. The development of glacial chronologies is essential for reconstructing former terrestrial climates and it contributes to an understanding of the cause of major ice ages and the physical mechanisms responsible for the transmission of global climates. At present, these processes are not well-understood. There is general consensus that long-term variations in the characteristic of Earth's orbit around the Sun plays a critical role. The so-called 'Milankovitch cycles' affect the intensity of solar radiation received across the Earth's surface, with lower summer insolation (i.e., with shorter and/or cooler summers) promoting ice growth as winter snowfalls persist throughout the ablation season (e.g., Huybers, 2006). Marine and ice core data show strong correlation with orbital frequencies, particularly the ~100 ka eccentricity cycle for the past ca. 600 ka to 800 ka, and the ~40 ka obliquity cycle prior to ca. 1 Ma (e.g., Hays et al., 1976).

There is no consensus on exactly how orbital variations influence or modulate global climates as observed in proxy records (e.g., Karner and Muller, 2000). Orbital variations alone may not be significant enough to initiate an ice age (e.g., see Wunsch, 2004), and other triggers and feedback mechanisms may be necessary to explain their initiation and the transmission of climates across the globe. Potential triggers include the changing concentration of greenhouse gases such as CO_2 and slowdown or shutdown of thermohaline ocean circulation which brings warm ocean

currents to the higher latitudes (e.g., Broecker and Denton, 1989). However, it is unclear if such changes are initiated in the northern hemisphere (e.g., Bender et al., 1994) or the southern hemisphere (e.g., Blunier et al., 1998). Thus, determining the leads and lags of climatic changes in opposing hemispheres is one way to better understand the processes involved. Accurate dating of glacial moraines in both hemispheres is one way to compare the timing of terrestrial climate changes and to further investigate the causes and mechanisms that drive global climate changes. Geochronometers such as radiocarbon and cosmogenic nuclide dating are becoming increasingly accurate and thus able to resolve these differences, at least for the last glacial cycle (e.g., Denton et al., 1999a; Kaplan et al., 2004).

The Patagonian glacial record has provided useful insight into climate changes since the LGM. Previous studies have shown millennial-scale fluctuations of Patagonian glaciers that are synchronous with northern hemisphere climate signals; these wide-spread rapid climate changes in both hemispheres suggest atmospheric causes for the transmission of global climate during the LGM (e.g., Denton et al., 1999a; Kaplan et al., 2004). In southernmost Patagonia, Late-glacial deviation from the dominant northern hemisphere signal is evident on millennial time-scales where glaciers advanced synchronous with southern hemisphere forcing as observed in Antarctic ice cores (i.e., the Antarctic Cold Reversal) (Fogwill and Kubik, 2005; McCulloch et al., 2005; Moreno et al., 2009; Sugden et al., 2005); thus the climate and Patagonian glacier response is complicated. Little is known about southern hemisphere terrestrial climate prior to the LGM. The Patagonian glacial record provides a unique opportunity to investigate long-term climate changes in the southern

hemisphere since the Early Pleistocene. While the dating resolution of cosmogenic nuclides precludes resolving hemispheric leads and lags for pre-LGM glacial sequences, determining the presence or absence and extent of particular glacial stages gives important insight into the relative severity of different glacial stages; this offers the potential to provide a wealth of new information with respect to atmospheric circulation (i.e., the strength and position of the southern westerlies), the contribution of Patagonian glaciers to global sea-level and to the evolution of the Patagonian landscape throughout the Quaternary.

1.4 Study area

This thesis focuses on the glacial geologic record in the Lago Pueyrredón valley, which is situated at 47.5º S in central Patagonia and is located east of the present-day North Patagonian Icefield and immediately south of the Lago Buenos Aires (LBA) valley, 46.5º S. The valley was a major eastern outlet of former Patagonian ice sheets. The close proximity to LBA is advantageous for this study because the glacial sequences in the LBA valley are constrained by K-Ar and $^{40}Ar/^{39}Ar$ dated lava flows (Singer et al., 2004) and cosmogenic-nuclide surface exposure ages (^{10}Be, ^{26}Al, ^{3}He; Douglass et al., 2006; Kaplan et al., 2004; Kaplan et al., 2005), thus comparisons can be drawn against equivalent and previously dated glacial sequences in this nearby valley. In addition, environmental conditions are similar and thus are known to be suitable for cosmogenic-nuclide surface exposure age dating (cf. Kaplan et al., 2005). The glacial sequences in the Lago Pueyrredón valley (Fig. 1.5) are

well-preserved but the chronology is not well constrained, making it an ideal location for

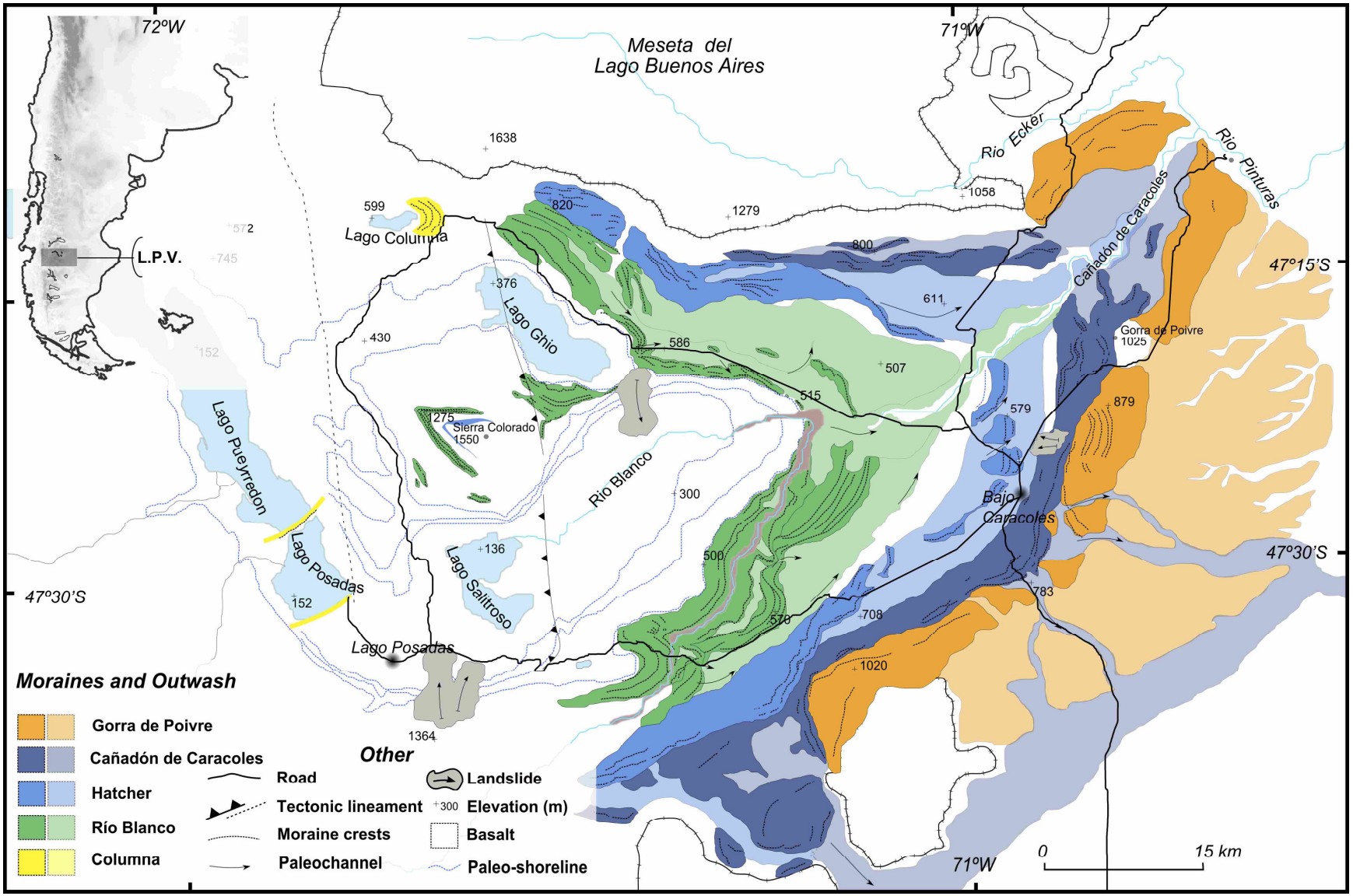

Figure 1.5. Geomorphic map of the Lago Pueyrredón valley

this study. The local geology, climate and glacial sequences in and around the Lago Pueyrredón valley are discussed in Chapters Three to Five.

The valley contains a rich geomorphic record that includes glacial features such as moraines, outwash terraces, rock drumlins and striated and grooved bedrock (Fig. 1.6). In addition to glacial features, the geomorphic record also includes paleolake levels (Fig. 1.7), large landslide deposits (Fig. 1.7), faults and cave paintings and etchings (Fig. 1.8). Given the size of the field area (ca. 5,000 km^2), I necessarily focus on the main geomorphic features as interpreted in the field, and thus have only scratched the surface with respect to the fascinating geomorphology in this valley. There is no doubt that more comprehensive mapping will reveal further intricacies in the detail of the geomorphic record that is presented here.

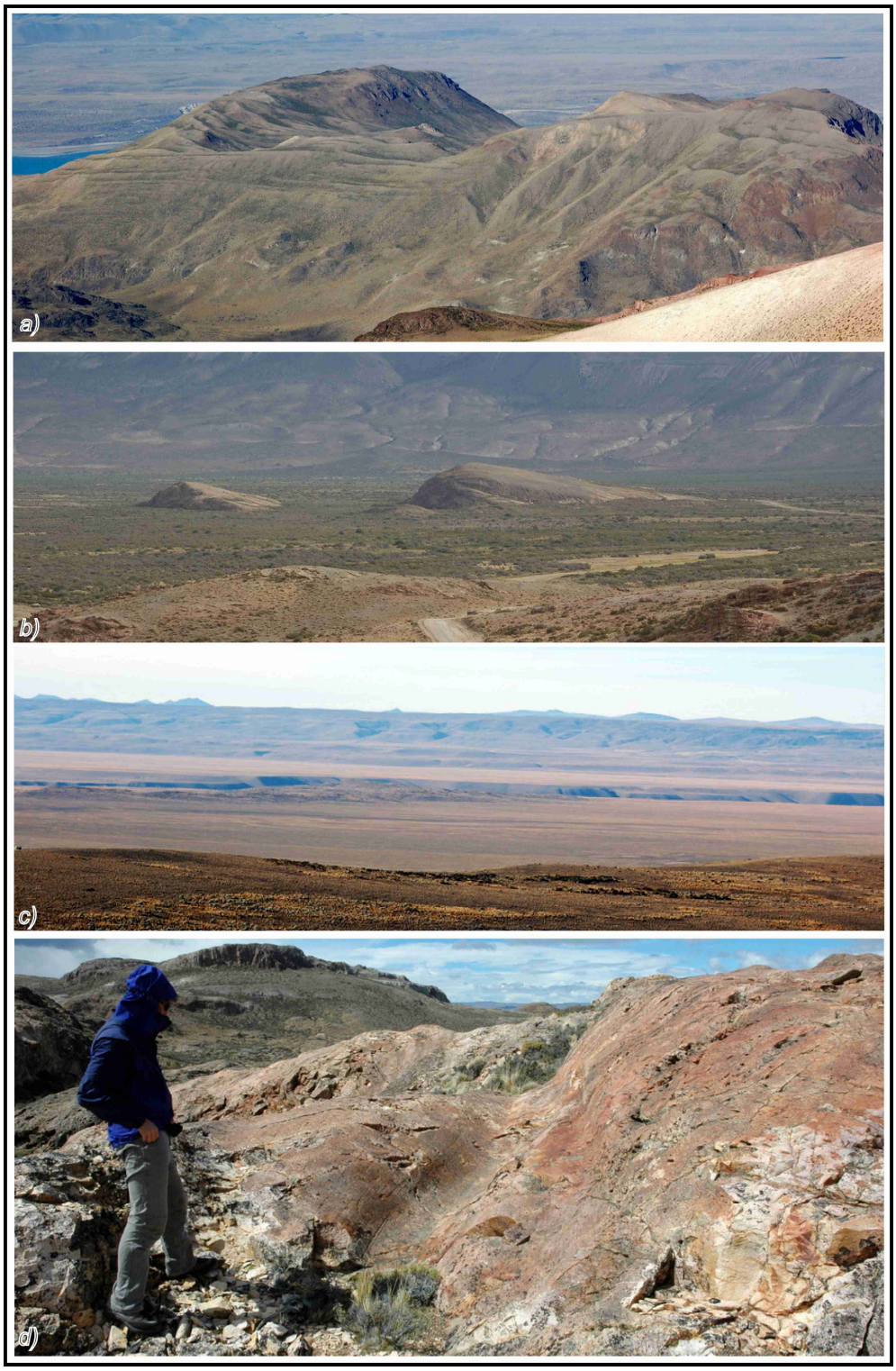

Figure 1.6. Photos of the Lago Pueyrredón valley

a) Series of moraines located on a hill (~2 km width) north of Sierra Colorado, from which the photo was taken. b) Rock drumlins in the Lago Pueyrredón valley west of Lago Posadas village. The height is about 50 meters. c) The Hatcher outwash terrace; or scale, the terrace in the center spans ~10 km left to right. d) Striated and grooved bedrock with A. Hein for scale.

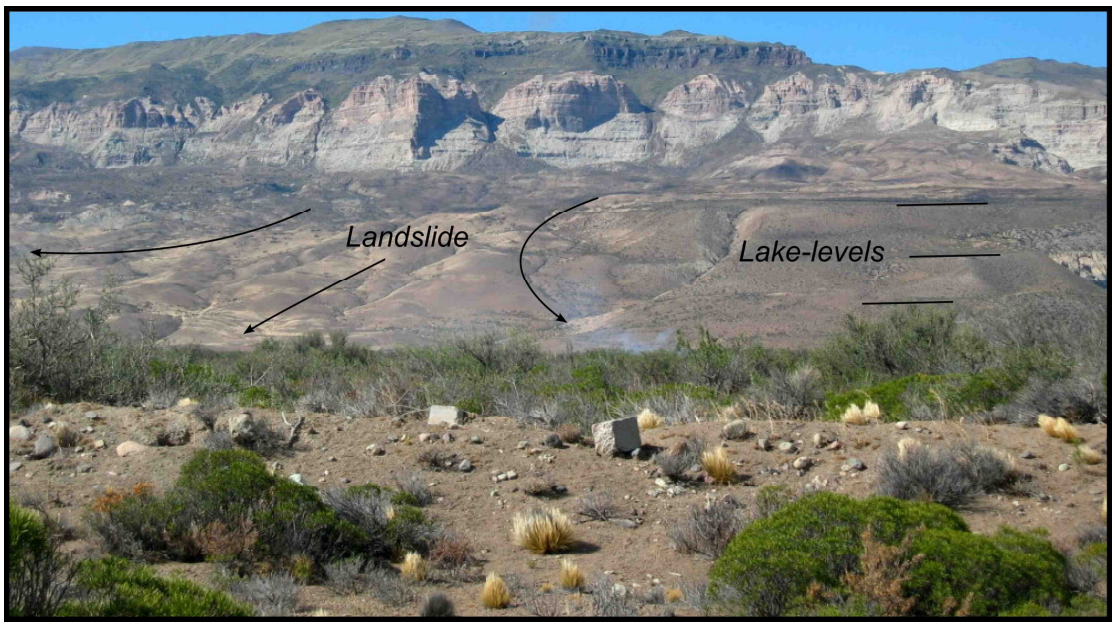

Figure 1.7. Landslides and lake levels

Large landslide cross-cutting paleolake levels (the levels are ca. 100m apart).



Figure 1.8. Cave paintings

Cave painting located near Cerro de los Indios, south of Lago Posadas village (Fig. 1.5). These paintings are estimated to be ca. 3.8 ka old however this age has not been confirmed.

1.5 Objectives

Given the aims of this research, I focus on developing the chronology of the glacial sequences in the Lago Pueyrredón valley, Argentina. Cosmogenic-nuclide surface exposure age dating methods are utilized to achieve the following specific research objectives:

1. Determine if the youngest moraines on the eastern margin of the valley date to the LGM or to the Late-glacial to Holocene period as previously suggested (Wenzens, 2005). This has major implications for paleoclimates in central Patagonia (Chapter Three).
2. Develop a more reliable approach to directly dating old (i.e., pre-LGM) glacial sequences by cosmogenic-nuclide surface exposure methods and test the approach by dating the penultimate glacial sequence in the valley (Chapter Four).
3. Evaluate how robust the approach is by directly dating the oldest glacial sequences in the valley; these are age-equivalent to the independently dated 'Greatest Patagonian Glaciation' at ca. 1.1 Ma (Chapter Five).

1.6 Thesis scope

A chronology based on surface exposure dating is necessarily limited to ice contact and associated landforms; these are known to span more than one million years in Patagonia. Although older glacial deposits exist as isolated till sheets, they are not discussed further in this thesis. Therefore, the 'oldest' glacial sequences in Patagonia

are discussed with reference to deposits with identifiable ice limits (i.e., moraines) as opposed to till sheets that may be older but from which no further information on former ice extent can be obtained. This work will show that it is possible to obtain reliable age constraints from even the oldest glacial sequences in the Lago Pueyrredón valley by surface exposure methods.

Chapter Two briefly introduces cosmogenic-nuclide surface exposure age dating methods which form the principal analytical technique utilized in this study. Chapters Three to Five detail the chronology of the different glacial sequences in the Lago Pueyrredón valley. Each chapter is written in the form of a journal article and details of authorship and publication status are provided where appropriate.

Chapter Three details the last glacial chronology of the Lago Pueyrredón valley. This includes the timing of the LGM maximum extent, the onset of deglaciation and the development of a series of linked pro-glacial lakes in the region. In addition, it synthesizes existing radiocarbon and cosmogenic nuclide ages in central Patagonia and other ice limits with age constraints throughout Patagonia.

Chapter Four details the approach used to date pre-LGM glacial deposits by cosmogenic-nuclide surface exposure methods. Surface cobbles on stable outwash terraces are used to date the penultimate glacial sequence in the valley at 260 ka or Marine Isotope Stage 8.

Chapter Five evaluates this approach by directly dating the oldest glacial sequence in the valley. ^{10}Be exposure ages of 1.0 – 1.2 Ma are consistent with independent age constraints of ca. 1.1 Ma (Singer et al., 2004; Ton-That et al., 1999) dated elsewhere on stratigraphically equivalent deposits. Additionally, exposure ages of ca. 600 ka indicate a glacial advance that may correspond with Marine Isotope Stage 16.

Chapter Six summarizes the approach used to date old glacial sequences and synthesizes the chronology developed. In particular, it draws comparisons to glacial chronologies dated in Patagonia and around the world, and to marine and ice core records. It discusses the potential role of the southern westerlies and other non-climatic influences on the pattern of preservation observed at Lago Pueyrredón.

Chapter 2 Methodology

2.1 Introduction

My approach to developing a better understanding of the nature and timing of Quaternary glaciations in Argentine Patagonia is to establish the geomorphic relationships and chronostratigraphy of glacial sequences in a major outlet of former Patagonian ice sheets, the Lago Pueyrredón valley. The glacial geomorphology in the valley was mapped previously by Caldenius (1932), Feruglio (1950) and more recently by Wenzens (2005), however the chronology has been limited to the techniques available to these authors through time. This work builds upon earlier work in the valley by providing a new chronology and, in places, a new interpretation of the geomorphic record. Thus, given that generally good maps were previously available, the main contribution of this study is the establishment of an extended and better constrained chronolology; this forms the basis of the following chapters. The geomorphic mapping is briefly discussed and the remainder of the chapter focuses on the cosmogenic-nuclide methodology which is the analytical technique that is considered most appropriate for dating the Quaternary glacial sequences in central Argentine Patagonia (Chapter 1.2). The chapter concludes with a short discussion on considerations for sampling and the limitations of the dating technique.

2.2 Geomorphic mapping

Detailed geomorphic maps were required to determine the relative ages of the different moraine crests and outwash terraces within a particular glacial sequence. This was necessary to establish logical places in which to sample the surface for cosmogenic-nuclide surface exposure age dating. In this study, I primarily focus on determining the timing of maximum extent for each glacial sequence; thus mapping the outermost moraine crest and associated outwash terrace was a priority. This allows us to determine when the climatic conditions that favored glaciation had peaked. The geomorphology of the younger Río Blanco glacial sequence is better preserved but with greater complexity. For this sequence, I wanted to determine not only the timing of maximum extent, but also the timing of key readvances and the onset of deglaciation, and thus a more detailed assessment of the geomorphology was required.

The mapping was completed using conventional techniques based on satellite remote sensing and field observations. The datasets include an SRTM (90m) DEM, an ASTER (30m) DEM, Landsat (30m) and ASTER (15m) multispectral imagery and imagery available in Google Earth. The DEMs were artificially illuminated using functions available in ESRI's ArcGIS program; this helped to identify moraine crests and terrace scarps. The bulk of the field work and mapping was undertaken in February 2007 over the course of three weeks. The focus was on resolving some of the complex areas identified in the satellite imagery, such as the southernmost moraine complex in the Río Blanco moraine system. This involved describing the geomorphic associations (e.g., cross-cutting relationships) and locating sections in

which the stratigraphy could be assessed. In general, my mapping is largely consistent with that of Wenzens (2005) but with some distinct differences regarding the relative ages of the different moraine sequences. The mapping has refined existing geomorphic maps and identified new ice limits and paleoshoreline associations. The mapping and these features are discussed further in Chapter Three.

2.3 Cosmogenic-nuclide methodology

Terrestrial cosmogenic nuclides (e.g., ^{10}Be, ^{26}Al, ^{36}Cl, ^{14}C, ^{3}He, ^{21}Ne) are formed in situ in near-surface rocks exposed to cosmic radiation. The routine measurement of their extremely low concentrations was made possible by the development of accelerator mass spectrometry (AMS) and highly sensitive noble-gas mass spectrometry in the early 1980s (Gosse and Phillips, 2001). Subsequently, their concentrations in near surface material have been used to quantify a wide range of surficial geologic/geomorphic processes such as the timing of glacial advances, fault-slip rates, bedrock and basin-wide erosion rates and sediment burial. This chapter introduces their application to exposure dating of glacial sediments.

Exposure dating allows for the direct dating of sediment exposed on glacial and glaciofluvial landforms. The assumption is that the sediment was first exposed to cosmic radiation at the time of deposition and remained fully exposed post-deposition. If the production rate of the cosmogenic nuclide is known, the age of the surface can be calculated by measuring the concentration of cosmogenic nuclides that have accumulated in the rock surface. The accuracy is dependent on many

factors that will be discussed throughout this chapter. In this study, I selected the cosmogenic nuclides ^{10}Be and ^{26}Al because their half-lives are appropriate and they are formed in quartz, which is abundant in typical Andean lithologies. The remainder of this chapter introduces the theory behind the technique and the factors that affect the production of cosmogenic nuclides. The aim is to provide sufficient background to enable the reader to appreciate the context of underlying arguments put forth in the following three chapters. It is not intended to be a comprehensive discussion on the topic and readers are directed elsewhere for such treatment (e.g., Gosse and Phillips, 2001).

2.3.1 Cosmic radiation

The Earth is continually showered by cosmic radiation causing the production of rare cosmogenic nuclides in terrestrial rocks. Primary cosmic rays are mainly galactic in origin and are composed of highly energetic particles (mostly between ~ 0.1 and 10 GeV) of which 87% are protons, 12% α-particles, and 1% heavy nuclei (Masarik and Beer, 1999; Masarik and Reedy, 1995). The trajectories of these charged particles within our solar system are heavily influenced by interplanetary magnetic fields that are carried by solar winds, and the geomagnetic field becomes the dominant influence on particle trajectories closer to the Earth (Pigati and Lifton, 2004). Incoming primary cosmic rays either penetrate the Earth's magnetic field or are deflected by it depending on the particle's 'rigidity' (momentum to charge ratio) and angle of incidence (Masarik and Beer, 1999). The cutoff rigidity is the threshold rigidity required for penetration; it changes depending on the incoming particle's angle of incidence and location relative to geomagnetic field lines, and thus it varies

with geomagnetic latitude. Cutoff rigidity is highest near the geomagnetic equator where field lines are perpendicular to the average trajectory of incoming primaries, and lowest at the poles where field lines are oriented near-vertical at high geomagnetic latitudes (> ca. 60º). Consequently all incoming primary cosmic rays exceed the cutoff rigidity and can enter Earth's atmosphere (Gosse and Phillips, 2001; Pigati and Lifton, 2004). Primary cosmic ray particles of solar origin have low energies (< 100 MeV) and can only enter Earth's atmosphere in polar regions, and can only produce cosmogenic nuclides in the upper atmosphere, except during periods of extreme solar activity (Masarik and Reedy, 1995). Therefore, they are relatively unimportant for studies of in-situ terrestrial cosmogenic nuclides and are not discussed further.

The primary galactic cosmic ray flux is essentially constant over the timescales relevant for most geomorphic applications (10^3 – 10^6 a), including the work presented in this thesis (Leya et al., 2000; Reedy et al., 1983). However, high frequency (10^0-10^2 a) variations occur, which can be relevant for deriving the models used to scale the production of cosmogenic nuclides. The high frequency variations are caused by solar modulation of mainly low energy galactic cosmic rays (cutoff rigidity < 1 GV) and are related to cyclic changes in solar activity (i.e., solar cycles)(Lal and Peters, 1967; Lifton et al., 2005). They mainly affect the cosmic ray flux at high latitudes where the cutoff rigidity is low (Lifton et al., 2005). However, they can be important to consider for scaling production of cosmogenic nuclides because the neutron flux data used to derive scaling models are influenced by solar

variability; and the long-term average solar influence on the galactic cosmic ray flux is not well known (Lifton et al., 2005).

The most significant variations in the long-term cosmic ray flux at the Earth's surface come from variations in the character of Earth's magnetic field, which exerts the primary influence on cosmic ray trajectories. The Earth's magnetic field closely approximates a geocentric axial dipole (GAD) on timescales of 10^3 to 10^5 a (Dunai, 2000; Dunai, 2001; Pigati and Lifton, 2004). However, non-dipole components can account for 10 – 25% of the total field strength at a given time and location (Dunai, 2001). Secular variations of intensity and position of the dipole and non-dipole components affect the flux of cosmic radiation received at Earth's surface (see Dunai, 2001). Some of these geomagnetic variations can be reconstructed through various proxy records (e.g., SINT800; Guyodo and Valet, 1999), and cosmogenic nuclide production rates can be scaled accordingly (e.g., Desilets and Zreda, 2003; Dunai, 2001; Lifton et al., 2005).

2.3.2 Secondary cosmic rays

The primary cosmic ray particles that penetrate Earth's atmosphere produce a shower of secondary particles that are responsible for production of most in-situ cosmogenic nuclides found in terrestrial rocks (Fig 2.1). The secondary particles are formed by collision of primary cosmic rays with atmospheric gas nuclei; they include high energy nucleons (e.g., protons and neutrons) and mesons (e.g., kaons, pions and muons)(Gosse and Phillips, 2001; Pigati and Lifton, 2004). Below an atmospheric depth of ca. 100 g cm^{-2}, the secondary nucleonic cosmic ray intensity decreases

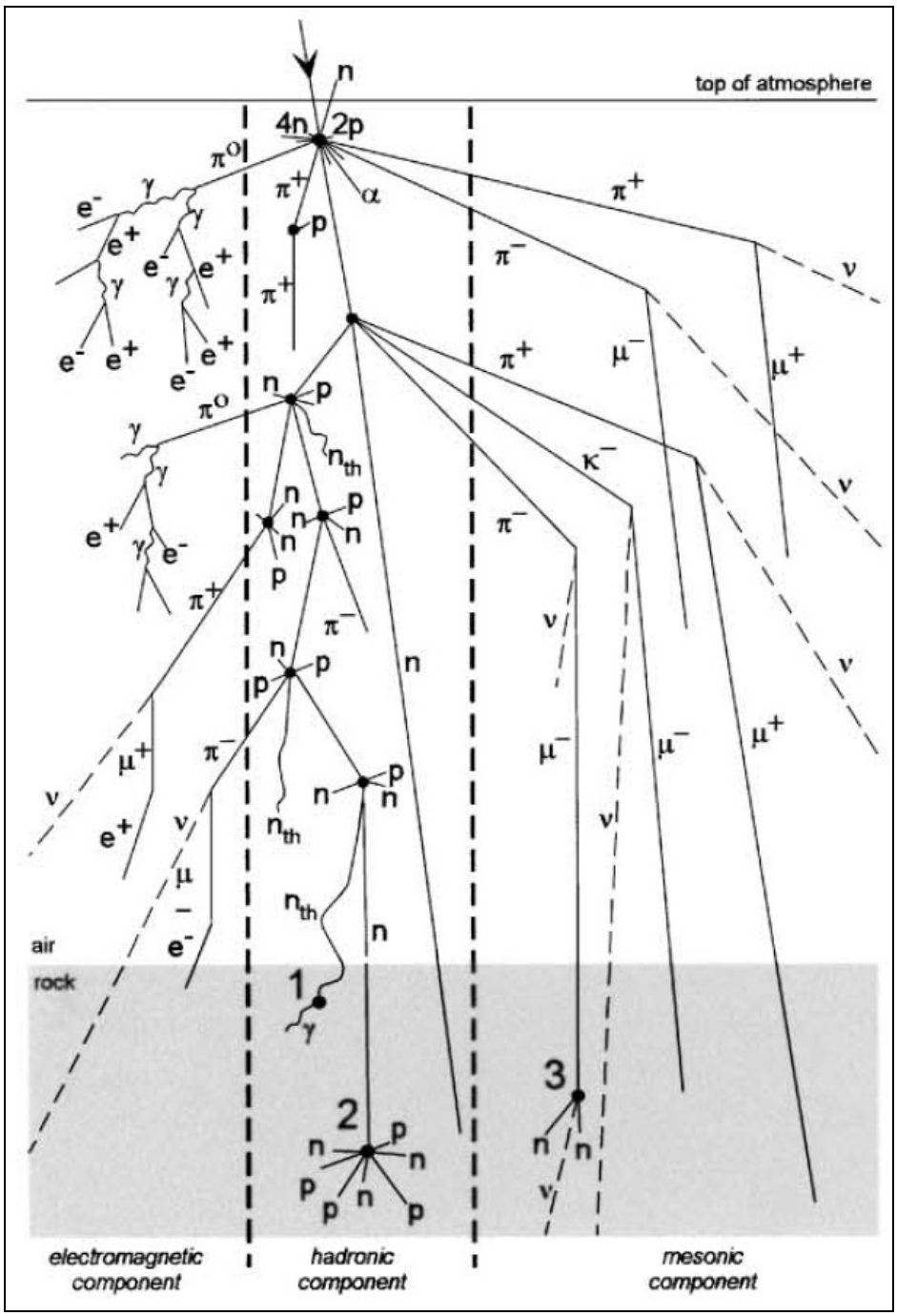

Figure 2.1. Cosmic ray nuclear cascade

Schematic of secondary cosmic ray flux resulting from interaction of a primary galactic cosmic ray particle with atmospheric nuclei. The high energy hadronic (nucleonic) component is highly reactive causing spallation reactions that dominate ^{10}Be and ^{26}Al production at the rock surface. Muons are low mass particles formed by decay of $\pi^{\pm}$ and $K^{\pm}$ mesons, are less reactive and have larger attenuation lengths. The numbers refer to example reactions 1) $^{35}Cl(n_{th},\gamma)^{36}Cl$; 2) $^{16}O(n,4p3n)^{10}Be$; 3) $^{28}Si(\mu^{-},2n)^{26}Al$ (figure from Gosse and Phillips, 2001).

roughly exponentially with increasing atmospheric depth. This attenuation of cosmic rays occurs as a result of further collisions and interactions (e.g., scattering, absorption) that dissipates energy (Gosse and Phillips, 2001). Thus, the intensity of the nucleonic cosmic ray flux decreases with altitude (i.e., at increasing atmospheric depths).

The attenuation length refers to the thickness (g cm^{-2}) of mass required to attenuate the cosmic ray intensity by a factor of e^{-1} (Gosse and Phillips, 2001). This is dependent on the geomagnetic latitude and altitude, and for fast nucleons in the atmosphere below mountain elevations, varies between roughly 130 to 150 g cm^{-2} at polar and equatorial regions, respectively (Dunai, 2000). The higher attenuation length at low latitudes reflects the greater rigidity required of incoming particles (Lingenfelter, 1963). Atmospheric conditions also affect the cosmic ray flux because air pressure (i.e., atmospheric depth) is not spatially or temporally uniform (e.g., Dunai, 2000; Staiger et al., 2007; Stone, 2000). The variable attenuation lengths caused by geomagnetic and atmospheric factors are important for the scaling of production rates of cosmogenic nuclides at the Earth's surface.

2.3.2.1 In-situ cosmogenic ^{10}Be and ^{26}Al production

Cosmogenic nuclides are produced in the atmosphere and in situ by reaction between secondary particles and various target nuclei. The secondary particles relevant for the production of in-situ terrestrial cosmogenic nuclides include high energy nucleons (mainly neutrons), low energy neutrons (thermal and epithermal) and muons. At the Earth's surface, about half of the cosmic ray flux is composed of

energetic muons and the nucleonic component is dominated by neutrons (Gosse and Phillips, 2001).

The production of ^{10}Be and ^{26}Al in quartz (SiO_2; the mineral target used in this study) at the rock surface is dominated (~97.5%) by spallation reactions (Stone, 2000). A spallation reaction occurs when a high energy nucleon (e.g., neutron) collides with a target nucleus thereby spalling off several lighter particles and leaving behind a lighter residual nucleus (Gosse and Phillips, 2001). ^{10}Be is most commonly formed by spallation on oxygen by the reaction $^{16}O(n,4p3n)^{10}Be$, and to a lesser degree on silicon by the reaction $^{28}Si(n, x)^{10}Be$ (Gosse and Phillips, 2001). ^{10}Be is produced at higher rates in the atmosphere; this 'meteoric' ^{10}Be can attach to mineral surfaces and thereby contaminate the in-situ concentration; however meteoric ^{10}Be can be removed by acid leaching (Kohl and Nishiizumi, 1992). ^{26}Al is most commonly formed by spallation on silicon nuclei by the reaction $^{28}Si(n,p2n)^{26}Al$ (Gosse and Phillips, 2001).

Attenuation lengths of ~150 – 170 g cm^{-2} have been derived for fast nucleons in surface rocks (e.g., Brown et al., 1992; Farber et al., 2008); thus the nucleonic cosmic ray flux is absorbed rapidly and roughly exponentially in the top few meters of terrestrial rock until unable to cause spallation reactions at energies < ~5 MeV (Gosse and Phillips, 2001).

Production of ^{10}Be and ^{26}Al in quartz also occurs to a lesser degree by muon reactions. Muons are formed by decay of unstable $\pi^{\pm}$ and $K^{\pm}$ mesons, a product of

primary cosmic ray reactions in the upper atmosphere (Gosse and Phillips, 2001). These low-mass particles, unlike the nucleonic component of the cosmic ray flux, are not highly reactive and thus can penetrate far beneath Earth's surface; the average attenuation length in rock being ~1500 g cm^{-2} (Brown et al., 1995; Gosse and Phillips, 2001). The muon production of ^{10}Be and ^{26}Al mainly occurs by capture of slow negative muons by charged nuclei (Heisinger et al., 2002a), and to some extent by interactions of fast muons (Heisinger et al., 2002b). Slow negative muon production of ^{10}Be in quartz occurs mainly by the reaction $^{16}O(\mu^-, 3p3n)^{10}Be$, and ^{26}Al by the reaction $^{28}Si(\mu^-,2n)^{26}Al$ (Nishiizumi et al., 1989). At the rock surface, muon production of ^{10}Be and ^{26}Al in quartz is relatively unimportant (~2.5%; Stone, 2000) compared to spallogenic reactions, but becomes increasingly significant at depth as spallogenic reactions decrease. Thus, production by muons is mainly of significance for studies of erosion rates, or where samples are taken from depth.

2.3.3 Production rates and scaling factors

To determine a surface exposure age based on the in-situ accumulation of a particular cosmogenic nuclide in a particular target mineral, the production rate is required. The production of in-situ cosmogenic nuclides in Earth surface material is dependent on the cosmic ray flux at the sample location. This varies with latitude, altitude and local shielding conditions. Thus, scaling factors are required to account for these various processes and factors. This section introduces scaling factors relevant to this study and reference production rates for ^{10}Be and ^{26}Al.

2.3.3.1 Scaling factors

Spatial

Several scaling models are available to account for latitudinal and altitudinal variations in the cosmic ray flux. More recent models incorporate temporal variations due to solar modulation (Lifton et al., 2005) and the changing geomagnetic field (e.g., Desilets et al., 2006; Dunai, 2001; Lifton et al., 2005). All scaling models in use today are based at least partly on the same neutron flux datasets (e.g., photographic emulsions, neutron monitors, cloud chambers) that were obtained by aircraft and ship-mounted instruments and fixed stations on land after the late 1940s (e.g., Desilets and Zreda, 2003; Dunai, 2000; Lifton et al., 2005). The scaling models differ on many levels, however they all fit geologic calibration data within uncertainty of each other and thus, at present, there is no reason to favor one model over another (Balco et al., 2008).

The first and most widely referenced scaling model is that of Lal (1991). Lal (1991) formulated a set of equations describing the variation of total production rates with geographic latitude and altitude based on a geocentric dipole field and a uniform standard atmosphere. Subsequent adaptations of Lal's basic model and derivation of new scaling models address some of the invalid assumptions inherent in the Lal (1991) model. For example, Stone (2000) reformulates Lal's (1991) basic scaling relationship as a function of atmospheric pressure as opposed to altitude, and includes separate altitudinal scaling for muons with a lower contribution (~2.5%) than Lal's 15%. This change allows regional deviations in atmospheric pressure (e.g., over Antarctica) to be included in the production rate calculations. Typically, the effect of incorporating a more realistic pressure field results in minor changes in

production rates of less than 3-4%, but can reach 30% around Antarctica for example (Stone, 2000).

The geomagnetic field is not a perfect geocentric dipole, and the non-dipole component of the total field strength reaches 10 – 25%; recognizing this, Dunai (2000) scales for dipole and non-dipole effects by ordering the neutron monitor data by geomagnetic inclination at the measurement site. The Dunai (2000) scaling model better characterizes the geomagnetic field (referenced to the International Geomagnetic Reference Field (IGRF) for 1955; Langel et al., 1988) while also allowing for variations in atmospheric depth. To include secular variations in the geomagnetic field (e.g., dipole moment, intensity) as recorded by various proxy records (e.g., SINT800; Guyodo and Valet, 1999), Dunai (2001) re-orders the neutron monitor data by the geomagnetic cutoff rigidity at the measurement site; this allows scaling for temporal variations in the geomagnetic field. Subsequent scaling models (e.g., Desilets and Zreda, 2003; Desilets et al., 2006; Lifton et al., 2005) also include time-dependent variations in the geomagnetic field, but differ in how they derive the cutoff rigidity. For example, Dunai (2001) calculates the cutoff rigidity based on inclination and horizontal field strengths whereas Lifton et al. (2005) and Desilets et al. (2006) calculate the cutoff rigidity directly by trajectory tracing (Balco et al., 2008). The time-dependent scaling models are generally in good agreement with each other and differ from the Lal(1991)/Stone(2000) model mainly in the altitudinal dependence, with the newer models predicting higher production rates at high altitudes and lower production rates at low altitudes (Balco et al., 2008). Fig. 2.2 demonstrates this effect at Lago Pueyrredón; however, the deposits in the valley

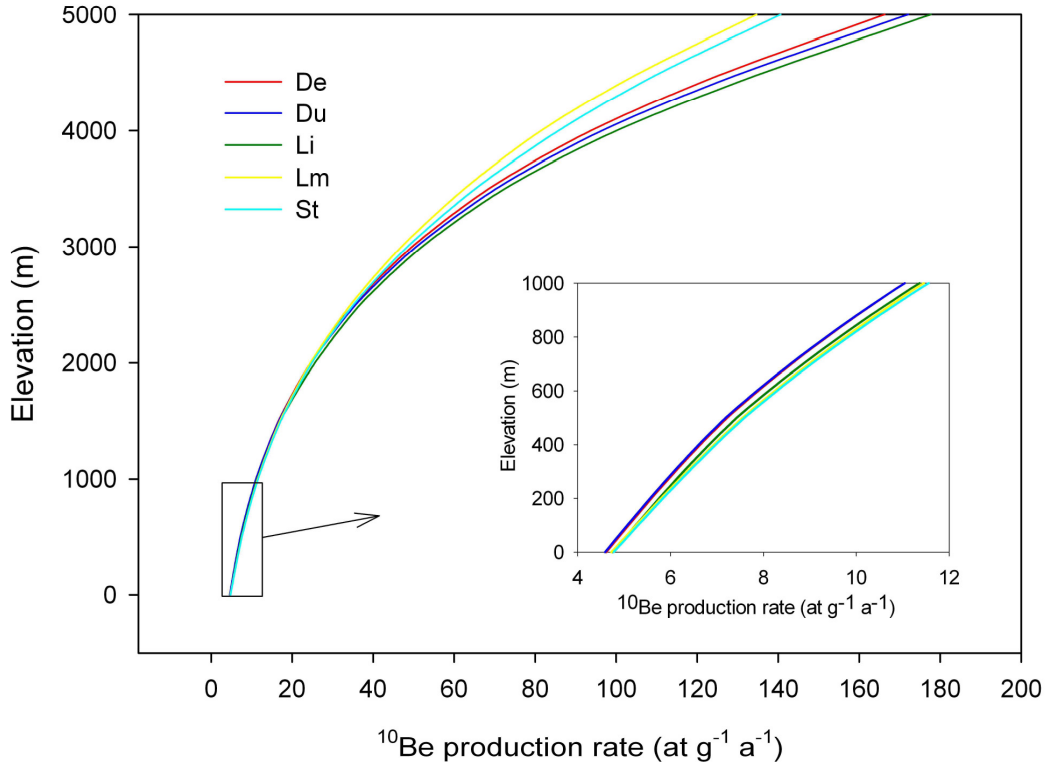

Figure 2.2. Production rate variation with altitude: Scaling model dependencies

Plot showing the variation in the total production rate with altitude at Lago Pueyrredón (47.5° S) based on five different scaling models: De (Desilets et al., 2006), Du (Dunai, 2001), Li (Lifton et al., 2005) Lm (Lal(1991)/Stone(2000)/Nishiizumi et al. (1989)), St (Lal(1991)/Stone(2000)). Production rates based on the CRONUS-Earth exposure age calculator (Balco et al., 2008). The De, Du and Li models yield 25-30% higher production rates than the Lm and St models at high altitudes, and slightly lower production rates at low altitudes. At elevations relevant for the glacial deposits at Lago Pueyrredón (ca. 300m – 900m; inset), production rates vary by less than 6%.

are generally at elevations of less than 900m and therefore production rates in this study vary by less than 6% depending on the choice of scaling model.

Topography and local obstructions

The cosmic ray flux at a particular sample location may be considerably reduced due to shielding by local obstructions such as surrounding topography (i.e., mountains), sloped surfaces, local rock formations, vegetation, etc. (e.g., Dunne et al., 1999).

The reduction in the cosmic ray flux will affect the local production rate and will lead to erroneously young exposure ages if not accounted for. Several authors formulate equations to scale for these obstructions (e.g., Dunne et al., 1999; Gosse and Phillips, 2001; Nishiizumi et al., 1989). Dunne et al. (1999) calculate the scaling factor (S_G) for a set of n obstructions blocking the full 2π horizon by calculating the ratio of the remaining flux to the maximum flux:

$$S_G = 1 - \frac{1}{360}\sum_{i=1}^{n} \Delta\phi_i \sin^{m+1}\theta_i \qquad (2.1)$$

where $\Delta\varphi_i$ is the change in azimuth, and m is an experimentally derived constant (m=2.3), and θ_i is the inclination angle from the horizon of each obstruction. Because the atmospheric depth is thickest for particles traveling at low angles of incidence, and thinnest for vertically incident particles, the cosmic ray flux is greatest overhead and decreases towards the horizon (Gosse and Phillips, 2001). As such, it takes appreciable shielding to significantly affect the cosmic ray flux at a sample site. At Lago Pueyrredón, surrounding topography was generally at angles of less than 5º from the horizon, resulting in a negligible scaling factor of 0.9997. In addition, samples were taken from flat surfaces (outwash terrace or moraine crest) and away from any potential shielding objects. Thus, no such scaling is required.

Sample thickness

Scaling is required to account for the thickness of the analyzed sample given that production rates are referenced to the rock surface and decrease exponentially below. The samples measured in this study were generally < 5 cm thick, leading to a

correction of less than 4% (Balco et al., 2008). Masarik and Reedy (1995), however, model an initially flat profile until 12 g cm^{-2} below the air/rock interface (~4.4 cm at ρ=2.7 g cm^{-3}) which may suggest that there is little attenuation of the nucleonic (spallation) component over typical sample thicknesses. If so, the calculated production rates may be underestimated by up to 3.7% (Gosse and Phillips, 2001). However, a recent study demonstrates that this effect does not affect ^{10}Be production (Farber et al., 2008).

Other factors

Samples taken from protruding objects such as boulders may lose some of the high energy neutrons back to the atmosphere (Masarik and Wieler, 2003). The loss of high energy neutrons to the atmosphere is estimated to lower spallation production rates in some boulders by as much as 10 – 12% when compared to a sample taken from an infinitely flat surface (Masarik and Wieler, 2003). Thus, in this study I minimize the effect by sampling away from sharp edges on large and flat-topped boulders (cf. Gosse and Phillips, 2001; Masarik and Wieler, 2003), or from cobbles embedded within a flat surface.

Shielding by annual snow cover (or sand, soil, loess) is problematic in many glacial environments and should be accounted for. However, I argue in the following chapters that shielding by annual snow cover is negligible at Lago Pueyrredón given the semi-arid climate and prevailing strong winds.

Isostatic recovery can affect the time-integrated cosmic ray flux in formerly glaciated regions; this can be accounted for in some areas where independent data are available to quantify rates. However, no such data are available at Lago Pueyrredón. The samples in this study were taken from the margins of the formerly glaciated region and would be less affected by such processes; thus I consider the effect of isostatic changes on production rates in this study to be negligible.

2.3.3.2 Production rates

Production rates of ^{10}Be and ^{26}Al in particular target minerals (e.g., quartz) have been derived based on models (e.g., Masarik and Reedy, 1995) and measurements in both natural (e.g., Balco et al., 2009; Nishiizumi et al., 1989) and artificial targets (Nishiizumi et al., 1996). Natural geologic targets are most commonly used to derive production rates. The ideal calibration site contains non-weathered rock surfaces (i.e., where negligible erosion is evident) that are well dated by independent methods. This could mean, for example, a striated moraine boulder tightly bracketed in age by radiocarbon ages, or an historic rock avalanche, a lava flow (^{3}He) dated by K-Ar or ^{40}Ar/^{39}Ar methods, etc. By measuring the concentration of nuclides in the rock surface and correcting (i.e., scaling) for appropriate *local* shielding of the cosmic ray flux, the time-averaged local production rate is obtained. To make this production rate useful for exposure dating (or for other applications) at different geographic locations, it needs to be scaled to a reference location (present day sea-level, high latitude [SLHL] is used by convention) and then scaled back to the site of geologic interest using one of the scaling models discussed in Section 2.3.3.1.

The reference production rate is derived by averaging all (SLHL) production rates obtained from the entire network of globally distributed calibration sites. The reference production rate value is dependent on the scaling model used, the calibration sites included and the way in which the calibration data are averaged (i.e., as one production rate average for the calibration site, or as a series of individually scaled production rates). It is important to emphasize that the reference production rate is unique to the scaling model used. Therefore, the same scaling model must be used to scale back to the site of geologic interest. Table 2.1 gives the derived reference production rates for a range of scaling models based on the calibration dataset used in version 2.2 of the Cosmic-Ray Produced Nuclide Systematics on Earth (CRONUS-Earth) online exposure age calculator. The rather large uncertainties (ca. 10%) could be improved upon by increasing the quantity, quality and global distribution of calibration sites; this work is currently underway (e.g., Balco et al., 2009; Dunai and Team, 2005; Putnam, submitted; Schaefer, 2005).

Table 2.1. Reference production rates

Based on v. 2.2 of CRONUS-Earth exposure age calculator (Balco et al., 2008).

ID[a]	^{10}Be[b] (at g^{-1} a^{-1})	^{26}Al[c] (at g^{-1} a^{-1})
St	4.49±0.39	30.2±2.6
De	4.41±0.52	29.8±3.4
Du	4.43±0.52	29.9±3.4
Li	4.87±0.48	32.9±3.2
Lm	4.39±0.37	29.6±2.5

[a] Scaling models St=Lal(1991)/Stone(2000); De=Desilets et al. (2006); Du=Dunai(2001); Li=Lifton et al. (2005); Lm=Lal(1991)/Stone(2000)/Nishiizumi et al. (1989).

[b] Based on ^{10}Be half-live 1.36 Ma (Nishiizumi et al. (2007).

[c] ^{26}Al production rate calculated from ^{10}Be production rate; ratio is 6.75.

2.3.3.3 $^{26}Al/^{10}Be$ ratio

Lal and Arnold (1985) suggested the $^{26}Al/^{10}Be$ ratio could be used to calculate both the exposure age and the erosion rate of a sample. As radioactive nuclides, the production of ^{10}Be (recently revised half-life ~ 1.36 Ma; Nishiizumi et al., 2007) and ^{26}Al (half-life 0.705 Ma; Nishiizumi, 2004) isotopes will eventually equal their loss through radioactive decay and erosion as they become saturated (Gosse and Phillips, 2001). The production rate of ^{26}Al in quartz is higher than that of ^{10}Be. The $^{26}Al/^{10}Be$ production rate ratio is ~ 6.75 using the revised ^{10}Be half-life. Through time, the ratio of ^{26}Al to ^{10}Be in a sample will change because ^{26}Al decays faster (~x2) than ^{10}Be. The changing ratio can be exploited to assess the age, erosion rate and exposure history of a sample (e.g., Bierman et al., 1999; Fabel et al., 2002; Granger et al., 1997; Nishiizumi et al., 1991).

Fig. 2.3 shows the normalized $^{26}Al/^{10}Be$ ratio plotted against the ^{10}Be concentration (logscale) normalized to SLHL. Lal (1991) demonstrates that a continuously exposed sample eroding at a constant rate should plot on an erosion curve within the steady-state 'erosion island' that corresponds to a particular exposure age and erosion rate. In practice, the uncertainties are nearly always as large as or larger than the $^{26}Al/^{10}Be$ erosion island itself, making it difficult to solve for both age and erosion. This is particularly true for young samples where it is nearly impossible to distinguish low erosion rates from very high erosion rates (Gosse and Phillips, 2001). However, the size of the erosion island can be increased by pairing nuclides with vastly different half-lives or production profiles. For example, pairing a radioactive and stable nuclide (e.g., $^{10}Be/^{21}Ne$) or a spallogenic and thermal-neutron nuclide

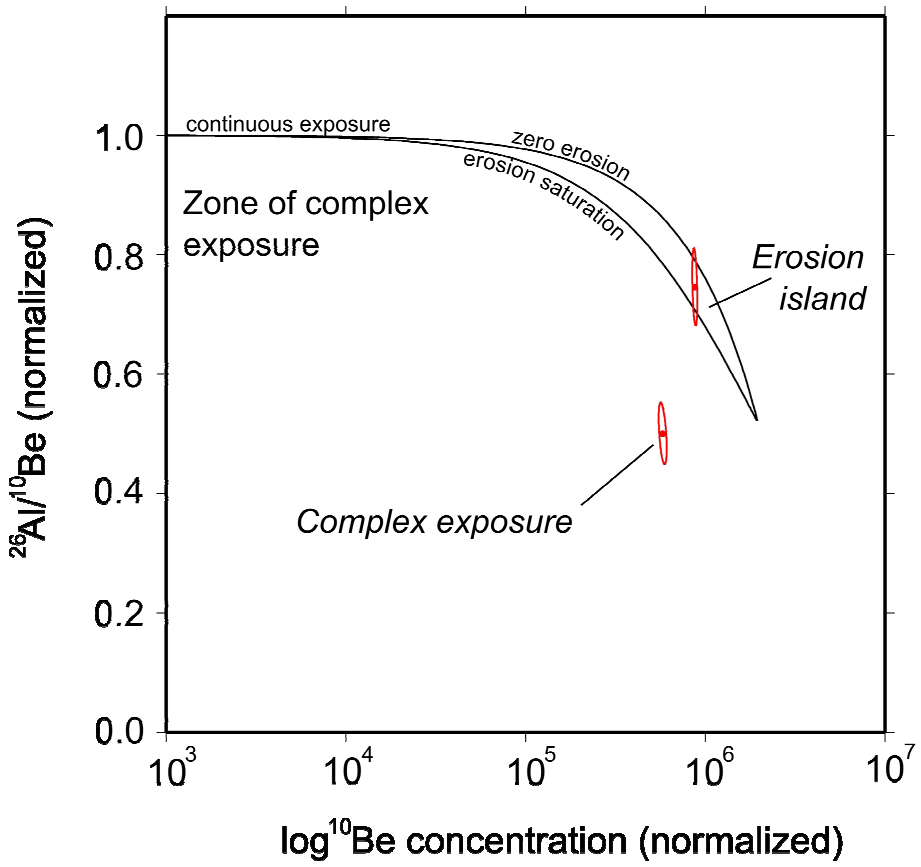

Figure 2.3. ^{26}Al/^{10}Be production ratio plot

Plot of the ^{26}Al/^{10}Be ratio (6.75 normalized to 1) against ^{10}Be (log-scale) normalized to SLHL. The top curve is the production ratio profile for continuous exposure with zero erosion. The lower curve marks the steady-state erosion end-points (saturation) for continuous exposure. The erosion island is the area between these curves; the erosion rate and exposure age can be calculated for ratios plotting within the erosion island, however ratio uncertainties are often as large as the width of the island (see ratio plotted in erosion island). Ratios that plot below the steady-state erosion island are interpreted to have complex exposure histories involving at least one shielding event (Gosse and Phillips, 2001).

(^{10}Be/^{36}Cl; Fig. 2.4) would increase the erosion island and allow a better estimate of both age and erosion (Gosse and Phillips, 2001).

A sample's exposure history can be assessed based on where its ^{26}Al/^{10}Be ratio plots relative to the steady-state erosion island (Lal, 1991). A ratio plotting above the curve cannot be explained by exposure, erosion, burial or inheritance, and likely

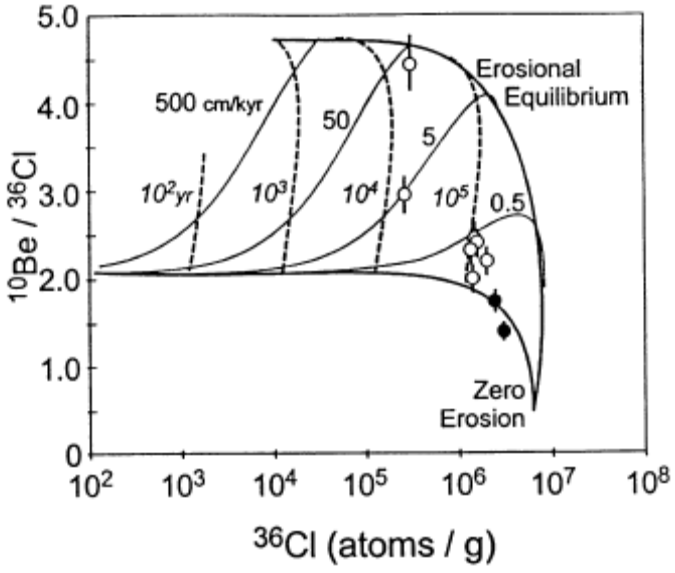

Figure 2.4. ^{10}Be/^{36}Cl production ratio plot

Plot of ^{10}Be/^{36}Cl ratio against ^{36}Cl (log-scale) for moraine boulders in the Wind River Range, USA (Phillips et al., 1997; figure modified by Gosse and Phillips, 2001). The erosion island is much larger when the ratios of two nuclides with different production profiles (i.e., spallogenic ^{10}Be, thermal neutron ^{36}Cl) are used; erosion rates for these moraine boulders are low.

occurs due to analytical errors, or possibly due to radiogenic production (Gosse and Phillips, 2001). A ratio plotting to the right of the curve could be explained by a lower production rate than what was assumed (Gosse and Phillips, 2001). As previously stated, a ratio plotting within the erosion island can be explained by some combination of exposure and erosion. Ratios plotting below the erosion island are interpreted to have a complex exposure history involving periods of exposure and shielding. For example, shielding by snow, soil or ice for part of its 'exposure' period would cause a more rapid loss of ^{26}Al through radioactive decay and a lowering of the ^{26}Al/^{10}Be ratio (e.g., Bierman et al., 1999; Granger et al., 1997). If the type of shielding is known (e.g., periodic glacier coverage) and bracketing ages exist, an estimate of the minimum exposure and burial duration can be inversely modeled (e.g., Fabel et al., 2002; Gosse and Phillips, 2001; Granger et al., 1997). In

sum, the $^{26}Al/^{10}Be$ ratio provides useful information on exposure histories that is not available if only one nuclide is measured.

2.3.4 Exposure ages

With the production rate known, the exposure age of a surface can be determined by measuring the concentration of ^{10}Be and/or ^{26}Al that has accumulated in the rock surface. The chemistry involved in isolating the in-situ cosmogenic ^{10}Be and ^{26}Al is laborious. It involves a series of steps aimed at isolating pure quartz grains from the rock sample. This is followed by a series of chemical procedures aimed at extracting and purifying the ^{10}Be and ^{26}Al targets. An outline of the procedure is provided in Appendix A.1, it follows an adaptation (Binnie, 2004) of the methods of Bierman et al. (2002), Ivy-Ochs (1996) and Kohl and Nishiizumi (1992). The pressed targets are taken to the Scottish Universities Environmental Research Centre (SUERC) for AMS analysis (Appendix A.2). Details of the SUERC AMS (NEC 5MV Pelletron) operation are provided by Freeman et al. (2007; 2004), Schnabel et al. (2007) and Maden et al. (2007). The full AMS IDs of each sample submitted are provided in the relevant data tables together with details of the measurement standards and process blanks. The method of converting the $^{10}Be/^{9}Be$ and $^{26}Al/^{27}Al$ isotopic ratios (the measurement returned by the AMS facility) into nuclide concentrations is given in Appendix A.3.

By measuring the nuclide concentration in a sample, and scaling production rates to the sampling location, the exposure age of a surface can be calculated. Lal (1991)

formulated the basic equation for calculating an exposure age (t) based on spallation production:

$$t = \frac{-1}{\lambda + \varepsilon\rho/\Lambda} \ln\left(1 - \frac{N\left(\lambda + \varepsilon\rho/\Lambda\right)}{P}\right) \tag{2.2}$$

where λ is the radioactive decay constant of ^{10}Be [5.1e^{-7} a^{-1}; (Nishiizumi et al., 2007)] or ^{26}Al [9.83e^{-7} a^{-1}; (Nishiizumi, 2004)], ε is the independently determined rock surface erosion rate (cm a^{-1}), ρ is the density of the rock (g cm^{-3}), Λ is the effective attenuation length for spallogenic production (~160 g cm^{-2}), N is the measured nuclide concentration (at g^{-1}) and P is the surface production rate (at g^{-1} a^{-1}). The erosion rate is the only other unknown in this equation, and must be independently determined or estimated. In this study, I report exposure ages based on zero erosion. This means the resulting exposure ages are minimum ages. However, I also include a correction for erosion on the *boulder* surfaces; an average erosion rate of 1.4 mm ka^{-1} was derived by Kaplan et al. (2005) on boulder surfaces at nearby Lago Buenos Aires. I use this correction to document the effect on boulder surfaces in this valley.

Equation 2.2 is appropriate for most surface exposure dating applications because ~97.5% of ^{10}Be and ^{26}Al production is by spallation reactions (Stone, 2000) and production by muons is therefore inconsequential. There are other formulations that additionally include production by muons (e.g., Balco et al., 2008; Gosse and Phillips, 2001; Granger and Smith, 2000). In an effort to report consistent and easily reproducible results, I use a community exposure age calculator to derive all

exposure ages in this study. The advantage of using a community calculator is that exposure ages are derived in a consistent manner and they can be easily compared and re-calculated on a common basis (e.g., by using the same geologic calibration datasets, scaling models and analytical equations). This is important because future refinement of production rates (and constants) will necessitate recalculation of existing published data, and standard reporting of cosmogenic nuclide data in publications will help to facilitate this (cf. Dunai and Stuart, in press). The calculator was developed by Greg Balco and colleagues (Balco et al., 2008) as part of the CRONUS-Earth project (Schaefer, 2005) which, together with CRONUS-EU (Dunai and Team, 2005), aims to improve the accuracy and reliability of the cosmogenic nuclide technique; this includes the overall uncertainties associated with AMS measurements, production rates, scaling factors, the ^{10}Be half-life and analysis and interpretation of cosmogenic nuclide data. The exposure age calculations are based on previously published equations and currently accepted practices (Balco et al., 2008). I use version 2.2 of the online exposure age calculator which implements the revised ^{10}Be half-life of 1.36 Ma (Nishiizumi et al., 2007). The full documentation for version 2.1 is provided by Balco et al. (2008). The updates for version 2.2, together with all MATLAB codes are available at the website (http://hess.ess.washington.edu/math/index.html). A description of the most relevant features of the CRONUS-Earth online exposure age calculator, including user input, the calculations performed, and output, is provided in Appendix B.

2.3.5 Sampling considerations and limitations

In addition to the production rates discussed above, the accuracy of exposure dating is also dependent on good sampling strategies. As discussed in the following chapters, a good sampling strategy may depend on environmental conditions and the expected age of deposits. A good sampling strategy is one that minimizes the potential complications that can affect the continuous exposure of the sampled surface. Gosse and Phillips (2001) give a useful guide to field sampling with particular emphasis on sampling glacial moraine boulders, and I followed these recommendations in this study. Some of the challenges most relevant to exposure dating include 1) the potential existence of inherited nuclides from a previous exposure, 2) the potential for post-depositional burial of the rock surface, and 3) accurately estimating rock surface erosion rates.

As discussed above and in the following chapters, I minimized the effect of rock surface erosion by sampling from, where possible, boulder surfaces that showed minimal evidence of erosion (e.g., striations, polish) and from cobbles and pebbles with a fluvial form, the preservation of which indicates negligible erosion. Inheritance is not considered problematic because the sampled clasts were transported by glaciers at least ~60 km and thus should have been eroded sufficiently to remove any previously accumulated cosmogenic nuclides. This assumption is convincingly confirmed in Chapter Four. Semi-arid and windy environmental conditions likely persisted over the long-term and therefore post-depositional shielding by snow cover, soil, etc. is unlikely to be problematic in this environment. These issues are discussed at depth in the following chapters. However, to help identify outliers as a result of these processes, I measured at least four samples from

each surface where this was possible. The following chapters discuss these sources of uncertainty in more detail.

In summary, the accuracy of the cosmogenic nuclide technique is being continually refined with improvements in the field and laboratory, and in particular with better and more geographically wide-spread production rate calibration sites (e.g., Balco et al., 2009; Dunai and Team, 2005; Putnam, submitted; Schaefer, 2005). These improvements will result in changes to the exposure ages presented in this study, and in a reduction in the reported external uncertainties associated with the production rates and scaling models. At present, these uncertainties limit the degree to which cosmogenic nuclide chronologies can be used to resolve millennial scale events such as the Younger Dryas or the Antarctic Cold Reversal, and the ability to resolve individual glacial stages (100 ka glacial cycles) beyond about the mid-Quaternary. However, with continued refinement, this should be possible in the future. The conclusions made in the following chapters are considered insensitive to future production rate refinements.

Chapter 3 The chronology of the Last Glacial Maximum and deglacial events in central Argentine Patagonia

This chapter details the chronology of the youngest "Río Blanco" moraine system in the Lago Pueyrredón valley. It further details the process of deglaciation in the region and draws regional comparisons to existing glacial chronologies. This chapter has been submitted for publication as follows:

Hein, A.S., Hulton, N.R.J., Dunai, T.J., Sugden, D.E., Kaplan, M.R., Xu, S. (submitted). The chronology of the Last Glacial Maximum and deglacial events in central Argentine Patagonia. *Quaternary Science Reviews*.

I wrote the manuscript and developed the original ideas in this chapter; Hulton accompanied me in the field; Hulton, Dunai and Sugden made comments that improved and helped to clarify the text; Kaplan made helpful comments; Xu performed the AMS measurements.



Abstract

This paper evaluates the chronology of the last glacial cycle and deglaciation in the Lago Pueyrredón valley of central Patagonia, 47.5º S, Argentina. The valley was a major outlet of the former Patagonian Ice Sheet and the moraines that record its fluctuations are an important proxy record of climate change in southern South America. Such moraines are well-preserved in the Lago Pueyrredón valley owing in part to the semi-arid environment east of the mountain front. Here, we provide the first direct chronology for the age of the "Rio Blanco" moraine system by utilizing cosmogenic-nuclide surface exposure ages. Boulders on the moraines give ^{10}Be exposure ages that indicate the Last Glacial Maximum (LGM) maximum extent occurred by 27 – 25 ka. Subsequent advances occurred at ca. 23 ka, ca. 19 ka, and ca. 18 – 17 ka. Initial deglaciation began after 18 – 17 ka and was interrupted as evidenced by the Lago Columna moraines upvalley. Subsequently the outlet glaciers occupying both the Lago Pueyrredón basin (Chilean name: Lago Cochrane) and the Lago Buenos Aires basin (Chilean name: Lago General Carrera) to the north, rapidly retreated more than 80 kilometers at around 16.5 – 15 ka. The timing of the LGM maximum extent and the onset of deglaciation occurred broadly synchronously throughout Patagonia. Deglaciation resulted in a series of interconnected glacier-dammed lakes in the region that initially drained toward the Atlantic Ocean and later drained to the Pacific Ocean as a consequence of disintegrating ice in the Andes.

3.1 Introduction

The main purpose of this paper is to establish the chronology of the Last Glacial and deglacial events in the Lago Pueyrredón valley, 47.5º S, Argentina. Specifically, we use cosmogenic ^{10}Be surface exposure ages to determine the age of the 'Río Blanco' moraine system (Caldenius, 1932), which are the innermost (westernmost) of a series of moraine groups preserved on the eastern margin of this former lobe of the Patagonian ice sheet. In addition, we aim to synthesize (1) the central Patagonian glacier response with other Patagonian glacial chronologies; and (2) the regional paleolake history; this has implications for continental drainage diversions as the ice disintegrated in the Andes.

Well-dated glacial chronologies are required to address important questions regarding southern hemisphere climate and ice age theory. For example, Huybers and Denton (2008) argue that the common interpretation that northern insolation (intensity) controls southern climate is problematic. This is because the proposed driving mechanisms for widespread climate change are inconsistent with southern climate changes which appear to be in phase with or to lead northern hemisphere changes. To address such problems and to further evaluate different ice age theories, a better understanding of the timing and spatial variability of mountain ice field and glacier fluctuations in both hemispheres is required. Mountain glaciers are sensitive to local climates; thus moraines record a snap-shot in time of a particular climatic state (Schaefer et al., 2006). The Andes span a wide range of latitudes and associated climates in South America. They host an important source of long-term

terrestrial climate information in the dominantly oceanic southern hemisphere. Given the range of Andean climates, some variability in the timing of climatically related events in the glacial geologic record may be expected. What is essential, however, is to identify differences that are climatic in origin from those that may reflect different geologic or topographic conditions, moraine preservation, or the limitation of the particular geochronometer used (Kaplan et al., 2008b). Developing multiple glacial chronologies from nearby valleys helps to distinguish the overriding climatic signal from the local signal. In addition, well-dated ice limits and constraints on ice thickness are necessary to constrain high resolution glaciological models (e.g., Hubbard et al., 2005; Hubbard, 1997; Hulton et al., 2002) that are capable of investigating the time-transgressive properties of the glacier and the underlying climate as a whole (Hulton et al., 2003).

3.1.1 LGM in southern South America

In southern South America, glacial chronologies were first developed in moisture-rich zones such as the Chilean Lake District (~ 42º S) and the Magellan region (~53º S) of southernmost South America where organic material is comparatively plentiful for radiocarbon age dating (Denton et al., 1999b; Lowell et al., 1995; McCulloch et al., 2000). More recently, cosmogenic-nuclide surface exposure ages of glacial landforms has further improved the chronologic base for deposits of Last Glacial age, both in Patagonia (e.g., Fogwill and Kubik, 2005; Kaplan et al., 2007; McCulloch et al., 2005) and further north in the tropical Andes (e.g., Farber et al., 2005; Smith et al., 2005; Zech et al., 2007b). The radiocarbon and cosmogenic nuclide chronologies indicate that the LGM and its termination occurred broadly synchronously in both

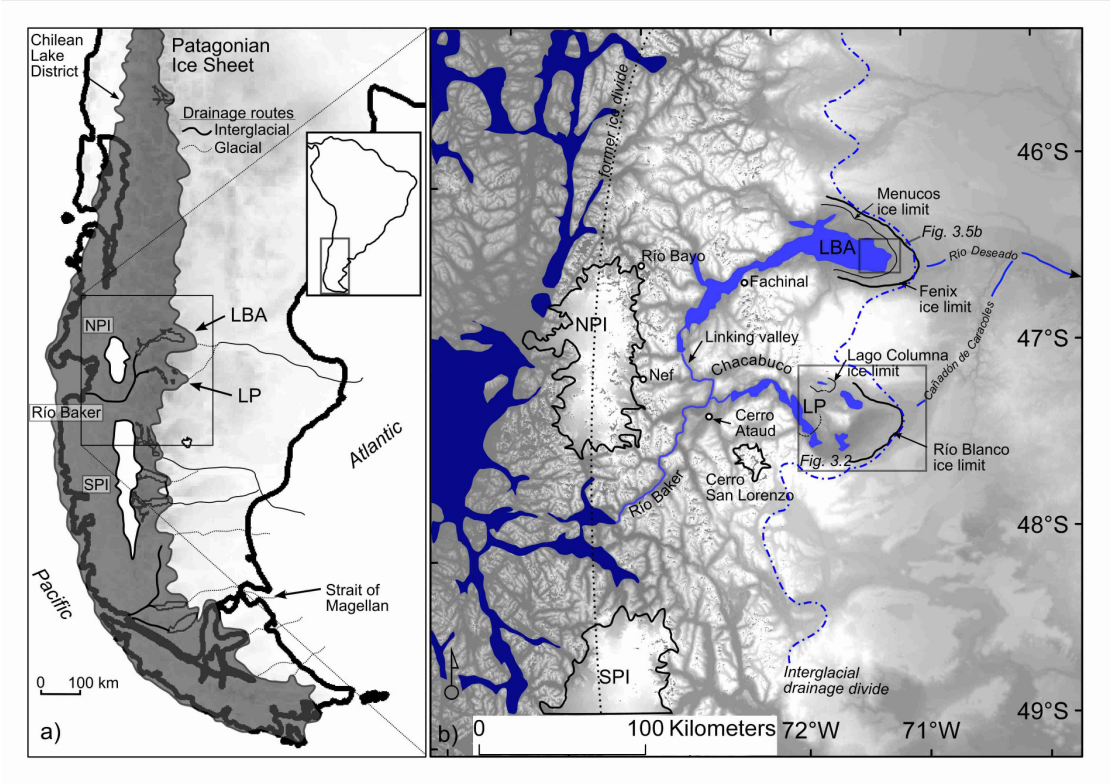

Figure 3.1. Context map

a) The general form of the Patagonian ice sheet during the LGM, showing the location of the Lago Buenos Aires (LBA) and Lago Pueyrredón (LP) valleys, principal drainage routes and the present day North (NPI) and South Patagonian Icefields (SPI). b) The study area, including key locations mentioned in the text. Estimated position of the former ice divide and present drainage divide are shown to illustrate the different hydrologic conditions.

hemispheres with maximum extents largely dated at ca. 25 – 27 ka and with termination after ca. 17.5 ka (Glasser et al., 2008; Rabassa, 2008). There are regional anomalies. For example, some glaciers in the northern Chilean Lake District reached their maximum extent earlier at 35 cal ka and 32 cal ka (29.4 – 26.8 ^{14}C; late MIS 3) based on radiocarbon age dating (Denton et al., 1999a; Lowell et al., 1995). Similar ^{10}Be exposure ages are obtained further north at 32° S in Chile (~ 31 ka), and 39° S in Argentina (ca. 35 ka; Zech et al., 2007a). Further south, departure from the dominant 'northern hemisphere' signal becomes apparent on millennial time scales during the glacial-interglacial transition, particularly south of 46° S

(Sugden et al., 2005). For example, evidence of glacier advances during the Antarctic Cold Reversal (~ 15 – 12 ka) have been reported at ~ 47º S (e.g., Douglass et al., 2006; Turner et al., 2005), ~51º S (e.g., Fogwill and Kubik, 2005; Marden and Clapperton, 1995; Moreno et al., 2009; Wenzens, 1999) and ~53º S (McCulloch et al., 2005). In contrast, Ackert et al. (2008) date a significant advance of the South Patagonian Icefield (50º S) to the end of, or after, the northern hemisphere's Younger Dryas cooling, coincident with peak temperatures in Antarctica. These data exemplify both the complexity of the glacial geologic record and the need for more detailed chronologies to better constrain the underlying climatic controls.

3.2 Regional setting

3.2.1 Geology

The Lago Pueyrredón valley is situated immediately south of the Lago Buenos Aires valley and 600 kilometers north of the Strait of Magellan (Fig. 3.1a). The valley was a major outlet of former expanded Patagonian ice sheets, and a series of well-preserved moraines as old as 1.1 Ma are situated 150 – 200 kilometers east of present day outlets of the North Patagonian Icefield (Mercer, 1976; Singer et al., 2004; Ton-That et al., 1999). The deposits have received little attention following their initial observation by Hatcher in 1903, and later mapping by Caldenius (1932), with some notable exceptions (e.g., Feruglio, 1950; Wenzens, 2005).

The region is characterized by large west-east trending valleys that have been over-deepened through glacial erosion (Fig. 3.1b). The cross-border lakes of Lago Buenos

Aires (Chilean name: Lago General Carrera) and Lago Pueyrredón (Chilean name: Lago Cochrane) occupy two such glacial depressions east of the present day North Patagonian Icefield. Local tectonics in the central Patagonian region have resulted in a significant break in the chain of the Andes at 48º S. This tectonic depression separates the present day North and South Patagonian Icefields by ~100 kilometers, exposing a low-level drainage route to the Pacific Ocean that crosses the former ice divide. The Río Baker occupies this depression. The present drainage divide is located within the terminal moraine complex at the eastern ends of Lago Buenos Aires and Lago Pueyrredón, ~50 kilometers east of the mountain front (Fig. 3.1b). Therefore, despite their position on the eastern side of the Andes, the lakes drain to the Pacific Ocean via the Río Baker.

3.2.2 Geologic implications

The Lago Buenos Aires and Lago Pueyrredón valleys were linked during the process of deglaciation. When mountain glaciers expanded and coalesced into a continuous ice sheet, the eastern outlet glaciers drained via their respective meltwater channels to the Atlantic Ocean (Fig. 3.1a). During the LGM, meltwater drained via the Río Deseado (~380m a.s.l.) east of Lago Buenos Aires, and ~100 meters higher via the Cañadón de Caracoles (~475m a.s.l.) east of Lago Pueyrredón. Withdrawal of ice from terminal positions resulted in pro-glacial lakes that continued to drain to the east while ice occupied the valley. This condition changed when glaciers in both valleys withdrew from their LGM limits by more than 125 kilometers and exposed the valley linking the two lake basins (Fig. 3.1b). At this time, the lake level at Lago Pueyrredón would have dropped by ~ 100 meters as the lake 'united' with Lago

Buenos Aires and drained via its outlet, the Río Deseado (cf. Turner et al., 2005). With continued deglaciation, this 'united' lake eventually drained westward when the Río Baker depression became unblocked.

3.2.3 Existing chronology

The only recent mapping and chronology available for the Río Blanco moraine system (a name used in this study following Caldenius, 1932) located on the eastern side of the Lago Pueyrredón valley is by Wenzens (2005). Wenzens (2005) bases the chronology on three radiocarbon ages. The first age is from a mollusk shell located in lake sediments at the foot of the Cañadón de Caracoles escarpment; this yields a age of 17.2 ^{14}C ka, suggesting the (Hatcher) moraines that impounded the lake are LGM in age (Fig. 3.2). The second age of 11.8 ^{14}C ka (Mercer, 1982) from the Cañadón de Caracoles drainage channel provides a minimum age for the Río Blanco moraines that drained via this route. A third age associated with the younger Río Blanco moraines gives a minimum Holocene age of 8.3 ^{14}C ka BP. Wenzens (2005; 2006a) concludes that the Río Blanco moraines represent a series of Late-glacial to Holocene advances. However, recent cosmogenic-nuclide surface exposure ages indicates that the Hatcher moraines are much older (MIS 8; Hein et al., 2009). Wenzens' (2002; 2005; 2006a) determination that Holocene ice extended to the eastern end of Lago Pueyrredón is at odds with available data which indicate, rather, that ice was limited to the high mountains in the Holocene. Evidence for relatively restricted Holocene ice in the region was first established by Mercer (1976) who obtained a radiocarbon age of 11.0 ^{14}C ka from near the present day terminus of glacier Témpano which drains the South Patagonian Icefield. Further evidence in

support of relatively restricted Holocene ice is found in the Nef (Turner et al., 2005) and Río Bayo valleys (Glasser et al., 2006), Fachinal moraines (Douglass et al., 2005) and east of Lago Buenos Aires (Kaplan et al., 2004)(Fig. 3.1b).

The most detailed chronology for LGM deposits in the area to date is found east of Lago Buenos Aires. Kaplan et al. (2004) and Douglass et al. (2006) date the Fenix I-V moraines at ca. 16 – 23 ka using cosmogenic-nuclide surface exposure methods (^{10}Be,^{26}Al,^{3}He) and radiocarbon ages. Turner et al. (2005) obtained radiocarbon ages ranging from 13.6 ka to 16.3 ka from material associated with a paleoshoreline from a 'united lake' at the base of Cerro Ataud, which is located ~110 kilometers west of the Río Blanco moraines in the Lago Pueyrredón valley (Fig. 3.1b). Given that the innermost Fenix moraines at Lago Buenos Aires are dated at ~ 16 ka (Kaplan et al., 2004), and the 'united lake' could only have existed when ice had withdrawn from both valleys (Section 3.2.2.), these data require a rapid retreat of the ice sheet at ca. 15 – 16 ka (Turner et al., 2005). However, recent surface exposure ages for the Menucos moraines (stratigraphically younger than the Fenix moraines at Lago Buenos Aires) indicate that ice was at the eastern end of Lago Buenos Aires at ~14.4 ± 0.9 ka (Douglass et al., 2006); this result conflicts with some of the radiocarbon ages obtained by Turner et al. (2005).

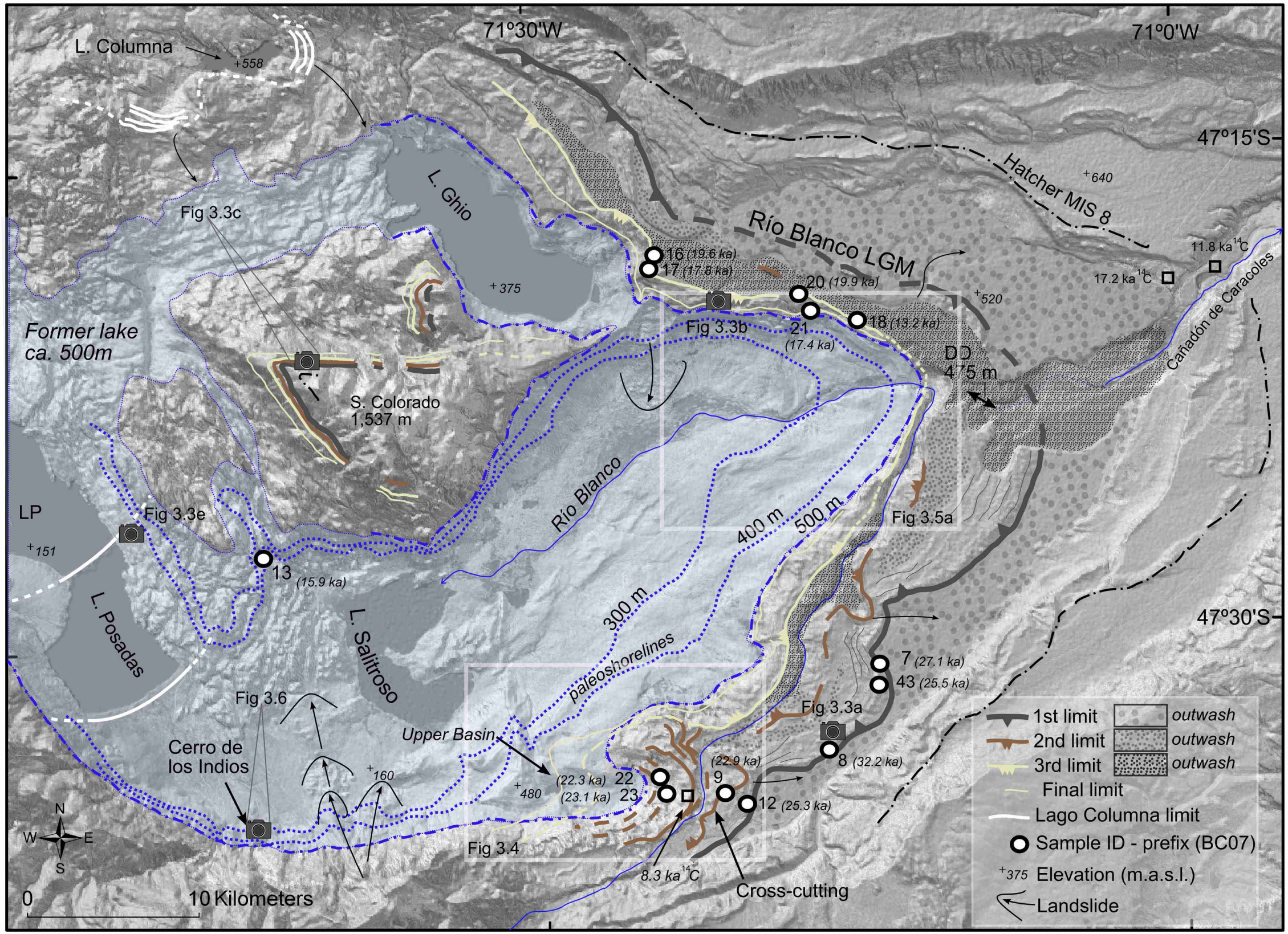

Figure 3.2. Geomorphic map of the Lago Pueyrredón valley

Geomorphic map of the Lago Pueyrredón valley with the principal ice limits, lake levels and sample sites identified in the text. Generally, only the outermost moraine crest marking each ice limit is mapped. The outwash terraces are distinguished based on their associations with former ice limits; these slope gently eastward at ca. 0.5°. The numbers in parenthesis are the ^{10}Be exposure ages derived in this study. The radiocarbon ages are from Wenzens (2005) and Mercer (1982). The base map is composed of an SRTM 90m DEM and LandSat imagery.

3.3 Materials and methods

3.3.1 Geomorphic mapping

To establish the chronology of the Río Blanco moraine system and to help resolve some of the inconsistencies, we mapped the deposits and provide age control using cosmogenic-nuclide surface exposure methods. The geomorphic map presented in Fig. 3.2 is based on satellite imagery (LandSat, ASTER), digital elevation models (SRTM 90m) and detailed field observations made during three field seasons (2006 – 2009). The elevations presented are based on GPS and digital barometric altimeter measurements or digital elevation models referenced to field measurements. The values are referenced to modern sea level with estimated uncertainties of ± 10 meters. Our mapping revealed a series of moraines, outwash terraces, paleoshoreline levels and landslide deposits.

3.3.1.1 Río Blanco and recessional moraines

A series of moraines were mapped and distinguished based on their surface morphology, geomorphic relationships and sedimentological characteristics. The moraines, with arcuate plans and regular gradients, vary from hummocky continuous landforms with slope angles of ~17º - 20º and relief of 20 – 50 meters (Fig. 3.3a), to distinct sharp-crested continuous landforms with slopes of 20º - 28º and relief of 20 – 40 meters (Fig. 3.3b). Cross-cutting relationships were identified in the field (e.g., Fig. 3.3c), and the stratigraphy and sedimentology were examined where possible (e.g., Fig. 3.3d and Fig. 3.4). Moraine boulder weathering ranges in severity from minor aeolian erosion and spalling (depth < 2 centimeters), to surfaces that are

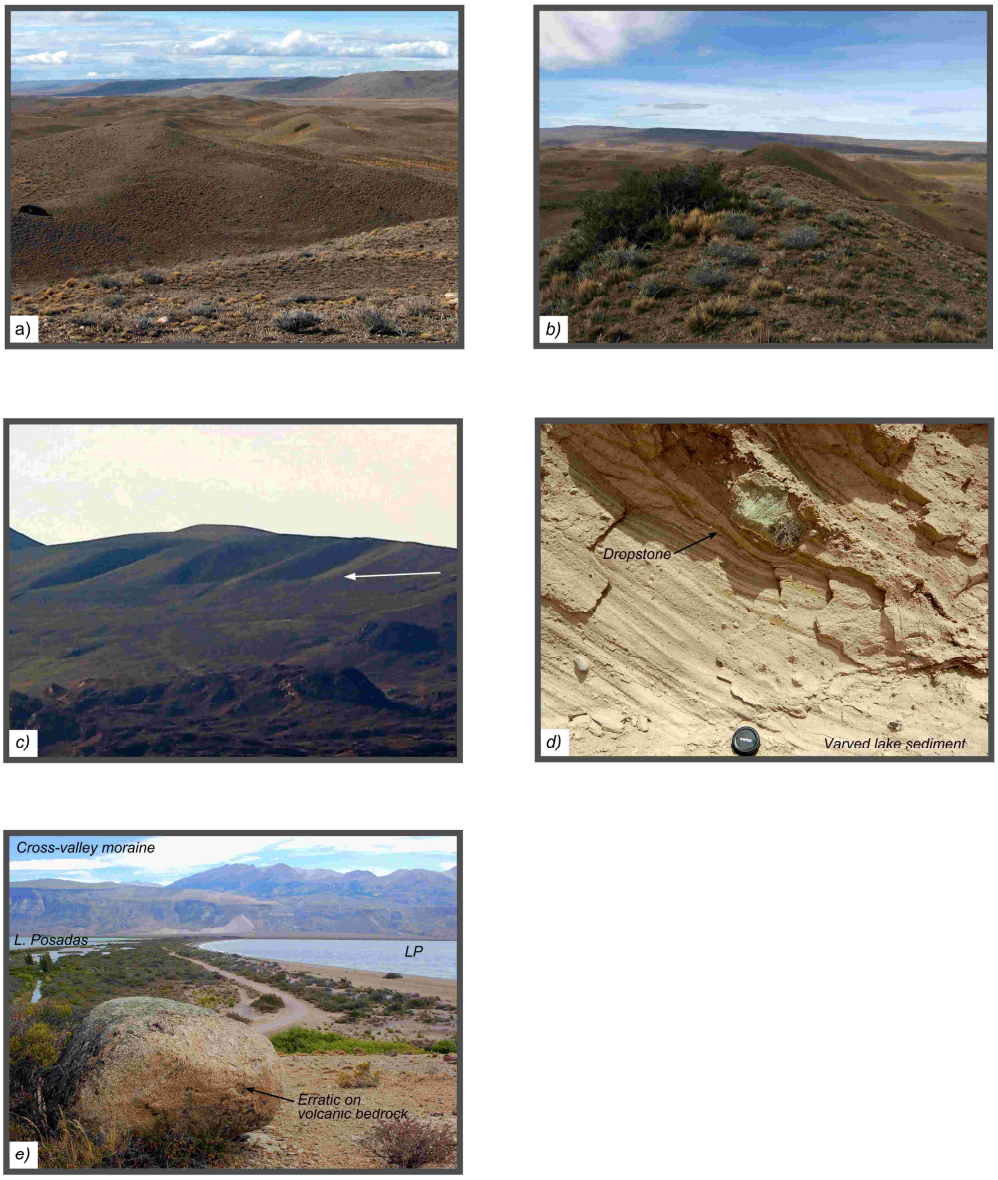

Figure 3.3. Photos of glacial features

a) The hummocky, continuous form of moraines associated with the 'first limit'. Five to six moraine crests associated with the first limit are preserved on the south side of the valley. b) The distinct sharp-crested continuous form typical of moraines marking the 'third limit'. c) A site on Sierra Colorado (see Fig. 3.2) where LGM moraines (arrow) at 1,000 – 1,180 m elevation cross-cut three large drainage channels that descend from the ridgeline. An older series of moraines (not visible) is located above the drainage channels at 1,400m elevation. d) The photo shows deformed varved lake sediment containing dropstones. The deposit is located at ca. 570 meters in the upper lake basin (Fig. 3.4). The section contains two sequences of till overlain by lake sediments, suggesting at least two advances occurred in the upper basin, each followed by the formation of a lake. e) The cross-valley moraine separating Lago Posadas from Lago Pueyrredón (LP).

smoothly polished. Our mapping reveals three distinct ice limit associations in the Río Blanco moraine system (Fig. 3.2); these are composed of numerous moraines marking readvances or standstills. The moraines are best preserved in the south. In the north, meltwater sourced from the Lago Ghio lobe removed most of the moraines associated with the first and second ice limits. The first limit marks the maximum extent. Moraines of the second limit cross-cut these in places producing locally high relief (20 – 30 m above nearby crests). The third and final limits are largely continuous and encompass the basin.

To the west of the Río Blanco moraines are further probable ice limits. A distinct causeway (ca. 300 meters wide by 3 kilometers long) separates Lago Posadas from Lago Pueyrredón, extending out from the modern day alluvial fan at right angle to the prominent wind direction from the west (Fig. 3.2). It is primarily composed of well rounded cobbles and pebbles and is covered by sand dunes to the south. The density of erratic boulders situated on the surrounding volcanic bedrock is noticeably higher in close proximity to the causeway (Fig. 3.3e). While the surface is level, the causeway has the planimetric form of an asymmetric cross-valley moraine (Andrews and Smithson, 1966). Therefore, we interpret the feature as a moraine that marks the grounding line of a glacier terminated in a pro-glacial lake. The eastern shore of Lago Posadas displays similar morphology, and may also reflect a former ice limit. These moraines are correlated to those deposited near Lago Columna by the glacier occupying the Chacabuco valley.

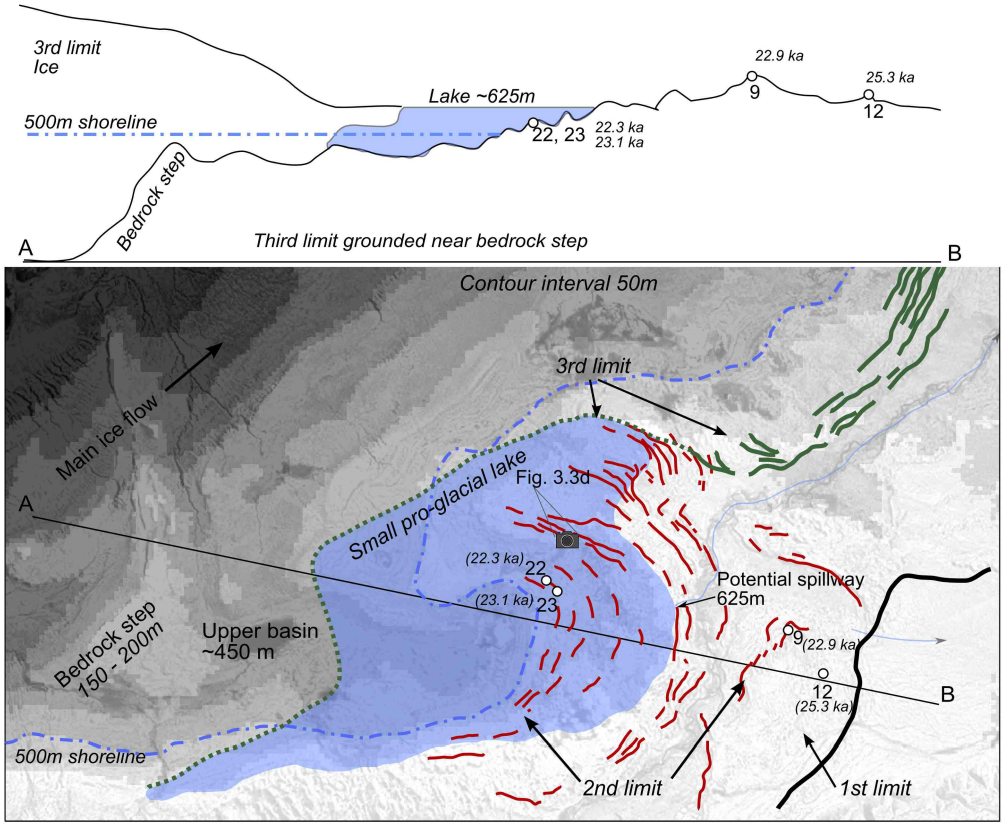

Figure 3.4. Detailed geomorphic relationships

The geomorphology of the southernmost part of the moraine system (see Fig. 3.2). A bedrock step effectively isolates an upper basin from the main ice flow. The arcuate terminal moraines enclosing the basin are mantled by lacustrine sediments below 625 meters. The inferred lake and ice limit of the third advance are shown. The cross-section (not to scale) depicts the general form of the basin and presumed grounding line of the third advance. We speculate that only the first and second advances were voluminous enough to fully occupy the upper basin. Later advances were likely grounded to the west due to the relatively thin ice and resultant lower ice flux.

3.3.1.2 Paleoshorelines

A series of paleoshoreline levels and associated deposits were mapped and distinguished based on elevations and surface morphology. In satellite imagery and in the field, paleoshorelines are commonly associated with a distinct 5 – 10 meter scarp at a constant elevation; these encompass the former lake basin inside the Río Blanco moraine limits (Fig. 3.5a). Multiple closely spaced beaches with well-

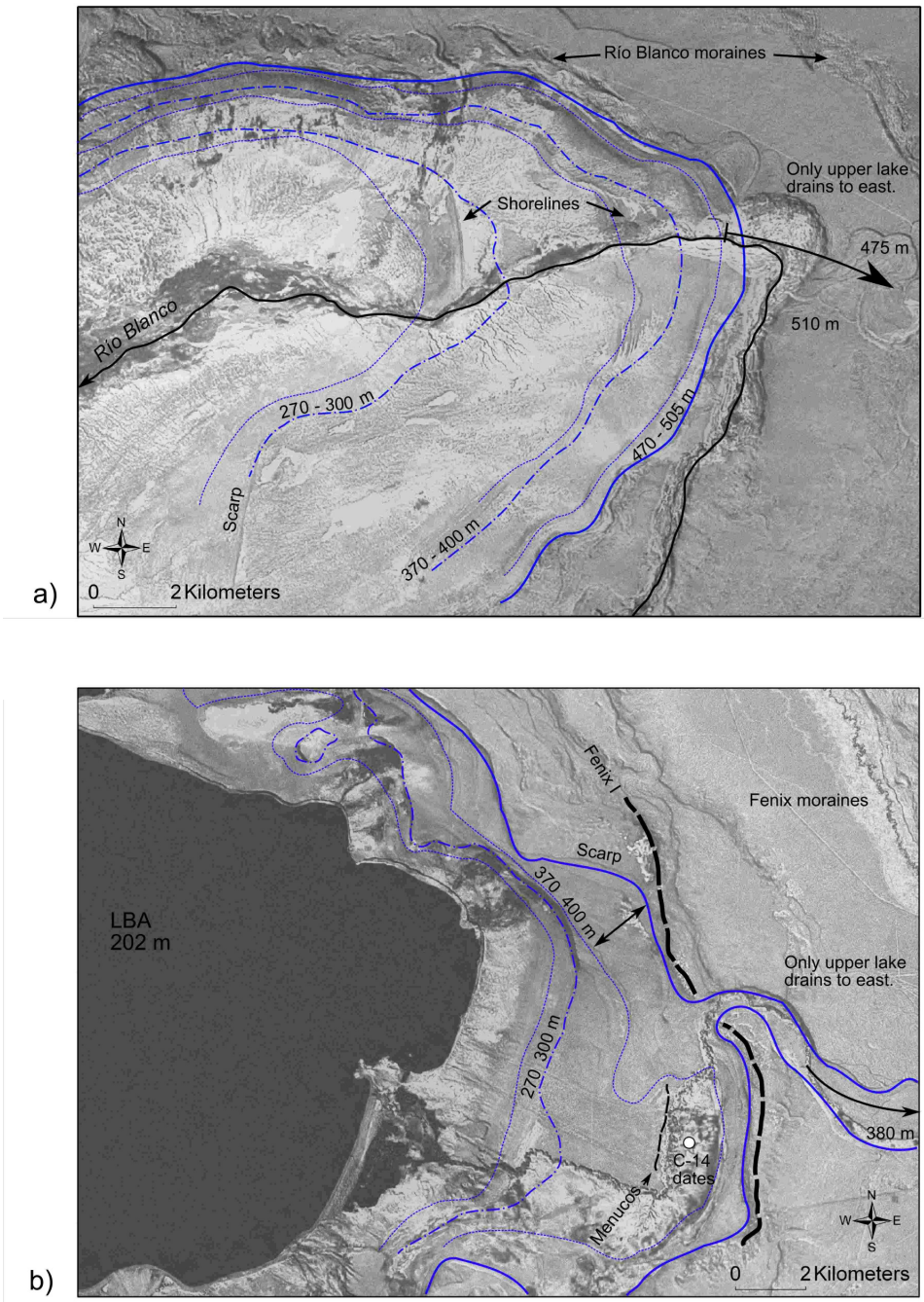

Figure 3.5. Paleoshoreline relationships

a) The map shows the principal paleoshoreline levels preserved in the Lago Pueyrredón valley. The lower two levels are shared with Lago Buenos Aires. b) The shared paleoshoreline levels at 400 – 370m and 300 – 270m at Lago Buenos Aires; the upper lake drained to the east while the lower lake drained to the west. Also shown are the location of moraines and ^{14}C ages that are discussed in text.

rounded cobbles parallel the scarps at some locations. A series of deltas grade to the former lake levels, and wave-polished boulders and rock shelters occur on the lowest paleoshoreline level at Cerro de los Indios (Fig. 3.6). Three distinct paleoshoreline levels are distinguishable at ca. 505 – 470 meters, ca. 400 – 370 meters and ca. 300 – 270 meters (Figs. 3.5a and 3.6). The Cañadón de Caracoles spillway is situated at ~475 meters; this is the only drainage route to the east. Our interpretation is that the upper lake level coincides with a time when ice occupied the Lago Pueyrredón valley and drainage was towards the east. The lower two paleoshoreline levels are shared in the Lago Buenos Aires valley (Fig. 3.5). We interpret these paleoshorelines to represent the 'united lake' that formed when ice occupying both valleys had withdrawn sufficiently to allow Lago Pueyrredón to drain into Lago Buenos Aires. The upper lake drained via the Río Deseado at Lago Buenos Aires (spillway ~380m; Fig. 3.5b) while the lower would have drained westward to the Pacific (Bell, 2008).

3.3.1.3 Inter-relationships

In the south of the valley, a bedrock step (150 – 200 m) effectively isolates an upper basin from the main ice flow (Figs. 3.2 and 3.4); the basin extends 8 kilometers eastward. A series of arcuate terminal moraines enclose the basin to the east and are mantled by lacustrine sediments below 625 meters (i.e., above the principal Cañadón de Caracoles spillway). A sediment section (570 meters) reveals till overlain by a 2 meter thick sequence of varved lacustrine sediments containing dropstones (Fig. 3.3d); these were deformed by a later advance that deposited a second till layer that is in turn covered by ~ 50 cm of lacustrine sediments. Based on the mapping and

subsequent exposure ages, we make the following interpretation: The moraines of the

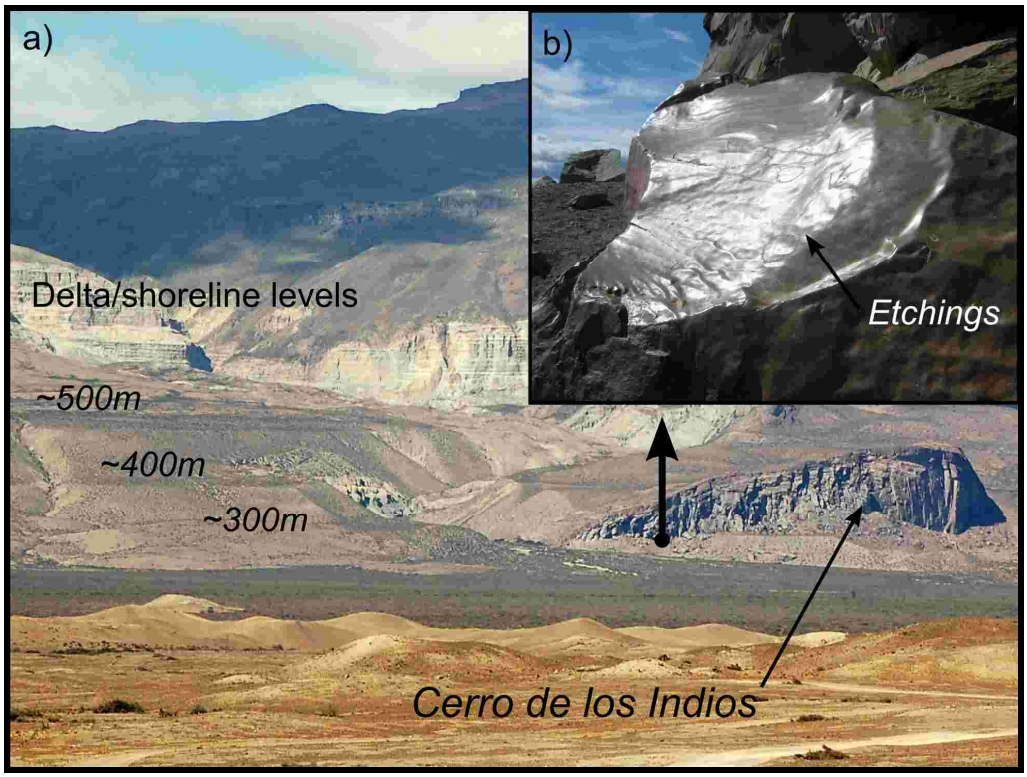

Figure 3.6. Photo of paleoshorelines

a) Deltas associated with the three main paleoshoreline levels at Lago Pueyrredón. The location of the photograph is shown in Fig. 3.2. b) The wave-polished boulders at the base of Cerro de los Indios (275m) were etched and painted by the Tehuelche Indians.

second limit were deposited rapidly as the relatively thin ice occupying the upper basin became increasingly decoupled from the main ice flow. In the process, the moraines dammed a small lake (spillway at ca. 625m) in between the main ice body to the west. Subsequent advances may have produced a lake but were likely grounded near the bedrock step.

3.3.2 Surface exposure ages

Moraine boulders were sampled to obtain ^{10}Be exposure ages for the key Río Blanco ice limits identified in Fig. 3.2. The surrounding geology is composed of Jurassic silicic volcanics and Cretaceous to Miocene mixed marine and continental sediments (Gorring et al., 2003). The nearest granitic rocks are within the San Lorenzo Plutonic Complex, about 80 kilometers from the innermost moraines (Suárez and De La Cruz, 2001). Therefore, transport distances for most sampled boulders (mainly granites) are large, and erosion should have been sufficient enough to have removed any cosmogenic nuclides accumulated prior to mobilization. Samples were collected with hammer and chisel following standard sampling protocols (e.g., Gosse and Phillips, 2001). Preference was given to large flat topped and stable boulders located on moraine crests. The sampled boulders showed few erosion features (e.g., pitting, spalling, ventifaction). The top few centimeters were sampled away from edges and where erosion appeared minimal; these were later crushed and sieved to obtain the 250 – 710 μm fraction. Shielding by local topography was measured using an inclinometer. In most cases, horizons were less than 3º resulting in a negligible scaling factor for topographic shielding. Vegetation is limited to small shrubs, and historical snow accumulation has been thin and short-lived in this semi-arid (~200 mm a^{-1})[2] and windy environment. Moreover, models predict increased aridity during glacial times (Hulton et al., 2002). Therefore, given the large (> 75cm) and exposed moraine boulders sampled in this study, we apply no post-depositional shielding correction for snow or vegetation.

[2] NCEP-NCAR reanalysis (www.cdc.noaa.gov/ncep_reanalysis/)



Figure 3.7. Photos of boulder samples

Boulders used for exposure age dating and their ^{10}Be ages: a) Large (3.1m) boulder from the outermost position of the first limit. b) Large (2.5m) boulder from the innermost moraine of the second limit showing evidence of spalling on the left side. c) Fresh boulder (1.0m) from the third limit near Lago Ghio. d) Small boulder (0.75m) resting on striated volcanic bedrock.

3.3.2.1 Sampling strategy

Moraine boulders marking each distinct ice limit were sampled (Fig. 3.7). The outermost moraines of the first limit were sampled at four locations (BC07-7, 8, 12, 43) to the south (Fig. 3.2). These samples are associated with the maximum ice extent. Three samples (BC07-9, 22, 23) marking the second limit were sampled from the outer and innermost moraines of this group. Four samples (BC07-16, 17, 18, 20) were sampled from the long and continuous moraine sequence marking the

distinct third limit. A fifth (BC07-21) was sampled from the youngest of the moraines located just above the highest (500m) paleoshoreline level. This sample marks the last ice advance prior to deglaciation. A final sample (BC07-13) resting on bedrock at an elevation of 352m was sampled to mark deglaciation (Fig. 3.7d). The assumption is that this sample was deposited in a pro-glacial lake by retreating ice, thus it would have been shielded from cosmic radiation by ~100 meters of water. This would reduce spallation and muonogenic production of ^{10}Be by over 99.9%. Subsequently, it became exposed when Lago Pueyrredón drained into Lago Buenos Aires and the lake level dropped from ~505 – 470 meters to ~400 – 370 meters. Further shielding may or may not have occurred at this stage given the uncertainty in elevations and lake levels (± 10m). Therefore, the sample should 1) mark a minimum date for the withdrawal of ice (~125km) from both valleys, which allowed the lakes to unite, 2) date the abandonment of the Cañadón de Caracoles drainage channel to the east, and 3) provide a minimum age for the Lago Columna moraines that were not sampled in this study.

3.3.2.2 Exposure age calculations and production rates

Samples were prepared at the University of Edinburgh's Cosmogenic Isotope Laboratory following procedures adapted from the methods of Bierman et al. (2002) and Kohl and Nishiizumi (1992). The ^{10}Be exposure ages were calculated using the CRONUS-Earth web-based calculator (version 2.2; Balco et al., 2008) which implements the revised ^{10}Be standardization and half-life (1.36 Ma) of Nishiizumi et al. (2007). The revised half-life has little effect (~1%) on exposure ages of Last Glacial age. We use the calculator's 'standard atmosphere' default setting for the

elevation – pressure relationship; this incorporates geographically variable mean sea-level pressure and 1000 mbar temperature fields obtained from the NCEP-NCAR reanalysis. Sample thickness (Table 3.1) and density (2.7 g cm^3) are used to normalize ^{10}Be concentrations to the boulder surface. Topographic shielding was measured but no correction was required except for sample BC07-13 (0.996). Exposure ages do not include any correction for boulder surface erosion; however a long-term maximum erosion rate of 1.4 mm ka^{-1} has been estimated for the Telken moraines (ca. 760 – 1100 ka) at nearby Lago Buenos Aires (Kaplan et al., 2005). Using this erosion rate increases exposure ages by ca. 2 – 3% for the youngest and oldest exposure ages reported, respectively. To facilitate cross-comparison with other cosmogenic nuclide chronologies, we report exposure ages based on all five scaling models implemented in the exposure age calculator (Table 3.2). The range in exposure ages derived using the different scaling models approaches 6%. Exposure ages are discussed with respect to the Dunai (2001) scaling model with a reference (sea level high latitude) ^{10}Be spallogenic production rate of 4.43 ± 0.52 atoms $g^{-1}(Si0_2)a^{-1}$ (±1σ; Balco et al., 2008) with muonic production of ^{10}Be calculated following Heisinger et al. (2002a; negative muon capture) and Heisinger et al. (2002b; fast muon interaction).

At Lago Pueyrredón, the production rate value itself is more uncertain than the uncertainty in scaling models. Current estimates of the uncertainty of the ^{10}Be production rate in quartz are in excess of 10% (Balco et al., 2009; Balco et al., 2008). This uncertainty becomes problematic when trying to resolve on millennial timescales (Kaplan et al., 2008b). Recent international efforts of the CRONUS-Earth

(Schaefer, 2005) and CRONUS-EU (Dunai and Team, 2005) projects have focused on refining our knowledge of terrestrial cosmogenic nuclide production rates, scaling models and decay constants with the ultimate aim to reduce 'external' uncertainties to better than 5%. Future refinement of the ^{10}Be production rate will affect the exposure ages and uncertainties reported in this study. However they are likely to be small so as not to affect our main conclusions. In this study, we make no correction for the higher (5 – 11%) long-term 'glacial' production rates estimated for the region (see Ackert et al., 2003; Hein et al., 2009; Staiger et al., 2007) because the samples were only exposed to elevated 'glacial' production rates for less than half of their exposure histories.

Given the proximity to and associations with glaciation in the Lago Buenos Aires valley, we recalculate some of the ^{10}Be cosmogenic nuclide ages published by Kaplan et al. (2004) and Douglass et al. (2006). When discussing 'recalculated exposure ages' with reference to Lago Buenos Aires, we refer to the data that was originally published by these authors as reported in Table 3.3. The recalculation makes a direct comparison of the data sets possible because the samples were taken from a similar latitude, elevation and geomorphic environment and because they are based on the same production rate, scaling factor and underlying geologic and geomorphic assumptions. Thus, systematic uncertainties for scaling factors are reduced. Most important, any changes in the production rate value itself will not affect comparisons made between the data sets. Data from the Strait of Magellan originally published by McCulloch et al (2005) and Kaplan et al. (2008a) are also recalculated (Table 3.3) in the same manner. Radiocarbon ages presented from this

point forward are reported as calibrated years before 1950 using the calibration curve of Fairbanks et al. (2005; v. Fairbanks0107).

3.4 Results

The cosmogenic nuclide results are presented in Tables 3.1 & 3.2 and are summarized in Fig. 3.8. Unless stated otherwise, uncertainties are 1σ analytical (internal) in the case of individual ages. For means, the uncertainty is based on an average of the upper and lower age limits. The upper limit is the exposure age plus one sigma, and the lower limit is the exposure age minus one sigma.

The four samples marking the most extensive limit (1st limit) range from 25.4 – 32.2 ka. The oldest sample (BC07-8) falls outside of 2σ uncertainty of the remaining population. This sample was either re-worked and as a result contains inherited nuclides from a previous exposure, or it suggests that the outermost Río Blanco moraine is a compound feature marking more than one advance. Clear evidence for glacier advances at this time exists in the northern Chilean Lake District (ca. 32 cal ka and 35 cal ka; Denton et al., 1999a; Lowell et al., 1995), and there is evidence of repeated occupation of LGM ice limits in the Strait of Magellan (Benn and Clapperton, 2000). Sugden et al. (2009) correlate dust peaks in Antarctic ice cores to outwash plain activity in southernmost South America. A clear dust peak at 31 ka in the EPICA Dome C ice core (Delmonte et al., 2004) may indicate that glaciers in southern South America advanced at this time. Therefore, the sample may date an earlier advance in the Lago Pueyrredón valley. Excluding this outlier from the

Table 3.1. ^{10}Be data for the Río Blanco moraines

Sample I.D.	AMS I.D.	Latitude (dd)	Longitude (dd)	Altitude (m asl)	Boulder height (cm)	Thick (cm)	Quartz mass (g)	^{10}Be concentration[a] ± 1σ[b] (10^5 atom g^{-1})
Río Blanco								
1st limit[c]								
BC07-7	b2050	-47.5186	-71.2361	564	225	2.5	20.9284	2.00 ± 0.07
BC07-8	b2043	-47.5564	-71.2629	587	190	1.5	27.7948	2.45 ± 0.08
BC07-12	b2036	-47.5840	-71.3548	665	310	1.5	24.1815	2.07 ± 0.07
BC07-43	b2055	-47.5079	-71.2451	581	80	1.5	25.7394	1.93 ± 0.06
2nd limit								
BC07-9	b2079	-47.5796	-71.3582	709	95	3	27.0887	1.91 ± 0.06
BC07-22	b2090	-47.5726	-71.4171	544	250	1.5	31.7051	1.63 ± 0.06
BC07-23	b2951	-47.5758	-71.4126	541	130	3.5	8.5658	1.66 ± 0.10
3rd limit								
BC07-16	b2953	-47.3041	-71.4029	620	100	1	26.0982	1.53 ± 0.05
BC07-17	b1766	-47.3087	-71.4050	614	100	2	27.8613	1.37 ± 0.06
BC07-18	b1770	-47.3380	-71.2490	570	140	2	27.9337	0.97 ± 0.05
BC07-20	b2954	-47.3259	-71.2938	565	75	2	31.3211	1.47 ± 0.04
Final Advance								
BC07-21	b2051	-47.3361	-71.2830	509	95	2	28.527	1.23 ± 0.05
Lake draining								
boulder on bedrock								
BC07-13*	b2042	-47.4525	-71.7120	352	75	1.5	30.9626	0.967 ± 0.051

* No correction for topographic shielding is applied to the data (horizons <~3º), except for sample BC07-13: the correction is 0.996.
[a]Normalized to NIST SRM-4325 Be standard with revised ^{10}Be/^{9}Be ratio of 2.79 x 10^{-11} and half-life 1.36 Ma (Nishiizumi et al., 2007).
Concentrations are corrected for ^{10}Be/^{9}Be of procedural blanks (0.9 - 1.7 x 10^{-14}; <10% of total ^{10}Be atoms in sample; ^{10}Be/^{9}Be: 0.9 - 1.7 x 10^{-14}).
[b]Uncertainties include propagated sample and blank ^{10}Be/^{9}Be analytical uncertainties and a 2% carrier addition uncertainty.
[c]Published by Hein et al. (2009). All AMS measurements made at the Scottish Universities Environmental Research Centre (S.U.E.R.C.)

remaining population reduces the range to 25.3 – 27.1 ka, with an arithmetic mean age of 26.0 ± 0.9 ka.

Table 3.2. ^{10}Be exposure ages from the Río Blanco moraine system

ε = 0 mm ka^{-1}		Lal (1991)/Stone (2000)	Time-dependent L/S	Lifton et al. (2005)	Desilets et al. (2003, 2006)	**Dunai (2001)**	Dunai (2001) *ε=1.4 mm ka^{-1}*	**Analytical uncertainty**	**External uncertainty** ε = 0 mm ka^{-1}
	Sample	± 1σ	± 1σ	± 1σ	± 1σ	± 1σ	± 1σ	± 1σ	(Dunai, 2001) ± 1σ
Context	I.D.	(x10^{3}a)	(x10^{3}a)	(x10^{3}a)	(x10^{3}a)	(x10^{3}a)	(x10^{3}a)	(x10^{3}a)	(x10^{3}a)
1st limit[a]	BC07-7	25.7	25.8	26.3	27.0	**27.1**	*28.0*	**0.9**	**3.3**
	BC07-8*	30.6	30.6	31.0	32.0	**32.2**	*33.4*	**1.0**	**3.9**
	BC07-12	24.0	24.2	24.6	25.3	**25.3**	*26.1*	**0.8**	**3.1**
	BC07-43	24.1	24.3	24.7	25.4	**25.5**	*26.2*	**0.8**	**3.1**
	Arithmetic mean:	*24.6 ± 0.9*	*24.8 ± 0.9*	*25.2 ± 0.9*	*25.9 ± 0.9*	*26.0 ± 0.9*	*26.8 ± 0.9*		
2nd limit	BC07-9	21.7	21.8	22.2	22.8	**22.9**	*23.5*	**0.7**	**2.8**
	BC07-22	21.0	21.2	21.7	22.2	**22.3**	*22.9*	**0.8**	**2.8**
	BC07-23	21.8	22.0	22.4	23.0	**23.1**	*23.7*	**1.3**	**3.0**
	Arithmetic mean:	*21.5 ± 0.9*	*21.7 ± 1.0*	*22.1 ± 0.9*	*22.7 ± 1.0*	*22.8 ± 1.0*	*23.4 ± 1.0*		
3rd limit	BC07-16	18.5	18.7	19.1	19.6	**19.6**	*20.1*	**0.6**	**2.4**
	BC07-17	16.8	17.0	17.4	17.8	**17.8**	*18.2*	**0.8**	**2.3**
	BC07-18*	12.4	12.6	12.9	13.2	**13.2**	*13.4*	**0.6**	**1.7**
	BC07-20	18.8	19.0	19.4	19.9	**19.9**	*20.4*	**0.6**	**2.4**
	Arithmetic mean:	*18.0 ± 0.7*	*18.2 ± 0.7*	*18.6 ± 0.7*	*19.1 ± 0.7*	*19.1 ± 0.7*	*19.5 ± 0.7*		
Final limit	BC07-21	16.4	16.6	17.0	17.4	**17.4**	*17.8*	**0.7**	**2.2**
Lake draining	BC07-13	14.9	15.1	15.5	15.8	**15.9**	*16.1*	**0.8**	**2.0**

* Sample excluded from calculation of arithmetic mean age.

[a]Published by Hein et al. (2009).
Exposure ages calculated with the CRONUS-Earth web-based calculator (v.2.2; http://hess.ess.washington.edu/math/index_dev.html; Balco et al., 2008).

Exposure ages calculated assuming a rock density of 2.7 g cm^{-3} and no correction for erosion is applied except where noted.

Shielding negligible for all samples except BC07-13 (0.996).

The outermost sample marking the second limit (BC07-9) yields an age of 22.9 ± 0.7 ka. The two innermost samples yield ages of 22.3 ± 0.8 ka (BC07-22) and 23.1 ± 1.3 ka (BC07-23). The indistinguishable ages obtained from the outer and innermost moraines of this advance suggest deposition over a short time period; additionally, it suggests that subsequent lakes that would have shielded the innermost samples from cosmic radiation must have been relatively short-lived (Fig. 3.4). The arithmetic mean age for the second advance is 22.8 ± 1.0 ka.

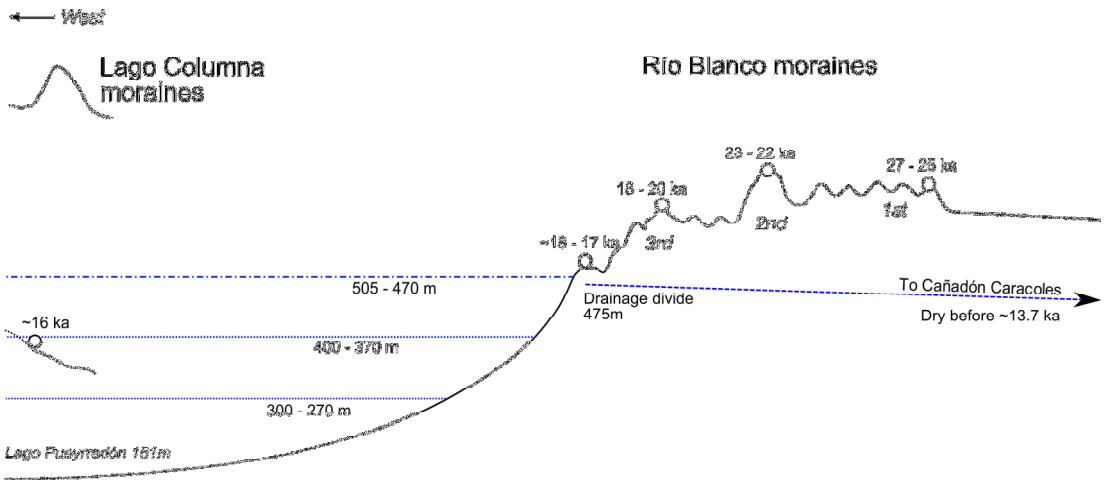

Figure 3.8. Geomorphic context of exposure ages

Approximate exposure ages and their geomorphic context (not to scale). The Cañadón de Caracoles dried after the lake level dropped to the 400m level; our exposure age of ca. 16 ka is consistent with the radiocarbon ages obtained by Mercer [1976, 1982] and Turner *et al.* [2005].

The four samples from the moraines marking the third limit yield ages of 13.2 – 19.9 ka. Sample BC07-18 (13.2 ka) is a clear outlier (3σ). This sample was perched near the edge of a steep sided (28º) moraine and likely shifted post-deposition. Excluding this sample, the range is 17.8 – 19.9 ka with an arithmetic mean age of 19.1 ± 0.7 ka. The final sample from the youngest Río Blanco moraine situated directly above the upper (500m) paleoshoreline level yields an age of 17.4 ± 0.7 ka, thus marking the final advance prior to deglaciation.

Finally, sample BC07-13 located on bedrock below paleolake level yields an age of 15.9 ± 0.8 ka. The implication is that both the Lago Pueyrredón and Lago Buenos Aires outlet glaciers had fully withdrawn from their valleys by this time, allowing the lakes to unite.

Table 3.3. Recalculated ^{10}Be ages from LBA and the Strait of Magellan

ε = 0 mm ka^{-1}		Lal (1991)/Stone (2000)	Time-dependent L/S	Lifton et al. (2005)	Desilets et al. (2003, 2006)	**Dunai (2001)**	Dunai (2001) *ε=1.4 mm ka^{-1}*	**Analytical uncertainty**	**External uncertainty** ε = 0 mm ka^{-1}
Context	Sample I.D.	± 1σ (x10^{3}a)	± 1σ (x10^{3}a)	± 1σ (x10^{3}a)	± 1σ (x10^{3}a)	± 1σ (x10^{3}a)	± 1σ (x10^{3}a)	± 1σ (x10^{3}a)	(Dunai, 2001) ± 1σ (x10^{3}a)
Lago Buenos Aires[a]									
Fenix V	LBA-01-60[a]	24.4	24.5	25.1	25.7	**25.8**	26.6	**1.0**	3.2
	LBA-02-20[b]	23.2	23.3	23.9	24.5	**24.5**	25.2	**1.6**	3.3
	LBA-98-135[a]	22.3	22.4	23.0	23.5	**23.6**	24.2	**0.8**	2.9
	LBA-01-22[a]	22.2	22.3	22.9	23.4	**23.5**	24.1	**0.8**	2.9
	LBA-02-21[b]	22.0	22.2	22.7	23.2	**23.3**	23.9	**2.3**	3.7
	LBA-02-24[b]	21.0	21.1	21.7	22.1	**22.2**	22.8	**0.9**	2.8
	LBA-02-22[b*]	17.9	18.1	18.6	19.0	**19.0**	19.4	**1.3**	2.6
	LBA-02-23[b*]	16.5	16.6	17.1	17.5	**17.5**	17.8	**0.9**	2.3
	Arithmetic mean:	*22.5 ± 1.3*	*22.6 ± 1.3*	*23.2 ± 1.3*	*23.7 ± 1.3*	***23.8 ± 1.3***	*24.5 ± 1.3*		
Fenix I	LBA-01-06[a]	17.8	18	18.5	18.9	**18.9**	19.3	**1.4**	2.7
	LBA-02-11[b]	16.6	16.7	17.2	17.6	**17.6**	17.9	**1.3**	2.5
	LBA-03-23[b]	16.5	16.7	17	17.4	**17.4**	17.7	**1.1**	2.3
	LBA-01-04[b]	16.4	16.6	17.1	17.4	**17.4**	17.8	**0.9**	2.3
	LBA-02-10[b]	15.6	15.8	16.3	16.6	**16.6**	16.9	**0.9**	2.2
	LBA-01-05[a]	15.2	15.4	15.8	16.1	**16.1**	16.5	**0.5**	2.0
	LBA-02-13[b]	14.6	14.8	15.3	15.6	**15.6**	15.9	**2.0**	2.8
	LBA-02-12[b]	14.3	14.5	14.9	15.2	**15.2**	15.4	**1.6**	2.5
	LBA-03-19[b]	13.8	13.9	14.3	14.6	**14.5**	14.8	**1.0**	2.0
	LBA-03-21[b*]	10	10.2	10.5	10.7	**10.6**	10.8	**1.0**	1.6
	Arithmetic mean:	*15.6 ± 1.2*	*15.8 ± 1.2*	*16.3 ± 1.2*	*16.6 ± 1.2*	***16.6 ± 1.2***	*16.9 ± 1.2*		
Menucos	LBA-03-11[b]	15.6	15.8	16.2	16.5	**16.5**	16.8	**3.0**	3.7
	LBA-04-12[b]	14.9	15.1	15.5	15.8	**15.8**	16.0	**1.0**	2.2
	LBA-03-13[b]	14.8	15	15.4	15.7	**15.7**	15.9	**1.0**	2.1
	LBA-04-14[b]	14.8	15	15.3	15.7	**15.6**	15.9	**0.8**	2.0
	LBA-03-10[b]	13.3	13.4	13.8	14.1	**14.0**	14.3	**1.2**	2.1
	LBA-03-17[b]	12.9	13	13.4	13.7	**13.6**	13.8	**0.9**	1.8
	LBA-03-14[b*]	10.6	10.8	11.1	11.3	**11.2**	11.4	**0.7**	1.5
	LBA-03-15[b*]	10.7	10.9	11.2	11.4	**11.4**	11.5	**0.9**	1.6
	LBA-04-13[b*]	10.8	11	11.2	11.5	**11.4**	11.6	**0.6**	1.5
	Arithmetic mean:	*14.4 ± 1.3*	*14.6 ± 1.3*	*14.9 ± 1.3*	*15.3 ± 1.3*	***15.2 ± 1.3***	*15.5 ± 1.3*		
Strait of Magellan									
Stage B	BGG-C1[c]	25.3	25.8	25.6	26.6	**26.7**	27.4	**1.9**	3.8
	BGG-C2[c]	24.2	24.7	24.6	25.5	**25.6**	26.3	**2.4**	4.0
	BGG-C3[d]	23.9	24.5	24.3	25.3	**25.4**	26.0	**1.0**	3.2
	BGG-C4[c]	22.8	23.3	23.1	24.0	**24.1**	24.7	**1.4**	3.2
	Arithmetic mean:	*24.0 ± 1.7*	*24.6 ± 1.7*	*24.4 ± 1.7*	*25.4 ± 1.7*	***25.5 ± 1.7***	*26.1 ± 1.7*		
Stage D	SM-02-21[d]	17.7	18.1	18.0	18.7	**18.8**	19.2	**5.2**	5.9
	BI-C3[c]	17.2	17.6	17.5	18.1	**18.3**	18.6	**1.9**	2.9
	BI-C2[c]	17.1	17.5	17.4	18.0	**18.1**	18.5	**2.6**	3.5
	BI-C1[c]	16.4	16.7	16.7	17.3	**17.4**	17.7	**1.4**	2.5
	SM-02-23[d]	15.5	15.8	15.8	16.3	**16.4**	16.7	**1.5**	2.5
	Arithmetic mean:	*16.9 ± 2.6*	*17.2 ± 2.6*	*17.2 ± 2.6*	*17.8 ± 2.6*	***17.8 ± 2.6***	*18.2 ± 2.6*		

[a] Kaplan et al. (2004) [b] Douglass et al. (2006) [c] McCulloch et al. (2005) [d] Kaplan et al. (2008)

* Sample excluded from calculation of arithmetic mean age following original publications.

All exposure ages calculated with the CRONUS-Earth web-based calculator (v.2.2; http://hess.ess.washington.edu/math/; Balco et al., 2008).

Rock density and sample shielding as per original publications.

3.5 Discussion

3.5.1 Río Blanco moraines – revised chronology

The cosmogenic nuclide ages are internally consistent and suggest the moraines were deposited over an 8 – 10 ka period between ca. 25 – 27 ka and ca. 17.5 ka. The cosmogenic nuclide chronology concurs with the stratigraphy. The oldest moraine boulders are situated on the outermost moraine limit, and boulders on stratigraphically younger moraines yield successively younger cosmogenic-nuclide surface exposure ages. The data indicate that all of the Río Blanco moraines were deposited during the Last Glacial period with key advances at ca. 26 ka, ca. 23 ka and ca. 19 ka, and with deglaciation after ca. 17.5 ka.

The results differ from the Late-glacial to Holocene ages previously reported for the same moraine system (Wenzens, 2005). Wenzens (2005) argument for Holocene ice at the eastern end of the Lago Pueyrredón valley is partly based on a radiocarbon age of 8.3 ^{14}C ka (9.3 cal ka) obtained from the humic base of a kettle hole located within what he considers to be the youngest of the Río Blanco moraines (the 'second limit' of this study). However, with a glacier occupying the valley, meltwater from the glacier would be forced to drain eastward via the Cañadón de Caracoles (Section 3.2.2.), the only drainage route that penetrates the outer moraine systems (Fig. 3.2). Independent ^{14}C ages on peat located at the base of a ~4 meter core in the Cañadón de Caracoles indicate that this outlet had dried by ca. 13.7 cal ka (11.8 ^{14}C ka; Mercer, 1976; Mercer, 1982; Turner et al., 2005). This is inconsistent with a Holocene advance to the eastern end of Lago Pueyrredón. Moreover, in this arid

environment, organic material may not begin to accumulate immediately following moraine deposition (or channel drying), but instead may reflect the onset of more humid conditions (McCulloch et al., 2005). Therefore, the ^{14}C ages based on the accumulation of organic material should not be considered close minimum ages for deglaciation in this semi-arid environment on the eastern side of the Andes. Our independent age for drying of the Cañadón de Caracoles at 15.9 ± 0.8 ka (i.e., joining of the lakes) is consistent in this context with the minimum ^{14}C age of 13.7 cal ka obtained by Mercer (1982) and Turner (2005) for the same event. Based on the available data, we reach the same conclusion originally made by Mercer (1976); Any Younger Dryas or Holocene glacier advances in the region were restricted to the cordillera.

3.5.2 Regional significance of the new chronology

We date the maximum extent of ice during the last glacial period in the Lago Pueyrredón valley at 25 – 27 ka; the mean value is 26.0 ± 0.9 ka. The timing of the LGM advance is in good agreement with other Patagonian records (Fig. 3.9). Across much of the Chilean Lake District, the most extensive LGM advance occurred at 27 cal ka (22.5 ^{14}C ka; Denton et al., 1999a). In the Strait of Magellan, four recalculated ^{10}Be exposure ages obtained by McCulloch et al. (2005) and Kaplan et al. (2008a) span the same time period of ca. 24 – 27 ka, with a mean of 25.5 ± 1.7 (Table 3.3). Thus overall, the timing of the maximum extent appears to be broadly in phase throughout Patagonia.

The dating of the LGM maximum extent in the Lago Pueyrredón and nearby Lago Buenos Aires valley's exemplifies the benefit of obtaining multiple chronologies to better characterize the regional glacier response. Specifically, the LGM maximum extent at Lago Buenos Aires (Fenix V moraines) is dated at ca. 4 ka later than the most extensive glacier extents in the Chilean Lake District (Douglass et al., 2006; Kaplan et al., 2004). Whereas the ages from nearby Lago Pueyrredón (26.0 ± 1.0 ka) instead suggest that the central Patagonian response was broadly synchronous. Thus, given the chronology at nearby Lago Pueyrredón, we find that the late LGM maximum at Lago Buenos Aires is not likely characteristic for all central Patagonian glaciers.

Deglaciation began after 17.4 ± 0.7 ka based on the exposure age from a boulder located on the innermost Río Blanco moraine crest. The age is consistent with respect to three ages from the moraines marking the third limit (ca 19.1 ± 1.1 ka) and with the age obtained to mark final retreat of the lobe (15.9 ± 0.8 ka). Increasing the number of samples would help to refine the age, but few boulders were found. Given the internal consistency of the data, we consider the single age representative of the timing of the final advance at Lago Pueyrredón.

If so, the timing of the final advance is similar to that of other Patagonian records (Fig. 3.9). For example, in the Chilean Lake District, the final advance is dated at 17.9 cal ka (Denton et al., 1999b; Heusser et al., 1999; Lowell et al., 1995; Moreno et al., 1999) and warming began at 17.5 cal ka (Massaferro et al., 2009; Moreno and Leon, 2003). In the Strait of Magellan, the final advance occurred prior to ca. 17 cal

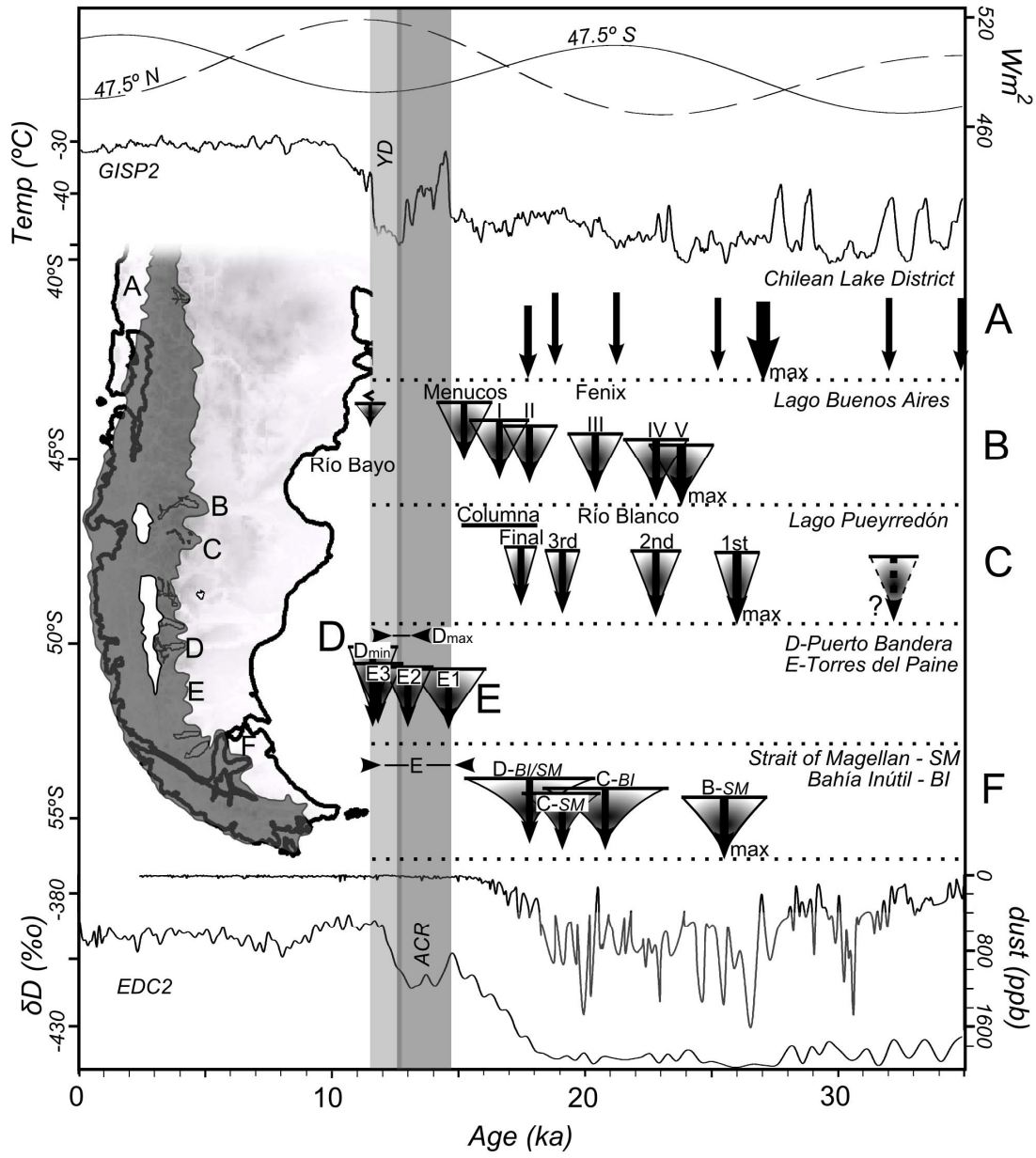

Figure 3.9. Synthesis of dated ice limits in Patagonia

A comparison of available ^{10}Be exposure ages for moraines in Patagonia calculated on a common basis. The figure does not attempt to compare moraines with bracketing radiocarbon ages except where noted and thus only analytical uncertainties are presented. All ^{10}Be exposure ages were re-calculated with the CRONUS-Earth exposure age calculator (version 2.2; [Balco *et al.,* 2008]) according to the Dunai [2001] scaling model, and assumed no rock surface erosion. The mean age for each moraine is indicated by the arrow point, while the 1σ analytical uncertainty is indicated by the width of the triangle; the uncertainty is calculated as discussed in the text. The relative extent of each moraine-defined limit is shown decreasing from the LGM maximum limit which is denoted by the dotted horizontal line at each site. Data sources are: EDC2 deuterium and dust [EPICA *community members*, 2004]; Strait of Magellan and Bahía Inútil glacier advances B, C, D and E (note: stage E is based on bracketing radiocarbon ages) ((McCulloch et al., 2005) and (Kaplan et al., 2008a)); Torres del Paine (note: E1 – is the 'outermost moraine', E2 – is 'within outermost moraine'

and E3 – is the 'innermost moraine' as discussed by Moreno *et al.* (2009), and the data from both valleys have been averaged together ((Fogwill and Kubik, 2005) and (Moreno et al., 2009)); the chronology for the Puerto Bandera moraines is by Ackert *et al.* (2008) (^{10}Be – Dmin) and ((Strelin and Malagnino, 2000) and (Strelin and Denton, 2005))(^{14}C – Dmax); Lago Pueyrredón (This study); Lago Buenos Aires ((Kaplan et al., 2004) and (Douglass et al., 2006)); Río Bayo is a minimum age (Glasser et al., 2006); radiocarbon ages from the Chilean Lake District (Denton et al., 1999b); GISP2 temperature (Alley, 2000); Insolation (Berger, 1978).

ka based on minimum radiocarbon ages (McCulloch and Davies, 2001; McCulloch et al., 2005). Recalculated ^{10}Be exposure ages for the final advance (Stage D) in the Strait of Magellan are 16.4 – 18.7 ka with a mean of 17.8 ± 2.6 ka. At Lago Buenos Aires, the recalculated ^{10}Be exposure ages (Fenix I) are 14.5 – 18.9 ka with a mean of 16.6 ± 1.2 ka. Bearing the uncertainties in mind, there appears to be good agreement on the general timing of the final advances (ca. 17 - 18 ka) and with the onset of deglaciation throughout Patagonia.

3.5.3 The evolution and diversion of paleolakes

The sequence and timing of deglaciation has implications for the development and drainage of a series of interconnected glacier-dammed lakes. Based on the available ^{10}Be exposure ages and radiocarbon ages, we present a conceptual model of deglaciation for the region in Fig. 3.10. The process of deglaciation in the Lago Pueyrredón valley was interrupted by a readvance that deposited the Lago Columna moraines (Figs. 3.2 and 3.10b). No direct ages for the Lago Columna moraines were obtained. However, they are stratigraphically younger than the youngest Río Blanco moraine dated at 17.4 ± 0.7 ka. In addition, based on our mapping and correlation with what is considered an equivalent ice limit in the Lago Pueyrredón valley (Fig. 3.2), we conclude that the moraines were deposited at a time when ice occupied the

Lago Pueyrredón valley and drainage of the pro-glacial lake was eastward via the Cañadón de Caracoles (Fig. 3.10b). Therefore, the Lago Columna moraines are likely older than the drying of this channel with a minimum age of 13.7 cal ka. Our independent age for this event (Section 3.4) further constrains the

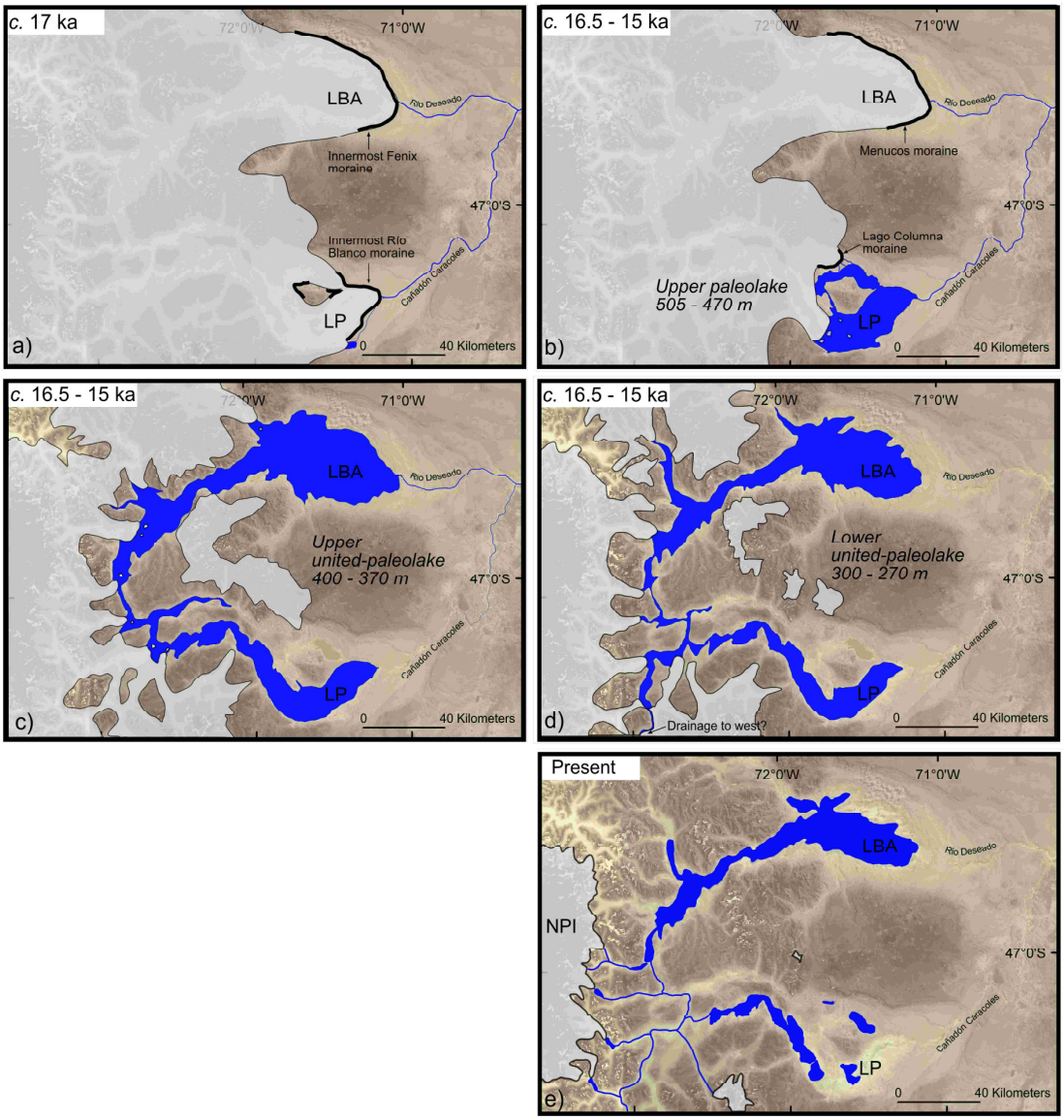

Figure 3.10. Conceptual model for deglaciation

A conceptual model that approximates the pattern and timing of deglaciation in the region as discussed in the text. As such, it is not based on any known configuration of the outlet glaciers during the stated time intervals, except where noted and where ice margins are marked in bold and sources are cited. We make no attempt to distinguish the height of the ice sheet except where this was mapped in the Lago Pueyrredón (LP) valley, and thus we do not attempt to distinguish nunataks or other ice free areas in the interior.

a) ca. 17 ka: Glaciers fill the lake basins of Lago Buenos Aires (LBA) and Lago Pueyrredón and terminate at the innermost Fenix moraine ((Douglass et al., 2006) and (Kaplan et al., 2004)) and the innermost Río Blanco moraine, respectively.
b) 16.5 – 15 ka: Deglaciation is interrupted by a readvance that deposits the Menucos ((Douglass et al., 2006) and (Kaplan et al., 2004)) and Lago Columna moraines; the upper paleolake in the Lago Pueyrredón valley forms around this time.
c) 16.5 – 15 ka: The Lago Pueyrredón and Lago Buenos Aires outlet glaciers rapidly retreat to expose the valley linking the two lake basins, this allows the two lakes to join as one united lake (upper united-paleolake) that drains eastward via the Río Deseado.
d) 16.5 – 15 ka: The glaciers retreat sufficiently to allow westward drainage and establishment of the lower united-paleolake around this time. The present day configuration was established when the Río Baker became ice free which allowed the lower united-paleolake to drain freely into the Pacific Ocean. Estimates on the timing range from 12.8 ka (Turner et al., 2005) to after ca. 6.2 ka ((Bell, 2008) and (Douglass et al., 2005)).

deposition age of the Lago Columna moraines to between 15.9 ± 0.8 ka and 17.4 ± 0.7 ka.

In the Lago Buenos Aires valley, a readvance deposited the Menucos moraines to within a few kilometers of the Fenix I ice limit (Fig. 3.5b). The Menucos limit occupies a similar stratigraphic position as the Lago Columna limit, and they may be correlative. The Menucos moraines are dated at 14.4 ± 0.9 ka (weighted mean age and 2σ analytical uncertainties; (Douglass et al., 2006)). The recalculated ^{10}Be exposure ages range from 13.6 – 16.5 ka with an arithmetic mean age of 15.2 ± 1.3 ka. Thus, the recalculated ages from the Menucos limit are consistent with the inferred minimum ages for the Lago Columna limit. At Lago Buenos Aires, an additional constraint on the maximum age of the Menucos moraines comes from three radiocarbon ages obtained from carbonate-cemented concretions in varved lake sediments located stratigraphically between the Menucos and Fenix I moraines (Caldenius, 1932; Douglass et al., 2006; Kaplan et al., 2004; Sylwan, 1989). The radiocarbon ages range from 15.0 ± 0.2 cal ka to 16.5 ± 0.5 cal ka (1σ analytical).

Following deposition of the Menucos and Lago Columna moraines, the glaciers in both valleys withdrew by 80 – 140 kilometers to within 20 kilometers of present day margins; this allowed Lago Pueyrredón to join Lago Buenos Aires as one united lake that drained eastward via the Río Deseado (Fig. 3.10c). At Lago Pueyrredón, a boulder resting on bedrock at an elevation near the upper 'united lake' level was sampled. If our assumptions are correct (Section 3.3.2.1), the exposure age of 15.9 ± 0.8 ka ages the draining of Lago Pueyrredón into Lago Buenos Aires following deposition of both the Menucos and Lago Columna moraines. Further independent ages published by Turner et al. (2005) support withdrawal of ice at this time. Turner et al. (2005) sampled from ice marginal deposits at the base of Cerro Ataud (Fig. 3.1b). Peat and plant macrofossils were sampled at ca. 350 meters elevation from two kettle holes associated with the lower 'united lake' level. The two peat samples yield radiocarbon ages of 15.773 ± 0.153 cal ka and 13.897 ± 0.086 cal ka. To confirm the old peat ages, Plant macrofossils were sampled and analyzed from the same cores, these yield ages of 15.266 ± 0.136 cal ka and 13.443 ± 0.085 cal ka. Turner et al. (2005) interpret the data as evidence for early deglaciation near Cerro Ataud, and they suggest a rapid retreat of glaciers occurred previously at 15 – 16 ka.

In summary, the data indicate the Patagonian ice sheet readvanced to near the eastern ends of two major outlet valleys at 15.2 ± 1.1 ka (Lago Buenos Aires) and between 15.9 ± 0.8 ka and 17.4 ± 0.7 ka (Lago Pueyrredón). These two glaciers had withdrawn 80 – 140 kilometers by 15.9 ± 0.8 ka (i.e., when the lakes joined), and deglaciation had progressed enough to establish the lower 'united lake' thereby

exposing the base of Cerro Ataud near present day glacier margins by ca.13.4 – 15.9 cal ka. These data require a rapid retreat of both outlet glaciers within perhaps just hundreds of years. Rapid glacier retreat is supported by previous ice sheet model results (Hubbard et al., 2005), and is consistent with rapid glacier retreat (ca. 80 kilometers) reported in the Strait of Magellan near this time (McCulloch et al., 2005); the retreat was likely accelerated by an active calving margin. The proposed timing of retreat coincides with a time when temperatures in the Chilean Lake District had reached modern levels of warmth (ca. 15.6 - 15.3 cal ka; Lowell et al., 1995).

3.5.4 Wider implications

The overall structure of the LGM at Lago Pueyrredón bears similarities to other paleoclimate records in southern South America and in other parts of the world. The maximum ice extent occurred at ca. 25 – 27 ka and the glacial climate persisted over an 8 – 10 ka period as evident by several readvances, the last of which occurred at ca. 17.5 ka, before the onset of deglaciation in the valley. The LGM occurred during Marine Isotope Stage 2. Glaciers reached their maximum extent coincident with minimum northern hemisphere temperatures (e.g., GISP2; Alley, 2000) and despite a peak in summer insolation intensity at middle latitudes in the southern hemisphere at this time (Fig. 3.9). These data lend further support to the idea that global climates are broadly synchronized on orbital timescales (Denton et al., 1999a).

During the glacial-interglacial transition, glaciers east of the North Patagonian Icefield appear to reflect southern hemisphere forcing. Specifically, the rapid deglaciation of the Lago Buenos Aires and Lago Pueyrredón outlet glaciers was

interrupted when ice margins stabilized (Turner et al., 2005) or readvanced (Douglass et al., 2006) during the Antarctic Cold Reversal (ca. 14.8 - 12.7 ka; Blunier et al., 1998). Hubbard et al. (2005) reach the same conclusion using an ice sheet model driven by a re-scaled Vostok temperature record. The pattern of glacier retreat followed by stabilization during the Antarctic Cold Reversal bears similarities to paleoecological records in the Chilean Lake District. A chironomid and pollen record indicates that climate warming intensified at 15.7 cal ka and peaked at 14.5 cal ka; this was followed by cooling peaks at 14 cal ka and 13.5 cal ka (Massaferro et al., 2009). A similar pattern is found in southernmost Patagonia where distinct glacier readvances occurred during the Antarctic Cold Reversal (Fogwill and Kubik, 2005; McCulloch et al., 2005; Moreno et al., 2009). However, paleoecological records from the Península de Taitao located west of the North Patagonian Icefield, instead suggests that no significant cooling capable of reversing forest development occurred during either the Antarctic Cold Reversal or the Younger Dryas stadial at these latitudes (Bennett et al., 2000; Hoganson and Ashworth, 1992; Lumley and Switsur, 1993).

During the northern hemisphere Younger Dryas stadial, the regional glacier response is equivocal. Mercer (1976) concludes that the Younger Dryas and Holocene advances remained within neoglacial limits, at least in the case of one glacier (Témpano). Turner et al. (2005) suggest further that deglaciation may have begun during the Younger Dryas, which allowed the lower united lake to empty into the Pacific. In contrast, Douglass et al. (2005) and Bell (2008) suggest that the glaciers damming the lower united lake may have persisted until as late as ca. 6 ka (Fig.

3.10d). Paleoecological records from the Península de Taitao indicate the climate was somewhat cooler and drier during the Younger Dryas (Massaferro and Brooks, 2002), but they do not support a significant climate reversal during this period. While there remains uncertainty over the Younger Dryas response, collectively the available evidence in the region do not suggest a significant glacial readvance at this time; however, the presence of large pro-glacial lakes may have precluded the preservation of such records.

The glacial geologic and paleoecologic records in central Patagonia do not echo a distinct Antarctic or northern hemisphere influence on millennial-scale climate variability during the last glacial-interglacial transition. In southernmost Patagonia and Tierra del Fuego (ca. 51 – 53º S), some antiphase (i.e., Antarctic) behavior to the dominant northern hemisphere signal is evident based on glaciers that readvanced during the Antarctic Cold Reversal and then retreated during the Younger Dryas period (McCulloch et al., 2005; Sugden et al., 2005). In the Chilean Lake District of northwestern Patagonia (ca. 41 – 43º S), a more 'northern' signal is evident by glaciers that advanced coincident with a Younger Dryas or equivalent cooling (Ariztegui et al., 1997; Hajdas et al., 2003). In contrast, the central Patagonian (ca. 46 – 48º S) climate and glacier response appears muted by comparison if one accepts that ice margins stabilized during the Antarctic Cold Reversal, rather than readvancing significantly. The paleoecological records at these latitudes (Península de Taitao) do not mirror Antarctic or northern hemisphere climate influences during the glacial-interglacial transition. Thus, the central Patagonian records may reflect

some blending of Antarctic and northern hemisphere influences as previously suggested (Sugden et al., 2005).

3.6 Conclusions

Our mapping and cosmogenic ^{10}Be surface exposure ages allow us to draw the following conclusions:

1. The LGM maximum ice extent in the Lago Pueyrredón valley (~47.5º S) corresponds to the outermost limit of the Río Blanco moraine system; this maximum ice limit occurred by 27 – 25 ka, and is consistent with other Patagonian records in the Chilean Lake District (~42º S) and the Strait of Magellan (~53º S).

2. Slightly less-extensive Río Blanco ice limits are dated at 23 - 22 ka, 20 – 18 ka and ca. 18 – 17 ka. The overall timing of the LGM in the Lago Pueyrredón valley, with the maximum extent by 27 – 25 ka and deglaciation after ca. 18 – 17 ka, is broadly synchronous with other glacier chronologies in both hemispheres (e.g., (Clark et al., 2009) and (Schaefer et al., 2006)).

3. The new chronology indicates that the Río Blanco moraine system was not deposited during the Late-glacial to Holocene period as previously suggested (Wenzens, 2005).

4. Glaciers in both the Lago Buenos Aires and Lago Pueyrredón valleys retreated rapidly at around 16.5 – 15 ka. This retreat was associated with the evolution of a series of linked glacier-dammed lakes whose drainage

shifted across the continental divide as a consequence of disintegrating ice.

3.7 Acknowledgements

We thank for logistical support: C. Risso, O. Martínez, P. Alvarez; for field support: J. Boex; and for assistance with laboratory work: E. McDougall. For financial support we thank the UK Natural Environment Research Council (NERC) for A. Hein's studentship and sample analysis, the Royal Geographic Society (with IBG) - Rio Tinto plc award, the Royal Scottish Geographic Society, the Carnegie Trust for the Universities of Scotland and the Scottish Universities Environmental Research Centre (S.U.E.R.C.) for support of sample analysis.

Chapter 4 Middle Pleistocene glaciation in Patagonia dated by cosmogenic-nuclide measurements on outwash gravels

This chapter demonstrates a new approach to dating old glacial sequences by cosmogenic-nuclide surface exposure methods on outwash gravels, and draws comparisons to the traditional approach based on moraine surface boulders. It establishes the age of the penultimate "Hatcher" glacial sequence in the Lago Pueyrredón valley. This chapter has been published as follows:

Hein, A.S., Hulton, N.R.J., Dunai, T.J., Schnabel, C., Kaplan, M.R., Naylor, M., Xu, S. (2009). Middle Pleistocene glaciation in Patagonia dated by cosmogenic-nuclide measurements on outwash gravels. *Earth and Planetary Science Letters.* doi:10.1016/j.epsl.2009.06.026.

I wrote the manuscript; the original idea for targeting outwash terraces came from Dunai, Hulton and Kaplan; the depth-profile opportunity came when I was working alone; both supervisors accompanied me for part of my field-work; Schnabel, Kaplan, Dunai and Hulton provided helpful comments on the manuscript; Naylor provided help with the mathematical model; Xu performed the AMS measurements.

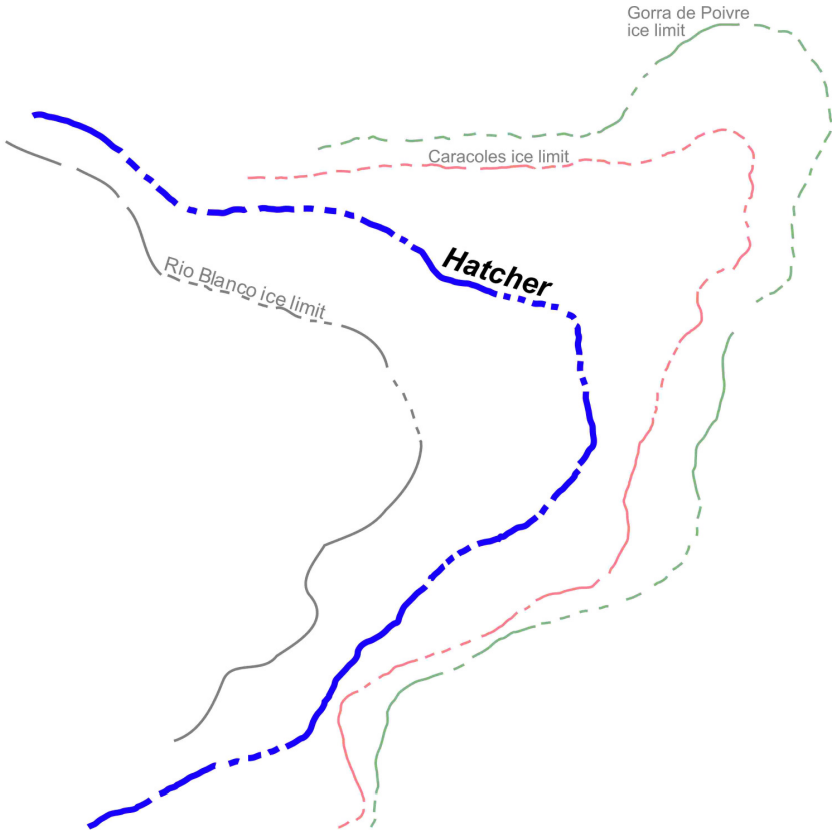

Abstract

The well-preserved glacial record in Argentine Patagonia offers a ~1 Ma archive of terrestrial climate extremes in southern South America. These glacial deposits remain largely undated beyond the range of radiocarbon age dating at ca. 40 ka. Dating old glacial deposits (> several 10^5 a) by cosmogenic-nuclide surface exposure methods is problematic because of the uncertainty in moraine degradation and boulder erosion rates. Here, we show that cobbles on outwash terraces can reliably date 'old' glacial deposits in the Lago Pueyrredón valley, 47.5º S, Argentina. Favorable environmental conditions (e.g., aridity and strong winds) have enabled continuous surface exposure of cobbles and preservation of outwash terraces. The data demonstrate that nuclide inheritance is negligible and we therefore use the oldest surface cobbles to date the deposit. ^{10}Be concentrations in outwash cobbles reveal a major glacial advance at ca. 260 ka, concurrent with Marine Isotope Stage 8 (MIS 8) and dust peaks in Antarctic ice cores. A ^{10}Be concentration depth-profile in the outwash terrace supports the age and suggests a low terrace erosion rate of ca. 0.5 mm ka^{-1}. We compare these data to exposure ages obtained from associated moraines and find that surface boulders under-estimate the age of the glaciation by ~100 ka; thus the oldest boulders in this area do not date closely moraine deposition. The ^{10}Be concentration in moraine cobbles help to constrain moraine degradation rates. These data together with constraints from measured ^{26}Al/^{10}Be ratios suggest that all moraine boulders were likely exhumed after original deposition. We determine the local Last Glacial Maximum (LGM) occurred at ~27 – 25 ka, consistent with the maximum LGM in other parts of Patagonia.

4.1 Introduction

The aim of this research is to establish a more reliable method of dating pre-Last Glacial Maximum (LGM) ice limits using cosmogenic-nuclide surface exposure age dating methods on glacial outwash terrace material as opposed to moraine boulders. Specifically, this approach is used to date the well-preserved sequence of Quaternary ice limits in Argentine Patagonia. These limits are well documented (e.g., Caldenius, 1932; Clapperton, 1993; Flint and Fidalgo, 1964; Mercer, 1976; Rabassa and Clapperton, 1990; Singer et al., 2004) but have proved difficult to date thus far. Our approach is to avoid the problems that inadvertently arise from dating boulders that have been exhumed as a moraine degrades. We achieve this by sampling fluvial rounded cobbles from stable outwash terrace surfaces that are stratigraphically associated with the moraines. Applicability of the method is dependent on three principal factors: First, linking outwash abandonment to a specific glacial event; second, on there being low nuclide inheritance in outwash sediment; and third, that there is no post-depositional burial, mixing or removal of the terrace sediment. We argue that these favorable conditions are met in parts of Argentine Patagonia and may occur in other arid and aeolian active environments elsewhere. In this paper, we compare ^{10}Be and ^{26}Al exposure ages obtained from (1) moraine boulders with (2) moraine cobbles and (3) outwash terrace cobbles of the same glacial event in the Lago Pueyrredón valley, 47.5º S, Argentina. The palaeoclimatic significance of the new chronology developed in this study will be addressed in future publications.

4.1.1 Patagonian glacial history and the age gap

Well-dated moraines older than the LGM are sparse in Patagonia reflecting a lack of dateable material and the limit of radiocarbon age dating beyond ~40 ka. Most outlet valleys in arid Argentine Patagonia contain four to five groups of moraines and associated outwash terraces (Caldenius, 1932; Clapperton, 1993; Kaplan et al., 2009). The deposits range from the innermost LGM (~25 ka) deposits to the outermost 'Greatest Patagonian Glaciation' deposits dated at ~1.1 Ma (Meglioli, 1992; Mercer, 1976; Rabassa and Clapperton, 1990; Rabassa et al., 2000; Singer et al., 2004; Ton-That et al., 1999). In many cases, these end members often provide the only age framework for intermediate deposits (i.e., between LGM time and ~1.1 Ma). Recently, Kaplan et al. (2005) demonstrated the potential of cosmogenic-nuclide surface exposure methods to fill these gaps when they identified a glacial advance around 140 – 150 ka (MIS 6) and at least one prior to 200 ka at Lago Buenos Aires (LBA), 46.5° S, Argentina. Despite good moraine preservation and low boulder erosion rates (~1.4 mm ka^{-1}), the wide scatter in boulder exposure ages made interpretation of the age of older moraines challenging.

4.1.2 Exposure ages of old moraines

Boulders on old moraines (i.e., older than several 10^5 a) frequently yield wide scatter in exposure ages that is commonly attributed to boulder erosion rate uncertainty and exhumation (e.g., Benson et al., 2004; Briner et al., 2005; Kaplan et al., 2007; Kaplan et al., 2005; Owen et al., 2006; Phillips et al., 1990; Schäfer et al., 2008; Shanahan and Zreda, 2000). Poorly constrained (or non steady-state) boulder erosion rates are known to affect significantly the accuracy of older exposure ages, even with

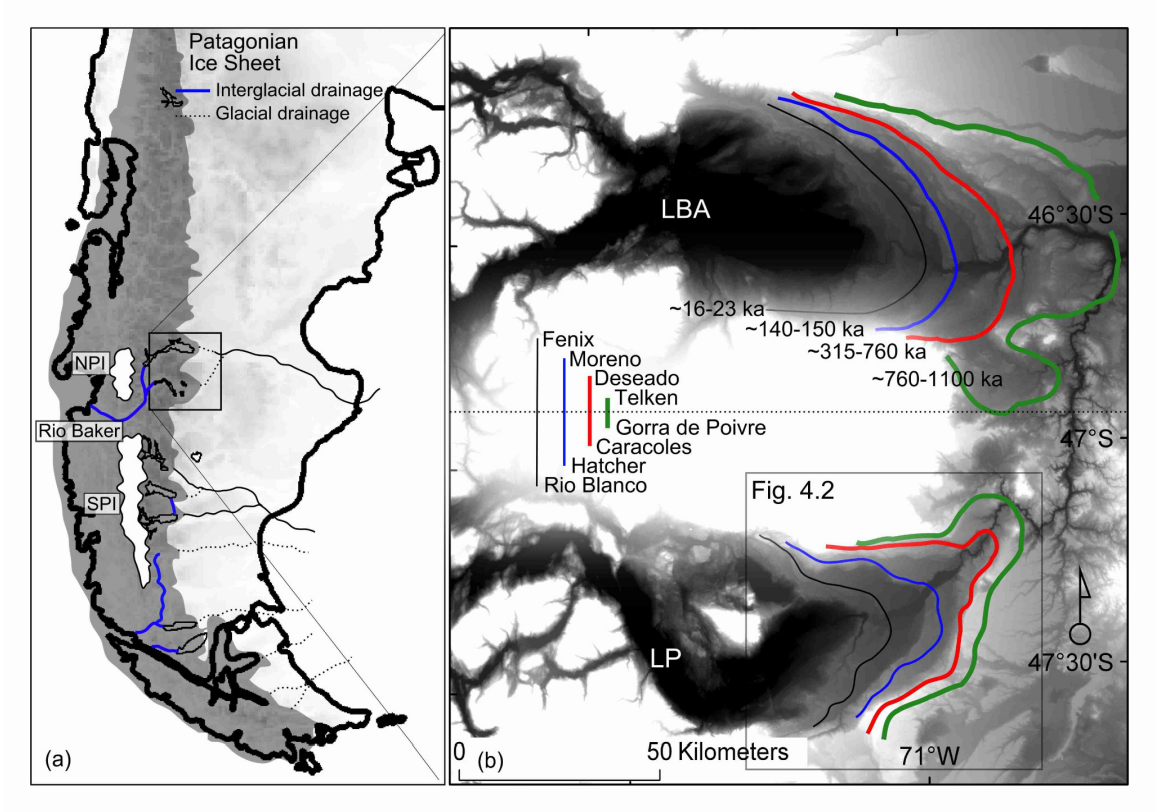

Figure 4.1. Context map

a) Location of study area showing an expanded Patagonian ice sheet and the present day North (NPI) and South (SPI) Patagonian Icefields with glacial/interglacial specific drainage pattern. The Rio Baker presently drains both Lago Buenos Aires (LBA) and Lago Pueyrredón (LP). b) The over-deepened (white=high elevation) LBA and LP outlet valleys with comparison of the broad glacial stratigraphy and mapping of Caldenius (1932). The chronology at LBA is based on cosmogenic exposure ages (^{3}He, ^{10}Be, ^{26}Al) by Kaplan et al. (2004, 2005) and Douglass et al. (2006) and limiting ^{40}Ar/^{39}Ar ages by Singer et al. (2004). The naming convention used for glacial units in the LP valley is based on Caldenius (1932).

relatively low rates of 1 mm ka^{-1} (Gillespie and Bierman, 1995). Moraine degradation leads to erroneously young boulder exposure ages (Hallet and Putkonen, 1994; Phillips et al., 1990; Putkonen and Swanson, 2003; Zreda et al., 1994) and therefore the oldest boulder can be used to date the deposit (cf. Zreda and Phillips, 1995). However, the rate of degradation is site-specific and is rarely quantifiable. Without additional constraints, the amount of moraine degradation and its effect on boulder exposure ages remains difficult to assess and is not routinely considered.

Recent model findings suggest degradation may be ubiquitous and high (Putkonen et al., 2008; Putkonen and O'Neal, 2006); thus even the oldest boulder ages may not date closely moraine deposition. The increasing uncertainty on exhumation and erosion rates with increasing moraine ages often limits the results to minimum limiting ages.

4.1.3 Exposure ages of outwash terraces

Glacial outwash terraces can often be directly linked to moraines that mark former ice limits. They are frequently better preserved than moraines owing to their low-gradient surfaces which are less prone to degradation. The surfaces may contain fluvial rounded cobbles and original surface channel morphology that, providing the terrace has not been reactivated post-depositionally, indicate minimal clast erosion or exhumation since deposition. This suggests outwash terraces may be feasible for exposure age dating. However, small clasts on flat surfaces are more prone to burial (e.g., seasonal snow cover, soil, loess) and mixing (e.g., cryo- or bio-turbation, up-freezing, overturning) than large moraine boulders, which together with potential inflation or deflation of the terrace surface, can complicate the exposure history (Gosse and Phillips, 2001).

Fluvial terraces associated with glacial events have been dated in previous studies (e.g., Brocard et al., 2003; Chadwick et al., 1997; Hancock et al., 1999; Phillips et al., 1997; Repka et al., 1997; Schildgen et al., 2002). Surface clasts may contain inherited nuclides obtained prior to mobilization and during clast transport to the site of final deposition. Methods have been developed to quantify the average nuclide

inheritance in a fluvial deposit (e.g., Anderson et al., 1996; Hancock et al., 1999; Repka et al., 1997), but nuclide inheritance in individual clasts can vary significantly around this mean (e.g., Hancock et al., 1999). Zentmire et al. (1999) measured ^{10}Be concentrations in cobbles of modern day glacial outwash. These samples contained negligible inherited nuclides which they attribute to both sub-glacial erosion and shielding by the overriding glacier prior to deposition (Gosse and Phillips, 2001). If both nuclide inheritance and clast mixing can be shown to be negligible, and ^{26}Al/^{10}Be ratios indicate no prolonged burial, then individual surface clasts from outwash terraces could be suitable targets for dating old glacial events in regions where boulder exhumation and erosion is an issue. With this in mind, we targeted a well-preserved moraine and outwash sequence in Patagonia.

4.2 The Lago Pueyrredón valley, 47.5º S, Argentina

The Lago Pueyrredón valley (Fig. 4.1) was a major outlet of former Patagonian ice sheets and the glacial record is exceptionally well-preserved (Fig. 4.2). It is located in close proximity to the dated long-term glacial record at Lago Buenos Aires (LBA).

4.2.1 Geology

The Lago Pueyrredón valley is a west – east trending glacial depression separating the Meseta del Lago Buenos Aires to the north and the Mesetas Belgrano and Olnie to the south (Fig. 4.2). The nearest granitic rocks are within the San Lorenzo Plutonic Complex, about 80 km from the innermost moraines (Suárez and De La Cruz, 2001). The nearest sources for quartz cobbles are veins in the Eastern Andes

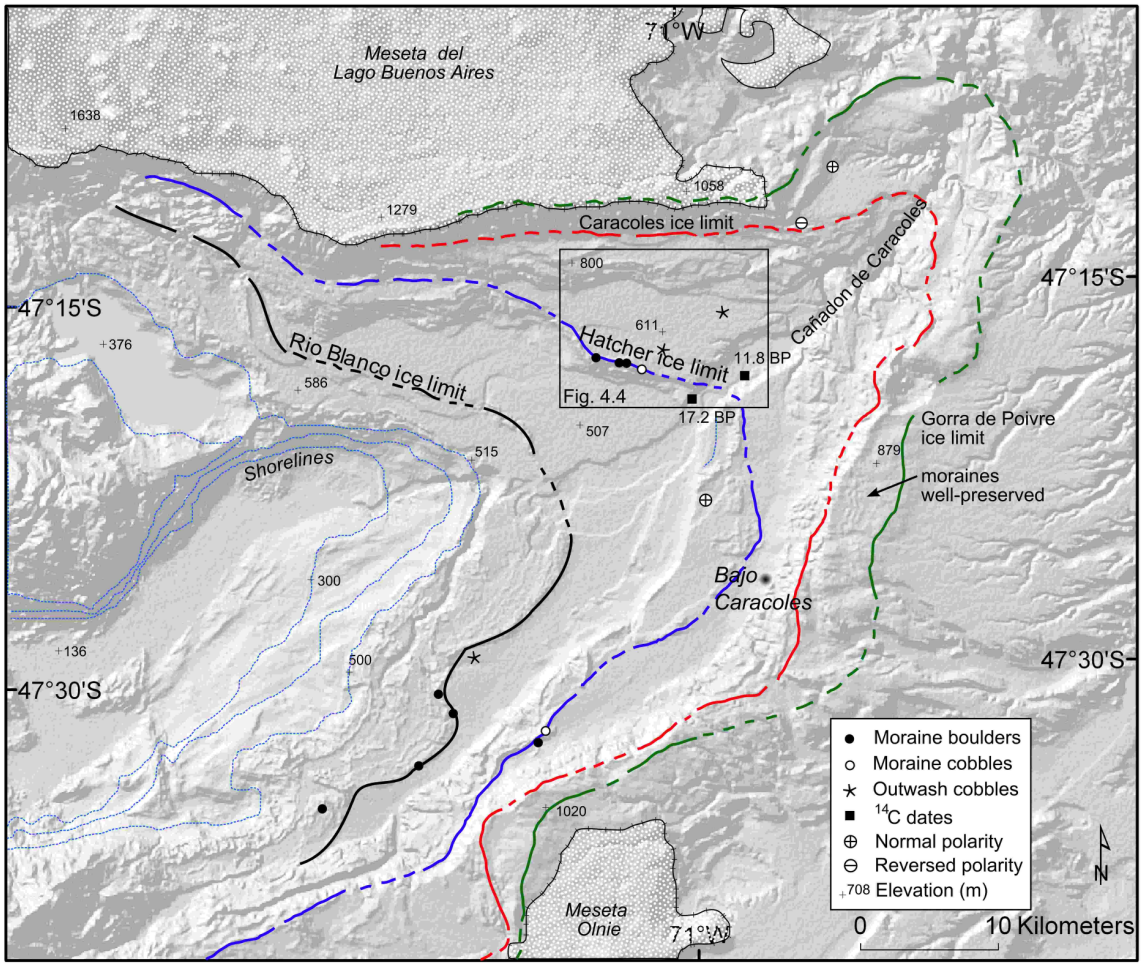

Figure 4.2. Ice limits and sample locations

DEM (SRTM 90m, artificially illuminated) of the Lago Pueyrredón valley showing ice limits of the four major glacial units and the exceptional preservation of moraine and outwash terraces. The well-preserved moraines of the Gorra de Poivre ice limit are inferred to be 1.1 Ma. The sampled locations for each sample type in this study are shown along with 14C ages by Wenzens (2005) and Mercer (1982) and magnetic polarity measurements by Sylwan et al. (1991)(see Section 4.2.3).

Metamorphic Complex located 65 km west of the innermost moraines; thus clast transport distances of the sampled lithologies are large.

Based on the pioneering work of Caldenius (1932), four major glacial units are distinguished over a range of 40 km with the outermost deposits situated more than 350 meters higher than the innermost (Fig. 4.2). Each unit is separated by

escarpments of up to 100 meters. This over-deepened valley shares a peculiarity in drainage common throughout Patagonia; lakes and rivers on the eastern mountain front drain to the Pacific Ocean, except during glacial times when the continuous N – S oriented ice sheet forced drainage eastward to the Atlantic Ocean (Fig. 4.1a). This unique hydrologic condition is partly responsible for the exceptional preservation of the deposits. Pre-LGM outwash terraces are also well-preserved because the trend in ice extent has in general decreased over time (Kaplan et al., 2009). During glacial maxima, melt-water discharged directly onto broad outwash plains until ice began to retreat and pro-glacial lakes formed, dammed by terminal moraines. This caused rivers to incise in response to the decreased sediment load (cf. Chorley et al., 1984), thereby abandoning outwash terraces. Pro-glacial lakes are evident by the preserved shorelines below the Hatcher and Río Blanco moraines (Fig. 4.2), these eventually drained westward when the Río Baker depression became ice free (Figure 1a; Mercer, 1976). We infer that outwash terraces stabilized shortly after glacial maximum conditions.

4.2.2 Climate

The current climate in the study area is semi-arid with precipitation levels of 200 mm a^{-1} and strong and persistent winds[3]. Annual snow cover is thin and short-lived (Local land owners, personal communication) and models predict increased aridity during glacial times (Hulton et al., 2002). Also, strong winds quickly removed ash deposited by the 1991 eruption of Volcán Hudson in Chile (Inbar et al., 1995) and an increase in the vigor of atmospheric circulation during glacial times (Petit et al.,

[3] NCEP/NCAR reanalysis; www.cdc.noaa.gov/ncep_reanalysis/

1999) would likely lead to higher wind velocities. Wind has observably been a dominant agent of erosion with boulders commonly exhibiting ventifacts and flutings (Fig. 4.3a). Cobbles and pebbles on the Hatcher outwash terrace often exhibit rock varnish on ventifacts (Fig. 4.3b) suggesting aeolian erosion was not recent. We propose that aeolian erosion was episodic in nature, occurring during glacial maxima when outwash plains were active, devoid of vegetation and debris was available for entrainment by wind (cf. Sugden et al., 2009). Therefore, we assume that post-depositional shielding by annual snow cover, loess or other deposits is limited today and during glacial times, even on flat outwash terraces.

4.2.3 Existing glacial chronology

The glacial chronology at Lago Pueyrredón previously was poorly developed. There was no direct chronology for the deposits at Lago Pueyrredón. The only ages come from three sources: First, Sylwan et al. (1991) measured magnetic polarity in glacial sediments and found that part of the outermost mapped Caracoles unit was deposited during the reversed Matuyama chron at more than 780 ka (Singer and Pringle, 1996); second, Mercer (1976; 1982) dated peat in the former melt-water drainage near the entrance to the Cañadón de Caracoles at ~11.8 ^{14}C ka (Fig. 4.2), providing a minimum age for the Río Blanco moraines (Wenzens, 2005); third, Wenzens (2005) dated a mollusk shell from a lake deposit at the foot of the Cañadón de Caracoles escarpment, inside the limit of the Hatcher moraines. The age of ~17.2 ^{14}C ka led Wenzens (2005) to conclude that the Hatcher moraines were deposited during the LGM as proposed by Caldenius (1932), and the Río Blanco moraines must therefore be late glacial in age. However, the lack of a firm chronology makes correlation to

deposits in nearby valleys tentative and subject to debate (Kaplan et al., 2006; Wenzens, 2006a). Additional age limits were estimated (initially, before results were obtained) based on correlation of Caldenius' (1932) mapping with deposits dated at LBA (Fig. 4.1b). Four major moraine groups are identified in both valleys. At LBA, cosmogenic age dating of the Fenix and Moreno I-II moraines indicated they are LGM (~16-23 ka; Douglass et al., 2006; Kaplan et al., 2004), and MIS 6 in age (~140-150 ka; Kaplan et al., 2005). Steadily older glacial events are represented through the mid Quaternary (~1.1 Ma) based on limiting $^{40}Ar/^{39}Ar$ ages (Singer et al., 2004).

4.3 Approach and methodology

To assess whether old glacial deposits can be dated more reliably using outwash terrace cobbles as opposed to moraine boulders, we compare ^{10}Be and ^{26}Al exposure ages obtained from both sample types on the Hatcher unit, assumed to be pre-LGM in age (Fig. 4.1b). In addition, we sampled the outermost moraine and associated outwash terrace of the younger (est. LGM) Río Blanco unit as a 'geologic blank' allowing a test of the following fundamental assumptions: (1) terraces stabilized shortly after moraine deposition; (2) nuclide inheritance is low; (3) post-depositional shielding is minimal; and (4) terrace sediment are not mixed post-depositionally. If valid, exposure ages from all samples of the younger Río Blanco unit should be indistinguishable and date the timing of the event.

For the Hatcher moraines, degradation and erosion is expected to complicate interpretation of boulder exposure ages. To address the relative magnitude of these processes, we sampled moraine cobbles. Because negligible rock surface erosion can be inferred from the preservation of smooth, rounded cobble surfaces, lower nuclide concentrations in cobbles relative to boulders will likely be the result of shielding by the moraine matrix, provided that $^{26}Al/^{10}Be$ ratios are not consistent with prolonged burial. Thus moraine cobble nuclide concentrations can help to estimate the amount of degradation. On the Hatcher outwash terrace we additionally sampled a ^{10}Be concentration depth-profile to exploit the depth dependency of cosmogenic nuclide production. These data provide further constraints on the average nuclide inheritance, deposition age and exposure history of the outwash sediment while allowing checks on sediment mixing that could affect exposure ages obtained from individual surface clasts.

4.3.1 Sampling

4.3.1.1 Sampling criteria and methods

Moraine boulders were sampled with hammer and chisel following established protocols (e.g., Gosse and Phillips, 2001). We preferentially sampled the top few centimeters of large (> 1 meter) stable boulders (granite) on or near moraine crests showing minimal evidence of surface erosion (Fig. 4.3c). Moraine and outwash cobbles of quartz (5 – 25 cm long axis) were sampled to obtain a sufficient quartz yield and because monomineralic quartz clasts are resistant to weathering. These were collected whole from well-preserved moraine crests (Fig. 4.3c) and from terrace surfaces away from moraines and scarps. The samples were later crushed whole

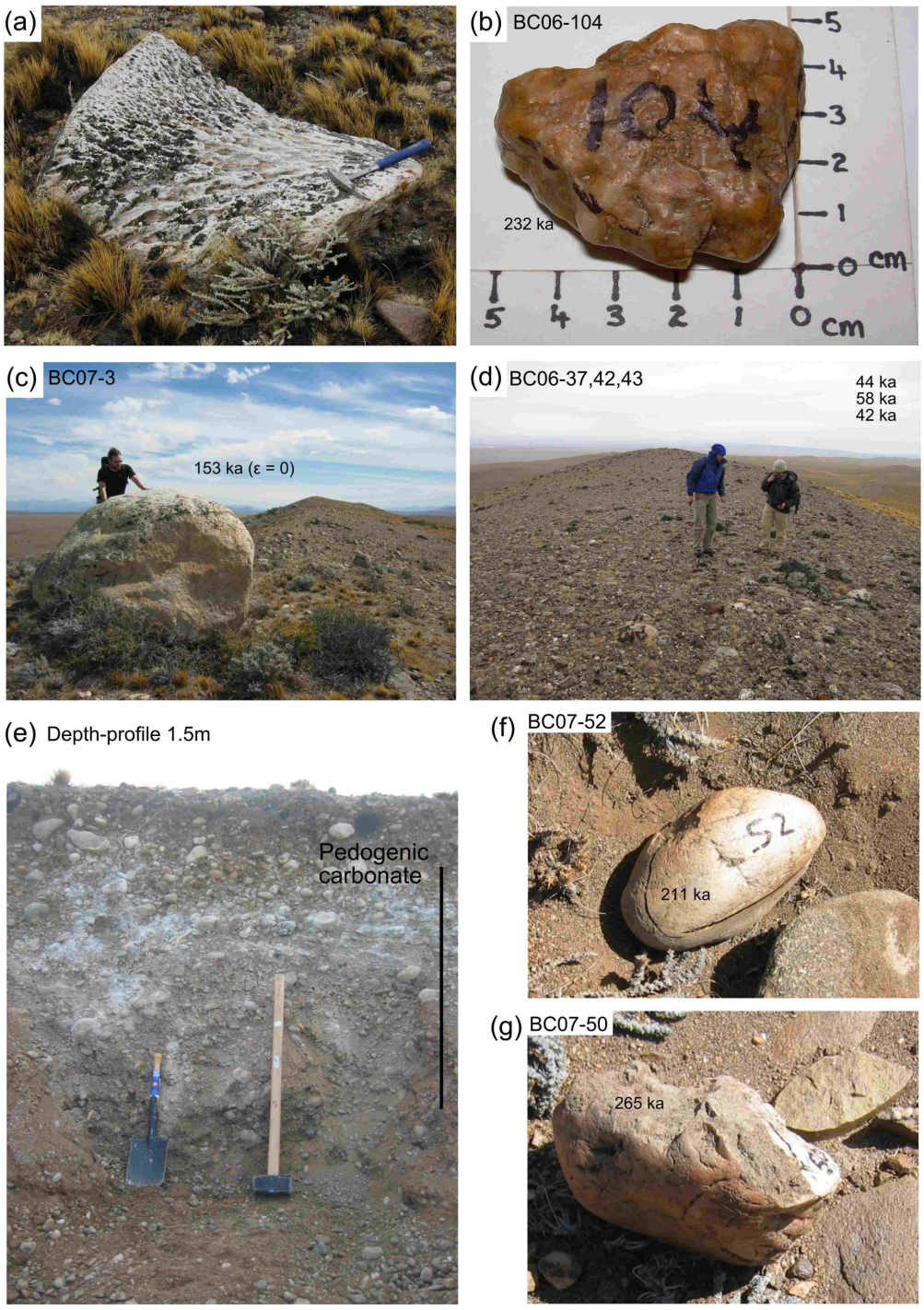

Figure 4.3. Photos of samples and sample sites

a) Boulder with flutings demonstrating the erosive power of debris laden wind. b) Quartz pebble from the Hatcher outwash terrace (S1) showing rock varnish on ventifacts which suggests aeolian erosion is episodic. c) The tallest (2m) and oldest boulder sampled from the sharp-crested Hatcher moraine on the north side of valley. d) Desert pavement on the Hatcher moraine crest on the south side of the valley. e) Photo of the depth-profile with pedogenic carbonate formed below ~30cm depth. The top of the profile was undisturbed and vegetated. The top 10 cm of the profile contains less than ~30% fine material.

(small cobbles/pebbles) or after cutting to an appropriate thickness, and subsequently sieved to obtain the 250 – 710 μm fraction.

The depth profile was sampled in a small quarry along Route 40 (Fig. 4.4) at a location where the surrounding surface appeared undisturbed by the excavation. The deposit is composed of cobbles to coarse sands throughout (Fig. 4.3e). Soils are poorly developed in the top 10 – 15 cm (< 30% fines at top of profile) and about 40% of the deposit is cemented by pedogenic carbonate at ~30 – 100 cm depth. The bulk density was estimated based on grain size distribution at 2.57 g cm^{-3} with an assumed error of ± 0.10 g cm^{-3} (cf. Hancock et al., 1999). This is based on the observation that 75% of the deposit contains grain sizes larger than coarse sands with a clast density of 2.7 g cm^{-3} (30% porosity), an interstitial sand density of 2.7 g cm^{-3} (30% porosity) and a pedogenic carbonate density of 2.4 g cm^{-3} occupying 40% of the remaining interstitial space. Eight samples were collected at depths ranging from 10 – 150 cm. Each sample was composed of ten to fifty quartz pebbles (2 – 4 cm) that were amalgamated following Repka et al. (1997). We use the thickness of the largest clast in each sample as measure of the uncertainty of depth (Table 4.1).

4.3.1.2 Sample location

Sample locations are shown in Figs. 4.2 and 4.4. We sampled the outermost moraine crest and, where possible, from outwash terraces that can be directly mapped to the corresponding dated moraine. Both moraine crests are generally sparsely vegetated with desert pavements (gravels – cobbles) formed at some locations (Fig. 4.3d). Most moraine boulders are ventifacted while rounded moraine cobbles are more

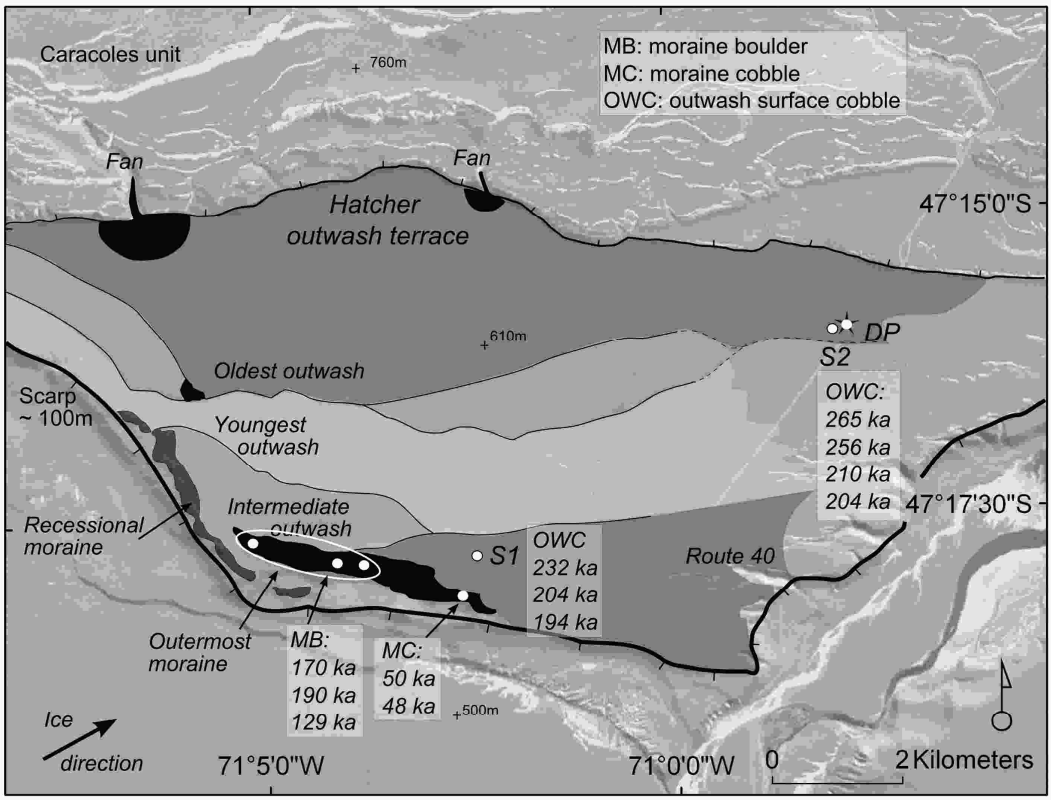

Figure 4.4. Geomorphology of the Hatcher sequence and sample sites

Geomorphic map of the Hatcher moraines and outwash terraces on the north side of valley (location shown in Fig. 4.2), showing sample locations and exposure ages. The moraine boulder ages include a correction for erosion of 1.4 mm ka^{-1}. Three small (1 – 3m difference in elevation) terrace levels related to recessional moraine limits are clearly distinguished close to their associated moraines, but grade to a common base level further east. Outwash was sampled at two sites (S1 and S2). S1 can be directly mapped to the dated moraine while S2 is located 8 km NE at a point where the small terrace levels coalesce; the exposure ages obtained from samples from S1 and S2 are indistinguishable. The location of outwash fans composed of older "Caracoles" material is shown. DP: depth-profile location.

often not; neither typically show rock varnish. The Río Blanco moraines were sampled on the south side of the valley where they are best preserved. The moraines are hummocky but largely continuous with ~20 – 25 meters of relief and slopes of ~20º. The Hatcher moraines are situated 100 m above the Río Blanco outwash and were sampled in more lateral positions on both sides of the valley (over 30 km apart). Moraine relief ranges from 20 – 30 m above the associated outwash terrace to the

east (~18º slopes) and from 40 – 50 m above an inter-moraine depression to the west (19º – 25º slopes).

The Río Blanco and Hatcher outwash terraces occupy ~240 km^2 and 325 km^2 in area, respectively. The surfaces dip gently eastward at < 0.5º and converge at the entrance to, and above the Cañadón de Caracoles (Fig. 4.2). Both terraces are composed of gravels and coarse sands with local concentrations of cobbles and pebbles. These small lag deposits are not underlain by fine sediments (i.e., they are not inflationary desert pavements). Vegetation cover is sparse. Shallow surface channels (1 – 3 m) are well-preserved with clear braiding patterns visible; these often grade to recessional moraine positions. Río Blanco outwash was sampled at a location where it could be directly traced to the dated moraine. The Hatcher outwash was sampled at two locations on the northern terrace (Fig. 4.4). Here, three minor (1 – 3m) terrace levels grade to a common base level and can be traced to Hatcher recessional ice limits further west. The first sample site (S1) can be directly mapped to the dated moraine. The second site (S2), which is also the location of the depth-profile, occupies a similar stratigraphic position but is located ~8 km from the dated moraine.

4.3.2 Depth-profile exposure model optimization

The depth-profile allows defining the age and erosion rate of the terrace surface and testing of several underlying assumptions. In-situ ^{10}Be production in the upper few meters of the Earth's surface is dominated by high-energy neutron spallation reactions that decrease exponentially with attenuation of the secondary cosmic ray flux at depth. Assuming the Hatcher terrace material was deposited in a single event

and remained stable with a single continuous erosion rate, we would expect to observe a smooth exponential decrease of nuclide concentration within the profile that can be described by an appropriately parameterized model. The expected ^{10}Be concentration at depth (z) can be modeled for any given terrace age (t), erosion rate (ε_{terr}), overburden density (ρ) and inherited nuclide concentration (N_{inh}) using the following analytical approximation for production at depth in a steadily eroding deposit (after Granger and Smith, 2000):

$$\begin{aligned} N &= N_{inh}e^{-t\lambda} \\ &+ \left[P_n e^{-\rho z/\Lambda} / \left(\lambda + \rho\varepsilon_{terr}/\Lambda\right)\right]\left[1 - e^{-t\left(\lambda+\rho\varepsilon_{terr}/\Lambda\right)}\right] \\ &+ \left[P_{\mu 1} e^{-\rho z/L_1} / \left(\lambda + \rho\varepsilon_{terr}/L_1\right)\right]\left[1 - e^{-t\left(\lambda+\rho\varepsilon_{terr}/L_1\right)}\right] \\ &+ \left[P_{\mu 2} e^{-\rho z/L_2} / \left(\lambda + \rho\varepsilon_{terr}/L_2\right)\right]\left[1 - e^{-t\left(\lambda+\rho\varepsilon_{terr}/L_2\right)}\right] \\ &+ \left[P_{\mu^{fast}} e^{-\rho z/L_3} / \left(\lambda + \rho\varepsilon_{terr}/L_3\right)\right]\left[1 - e^{-t\left(\lambda+\rho\varepsilon_{terr}/L_3\right)}\right] \end{aligned} \quad (1)$$

where N is the ^{10}Be concentration, N_{inh} is the inherited ^{10}Be concentration, λ is the ^{10}Be radioactive decay constant ($5.1\text{x}10^{-7}$ a^{-1})(Nishiizumi et al., 2007), P_n, $P_{\mu 1}$, $P_{\mu 2}$ and P_{μ}^{fast} are production rates due to neutron spallation, negative muon capture ($_{\mu 1}$, $_{\mu 2}$) and fast muon reactions, while Λ (160 g cm^{-2}), L_1 (738.6 g cm^{-2}), L_2 (2688 g cm^{-2}) and L_3 (4360 g cm^{-2}) are the respective attenuations lengths provided by Granger and Smith (2000). Production rates for each reaction were calculated as a fraction of the total surface production rate with f_n = 0.9724, $f_{\mu 1}$ = 0.0186, $f_{\mu 2}$ = 0.004 and f_{μ}^{fast} = 0.005 integrated over the sample thickness (*Pn* only; cf. Vermeesch, 2007). The time-averaged surface production rate value is 8.22 atoms ^{10}Be g^{-1} a^{-1} (Dunai, 2001)(see Appendix C.1).

Assuming the terrace deposit experienced a simple exposure history at a constant erosion rate, there should be only one combination of exposure age, terrace erosion rate, overburden density and nuclide inheritance that best fits all the measured data points in the profile. A forward model can be used to obtain the parameters that minimize the difference between the predicted and observed nuclide concentrations. In this study, we use the sum of chi-squared ($\Sigma\chi^2$) for the exposure model optimization. Because the bulk density was estimated in the field (Section 4.3.1.1), we solve for the exposure duration (t), erosion rate (ε_{terr}) and nuclide inheritance (N_{inh}) that best fit the measured profile data and their associated analytical uncertainties (σ_i), such that:

$$\Sigma\chi^2 \equiv \sum_{i=1}^{N}\left(\frac{y_i - y\left(t, \varepsilon_{terr}, N_{inh}\right)}{\sigma_i}\right)^2 \qquad (2)$$

where y_i is the measured ^{10}Be concentration at a particular sample depth and $y(t,\varepsilon_{terr},N_{inh})$ is the modeled ^{10}Be concentration at that depth for any given $(t,\varepsilon_{terr},N_{inh})$ solution. The analytical uncertainties (σ_i) include both sample and blank ^{10}Be/^{9}Be uncertainties and a 2% carrier addition/sample mass uncertainty. For a quantitative assessment of the model's ability to describe the measured data, we assess the 'goodness of fit' to the data using the reduced chi-squared (χ_r^2) value. The χ_r^2 is the sum of chi-squared divided by the degrees of freedom, and this value should approach 1 if the fitting function describes the data well (cf. Bevington and Robinson, 2003, p. 194). The exposure model therefore allows a best estimate of the

terrace age, erosion rate and average nuclide inheritance by the sum of chi-squared, and allows us to quantify (χ_r^2) how well the data fit the underlying model.

4.3.3 Exposure age calculations

The ^{10}Be and ^{26}Al exposure ages were calculated with the CRONUS-Earth exposure age calculator (version 2.2 ;Balco et al., 2008)[4] which implements the revised ^{10}Be standardization and half-life (1.36 Ma) of Nishiizumi et al. (2007). Exposure ages are reported based on the Dunai (2001) scaling model; these differ by up to ~5% depending on the choice of alternative scaling model. The calculator uses sample thickness (Table 4.2) and density (assumed 2.7 g cm^{-3}) to standardize nuclide concentrations to the rock surface. Topographic shielding was measured but is negligible (scaling factor < 0.9998). We apply no correction for snow or vegetation shielding. No erosion rate correction is applied to the cobble data, but an erosion rate of 1.4 mm ka^{-1} is used to document this effect on boulder exposure ages; this value was derived by Kaplan et al. (2005) for boulders on the Telken moraines at LBA, 60km to the north. Sample elevations were converted to air pressures for input into the calculator; we assumed a standard atmosphere for the elevation-pressure relationship. The local sea-level (SL) pressure and temperature (1009.3 hPa/285K)[5] was used to convert elevations to air pressures for samples of the younger Río Blanco unit. We used a lower SL pressure for the conversion of the older Hatcher samples as described below.

[4] (http://hess.ess.washington.edu/math/index_dev.html)
[5] NCEP-NCAR reanalysis; www.cdc.noaa.gov/ncep_reanalysis/

The time-averaged ^{10}Be and ^{26}Al production rates near Lago Pueyrredón have been estimated to be 5% and 11% higher than for standard atmospheric conditions by two independent studies that infer a low pressure anomaly during glacial times (cf. Ackert et al., 2003; Staiger et al., 2007). Following Staiger et al. (2007), we increase ^{10}Be and ^{26}Al production rates by ~5% for samples on the older Hatcher unit (for discussion see Appendix C.2). We note, however, that the conclusions of this paper are not sensitive to the choice of correction used. The 5% higher production rate was implemented within the exposure age calculator by artificially lowering the air pressure at the sampled locations, thereby increasing the production rates. Specifically, we lowered the SL pressure that was used in the conversion of sample elevations to sample air pressures; the present day SL pressure (1009.3 hPa) was lowered to 1002.3 hPa. The lower SL pressure reduces the calculated sample air pressures, and thereby increases the time-averaged production rate derived through the calculator by approximately 5% when compared against the value obtained from a calculation based on the present day SL pressure.

4.4 Results

The analytical results are presented in Tables 4.1 and 4.2 and Figs. 4.4 – 4.7. Samples were prepared at the University of Edinburgh's Cosmogenic Isotope Laboratory. Information on the chemical procedure is provided in chapter 2.5.1. The AMS measurements were conducted at the AMS-facility at SUERC. Measurements are normalized to the NIST SRM-4325 Be standard material with a revised (Nishiizumi et al., 2007) nominal ^{10}Be/^{9}Be ratio of 2.79 x 10^{-11}, and the

Purdue Z92-0222 Al standard material with a nominal $^{26}Al/^{27}Al$ ratio of 4.11 x 10^{-11} which agrees with the Al standard material of Nishiizumi (2004). The $^{26}Al/^{10}Be$ production rate ratio is 6.75. Samples are corrected for the number of ^{10}Be and ^{26}Al atoms in their associated blanks. Blanks (n = 8) were spiked with 250 μg ^{9}Be carrier and 1.5 mg ^{27}Al carrier. Samples were spiked with 250 μg ^{9}Be carrier and up to 1.5 mg ^{27}Al carrier (the latter value varied depending on the native Al-content of the sample). For each batch of 7 samples one blank was processed. The corresponding combined process and carrier blanks range between 115,000 ± 18,000 atoms ^{10}Be and 290,000 ± 40,000 atoms ^{10}Be (< 3% of total ^{10}Be atoms in sample; 0.9 – 1.7 x 10^{-14} [$^{10}Be/^{9}Be$]); and between 61,000 ± 12,000 atoms ^{26}Al and 190,000 ± 57,000 atoms ^{26}Al (< 1% of total ^{26}Al atoms in sample; 2.6 – 3.8 x 10^{-15} [$^{26}Al/^{27}Al$]). Sample and blank $^{10}Be/^{9}Be$ and $^{26}Al/^{27}Al$ analytical uncertainties and a 2% carrier addition uncertainty and 5% stable ^{27}Al measurement (ICP-OES) uncertainty are propagated into the 1σ analytical uncertainty for nuclide concentrations (Tables 4.1 and 4.2). Throughout the text, if not stated otherwise, uncertainties are reported as 1σ. Analytical uncertainties are reported. For means, the uncertainty is based on an average of the upper and lower age limits. The upper limit is the exposure age plus one sigma, and the lower limit is the exposure age minus one sigma.

Table 4.1. Hatcher depth-profile data

Sample ID – AMS ID	Latitude (dd)	Longitude (dd)	Altitude (m asl)	Depth (cm)	# clasts	Thick[a] (cm)	Quartz mass (g)	^{10}Be measured[b] (10^6 atom g^{-1}) (±1σ)
depth-profile (S2)								
BC07-48a – b2068	-47.26627	-70.96320	583	10	41	3	21.65	1.508 ± 0.047
BC07-48b – b2067				20	14	3.5	27.42	1.242 ± 0.039
BC07-48c – b2066				30	10	3.5	39.06	1.153 ± 0.033
BC07-48d – b2063				40	18	4	46.18	0.948 ± 0.029
BC07-48e – b2062				50	37	4	58.19	0.802 ± 0.023
BC07-48f – b2061				75	19	4	63.82	0.563 ± 0.018
BC07-48g – b2048				100	49	3.5	59.44	0.381 ± 0.010
BC07-48h – b2060				150	44	3	61.54	0.184 ± 0.006

a. Thickness of largest clast included in profile; this is used as a measure of depth uncertainty in the profile. b. Nuclide concentrations are normalized to revised ^{10}Be standards and half-life (1.36 Ma) of Nishiizumi et al. (2007) and include propagated AMS sample/lab-blank uncertainty and 2% carrier mass uncertainty. Clast density 2.7 g cm^{-3}. Topographic shielding at the profile site is negligible. All AMS measurements made at S.U.E.R.C.

Table 4.2. Data for the Río Blanco and Hatcher glacial sequences

Sample I.D.		Latitude	Longitude	Altitude	Boulder height	Thick	Quartz mass	Isotope -	Nuclide concentration[a]	$^{26}Al/^{10}Be$[b]	Age 1[c,d] (10^3 yrs) ε = 0		Age 2[c,d,e] (10^3 yrs) ε = 1.4 mm ka^{-1}	
		(dd)	(dd)	(m asl)	(cm)	(cm)	(g)	AMS ID[a]	(10^6 atom g^{-1})		Age + 1σ (int)	± 1σ (ext)	Age + 1σ (int)	± 1σ (ext)
Río Blanco[d]														
moraine boulder														
BC07-7		-47.5186	-71.2361	564	225	2.5	20.9284	^{10}Be – b2050	0.200 ± 0.007	-	27.1 ± 0.9	3.3	28.0 ± 0.9	3.6
BC07-8		-47.5564	-71.2629	587	190	1.5	27.7948	^{10}Be – b2043	0.245 ± 0.008	-	32.2 ± 1.0	3.9	33.4 ± 1.0	4.3
BC07-12		-47.5840	-71.3548	665	310	1.5	24.1815	^{10}Be – b2036	0.207 ± 0.007	-	25.4 ± 0.8	3.1	26.2 ± 0.8	3.3
BC07-43		-47.5079	-71.2451	581	80	1.5	25.7394	^{10}Be – b2055	0.193 ± 0.006	-	25.5 ± 0.8	3.1	26.2 ± 0.9	3.3
outwash terrace														
BC06-32		-47.48563	-71.21694	564	-	3.5	24.1803	^{10}Be – b2074	0.178 ± 0.006	-	24.3 ± 0.8	3.0	-	-
BC06-34		-47.48602	-71.21705	563	-	4	30.9418	^{10}Be – b2075	0.185 ± 0.006	-	25.3 ± 0.7	3.1	-	-
BC06-35		-47.48587	-71.21661	564	-	4	24.7066	^{10}Be – b2078	0.180 ± 0.006	-	24.6 ± 0.8	3.0	-	-
Hatcher[d]														
moraine boulder														
BC07-1		-47.2946	-71.0865	680	95	2	19.6454	^{10}Be – b2049	1.188 ± 0.030	-	139.9 ± 3.6	17.4	170.1 ± 5.3	26.3
BC07-3		-47.2987	-71.0579	673	200	1.5	18.6180	^{10}Be – b1767	1.290 ± 0.037	7.24 ± 0.48	152.8 ± 4.4	19.2	189.6 ± 6.8	30.5
								^{26}Al – a641	*9.545 ± 0.554*		*155.2 ± 10.6*	*24.9*	*226.6 ± 18.3*	*44.4*
BC07-4		-47.2988	-71.0576	678	100	2	20.4468	^{10}Be – b2038	0.952 ± 0.030	6.46 ± 0.41	111.7 ± 3.5	14.0	129.4 ± 4.7	19.1
								^{26}Al – a647	*6.154 ± 0.333*		*109.0 ± 6.0*	*14.9*	*126.0 ± 8.1*	*20.3*
BC07-5		-47.5408	-71.1509	783	135	2	20.0563	^{10}Be – b2039	0.889 ± 0.028	6.52 ± 0.41	95.0 ± 2.9	11.8	107.2 ± 3.7	15.2
								^{26}Al – a649	*5.798 ± 0.319*		*93.3 ± 5.2*	*12.7*	*105.2 ± 6.6*	*16.3*
moraine cobble														
BC06-98		-47.30247	-71.04547	653	-	5	19.6917	^{10}Be – b2087	0.394 ± 0.013	-	47.7 ± 1.5	5.9	-	-
BC06-99		-47.30246	-71.04553	652	-	3	21.2545	^{10}Be – b2080	0.420 ± 0.012	-	50.1 ± 1.4	6.1	-	-
BC06-37		-47.53	-71.14309	762	-	3.5	15.0548	^{10}Be – b1206	0.412 ± 0.020	6.54 ± 0.49	44.0 ± 2.1	5.6	-	-
								^{26}Al – a487	*2.691 ± 0.157*		*42.8 ± 2.5*	*5.7*	-	-
BC06-42		-47.53	-71.14294	763	-	4	15.0285	^{10}Be – b1207	0.526 ± 0.022	5.88 ± 0.41	57.9 ± 2.3	7.3	-	-
								^{26}Al – a488	*3.091 ± 0.171*		*50.5 ± 2.8*	*6.7*	-	-
BC06-43		-47.53	-71.14309	762	-	4	15.5849	^{10}Be – b1208	0.383 ± 0.014	6.75 ± 0.45	41.7 ± 1.5	5.2	-	-
								^{26}Al – a489	*2.587 ± 0.143*		*41.9 ± 2.3*	*5.5*	-	-
Outwash terrace cobble														
S1	BC06-103	-47.2998	-71.0362	620	-	2.5	19.2727	^{10}Be – b2892	1.610 ± 0.043	-	203.7 ± 5.5	25.8	-	-
	BC06-104	-47.2998	-71.0362	622	-	2	25.1177	^{10}Be – b2893	1.832 ± 0.052	-	232.2 ± 6.7	29.8	-	-
	BC06-106	-47.2998	-71.0363	622	-	3	20.9424	^{10}Be – b2896	1.530 ± 0.039	-	193.6 ± 5.0	24.4	-	-
S2	BC07-50	-47.2661	-70.9641	582	-	4	17.4325	^{10}Be – b1772	1.970 ± 0.061	6.35 ± 0.41	265.1 ± 8.4	34.5	-	-
								^{26}Al – a642	*12.51 ± 0.710*		*263.1 ± 16*	*39.1*	-	-
	BC07-51	-47.2661	-70.9642	582	-	2	19.7668	^{10}Be – b2056	1.567 ± 0.043	6.62 ± 0.41	204.0 ± 5.6	26.0	-	-
								^{26}Al – a657	*10.37 ± 0.57*		*209.0 ± 12*	*30.1*	-	-
	BC07-52	-47.2661	-70.9642	582	-	3.5	11.185	^{10}Be – b2037	1.592 ± 0.046	-	210.3 ± 6.2	26.8	-	-
	BC07-53	-47.2661	-70.9642	583	-	2.5	20.107	^{10}Be – b2057	1.932 ± 0.050	6.65 ± 0.46	256.0 ± 6.8	32.9	-	-
								^{26}Al – a658	*12.84 ± 0.82*		*266.9 ± 19*	*40.8*	-	-

Table 4.2 footnotes: Samples processed at the University of Edinburgh's Cosmogenic Isotope Laboratory; see Chapter 2.5.1 for details. Shielding negligible for all samples (<0.9998); rock density 2.7 g cm^{-3}
a. AMS measurements made at S.U.E.R.C. normalized to NIST SRM-4325 Be standard material with revised (Nishiizumi et al., 2007) nominal $^{10}Be/^{9}Be$ ratio (2.79×10^{-11}) and half-life (1.36 Ma), and the Purdue Z92-0222 Al standard material with nominal $^{26}Al/^{27}Al$ ratio of 4.11×10^{-11} that agrees with Al standard material of Nishiizumi et al. (2004). Nuclide concentrations include propagated AMS sample/lab-blank uncertainty, 2% carrier mass uncertainty (Be) and 5% stable ^{27}Al measurement (ICP-OES) uncertainty.
b. Surface production ratio begins at 6.75.
c. Exposure ages calculated using the CRONUS-Earth web based calculator version 2.2 (Balco et al., 2008) and Dunai (2001) scaling factors.
d. Production rate increased by 5% for Hatcher data only by reducing sample air pressure (SL pressure reduced to 1002.3 hPa).
e. Erosion rate from Kaplan et al.(2005) at LBA. (int) = internal (analytical) uncertainties; (ext) = propagated external uncertainties (Balco et al., 2008).

4.4.1 Río Blanco unit

The ^{10}Be boulder exposure ages from the outermost moraine crest range from 25.4 – 32.2 ka (no erosion). The oldest boulder (BC07-8) falls outside 2σ analytical uncertainty of the remaining population. Excluding this sample, the range is from 25 – 27 ka and the three ages overlap within error. The arithmetic mean age is 26.0 ± 0.9 ka, or 26.8 ± 0.9 including a correction for erosion (sect. 3.3). The three outwash cobbles yield ^{10}Be exposure ages of 24.3 ± 0.8 ka, 24.6 ± 0.8 ka and 25.3 ± 0.7 ka and thus are indistinguishable within uncertainties. The mean outwash cobble age (24.7 ± 0.8 ka) is indistinguishable from the boulder mean at 2σ. The low sample variability (std deviation = 0.5 ka) of outwash cobbles and indistinguishable ages from moraine boulders confirms our initial assumptions (1-4; see Section 4.3.0).

4.4.2 Hatcher unit

4.4.2.1 Moraine samples

The four moraine boulder samples yield a wide range of ^{10}Be exposure ages from 107.4 – 190 ka with a mean of 149.1 ± 5.1 ka (w/erosion; Fig. 4.5). The standard deviation of the individual exposure ages is high (± 37.6 ka), and highlights the significant variability often observed in 'old' moraine boulder ages. The age range

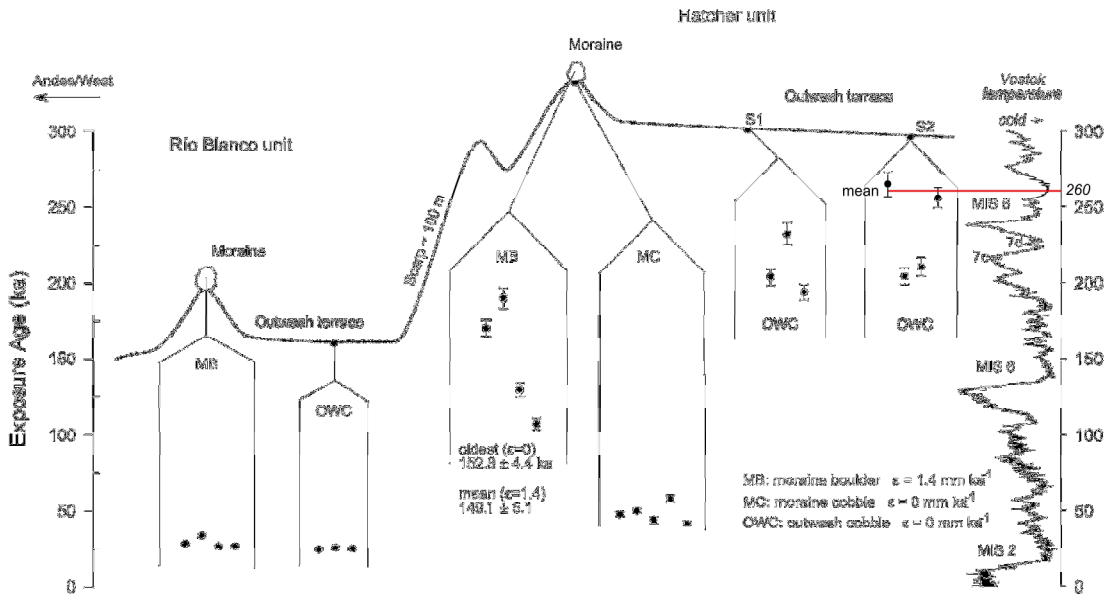

Figure 4.5. Illustration of ^{10}Be exposure age results

^{10}Be exposure ages obtained from samples of the Río Blanco and Hatcher units at Lago Pueyrredón, 47.5º S, Argentina, compared to the Vostok temperature curve (Petit et al., 1999). Data is ordered by sample type. Cartoon depicts moraine and outwash positions but is not to scale. S1 and S2 refer to sample sites on Hatcher outwash terrace (Fig. 4.4). Exposure ages obtained using the CRONUS-Earth exposure age calculator (http://hess.ess.washington.edu/math/index.html) version 2.2 (Balco et al., 2008) with a 5% higher production rate for Hatcher samples (Section 4.3.3) and Dunai (2001) scaling factors. Uncertainties are 1σ analytical. Boulder erosion rates from Kaplan et al. (2005). The Río Blanco data show little variability compared to the Hatcher data. The mean of the two oldest outwash terrace cobbles (red-line) is the interpreted age of the glacial advance, moraine boulders under-estimate this age by ~ 100 ka. See Table 4.2 for full sample details.

normalized to the oldest boulder (0.38) is typical for moraines (Putkonen and Swanson, 2003). The oldest boulder age (BC07-3) assuming no erosion is 152.8 ± 4.4 ka and corresponds to the tallest boulder sampled on the Hatcher moraines (2m; Fig. 4.3c). The ^{26}Al/^{10}Be ratios are consistent with relatively simple exposure histories without prolonged burial.

The moraine cobble ^{10}Be exposure ages range from 41.7 – 57.9 ka (Table 4.2, Fig. 4.5). The young ages are not thought to be caused by post-depositional burial and re-

exposure based on our assessment of the geomorphic environment (Section 4.2.2). In addition, the $^{26}Al/^{10}Be$ ratios are also consistent with a simple exposure history without prolonged burial. Based on this, we infer that low nuclide concentrations (i.e., young exposure ages) are the result of moraine degradation, which appears to be similar at both sample localities > 30 km apart.

4.4.2.2 ^{10}Be concentration depth-profile

The depth-profile data is presented in Table 4.1 and Figs. 4.6 and 4.7. Fig. 4.7 shows that the ^{10}Be concentration decreases exponentially with depth; consistent with post-deposition production in a stable terrace and no mixing of sediment. We modeled the expected ^{10}Be concentration at depth (see Section 4.3.2) for a range of exposure times (t = 0 – 500 ka; 200 a resolution), terrace erosion rates (ε = 0 – 3 mm ka^{-1}; 0.01 mm ka^{-1} resolution) and inherited ^{10}Be concentrations (0 – 180,000 atoms g^{-1}; 30000 atoms g^{-1} resolution) to obtain the parameters that yielded the minimum value for the sum of chi-squared ($\Sigma\chi^2_{min}$). The terrace erosion rate was restricted to positive values in this exercise because pedologic evidence (Section 4.3.1.1) and geomorphic observations indicate deflation (as opposed to inflation) of the terrace surface (Section 4.3.1.2). The best fit ($\Sigma\chi^2_{min}$) occurs with 233.8 ka exposure, a terrace erosion rate of 0 mm ka^{-1} and no inherited nuclides (Fig. 4.6). Fig. 4.6a is the $\log_{10}\Sigma\chi^2$ solution surface for the case of no inheritance. The 1σ and 2σ analytical uncertainty contours illustrate the strong correlation between the uncertainties in exposure age and erosion rate. The contours include a wide range of potential exposure age/erosion rate solutions.

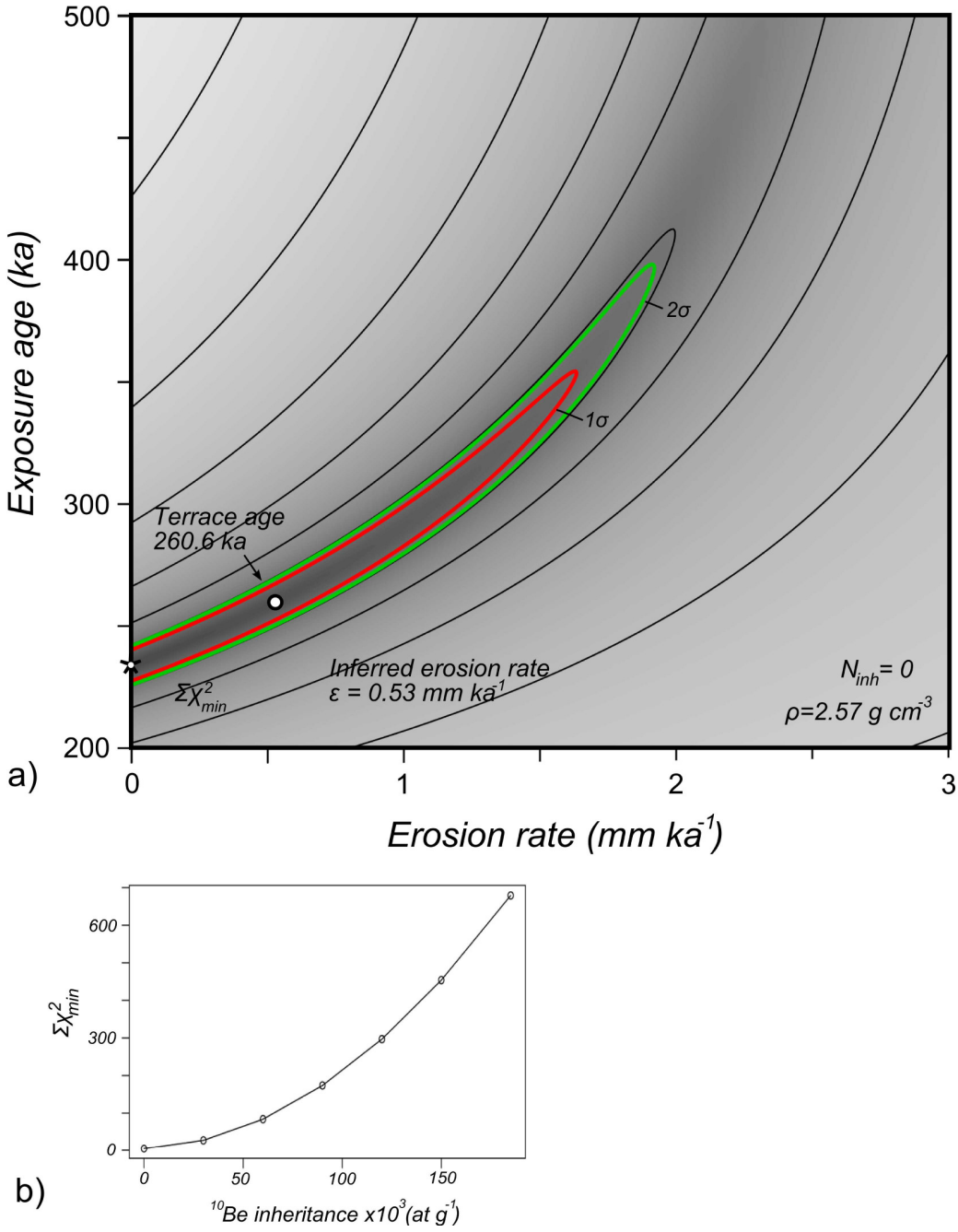

Figure 4.6. Plot of $\Sigma\chi^2$ solution surface

a) Plot of the gridded $\log_{10}(\Sigma\chi^2)$ values for a range of exposure ages and erosion rates for the case of no inherited nuclides; the plot is based on the depth-profile data and exposure model optimization. The sensitivity to inheritance is illustrated in Fig. 4.6b. The best-fit (star) occurs with an exposure age of 233.8 ka, an erosion rate of 0 mm ka^{-1} and no inherited nuclides. Contours are increments of 0.5 from the $\log_{10}(\Sigma\chi^2)$ minimum. The uncertainty contours mark the probability of occurrence (0.68/1σ, 0.95/2σ) for 5 degrees of freedom.

The model fits analytical sources of uncertainty as discussed in the text. The uncertainties of exposure age and erosion rate are strongly correlated. The inferred terrace age, based on the mean exposure age of the oldest surface cobbles (these were not included in the profile optimization), corresponds to a terrace erosion rate of ~0.53 mm ka^{-1}. b) Plot showing the effect of varying the exposure age, erosion rate and ^{10}Be inheritance on the $\Sigma\chi^2$ minimum value for a range of inheritance values. The maximum inheritance value was obtained from the nuclide concentration of the deepest sample in the profile (Table 4.1). The $\Sigma\chi^2$min steadily increases as the total inheritance increases; thus the best fit occurs with no inherited nuclides.

The reduced chi-squared χ_r^2 value of 0.97 indicates the model fit is as good as can be expected given the measurement uncertainties. Fig. 4.7a provides the predicted concentrations, based on the parameters obtained from the best-fit exposure model, against the measured data points. The deepest sample is critical to defining the best-fit parameters. Several exposure age/erosion rate solutions can fit the near surface data well, but are less able to fit the deepest sample. Fig. 4.7b gives the predicted nuclide concentration for two exposure age/erosion rate scenarios that fit most measured data points well, except the deepest samples. This illustrates the importance of deep samples to obtain robust age constraints from depth, and the value of forward modeling to obtain the best fitting parameters.

4.4.2.3 Outwash cobbles

Cobbles from the associated outwash terrace yield ^{10}Be exposure ages that are consistently older than boulder ages, ranging from 193.6 – 265.1 ka. Exposure ages from sample sites S1 and S2 are indistinguishable (Table 4.2, Figs. 4.4-4.5). The high variability in exposure ages likely stems from geomorphic processes as opposed to variable inherited nuclides. While the depth profile indicates that the terrace sediment has remained stable below 10 cm, all surface cobbles have similar or higher nuclide concentrations than the concentration at 10 cm in the profile. Thus a

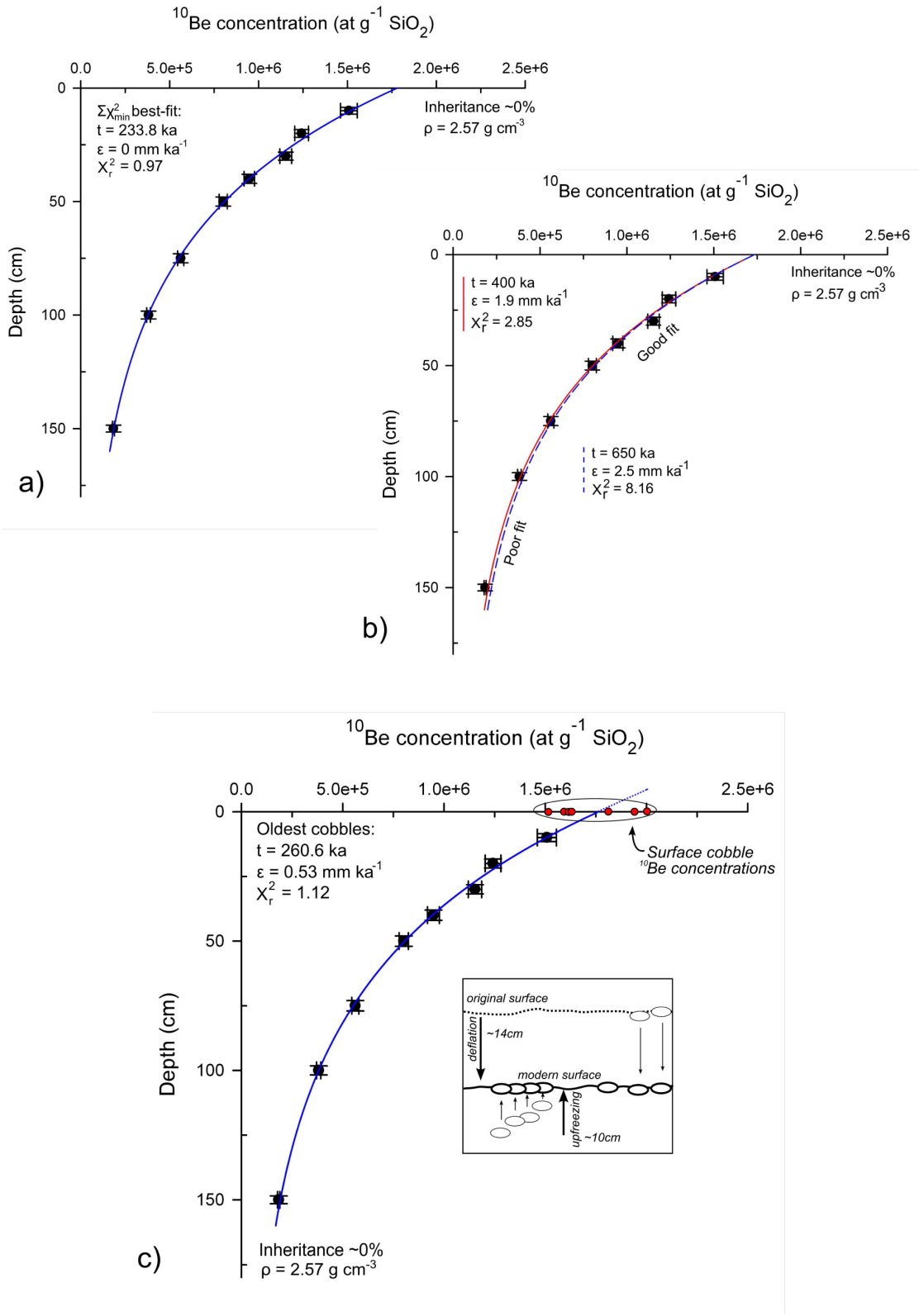

Figure 4.7. Plots of measured & modeled ^{10}Be concentrations with depth

Measured ^{10}Be concentration as a function of depth within the Hatcher outwash terrace. Data points (solid circles) are an amalgamation of pebble clasts following Repka et al. (1997) (Table 4.1). The (1σ) analytical uncertainties in ^{10}Be concentration were used in the

model optimization. The uncertainty with depth is based on the thickness of the largest clast (Table 4.1). a) Plot of modeled best-fit ($\Sigma\chi^2$min) ^{10}Be concentration based on the exposure model optimization. b) Plot of a scenario where the near surface data are well approximated while the deepest samples are not. This exemplifies the importance of deep profiles with several data points, and the value of exposure model optimization. The parameters of exposure age and erosion rate were obtained from the $\Sigma\chi^2$ solution surface (Fig. 4.6a). c) Plot of the modeled ^{10}Be concentration based on the exposure age of the oldest surface cobbles, and the corresponding erosion rate inferred from the $\Sigma\chi^2$ solution surface (Fig. 4.6a). The cartoon illustrates how a combination of terrace deflation and shallow turbation (< 10cm) can explain the wide range of measured ^{10}Be concentrations in surface cobbles.

combination of near surface turbation (e.g., cryoturbation) above 10 cm and terrace erosion by deflation can explain the observed age range. The geologic evidence supports deflation of the terrace surface (Section 4.3.1.2), causing previously buried cobbles to become exposed in the process (Fig. 4.7c). The scenario is consistent with an observation that the youngest samples at S2 fully retained their fluvial shape, while the oldest cobbles revealed significant ventifaction (Figs. 4.3f, 4.3g). With no lithologic difference between cobbles, we infer that ventifaction of surface cobbles indicates a longer surface residence time. The two oldest surface cobbles yield an arithmetic mean age of 260.6 ± 7.6 ka (1σ external ± 34 ka; Fig. 4.5). The old ages are unlikely to be the result of re-working of older sediment based on our assessment of nuclide inheritance (Section 4.5.1) and also because alluvial fans composed of older (Caracoles) sediment are clearly defined and over 5 km from the sampled location (Fig. 4.4). The ^{26}Al/^{10}Be ratios are consistent with a relatively simple exposure history without prolonged burial.

4.5 Discussion

4.5.1 Nuclide inheritance

We assess nuclide inheritance based on the ^{10}Be concentration depth-profile of pebble clasts, which averages inheritance over 10 to 50 individual pebble clasts per sample at each of the eight sample depths. These data indicate that the average inherited nuclide component in the Hatcher outwash terrace is negligible (Fig. 4.6b). This is in agreement with the low variability of ages found in outwash cobbles from the younger Río Blanco unit (σ = 0.5 ka), which suggests that the variability of inherited nuclides is low (i.e., within analytical uncertainties), and by inference inheritance (if inheritance would be large, its variability would be large). Thus we conclude that nuclide inheritance is negligible in outwash deposits of the Río Blanco and Hatcher units, and probably throughout the Lago Pueyrredón valley.

4.5.2 Age of the Hatcher unit

The Hatcher moraines and associated outwash terraces were deposited roughly coincidently, yet exposure ages differ by over 200 ka depending on the sample and nature of the sample location. Because nuclide inheritance is demonstrably low and most geologic processes act to reduce cosmogenic nuclide inventories (Phillips et al., 1990), the oldest ages are considered the best estimate for the deposition age of the unit. The oldest surface cobbles are likely closest to the deposition age at 260.6 ± 6.5 ka, analogous to the oldest boulder ages on a moraine (cf. Zreda and Phillips, 1995). This age is ~25 ka older than that indicated by the depth-profile $\Sigma\chi^2_{min}$ best-fit at

233.8 ka, but is indistinguishable at 1σ (Fig. 4.6a). The statistical best-fit ($\Sigma\chi^2_{min}$) occurs with a terrace erosion rate of 0 mm ka^{-1}. The geologic evidence, however, suggests minor terrace deflation (Section 4.3.1.2). Changes in bulk density occurring temporally (e.g., with soil and pedogenic carbonate formation) may have influenced the $\Sigma\chi^2_{min}$ fit, but the effect cannot be accurately accounted for and is expected to be small relative to age uncertainty. A terrace age of 260.6 ka corresponds with an inferred terrace erosion rate of ca. 0.53 mm ka^{-1} based on the depth-profile (χ_r^2= 1.12; Figs. 4.6a,4.7c). This suggests ~14 cm of terrace deflation over the exposure duration, with survival of the oldest clasts likely due to their resistant lithology. This amount of surface lowering is consistent with minor terrace deflation inferred at the sampled sites and with preservation of shallow surface channels with clear braiding patterns (~50cm relief). The $^{26}Al/^{10}Be$ ratios of surface cobbles and the depth-profile data are consistent with a single stage exposure history. Based on current knowledge of ^{10}Be production rates and the assumptions made in this paper, we estimate the age of the Hatcher unit to be 260.6 ± 6.5 ka (1σ external ± 34 ka; ε_{terr} = 0.53 mm ka^{-1}).

Of the five scaling schemes implemented in the CRONUS-Earth exposure age calculator, the time-dependent Lal (1991)/Stone (2000) scaling factors yield the youngest exposure ages by ~5%. Using these scaling factors reduces the interpreted minimum age to 248 ± 24 ka (1σ external). Within uncertainty this overlaps with the age of Substage 7d (~ 225 - 220 ka, Martinson et al., 1987). However, Substage 7d is short-lived relative to both MIS 6 and 8. The Hatcher unit is older than MIS 6, and its size and preservation suggests it was more extensive than MIS 6. Thus we

consider it unlikely that the Hatcher moraines are age-equivalent to the short-lived 7d substage, and consider it more likely that they are coeval with the more pronounced global cooling during MIS 8, as indicated by our estimated exposure age.

4.5.2.1 Discordant ages

The above results indicate that in certain environments the outwash terrace is a better target for exposure age dating old glacial sequences than the associated moraine. Outwash samples yield consistently older exposure ages than those from the moraines (Fig. 4.5). This result was expected based on the favorable environmental conditions and local geomorphology (Section 4.1.3 – 4.2). However, the significant disparity in ages between moraine boulders and outwash cobbles was not predicted. While large scatter is expected of old moraine boulders, the oldest age was thought to date closely moraine deposition. In this case, that age was more than 100 ka too young. Putkonen and Swanson (2003) recommend sampling at least 6 – 7 boulders from old and tall moraines to obtain a boulder age at ≥ 90% of the moraine age (95% confidence). Therefore we cannot rule-out under-sampling as a cause of the discrepancy. However, well-preserved boulders were rare.

The $^{26}Al/^{10}Be$ ratios provide no evidence to explain the young boulder ages. Boulder erosion rate uncertainty could explain the wide scatter and young ages, but the moraine cobble data (where negligible erosion is implicit) indicate that exhumation (moraine degradation) is likely the primary control. The moraine cobble with the highest ^{10}Be concentration (5.26×10^5 atoms g^{-1}) is used to infer minimum moraine degradation rates using model scenarios (Equation 1) that assume a deposition age of

260 ka and a till density of 2.2 g cm^{-3}. The minimum amount occurs with instant degradation of ~100 cm at the time of sampling. By comparison, the concentration can be achieved with a constant degradation rate of 12 mm ka^{-1}, equating to ~3.1 meters of surface lowering. The tallest boulder (2.0 m) has an exposure age that is within 30% of the age of the outwash terrace, which may indicate a relatively small amount of original cover. Concluding, we infer that exhumation is the primary cause of the young and scattering boulder exposure ages.

However, additional complexity may have been introduced by episodic boulder erosion. If significant aeolian erosion occurs when outwash plains are active (Section 4.2.2), then aeolian erosion episodes probably occurred during MIS 6 (ca. 150 ka) and during deposition of the Río Blanco outwash at ~25 ka. Because the erosion rate applied is a long-term average, a relatively recent pulse of boulder erosion may yield exposure ages that are too young (e.g., Small et al., 1997). However, aeolian erosion is normally restricted to less than 50 cm above the soil surface (Bagnold, 1941), thus the taller boulders may not have experienced it in the geologically recent past.

Moraine cobbles are rarely ventifacted, suggesting exhumation occurred after any recent (aeolian) erosion episode. For the sake of argument, if we assume soil degradation at a constant rate, the derived rate (12 mm ka^{-1}) is nearly double the maximum rate estimated for the older and more subdued Telken moraines at LBA (ca. 7 mm ka^{-1}; Ackert and Mukhopadhyay, 2005). By comparison, the Hatcher moraines are relatively sharp crested at the sampled locations (Figs. 4.3c, 4.3d).

Because environmental conditions are similar, the different rates could be explained by a differing moraine surface morphology. Models predict higher degradation on tall and steeply dipping moraines (Putkonen and O'Neal, 2006; Putkonen and Swanson, 2003). At the sampled location, the ice-contact flank of the moraine was taller (40 – 50 m high) and steeper dipping (19º – 25º) than both the down-ice flank, and more subdued terminal locations. It is possible this 'lateral moraine' morphology at the sampled locations could result in locally high degradation. If so, the large discrepancy in boulder and outwash ages could be due in part to our choice of sample location, despite seemingly good preservation.

Regardless of the cause, our data highlight the significant challenges of exposure age dating old glacial sequences using moraine boulders. Despite probable exhumation of all boulder samples and complexity introduced by boulder erosion, the data yield a typical spread of ages with the oldest boulder age (no erosion) and the average age (w/erosion) indistinguishable. This together with an observation of moraine ridges as old as 1.1 Ma still clearly preserved (Fig. 4.2) would suggest that moraine degradation rates are generally low in this environment. Given only this information, it would be reasonable to assume the exposure ages from boulder samples (~150 ka) dated closely moraine deposition. However, this interpretation would be erroneous by over 100 ka. It is worth noting that the smaller moraine cobbles are highly sensitive to moraine degradation in this environment. When interpreted as exposure ages, these samples underestimate the deposition age by over 200 ka. These results highlight the challenge of exposure age dating old moraines and suggest a cautious approach to interpreting such data.

4.5.3 Correlation to LBA record

The new cosmogenic exposure ages allow comparison to the record at LBA. We re-calculate the ^{10}Be boulder exposure ages published by Kaplan et al. (2004; 2005) and Douglass et al. (2006) for both the Fenix V and Moreno II moraines in order to compare directly the data presented in this study and the assumptions therein. The Río Blanco – Fenix correlation is valid based on LGM ages of 26.8 ± 1.0 ka and 24.5 ± 1.3 ka for the Río Blanco and Fenix moraines, respectively. The Hatcher – Moreno correlation is less convincing. On Moreno II, the oldest ^{10}Be boulder exposure age (no erosion) of 169.4 ka and mean age (w/erosion) of 168.8 ka is indistinguishable from the Hatcher boulders. If the supposed correlation is valid, then the Moreno moraines were also deposited at ~260 ka, and the young boulder exposure ages on the Moreno moraines are analogous to those of the Hatcher moraines. Alternatively, the correlation may not be valid and these are indeed two different glacial events preserved separately in each valley.

The available evidence supports the latter interpretation. First, the lowest ^{10}Be concentration of 5 moraine cobbles on Moreno I was found to be ~7.30 x 10^5 atoms g^{-1} (Table 4.3). With steady degradation, this concentration can be achieved with rates of 6.1 and 7.6 mm ka^{-1} for a surface ~170 ka (oldest boulder age) and ~260 ka (Hatcher age), respectively. These rates are consistent with the maximum rate estimated for the Telken moraines in this valley (Ackert and Mukhopadhyay, 2005), and equate to roughly 105 – 200 cm of moraine surface lowering. Thus degradation rates are apparently lower for the Moreno moraines and boulders may have been

continuously exposed. Second, 6-7 boulders (cf. Putkonen and Swanson, 2003) between 5 – 200 cm height were measured from the Moreno I-II moraines; these were age consistent (Kaplan et al., 2005). Third, ^{230}Th/U ages of soil carbonate formed in outwash gravels associated with the Moreno II moraines suggest onset of calcic pedogenesis at 170 ± 8.3 ka (Phillips et al., 2006). ^{230}Th/U data from the younger Fenix moraines indicates a brief interval (< 3 ka) between surface stabilization and the onset of calcic pedogenesis under glacial conditions. The re-calculated ^{10}Be boulder exposure ages are consistent with this new data. Therefore, based on the available evidence, the best estimate for the age of the Moreno I-II moraines is before ~170 ka, or MIS 6, and thus the correlation to the Hatcher moraines appears invalid on this basis.

Table 4.3. Data from Moreno 1 moraine cobbles at LBA

Sample ID	Latitude	Longitude	Altitude	Thickness	Quartz mass	^{10}Be measured[a] (10^5 atom g^{-1})
	(dd)	(dd)	(m asl)	(cm)	(g)	(±1σ)
LBA06-1	-46.5645	-70.8851	504	3	14.65	7.30 ± 0.24
LBA06-3	-46.5647	-70.8851	504	3.5	11.69	8.38 ± 0.29
LBA06-5	-46.5649	-70.8850	503	3	11.78	6.74 ± 0.25
LBA06-6	-46.5649	-70.8850	503	4	17.01	7.41 ± 0.39
LBA06-7	-46.5649	-70.8850	504	3	15.70	8.56 ± 0.27

a. All AMS measurements made at S.U.E.R.C. normalized to NIST SRM-4325 Be standard material with a revised (Nishiizumi et al., 2007) nominal ^{10}Be/^{9}Be ratio (2.79×10^{-11}) and half-life (1.36 Ma). Nuclide concentrations include propagated AMS sample/lab-blank uncertainty and 2% carrier mass uncertainty. Shielding is negligible for all samples (shielding factor <0.9998); rock density 2.7 g cm^{-3}.

4.6 Conclusions

- We demonstrate that outwash terrace sediments are better targets than associated moraine boulders for exposure age dating 'old' (i.e., pre-LGM)

glacial deposits in the Lago Pueyrredón valley, central Patagonia. A comparatively small number of outwash samples provide more consistently accurate results.

- We find that exposure ages from moraine boulders underestimate the deposition age by ~100 ka, and exposure ages from moraine cobbles, if interpreted as exposure ages, underestimate the deposition age by over 200 ka. We infer that exhumation as a consequence of moraine degradation is the primary cause of the age discrepancy between the moraine and outwash samples.
- A forward model inversion of a ^{10}Be depth-profile in the outwash terrace sediment, using the sum of chi-squared, is used to define the exposure age, erosion rate and inherited ^{10}Be concentration. This model, in conjunction with geologic observations and exposure ages from surface cobbles, indicates a terrace age of ca. 260 ka, a low terrace erosion rate of ca. 0.5 mm ka^{-1}, and no inherited nuclides.
- The result indicates that a major advance of a Patagonian ice sheet occurred at ~260 ka (MIS 8) and deposited the Hatcher moraines at Lago Pueyrredón. This finding differs from findings at Lago Buenos Aires, where the Moreno I-II moraines, which occupy a similar stratigraphic position relative to the LGM deposits, are dated to MIS 6 (Kaplan et al., 2005). This documents the value of more than one site in a region for reconstructing glacial chronologies.
- The local LGM maximum occurred at ~27 – 25 ka and is represented by the Río Blanco moraine system.

- No deposits relating to MIS 6 or MIS 4 were observed at Lago Pueyrredón.
- Our ages for the Río Blanco and Hatcher moraines are discrepant with the previously inferred chronology (Wenzens, 2005).

4.7 Acknowledgements

We thank C. Risso, P. Alvarez and O. Martínez for logistical support; A-S. Meriaux for fieldwork support; S. Binnie and E. McDougall for assistance with laboratory work and D. Sugden for helpful comments. For financial support we thank the UK Natural Environment Research Council (NERC) for A. Hein's studentship and sample analysis, the Royal Geographic Society (with IBG) - Rio Tinto plc award, the Royal Scottish Geographic Society, the Carnegie Trust for the Universities of Scotland and the Scottish Universities Environmental Research Centre (S.U.E.R.C.) for support of sample analysis. We are grateful for the constructive comments of two anonymous reviewers that greatly improved the manuscript. (This is L-DEO contribution number #7287 – M. Kaplan).

Chapter 5 Cosmogenic-nuclide ages of Early and Middle Pleistocene glacial sequences in Patagonia

This chapter further evaluates the approach to dating old glacial sequences that was demonstrated in Chapter Four. It provides direct ages for the two oldest glacial sequences in the Lago Pueyrredón valley, the "Cañadón de Caracoles" and the "Gorra de Poivre" sequences. This chapter is intended to be published as follows:

Hein, A.S., Dunai, T.J., Hulton, N.R.J., Xu, S. Cosmogenic-nuclid ages of Early and Middle Pleistocene glacial sequences in Patagonia.

I wrote the manuscript; Dunai accompanied me in the field when some of the rocks were collected; The remaining samples were collected by myself during the second field season; Hulton and Dunai made helpful comments; Xu performed the AMS measurements.

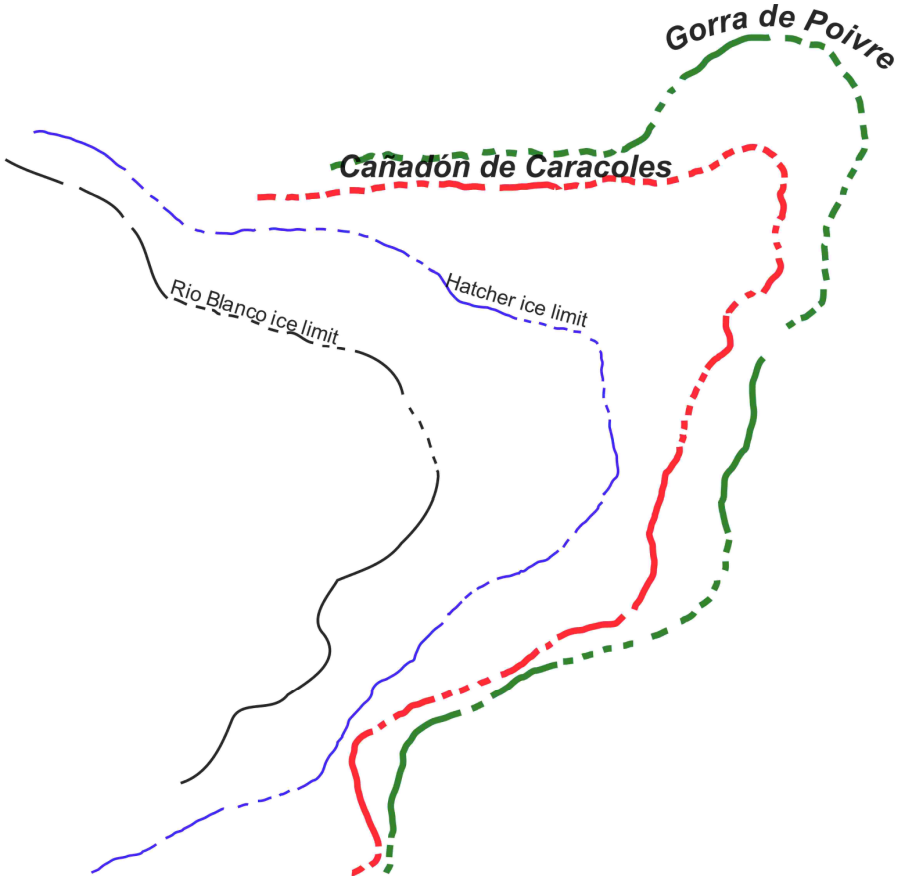

Abstract

The glacial geologic record in Argentine Patagonia is exceptionally well-preserved and spans more than one million years. The deposits provide a record of long-term terrestrial climate extremes at a key mid-latitude position in the southern hemisphere. Despite their value for paleoclimate reconstructions, the deposits have not been extensively dated. The exceptional preservation of ice contact landforms older than ca. 1 Ma indicates surface stability in the region and suggests that direct dating of the oldest glacial deposits by cosmogenic-nuclide surface exposure methods may be appropriate. In this study, cosmogenic ^{10}Be and ^{26}Al surface exposure ages are obtained from outwash gravels associated with two of the oldest glacial sequences in the Lago Pueyrredón valley, 47.5º S, Argentina. The exposure ages obtained from the oldest and most extensive outwash terrace give an age of ca. 1.2 Ma, the oldest such cosmogenic-nuclide surface exposure ages so far obtained from glacial deposits in Patagonia. The age is consistent with independent age constraints for the 'Greatest Patagonian Glaciation' that were obtained elsewhere by ^{40}Ar/^{39}Ar methods. Surface exposure ages of 600 ka are obtained from outwash gravels and a moraine boulder associated with a younger and less extensive ice limit. These data suggest a significant advance of the Patagonian ice sheet may have occurred during Marine Isotope Stage 16. The results indicate that our approach to directly dating old (i.e., pre-Last Glacial Maximum) glacial deposits is robust over the appropriate timescales. Thus, it should be possible to date the entire sequence of Quaternary ice limits in Argentine Patagonia with similar environmental conditions.

5.1 Introduction

The aim of this study is to evaluate the feasibility of dating the oldest glacial deposits in Patagonia (ca. 1.1 Ma) by cosmogenic-nuclide surface exposure methods on outwash gravels. In a previous study, Hein et al. (2009) establish that nuclide inheritance is negligible in outwash sediments and thus they use the oldest surface cobbles from a stable outwash terrace to date a deposit at ca. 260 ka. The surface cobbles display a wide scatter of ^{10}Be exposure ages (190 – 265 ka) which were interpreted to reflect both shallow mixing of terrace sediment and minor deflation of the terrace surface. Relatively fewer cosmogenic nuclides accumulated in sediments affected by mixing, causing underestimated surface exposure ages. The geologic processes that interrupt the continuous exposure of sediment on outwash terrace surfaces (e.g., bioturbation, cryoturbation, burial, soil formation) are expected to become increasingly important for older surfaces. Therefore, the feasibility of dating the oldest glacial deposits in Patagonia by this method is unknown. In this study, we evaluate the approach on older surfaces by dating two of the oldest glacial deposits in the Lago Pueyrredón valley, 47.5º S, Argentina. The oldest deposit has been independently dated at ca. 1.1 Ma (Singer et al., 2004) based on ages from Lago Buenos Aires, 40 km to the north of the study area, and from Río Gallegos, about 500 km to the south. By comparing the exposure ages obtained against an independently dated record, we critically evaluate the long-term stability of the outwash terrace surfaces and their suitability for cosmogenic-nuclide surface exposure age dating. We show that the method is robust over these timescales and it

should be possible to reconstruct the glacial history across much of Argentine Patagonia with similar environmental conditions.

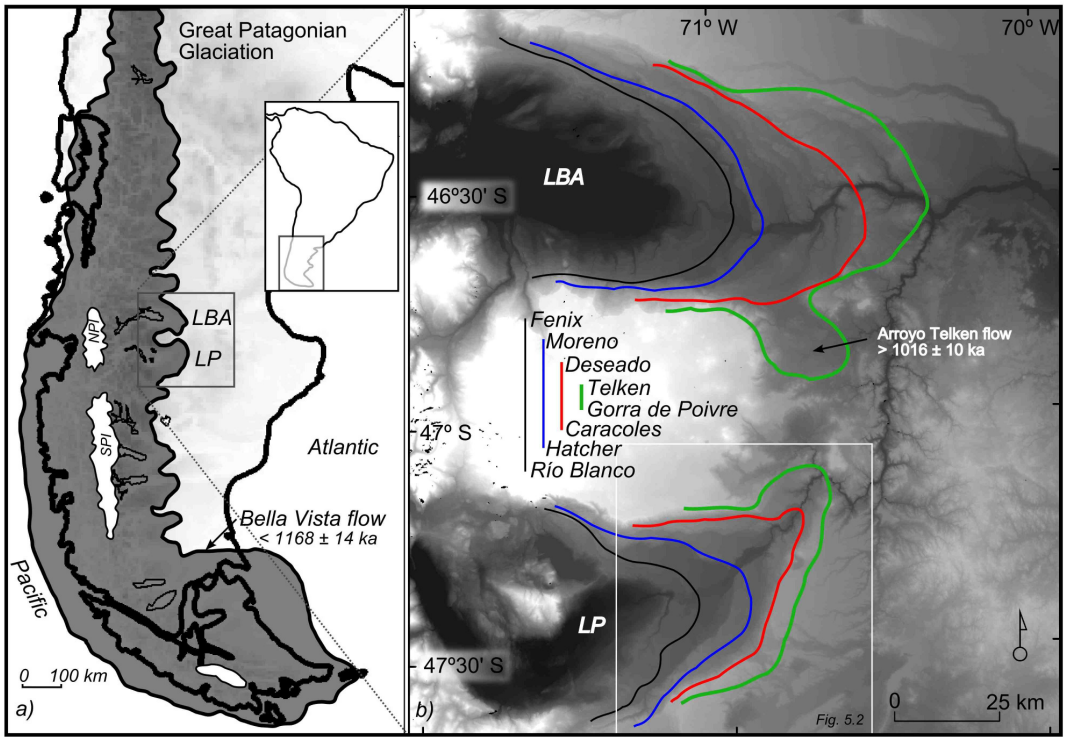

Figure 5.1. Context map

a)The study area and extent of the Greatest Patagonian Glaciation (Mercer, 1976) based on the mapping of Caldenius (1932). The modern North (NPI) and South Patagonian Icefields (SPI) and the location of the Lago Buenos Aires (LBA) and Lago Pueyrredón (LP) outlet glaciers are shown. The Bella Vista lava flow is a key constraint on the maximum age of the Greatest Patagonian Glaciation (Singer et al., 2004). b)Principal moraine groups in the Lago Pueyrredón and Lago Buenos Aires valleys based on the mapping of Caldenius (1932). The Arroyo Telken flow is a key constraint for the minimum age of the Greatest Patagonian Glaciation (Singer et al., 2004).

5.1.1 Underlying rationale

The glacial geologic record is an important source for terrestrial climate information. Well-dated glacial chronologies in both hemispheres are necessary to evaluate ice age theories and to understand better long-term climate and landscape evolution. Glacial chronologies are best developed for deposits of the Last Glacial cycle

because these are generally well-preserved and within the range of radiocarbon age dating. In contrast, there is a paucity of chronometric data for glacial deposits older than the Last Glacial Maximum (LGM) in both hemispheres; this reflects the limitations of certain geochronometers, and the reduction in quantity and quality of preserved glacial geologic records. Thus, our knowledge of long-term terrestrial climates remains limited, particularly in the southern hemisphere where there exists little landmass. Southern South America hosts one of the best preserved and temporally punctuated glacial sequences in the world (Clapperton, 1993). The deposits of former Patagonian ice sheets span a ~1 Ma time period (Mercer, 1976; Singer et al., 2004), but have remained undated in many areas because of a lack of dateable material. The Patagonian record is an important proxy for long-term terrestrial climate extremes at mid-latitudes in the southern hemisphere.

5.1.2 Geologic setting

The Lago Pueyrredón valley is one of the largest outlet valleys of former Patagonian ice sheets in central Patagonia (Fig. 5.1). The west – east trending glacial depression extends east of the present day North Patagonian Icefield and is bounded by upland areas of the Meseta del Lago Buenos Aires to the north and the Mesetas Belgrano and Olnie to the south (Fig. 5.2). The bounding mesetas are capped by plateau lavas (11 – 7 Ma) overlain by Pliocene to Quaternary alkaline lavas that are interbedded with glacial deposits in the adjacent Lago Buenos Aires valley (Brown et al., 2004; Ton-That et al., 1999); these lavas provide important constraints on the age of glacial deposits in the region (Fig. 5.1b). The surrounding geology consists of Jurassic silicic volcanics and Cretaceous to Miocene mixed marine and continental sediments

(Gorring et al., 2003). To the west, these overly highly deformed Paleozoic basement rocks of the Eastern Andes Metamorphic Complex, which are intruded and deformed by the Mesozoic Patagonian batholith and later plutonics in the Andean Cordillera (Lagabrielle et al., 2004; Ramos and Kay, 1992; Suárez and De La Cruz, 2001). Quaternary glacial and glaciofluvial sediments of Andean lithology fill the basin and extend eastward as outwash plains.

The glacial deposits were mapped originally by Caldenius (1932) who distinguished four groups of moraines and associated outwash terraces, a pattern he recognized in several eastern outlets of former Patagonian ice sheets. The outermost deposits are located ca. 350 meters higher and ca. 40 kilometers east of the innermost deposits, with each group separated by escarpments rising up to 100 meters towards the east. The over-deepening of the valley has led to a unique hydrologic condition in which eastward drainage occurs only when ice sheets are large enough to block lower drainage routes to the west (Chapter Three). Therefore, the glacial deposits have been largely protected from subsequent fluvial erosion. The survival of the glacial deposits is partly a result of this hydrologic situation together with an overall pattern of decreasing maximum ice extents through time (Kaplan et al., 2009). The quality of preservation is also the result of the semi-arid (ca. 200 mm a^{-1})[6] and windy environment which is thought to have persisted throughout glacial periods when the growth of an ice sheet up-wind would have enhanced drier conditions on the eastern and leeward side of the Andes (Hulton et al., 2002). The resulting low erosion rates and long-term landform stability in the region is exemplified by clear moraine ridges

[6] NCEP-NCAR reanalysis; www.cdc.noaa.gov/ncep_reanalysis/

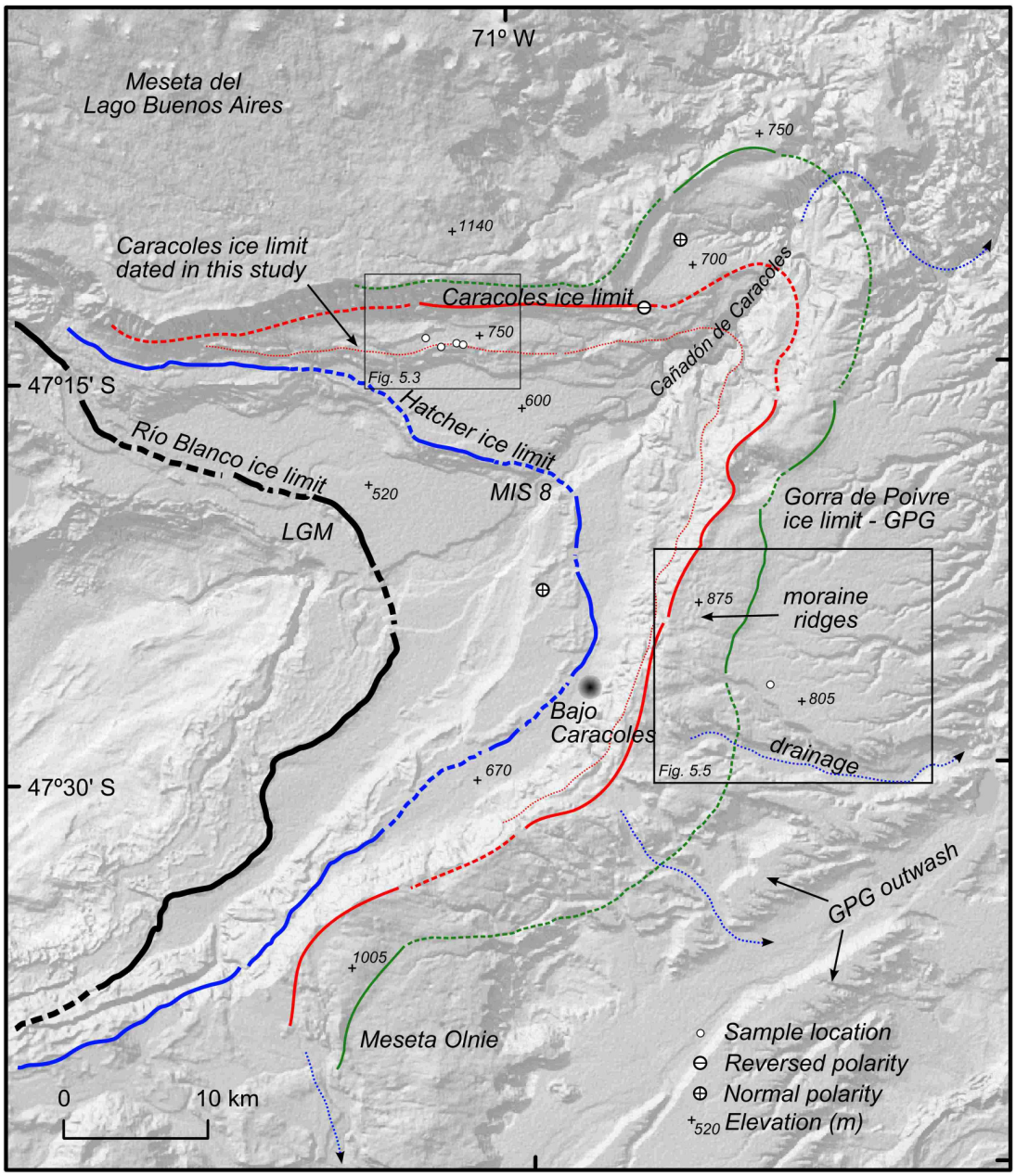

Figure 5.2. Ice limits and sample locations

Moraine limits, chronologic constraints, and sample locations in the Lago Pueyrredón valley. Dashed moraine limits are estimated. Magnetic polarity measurements are by Sylwan et al. (1991). The Río Blanco and Hatcher ice limits are dated at ca. 26 ka and ca. 260 ka, respectively (Hein et al., 2009). The outwash terraces east of the Río Blanco and Hatcher ice limits are the inferred primary source of windblown dust; the northern location of the Caracoles ice limit dated in this study is relatively protected from aeolian erosion given the persistent westerly winds in this region. Thus, boulder surface erosion rates may be lower at this location.

preserved on the oldest deposit in the valley (Fig. 5.2). The stability of glacial landforms suggests that cosmogenic-nuclide surface exposure age dating may be feasible on even the oldest glacial deposits in the region.

5.1.3 Existing chronology

The Lago Pueyrredón valley has received little attention following the pioneering work of Caldenius (1932), with a few notable exceptions (Feruglio, 1950; Sylwan et al., 1991; Wenzens, 2005). Until recently, chronometric ages were not available to constrain the age of glacial deposits (e.g., Coronato et al., 2004). Recently, the Río Blanco and Hatcher moraines and outwash terraces were dated by cosmogenic-nuclide surface exposure methods (Chapter Three and Four). The Río Blanco moraines are dated at ca. 17.5 – 27 ka (i.e., Last Glacial Maximum) and the penultimate Hatcher glacial deposits are dated at ca. 260 ka (i.e., Marine Isotope Stage 8; Fig. 5.2). Sylwan et al. (1991) measured magnetic polarity in glacial sediments and found that the outermost Caracoles moraines were deposited during the reversed Matuyama chron at more than 780 ka (Shackleton et al., 1990; Singer and Pringle, 1996). The outermost Gorra de Poivre moraines are the local equivalent of Mercer's (1976) "Greatest Patagonian Glaciation"; the most extensive ice advance in Patagonia. A key constraint on the age of these moraines comes from lava flows dated by $^{40}Ar/^{39}Ar$ and K-Ar methods at Lago Buenos Aires (Singer et al., 2004; Ton-That et al., 1999). The Arroyo Telken flow (Fig. 5.1b), which surrounds and overlies the outermost tills (Telken VII) identified at Lago Buenos Aires, is dated at 1,016 ± 10 ka (±2σ) by $^{40}Ar/^{39}Ar$ incremental heating (Singer et al., 2004; Ton-That et al., 1999). Therefore, the Greatest Patagonian Glaciation at these latitudes

occurred prior to 1,016 ka. Further constraints were obtained from the Bella Vista flow located south of the Río Gallegos in southernmost Patagonia (Fig. 5.1a). The Bella Vista flow underlies the most extensive glacial drift in the region (Caldenius, 1932) and represents Mercer's (1976) type section for the Greatest Patagonian Glaciation. The Bella Vista flow has been dated by whole-rock K-Ar methods at 1,170 ± 5 ka (±1σ; Mercer, 1976), by the $^{40}Ar/^{39}Ar$ total fusion method at 1,550 ± 3 ka (±1σ; Meglioli, 1992), and more recently by the $^{40}Ar/^{39}Ar$ incremental heating method at 1,168± 14 ka (±2σ; Singer et al., 2004; Ton-That et al., 1999). Thus, the Greatest Patagonian Glaciation in the region between Lago Buenos Aires (46.5º S) and Rio Gallegos (52º S) is thought to have occurred between 1,016 ± 10 ka and 1,168 ± 14 ka (Singer et al., 2004).

5.2 Approach and methodology

Hein et al. (2009) find that outwash terrace cobbles yield consistently older ages than associated moraine boulders. They attribute the age discrepancy to the different erosion rates on each type of surface. A higher erosion rate on moraines likely causes the exhumation of boulders that contain lower cosmogenic nuclide concentrations. In contrast, a ^{10}Be concentration depth-profile in the outwash sediment reveals the long-term stability of the terrace surface and the lack of inherited cosmogenic nuclides. We assume the demonstrated lack of inheritance for the Río Blanco and Hatcher outwash terraces is characteristic of outwash sediment in the valley. This assumption is reasonable given that the sediment sampled in this study was also transported by glaciers from source areas located over 75 kilometers

distant in the Andean cordillera. If the stability of outwash terrace surfaces has persisted over long time-scales, we expect the exposure ages from outwash surface sediment to date closely the glacial advances.

To test this, we targeted outwash sediment associated with the Gorra de Poivre moraines, the local equivalent of the independently dated Greatest Patagonian Glaciation (Fig. 5.2). In addition, outwash sediment and moraine boulders were sampled from a stratigraphically younger surface within the Cañadón de Caracoles moraines; these are known to be older than the Hatcher moraines dated at ca. 260 ka (Hein et al., 2009). The ^{10}Be and ^{26}Al concentrations in each sample were measured to assess the potential for complex exposure histories.

5.2.1 Intermediate moraines and outwash terraces

The Cañadón de Caracoles (shortened to: Caracoles) unit is composed of numerous individual moraines nested together on the margins of the Lago Pueyrredón basin (Fig. 5.3). The moraines are best preserved on the northern side of the valley where up to 10 individual moraine crests are distinguishable, occasionally with small intervening outwash terraces. The range of moraine crest elevations is in excess of 200 meters and outwash drainage channels cross-cut older deposits at some locations; this suggests the Caracoles moraines may represent more than one glacial advance. We sampled the most distinct and best preserved moraine and associated outwash terrace located midway between the innermost and outermost of the Caracoles ice limits (Figs. 5.3 and 5.4). The term 'Caracoles 2' is used to distinguish this limit from the outermost 'Caracoles 1' limit.

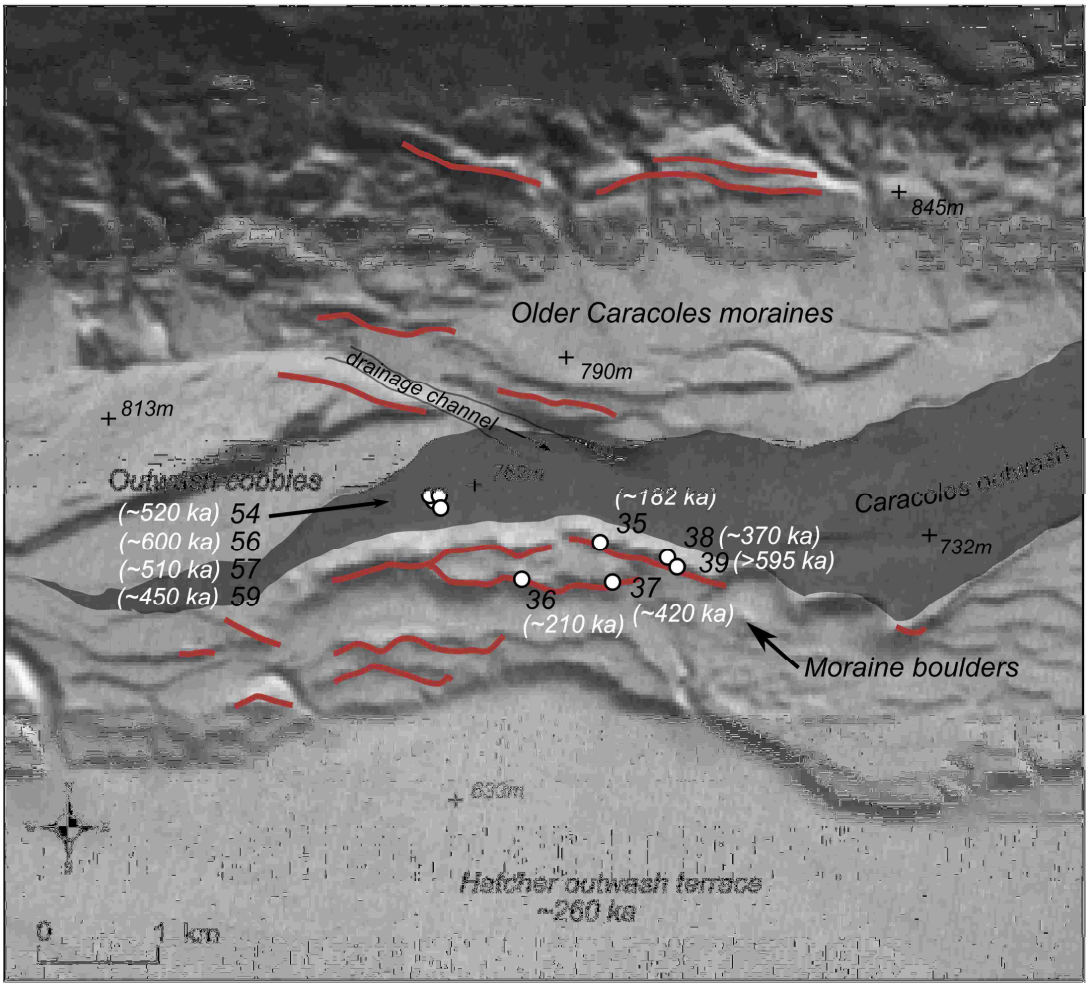

Figure 5.3. Cañadón de Caracoles sample locations

ASTER scene showing the sample location and ^{10}Be exposure ages from the Caracoles ice limit (see Fig. 5.2 for location). Older Caracoles moraines are banked against the escarpment of the Meseta del Lago Buenos Aires. A drainage channel cuts the older moraines and grades to the outwash terrace surface; the outwash terrace (shaded grey) was sampled to the west of this location. Spot elevations are marked with crosses.

The moraines at the sampled location are continuous and relatively sharp crested (ca. 10 meters wide) with slopes of ca. 8º and 12º and relief of ca. 20 and 50 meters on the ice-distal and ice-proximal sides, respectively. Moraine boulders are abundant (Fig. 5.4b) and often show signs of minor surface erosion; in particular, minor flaking (< 2 cm) and ventifacts are commonly observed (Fig. 5.4b). Granite boulders

were sampled with hammer and chisel following standard protocols (Gosse and Phillips, 2001). The top few centimeters were sampled from five large and stable boulders (> 60cm) located on two closely spaced moraine crests.

The associated outwash terrace (Fig. 5.4a) is situated between the sampled moraines and a series of older Caracoles moraines banked against the escarpment of the Meseta del Lago Buenos Aires. The outwash terrace is about 1.5 kilometers wide and can be traced for about 11 kilometers as it slopes gently toward the east at 0.5º. The moraines exterior to the outwash terrace have been incised by a drainage channel that grades to the outwash terrace (Fig. 5.3). At this location, sediment from the older surfaces could have been re-deposited on the outwash surface. Therefore, we sampled the terrace surface far to the west of this location where there is no evidence for re-deposition of older material. Surface channels with braiding patterns (ca. 40 cm relief) are present on the sampled surface. The terrace is sparsely vegetated and is composed of coarse sands with a high density of cobbles and small boulders (ca. 10 – 30 cm). The abundance of larger clast sizes reflects a high energy deposition environment close to the glacier snout. The surface clasts are nearly always ventifacted and occasionally are fractured; granular disintegration is observed in some granitic lithologies (Fig. 5.4c). Most cobbles are ventifacted to varying degrees on their exposed surface but the undersides of the cobbles are not. This suggests that the cobbles have not changed their orientation. Four quartz cobbles were sampled from the surface and the top few centimeters were removed for analysis (Figs. 5.4d, e).

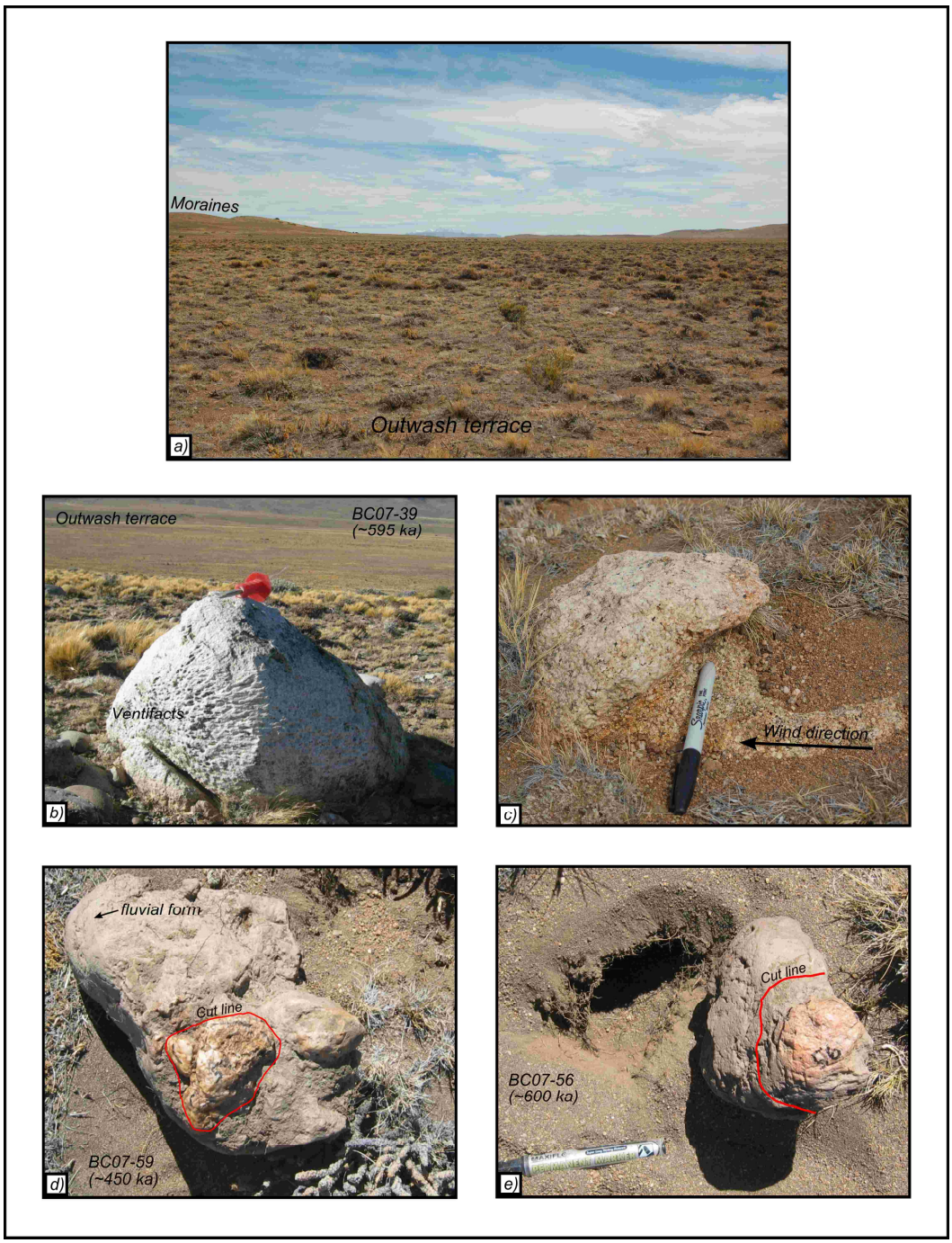

Figure 5.4. Cañadón de Caracoles sample photos

a) The Caracoles outwash terrace is ca. 1.5 km wide at the sampled location and is sparsely vegetated. The photo is oriented towards the west with the dated moraines visible. b) The oldest moraine boulder is 60 cm tall. Ventifacts are restricted to the lower 50 cm. The boulder is situated on the ice distal side of the 10 m wide moraine crest. c) Granular disintegration of a granite boulder on the outwash terrace surface. d) The youngest outwash cobble was severely eroded on the top surface; the bottom and sides showed a fluvial form. This cobble may have fractured; if so the sampled quartz nodule may not have been close to the initial rock surface. e) The oldest outwash cobble was only slightly ventifacted on the top surface.

5.2.2 Outermost moraines and outwash terraces

The Gorra de Poivre moraines mark the outer limit of ice expansion in the Lago Pueyrredón valley (Fig. 5.2). They are best preserved on the eastern edge of the

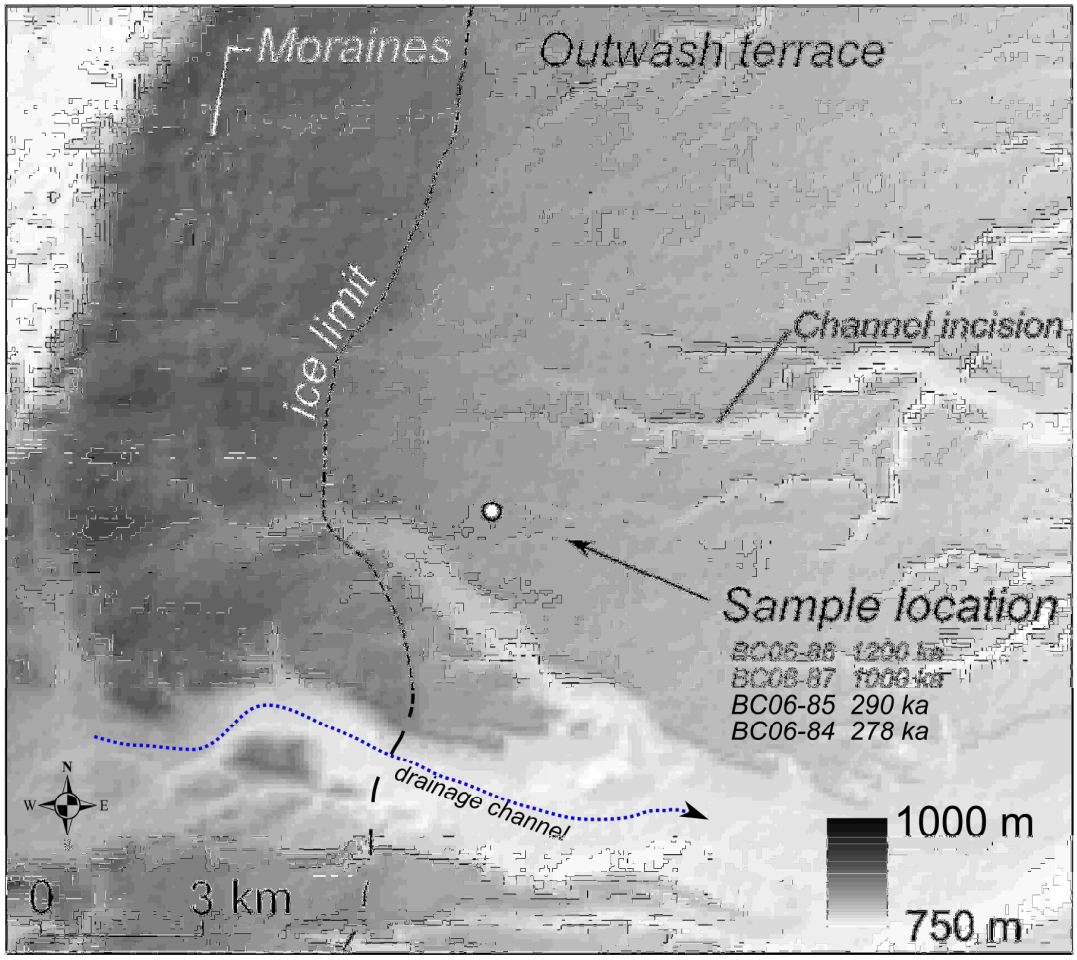

Figure 5.5. Gorra de Poivre sample locations

ASTER digital elevation model (30m) showing the sample location and ^{10}Be ages from the outermost Gorra de Poivre outwash terrace (see Fig. 5.2 for location). The samples were taken away from back-cutting drainage channels that have incised the terrace surface. Also shown are the clear moraine ridges preserved within this old moraine system.

basin where clear moraine ridges are distinguishable (Fig. 5.5). However, overall, the moraine system is characterized by broad, low relief and subdued moraines

deposited over a width of five kilometers. Moraine boulders are found infrequently on these surfaces and were not sampled in this study.

The associated outwash terrace is best preserved east of the basin, but several isolated outcrops surround the basin to the south (Fig. 5.2). The outwash terrace grades gently eastward at ca. 0.4º. The terrace was sampled at a location away from post-glacial drainage channels that have incised into the surface (Fig. 5.5). In common with other terrace surfaces in the valley, there is sparse vegetation and sediment ranging from coarse sands to cobbles. In contrast to other sampled terrace surfaces in the valley, there exists clear evidence of sediment mixing. Most cobbles are ventifacted not only on their exposed surface, but also their bottoms and sides which suggests that rotation of the cobble has occurred through time (Fig. 5.6). In addition, several clasts are oriented with their long-axis perpendicular to the terrace surface (Fig. 5.6). This observation suggests soil activity related to permafrost (Millar, 2006; Washburn, 1980). Fig. 5.6 shows the four cobbles that were sampled from the terrace surface. Because of their thickness (diameters 10 – 20 cm), the samples required trimming before analysis to reduce associated self-shielding uncertainties. The decision of where to cut and sample each cobble was based on our observations of the pattern of ventifacts which was used as a proxy for the cobble surface. For example, sample BC06-86 was oriented and cut so that the apex of three faceted surfaces was the 'top' surface of the cobble (Fig. 5.6f). As a result of the observed sediment mixing, the surface exposure ages may be reduced and provide minimum ages.

5.2.3 Cosmogenic nuclide analysis

The samples were prepared at the University of Edinburgh's Cosmogenic Isotope Laboratory following an adaptation of the methods of Kohl and Nishiizumi (1992) and Bierman et al. (2002). The AMS measurements were performed at the Scottish Universities Environmental Research Centre (S.U.E.R.C.). ^{10}Be concentrations are normalized to the NIST SRM-4325 Be standard material with a revised (Nishiizumi et al., 2007) nominal ^{10}Be/^{9}Be ratio of 2.79 x 10^{-11}. ^{26}Al concentrations are normalized to the Purdue Z92-0222 Al standard material with a nominal ^{26}Al/^{27}Al ratio of 4.11 x 10^{-11} which agrees with the Al standard material of Nishiizumi et al. (2004). The ^{26}Al/^{10}Be production rate ratio is 6.75.

Exposure ages were calculated with the CRONUS-Earth web-based calculator (version 2.2 ;Balco et al., 2008)[7] which implements the revised ^{10}Be standardization and half-life (1.36 Ma) of Nishiizumi et al. (2007). Sample thickness (Table 5.1) and density (2.7 g cm^3 assumed) are used to correct for self-shielding. Topographic shielding was measured with an inclinometer (horizons < 3º) but corrections are considered negligible for all samples (scaling factor < 0.9998). Present day winter snow cover is thin and short-lived and models predict increased aridity during glacial times (Hulton et al., 2002). Therefore, because the semi-arid conditions are thought to have persisted through time, no correction is applied for snow cover or for shielding by vegetation. No erosion rate correction is applied because the fluvial form of the cobbles suggests that total rock surface erosion is generally negligible. However, an erosion rate of 1.4 mm ka^{-1} is used to correct the moraine boulder

[7] (http://hess.ess.washington.edu/math/index_dev.html)

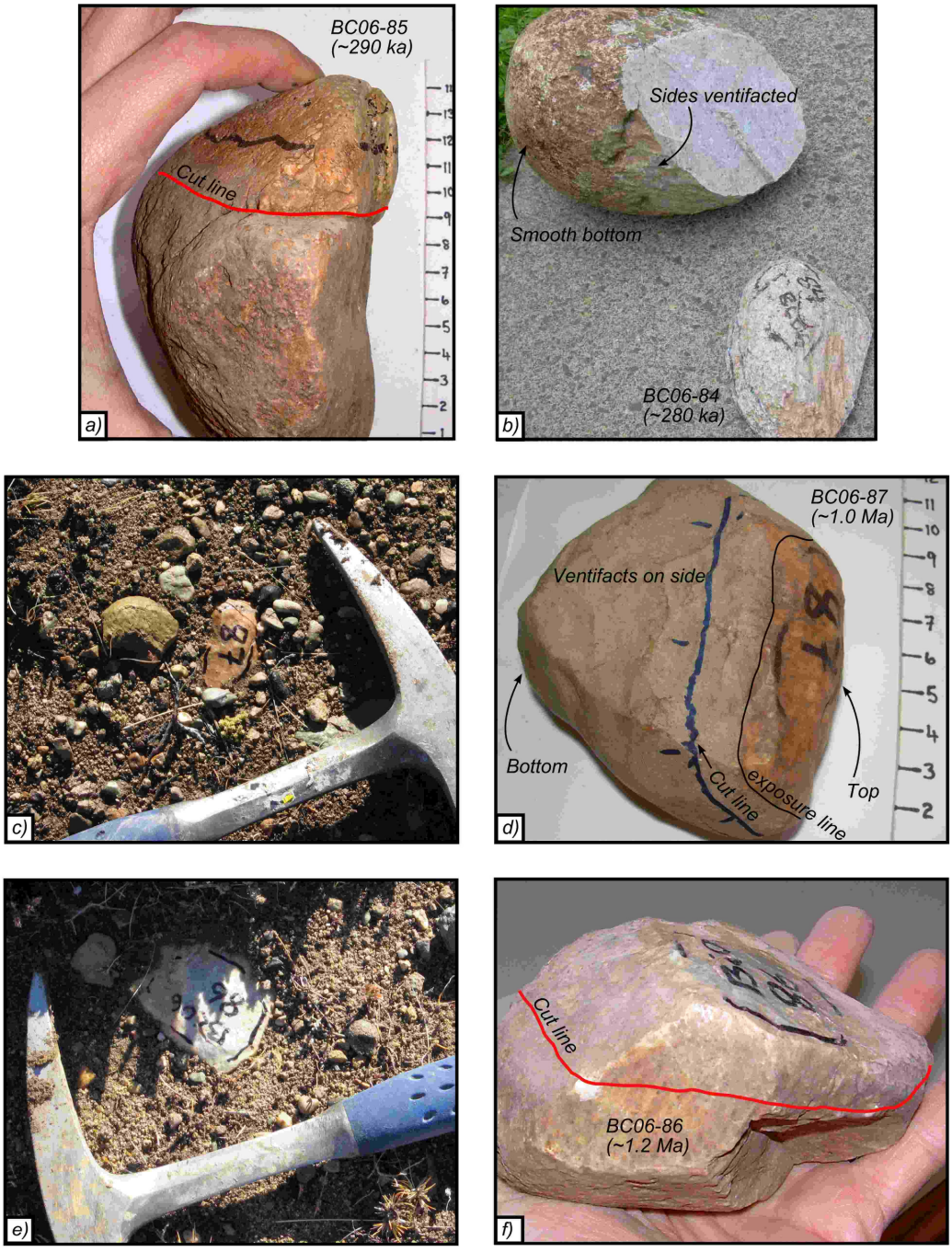

Figure 5.6. Gorra de Poivre sample photos

a) BC06-85 was slightly ventifacted on the top surface and was oriented like a 'tooth' with its long-axis perpendicular to the surface. The portion located above the 'cut line' was used for analysis. b) BC06-84 was large (20 cm) and tooth oriented with ventifacts on the top and one side; the analyzed portion is at bottom. c) BC06-87 in situ. d) BC06-87 was tooth oriented; it was ventifacted on all sides. The top was analyzed above the 'cut line'. e) BC06-86 in situ. f) BC06-86 yields the oldest ^{10}Be exposure age. The clast had three facets on its top surface. The sample was cut with the apex of the facets as the 'top' of the cobble.

exposure ages; this value was derived by Kaplan et al. (2005) for boulders on the Telken moraines at Lago Buenos Aires, 60 kilometers to the north. The exposure ages are reported based on the Dunai (2001) scaling model. Exposure ages differ by about 5% depending on the scaling model used.

The time-averaged ^{10}Be and ^{26}Al production rates near Lago Pueyrredón have been estimated to be 5% and 11% higher than for standard atmospheric conditions by two independent studies that infer a low pressure anomaly during glacial times (see Ackert et al., 2003; Hein et al., 2009; Staiger et al., 2007). Following Staiger et al.(2007), we increase the ^{10}Be and ^{26}Al production rates by 5%. Importantly, the choice of production rates does not affect our main conclusions. The higher production rate is implemented within the exposure age calculator by artificially lowering the air pressure at the sampled locations, thereby increasing the production rate (Hein et al., 2009). Specifically, we lower the sea-level pressure that is used in the conversion of sample elevations to sample air pressures; the present day sea-level pressure (1009.3 hPa)[8] is lowered to 1002.3 hPa. The lower sea-level pressure reduces the calculated sample air pressures, and thereby increases the time-averaged production rate derived through the calculator by approximately 5% when compared against the value obtained from a calculation based on the present day sea-level pressure.

[8] NCEP-NCAR reanalysis; www.cdc.noaa.gov/ncep_reanalysis/

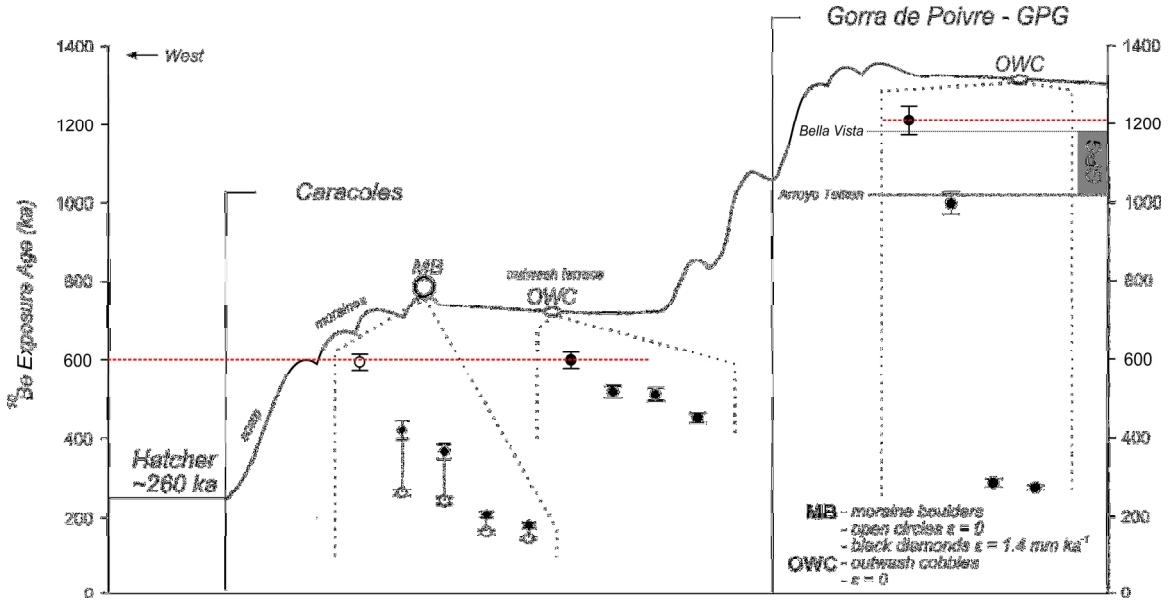

Figure 5.7. Illustration of exposure age results

The ^{10}Be exposure ages from the Caracoles and Gorra de Poivre units. The cartoon depicts moraine and outwash positions and sample types; it is not to scale. Moraine boulders ages are shown with and without an erosion rate correction. Uncertainties are 1σ analytical. The Gorra de Poivre moraines are the local equivalent to the Greatest Patagonian Glaciation (GPG) which is bracketed in age by the Bella Vista and Arroyo Telken lava flows (Singer et al., 2004). The interpreted age of each deposit is marked by the dashed line. Exposure ages were calculated with the CRONUS-Earth web-based exposure age calculator (Balco et al., 2008).

5.3 Results

The analytical results are presented in Table 5.1 and Figs. 5.7 – 5.8. Nuclide concentrations in Table 5.1 are corrected for the number of ^{10}Be and ^{26}Al atoms in their associated blanks. Blanks (n = 5) were spiked with 250 µg ^{9}Be carrier and 1.5 mg ^{27}Al carrier. Samples were spiked with 250 µg ^{9}Be carrier and up to 1.5 mg ^{27}Al carrier (the latter value varied depending on the native Al-content of the sample). For each batch of 7 samples one blank was processed. The corresponding combined process and carrier blanks range between 115,000 ± 18,000 atoms ^{10}Be and 290,000 ± 40,000 atoms ^{10}Be (< 1% of total ^{10}Be atoms in sample; 0.9 – 1.7 x 10^{-14}

[^{10}Be/^{9}Be]); and between 61,000 ± 12,000 atoms ^{26}Al and 190,000 ± 57,000 atoms ^{26}Al (< 1% of total ^{26}Al atoms in sample; 2.6 – 3.8 x 10^{-15} [^{26}Al/^{27}Al]). Sample and blank ^{10}Be/^{9}Be and ^{26}Al/^{27}Al analytical uncertainties and a 2% carrier addition uncertainty and 5% stable ^{27}Al measurement (ICP-OES) uncertainty are propagated into the 1σ analytical uncertainty for nuclide concentrations. In the following text, uncertainties are reported at 1σ. Analytical uncertainties are reported. The 'external' uncertainties include both production rate and scaling factor uncertainties (Balco et al., 2008).

5.3.1 Intermediate moraines and outwash terrace

The boulders from the Caracoles 2 moraines give ^{10}Be exposure ages that range between 148 – 595 ka assuming zero boulder surface erosion; correcting for an erosion rate of 1.4 mm ka^{-1} increases the youngest age to 182 ka and results in saturation of the oldest sample. The apparent saturation of sample BC07-39 indicates that the erosion rate applied is too high for this sample. The ^{26}Al/^{10}Be ratios are not consistent with post-depositional burial as an explanation for the young and scattering (~75%) boulder exposure ages (Fig. 5.8a).

The outwash terrace cobbles give ^{10}Be ages that range between 452 – 600 ka (Fig. 5.7). The data are less scattered (~25%) than the boulder data and they give on average older exposure ages. The oldest outwash cobble age of 600 ± 20 ka

Table 5.1. Cosmogenic nuclide data

.

Sample I.D.	Latitude	Longitude	Altitude	Boulder height	Thick	Quartz mass	Isotope -	Nuclide concentration[a]	$^{26}Al/^{10}Be$[b]	Age 1[c] (10^3 a) ε = 0		Age 2[c,d] (10^3 a) ε = 1.4 mm ka^{-1}	
	(dd)	(dd)	(m asl)	(cm)	(cm)	(g)	AMS ID[a]	(10^6 atom g^{-1})		Age ± 1σ (int)	± 1σ (ext)	Age ± 1σ (int)	± 1σ (ext)
Gorra de Poivre													
Outwash cobbles													
BC06-86	-47.44816	-70.77132	813		2	2.8949	^{10}Be – b2949	8.898 ± 0.202	5.06 ± 0.30	**1211 ± 36**	200		
							^{26}Al – a870	*45.019 ± 2.501*		*1103 ± 100*	*260*		
BC06-87	-47.44814	-70.77102	814		2	16.3597	^{10}Be – b2950	7.710 ± 0.172	5.21 ± 0.30	999.0 ± 28	160		
							^{26}Al – a871	*40.192 ± 2.108*		*909.3 ± 71*	*190*		
BC06-85	-47.44815	-70.77153	811		3	1.4703	^{10}Be – b2948	2.637 ± 0.086	6.63 ± 0.48	290.3 ± 9.8	38		
							^{26}Al – a867	*17.488 ± 1.136*		*305.1 ± 22*	*48*		
BC06-84	-47.44801	-70.77122	811		3	17.3231	^{10}Be – b2947	2.534 ± 0.056	6.03 ± 0.34	278.0 ± 6.4	36		
							^{26}Al – a866	*15.284 ± 0.788*		*261.4 ± 15*	*38*		
Caracoles													
Moraine boulder													
BC07-39	-47.23422	-71.03812	769	60	2.5	20.1155	^{10}Be – b2086	4.844 ± 1.44	5.48 ± 0.34	**594.4 ± 20**	84	Saturated	
							^{26}Al – a667	*26.54 ± 1.45*		*531.9 ± 36*	*90*	*Saturated*	
BC07-37	-47.23533	-71.04555	762	95	1	15.0548	^{10}Be – b2054	2.353 ± 0.073	5.83 ± 0.37	264.3 ± 8.5	34	422.4 ± 23	100
							^{26}Al – a656	*13.71 ± 0.751*		*237.9 ± 14*	*35*	*361.5 ± 35*	*91*
BC07-38	-47.23390	-71.03913	775	100	1.5	21.4400	^{10}Be – b2085	2.198 ± 0.067	6.71 ± 0.42	243.9 ± 7.7	32	368.1 ± 18	79
							^{26}Al – a664	*14.74 ± 0.810*		*256.5 ± 15*	*38*	*412.6 ± 44*	*120*
BC07-36	-47.23498	-71.05643	766	75	1.5	20.2027	^{10}Be – b2084	1.504 ± 0.046	6.45 ± 0.41	165.0 ± 5.1	21	209.2 ± 8.4	35
							^{26}Al – a663	*9.701 ± 0.532*		*162.7 ± 9.3*	*23*	*206.7 ± 15*	*39*
BC07-35	-47.23227	-71.04653	775	130	3	17.8902	^{10}Be – b2083	1.347 ± 0.038	6.47 ± 0.41	147.7 ± 4.2	19	181.9 ± 6.5	29
							^{26}Al – a662	*8.713 ± 0.493*		*145.5 ± 8.5*	*20*	*179.4 ± 13*	*32*
Outwash cobbles													
BC07-56	-47.22905	-71.06558	765		2.5	20.7016	^{10}Be – b1773	4.862 ± 1.46	5.71 ± 0.36	**599.6 ± 20**	85		
							^{26}Al – a645	*27.76 ± 1.52*		*566.9 ± 39*	*98*		
BC07-54	-47.23013	-71.06517	765		2.5	18.9782	^{10}Be – b2044	4.283 ± 1.14	6.01 ± 0.37	518.9 ± 15	72		
							^{26}Al – a650	*25.75 ± 1.41*		*514.3 ± 35*	*87*		
BC07-57	-47.22843	-71.06575	760		3	19.9434	^{10}Be – b1774	4.199 ± 1.30	--	512.0 ± 17	71		
						--	--	--	--	--			
BC07-59	-47.22927	-71.06602	765		2	18.3588	^{10}Be – b2045	3.813 ± 1.01	5.96 ± 0.36	452.4 ± 13	61		
							^{26}Al – a651	*22.73 ± 1.24*		*435.9 ± 28*	*70*		

***Table 5.1 footnotes**:* Samples processed at the University of Edinburgh's Cosmogenic Isotope Laboratory. Shielding is negligible for all samples; rock density is 2.7 g cm^{-3}; erosion rate (ε).
a) All AMS measurements made at S.U.E.R.C. normalized to NIST SRM-4325 Be standard material with a revised (Nishiizumi et al., 2007) nominal $^{10}Be/^{9}Be$ ratio (2.79×10^{-11}) and half-life (1.36 Ma), and the Purdue Z92-0222 Al standard material with a nominal $^{26}Al/^{27}Al$ ratio of 4.11×10^{-11} that agrees with Al standard material of Nishiizumi et al. (2004). Nuclide concentrations include propagated AMS sample/lab-blank uncertainty, 2% carrier mass uncertainty (Be) and 5% stable ^{27}Al measurement (ICP-OES) uncertainty.
b) Surface $^{26}Al/^{10}Be$ production ratio begins at 6.75.
c) Exposure ages calculated using the CRONUS-Earth web-based calculator version 2.2 (Balco et al., 2008) and Dunai (2001) scaling factors. The production rate was increased by 5% by reducing sample air pressures (the sea-level pressure was reduced from 1009.3 hPa to 1002.3 hPa – see text for details).
d) Erosion rate from Kaplan et al.(2005). (int) = internal (analytical) uncertainties; (ext) = propagated external uncertainties. Bold indicates the oldest ages from each group.

matches closely the oldest boulder age of 595 ± 20 ka. The $^{26}Al/^{10}Be$ ratios do not indicate prolonged post-depositional shielding of the terrace surface (Fig. 5.8b).

5.3.2 Outermost outwash terrace

The Gorra de Poivre outwash terrace cobbles give ^{10}Be exposure ages that range between 278 – 1211 ka. The two oldest ages of 1211 ± 36 ka and 999 ± 28 ka agree at 1σ with an independent $^{40}Ar/^{39}Ar$ constraint dated elsewhere on equivalent deposits at 1,016 ± 5 ka to 1,168± 7 ka (1σ; Singer et al., 2004). The data are highly scattered (~78%). The $^{26}Al/^{10}Be$ ratios do not support prolonged post-depositional burial as an explanation for the two youngest exposure ages (Fig. 5.8c).

5.4 Discussion

5.4.1 Evaluation and interpretation of exposure ages

The glacial deposits dated in this study have remained preserved throughout several ice ages. With the increased duration of exposure comes an increased potential for geologic processes that might affect the continuous exposure and nuclide

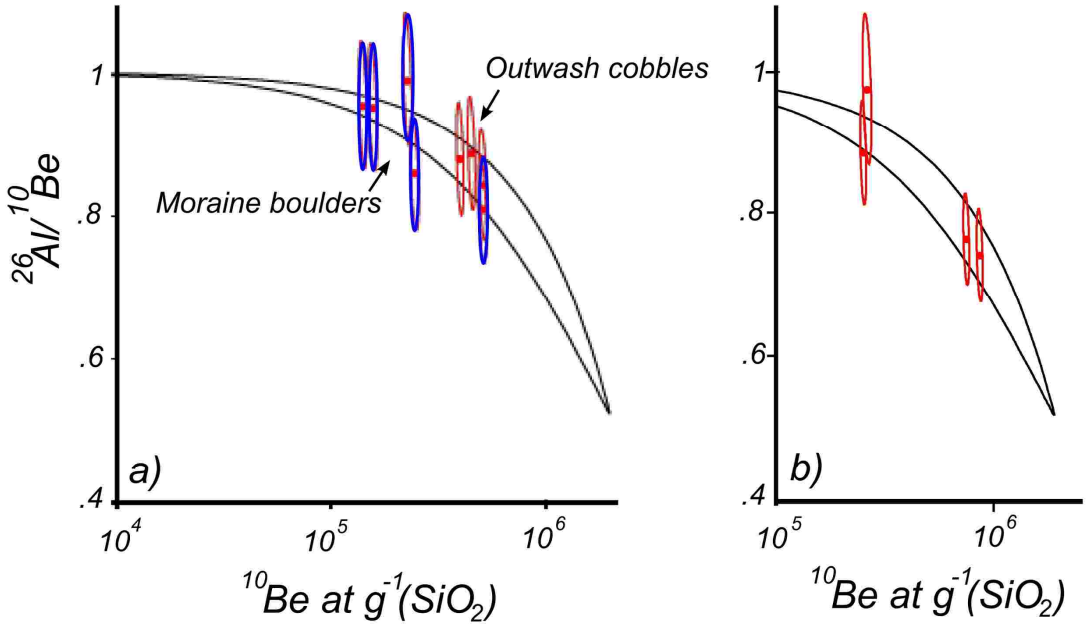

Figure 5.8. $^{26}Al/^{10}Be$ ratios

a) $^{26}Al/^{10}Be$ ratio (6.75:1) normalized to 1 and plotted against normalized ^{10}Be concentration (log-scale) for the Caracoles moraine boulders (blue) and outwash terrace cobbles (red). The data fall within the erosion island, thus there is no evidence for prolonged post-depositional shielding of the surface. The plot was derived from the CRONUS-Earth exposure age calculator (Balco et al., 2008). b) $^{26}Al/^{10}Be$ plot for the Gorra de Poivre outwash terrace cobbles yield similar results.

concentration in a sample. Geologic processes such as post-depositional shielding (e.g., by snow cover or soil formation), soil erosion (e.g., by moraine degradation or terrace deflation/inflation), soil turbation (e.g., bio- or cryoturbation) and rock surface erosion all act to reduce the cosmogenic nuclide inventory of a sample leading to young apparent exposure ages. We argue that nuclide inheritance is negligible in the outwash sediments dated in this study (Section 5.3). Thus, given the antiquity of the deposits, we favor the oldest exposure ages as the best estimate of the age of the surface.

5.4.1.1 Intermediate Cañadón de Caracoles sequence

The exposure ages from the outwash terrace cobbles give consistently older ages than the associated moraine boulders barring one exception. The same pattern occurs in the younger Hatcher unit and is considered to reflect primarily boulder exhumation as a consequence of moraine degradation (Hein et al., 2009). This result indicates that the outwash terrace surface remains stable and more suitable for exposure age dating old glacial deposits than the associated moraine ridges in this environment.

The oldest (^{10}Be) outwash cobble is thought to date closely the glacial advance at 600 ± 20 ka (± 85 ka; 1σ external) because the geologic evidence indicate long-term surface stability at the sampled location. Soils are poorly developed in the top ca. 10 centimeters and a high density of large cobbles and small boulders reduces the possibility of sediment mixing by cryogenic processes. Indeed, the general lack of ventifacts on the undersides of cobbles suggests that they most likely maintained their orientation with their top surfaces exposed to cosmic radiation throughout their exposure. The ^{26}Al/^{10}Be ratios do not indicate prolonged post-depositional shielding (Fig. 5.8b) that could have reduced nuclide concentrations. Total erosion of the oldest sample was negligible given the presence of its glaciofluvial form and minor ventifacts of less than a few millimeters (Fig. 5.4e). The surface channels with braiding patterns preserved in the terrace surface suggests overall stability of the surface with limited terrace erosion. Thus, there is no evidence to suggest that geologic processes have significantly reduced the cosmogenic nuclide concentrations in the oldest sample, and thus we argue that this sample dates closely the glacial advance at ca. 600 ka.

However, there remains a significant scatter in the outwash cobble data that cannot be explained by analytical uncertainties alone. The youngest cobble (BC07-59) was severely eroded (Fig. 5.4d). The sampled nodules from this clast may not have been as close to the original cobble surface as was initially thought, and we infer the young exposure age is a result of erosive mass-loss which is roughly estimated at < 3 cm at the sampled nodule; this was done by estimating the natural shape of the clast based on the fluvial curvature preserved on the sides of the clast. The remaining cobbles are less scattered (ca. 15%) and are indistinguishable at 3σ. The range of exposure ages could reflect similar localized processes that are inferred for the younger Hatcher outwash terrace, such as minor terrace deflation that may have caused the gradual exhumation of cobbles (Hein et al., 2009).

The oldest moraine boulder (BC07-39) ^{10}Be age of 595 ± 20 ka (no correction for erosion) is in good agreement with the oldest outwash cobble age. The steady state erosion rate for this particular sample must have been significantly lower than the value estimated based on boulders in the Lago Buenos Aires valley. The calculated exposure age is highly sensitive to the erosion rate. For example, the exposure age increases to 620 ka and 850 ka with erosion rates of 0.1 mm ka^{-1} and 0.5 mm ka^{-1}, respectively. The lower 50 centimeters of the boulder is ventifacted on the western (windward) side (Fig. 5.4b); the top and downwind surfaces display no clear erosion features. The sand and dust particles that become entrained by wind and thereby erode the rock surface, generally are not lifted above ca. 50 centimeters (Bagnold, 1941). Provided the boulder did not slowly exhume through the moraine matrix, this could explain why the top of this boulder was not ventifacted. Thus, the boulder

might have survived on the crest of the moraine with a low surface erosion rate and with aeolian erosion restricted to the lower 50 centimeters.

There is geologic evidence to suggest that overall, aeolian erosion was less severe near the sampled location on the northern margin of the Lago Pueyrredón basin. Specifically, ventifacts on moraine boulders and outwash cobbles are often more severe on stratigraphically younger surfaces near the center of the valley. Active outwash terrace sediment is the primary source of windblown dust in the region (cf. Sugden et al., 2009); if so, aeolian erosion likely occurs episodically during glacial maxima when fine sediment was being deposited on broad outwash plains. This sediment would have been entrained by the strong westerly winds leading to ventifaction of rock surfaces downwind (east) of the sediment source. Thus, the samples from the Caracoles moraine and outwash terrace may have been protected relative to samples in the center of the valley. While the sampled site (Fig. 5.2) is fully exposed to the dominant westerly winds, the main sediment sources (i.e., younger outwash terraces) are located further south. We therefore suspect that moraine boulder and outwash cobble erosion rates are comparatively lower at the sampled location, and that the erosion rate correction applied to the boulder data may be too high (Table 5.1).

The oldest moraine boulder would appear a clear outlier (3σ) with respect to the remaining boulder samples. This could have been misinterpreted as the result of inherited nuclides. Instead, the oldest boulder dates most closely the glacial advance. This exemplifies the challenge of dating old glacial deposits using moraine boulders.

The result suggests that an interpretation based on the oldest boulder age (cf. Putkonen and Swanson, 2003) may be most appropriate for pre-LGM moraines in this environment. However, most importantly, it suggests a cautious approach to interpreting such data. Based on the low erosion rates inferred for the boulder surfaces, and in common with previous findings in the valley (Hein et al., 2009), we argue again that boulder exhumation is the primary cause of the wide scatter and young moraine boulder exposure ages.

5.4.1.2 Outermost Gorra de Poivre sequence

The two oldest outwash cobbles yield cosmogenic ^{10}Be and ^{26}Al surface exposure ages that are consistent with independently dated ^{40}Ar/^{39}Ar constraints on the age of the Greatest Patagonian Glaciation. It is remarkable when considering that individual clasts have remained exposed to cosmic radiation over such timescales, despite clear evidence of sediment turning in the terrace surface. In line with our observation that distinct moraine ridges are preserved, this result highlights long-term landform stability in the region. The ^{26}Al/^{10}Be ratios do not indicate any prolonged post-depositional burial, and the oldest ^{10}Be exposure age is taken to best represent the minimum age of the Greatest Patagonian Glaciation in the Lago Pueyrredón valley at 1,211 ± 36 ka (± 200 ka 1σ external; Fig. 5.7). The age is ca. 200 ka older than the minimum age constraint obtained from the Arroyo Telken flow at nearby Lago Buenos Aires, and within analytical uncertainty of the Bella Vista flow marking the maximum age for the Greatest Patagonian Glaciation at 1,168 ± 14 ka (2σ; Singer et al., 2004). Given the geographic distribution of the minimum and maximum age constraints (section 5.2.1), it is possible that the most extensive

advance in central Patagonia occurred earlier than that in southernmost Patagonia (~52º S) where the maximum age constraint was obtained.

The scatter of exposure ages from the Gorra de Poivre outwash terrace is significant. The $^{26}Al/^{10}Be$ ratios provide no evidence for prolonged post-depositional burial that could explain the youngest ages (ca. 300 ka). The young ages probably resulted from several factors, but exhumation caused by sediment mixing (cryoturbation) likely influenced a primary control. The modern day climate does not support permafrost in the region. Modern winter (Jun – Aug) and summer (Dec – Feb) temperatures average 3º C and 12º C, respectively at the town of Perito Moreno located 80 km to the north[9]. However, during the Last Glacial Maximum, paleotemperatures at 40º S are estimated to have been about 6º – 7º C cooler (Denton et al., 1999a; Moreno et al., 1999). The temperature depression was sufficient for the development of permafrost throughout much of Argentine Patagonia (see Bockheim et al., in press; Martínez and Coronato, 2008; Trombotto, 2008). The orientation of these samples, with their long-axis perpendicular to the surface (Figs. 5.6a,b,d), is commonly observed in permafrost soils (Washburn, 1980). The low nuclide concentrations could therefore have resulted from cryoturbation during multiple ice ages that only recently brought the samples to the surface of the terrace. A short surface residence is indicated by the limited degree of ventifaction on the two youngest cobbles (Figs. 5.6a,b), while the oldest cobbles were ventifacted on multiple surfaces (Figs. 5.6d,f). This suggests a longer surface residence time considering repeated turning and erosion of the resistant clasts.

[9] United States National Center for Atmospheric Research dataset ds570.0 available at http://dss.ucar.edu/datasets/ds570.0/.

The results suggest that applying specific sampling criteria, it should be possible to date the full sequence of Patagonian glacial deposits by cosmogenic-nuclide surface exposure methods on outwash gravels. Currently, the biggest limitation is the uncertainty related to production rates and scaling of cosmogenic nuclides. For the oldest deposits, the total uncertainty (10 - 20%; Gosse and Phillips, 2001) precludes resolving with confidence the individual glacial stages (see Fig. 5.9). With time, as further geologic calibration sites are found, these external uncertainties should approach analytical precision.

5.4.2 Chronologic significance

The data presented allow an assessment of the timing of Early and Middle Pleistocene glacial events in the Lago Pueyrredón valley (Fig. 5.9). The Caracoles moraine and associated outwash terrace yield cosmogenic ^{10}Be surface exposure ages that indicate a significant advance of a Patagonian ice sheet occurred at ca. 600 ka. The nearest glacial stage is Marine Isotope Stage (MIS) 16 at ca. 620 – 675 ka (Lisiecki and Raymo, 2005). Shackleton (1987) identifies MIS 16 as one of the most significant ice ages in terms of northern hemisphere ice volume based on δ^{18}O values from deep sea sediment cores. These data also indicate that sea-level was lower during MIS 16 than during the LGM. In the southern hemisphere, a deuterium record from the EPICA Dome C ice core in Antarctica indicates that MIS 16 was one of the colder glacial stages of the past 800 ka, and was distinctly colder than other glacial stages that culminated between 400 – 800 ka (EPICA community members, 2004; Jouzel et al., 2007). Atmospheric CO_2 concentrations in the same ice core are

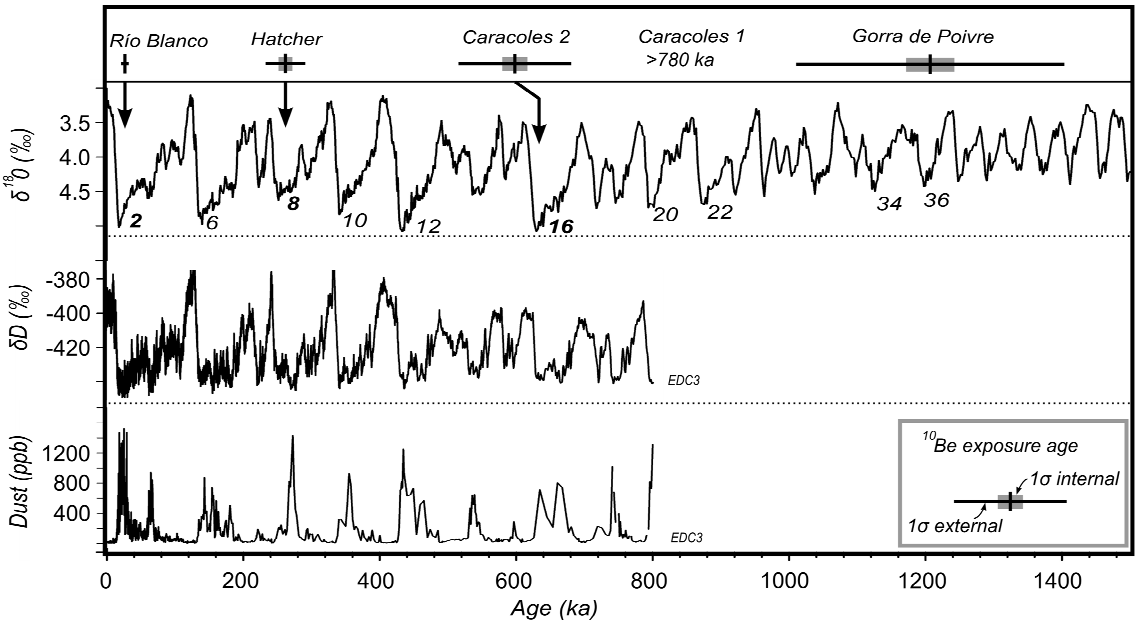

Figure 5.9. Glacier advances at Lago Pueyrredón against global records

A comparison of the ^{10}Be exposure dated ice limits in the Lago Pueyrredón valley (from this study and from Hein et al., 2009) against a marine benthic δ^{18}O stack (top plot; Lisiecki and Raymo, 2005) and the EPICA Dome C deuterium (middle plot; Jouzel et al., 2007) and dust (bottom plot; Lambert et al., 2008) records. The Caracoles 2 ice limit likely correlates with the nearest glacial stage, MIS 16; however, the external uncertainties associated with production rates and scaling factors for cosmogenic nuclides, at present, preclude resolving with confidence the individual glacial stages older than the middle Pleistocene.

the lowest ever found in an ice core during MIS 16 (Luthi et al., 2008). The significant southern South American sourced dust peak at 630 ka identified in the EPICA Dome C ice core (Delmonte et al., 2004; Lambert et al., 2008) (Fig. 5.9) suggests that Patagonian glaciers advanced at this time, providing the proposed link between glacier activity in Patagonia and dust peaks in Antarctic ice cores persists beyond the last glacial period (Sugden et al., 2009).

The available records indicate that MIS 16 was a severe glacial stage, globally and in the southern hemisphere. Therefore, deposits relating to an extensive Patagonian ice sheet might be expected at this time. Our surface exposure ages from the Caracoles

2 ice limit provide the first quantitative evidence of a significant advance of the Patagonian ice sheet during MIS 16.

Paleomagnetic data indicate that the outermost Caracoles 1 ice limit was deposited earlier, during the Matuyama reversed chron at more than 780 ka (Singer and Pringle, 1996; Sylwan et al., 1991). Thus, the Caracoles unit is probably composed of deposits from more than one glacial stage. The most significant glacial stages in terms of northern hemisphere ice volume occurring prior to ca. 780 ka are MIS 20 and MIS 22 at ca. 800 and 900 ka (Fig. 5.9). Possibly the outermost Caracoles moraines were deposited during one of these glacial stages.

The outermost and oldest Gorra de Poivre outwash terrace that marks the Greatest Patagonian Glaciation in the valley is dated at ca. 1.2 Ma based on the exposure ages presented in this study. The timing correlates with MIS 34 – 36. The Greatest Patagonian Glaciation occurred prior to the Mid-Pleistocene Transition (0.64 – 0.92 Ma) which marks the transition from the 41 ka (obliquity) to 100 ka (eccentricity) dominated glacial cycles (Mudelsee and Schulz, 1997). The advance occurred at a time when benthic marine $\delta^{18}O$ values were less extreme, indicating lower global ice volumes and a warmer global climate (Shackleton, 1987). The cause of the early maximum ice extent in Patagonia despite lower global ice volumes, and the pattern of decreasing maximum extents with each successive glacial stage, is not well understood; however several ideas have been postulated (Clapperton, 1990; Clapperton, 1993; Kaplan et al., 2009; Rabassa and Clapperton, 1990; Singer et al., 2004). Kaplan et al. (2009) infer a non-climatic cause through glacial modification

of the landscape, with the transition from fluvial V-shaped to glacial U-shaped valleys resulting in a more efficient glaciological system and successively less extensive glaciations. Jamieson (2008) describes this feedback process with a glaciological model that simulates the Patagonian landscape and climate. Thus, subsequent to the Greatest Patagonian Glaciation, glacial erosion may have contributed to less extensive glaciers through time.

5.5 Conclusions

We present cosmogenic ^{10}Be and ^{26}Al surface exposure ages from material associated with two of the oldest glacial deposits in the Lago Pueyrredón valley, 47.5º S, Argentina. The data allow the following firm conclusions:

- We directly date outwash surface sediment of the oldest glaciofluvial deposit in the Lago Pueyrredón valley by cosmogenic-nuclide surface exposure methods; the resulting ^{10}Be age of 1,211 ± 36 ka (± 200 ka 1σ external) for a sample on the Gorra de Poivre outwash terrace, agrees with independent ^{40}Ar/^{39}Ar constraints dated elsewhere that bracket the timing of the equivalent 'Greatest Patagonian Glaciation'. Why the maximum glacial advance in Patagonia occurred before the high amplitude Pleistocene cycle is unclear.
- This result suggests long-term stability of glacial outwash terraces in the region which makes them suitable for cosmogenic-nuclide surface exposure age dating over the relevant timescale. Thus, it may be possible to date the entire sequence of Quaternary glaciofluvial deposits in Argentine Patagonia.

- We obtain a ^{10}Be surface exposure age of 600 ± 20 ka (± 85 ka; 1σ external) from outwash sediment associated with an ice limit within the Caracoles moraine system. The exposure age indicates that a significant advance of a Patagonian ice sheet may have occurred during Marine Isotope Stage 16.
- Our geomorphic observations and exposure ages suggest that the Caracoles moraines are most likely composed of deposits from more than one glacial advance. The outermost limit is likely older than 780 ka based on magnetic polarity measurements (Sylwan et al., 1991).
- Following Hein et al.(2009), we find that outwash terrace cobbles yield on average, consistently older and more accurate surface exposure ages than associated moraine boulders. We infer that moraine degradation causes the observed scatter in boulder exposure ages on the Caracoles moraine system.

5.6 Acknowledgements

We thank C. Risso, P. Alvarez and O. Martínez for logistical support; A-S. Meriaux for fieldwork support; E. McDougall for assistance with laboratory work; and D. Sugden for helpful comments. For financial support we thank the UK Natural Environment Research Council (NERC) for A. Hein's studentship and sample analysis, the Royal Geographic Society (with IBG) - Rio Tinto plc award, the Royal Scottish Geographic Society, the Carnegie Trust for the Universities of Scotland and the Scottish Universities Environmental Research Centre (S.U.E.R.C.) for support of sample analysis.

Chapter 6 Synthesis and principal conclusions

This chapter summarizes the approach used to date old glacial sequences and synthesizes the resulting chronology. It is intended that parts of this chapter will be published in a paper detailing the long-term chronology.

6.1 Introduction

The chronology developed in this study provides one of the best constrained long-term records of former ice-extents in Patagonia and the southern hemisphere. Prior to this research, the glacial deposits in the Lago Pueyrredón valley, 47.5º S, Argentina, were only known to span the past ca. 1.1 Ma. There was debate over the basic chronology of the youngest moraines in this and nearby valleys (e.g., Kaplan et al., 2006; Wenzens, 2006a), and few chronometric constraints existed for the older deposits. As previously argued, the absence of age control, particularly for pre-Last Glacial Maximum (LGM) deposits, is common throughout Patagonia where a lack of suitable material precludes their dating.

Given the stability of glacial landforms in the region, I use cosmogenic-nuclide surface exposure methods to directly date the deposits in the Lago Pueyrredón valley. In doing so, I achieve the following research objectives:

- Determine if the youngest moraines in the Lago Pueyrredón valley (Río Blanco moraines) date to the LGM or, as argued by Wenzens (2005), to the Late-glacial to Holocene period. This has major implications for paleoclimates in central Patagonia (Chapter Three).
- Develop a more reliable approach to directly date pre-LGM glacial deposits in the Lago Pueyrredón valley by cosmogenic-nuclide surface exposure methods and test the approach by dating the penultimate (Hatcher) glacial deposits in the valley (Chapter Four).

- Evaluate how robust the approach is by directly dating the oldest glacial deposits in the valley; these are age-equivalent to the independently dated 'Greatest Patagonian Glaciation' at ca. 1.1 Ma (Chapter Five).

This chapter synthesizes the results and individual conclusions with respect to the glacial chronology developed and the cosmogenic nuclide methods utilized in this study. It further discusses the wider implications of the chronology and future research directions.

6.2 Exposure age dating utilizing cosmogenic nuclides

This work has employed a new approach to dating old (i.e., several 10^5 a) glacial deposits. It aims to minimize the impact of geologic processes that may affect cosmogenic nuclide accumulation in a surface sample; thus it has the potential to improve the accuracy of the surface exposure ages. Because of the implications it has for dating older features elsewhere, it is worth reviewing the overall characteristics of this methodology.

6.2.1 Approach

The scatter of moraine boulder ages on old moraines is commonly thought to reflect boulder exhumation as a consequence of moraine degradation and/or poorly constrained rock surface erosion rates (e.g., Benson et al., 2004; Briner et al., 2005; Hallet and Putkonen, 1994; Kaplan et al., 2007; Kaplan et al., 2005; Owen et al., 2006; Phillips et al., 1990; Putkonen and Swanson, 2003; Schäfer et al., 2008;

Shanahan and Zreda, 2000; Zreda et al., 1994). Both of these geologic processes become increasingly less well known and problematic on older surfaces. In this study, I demonstrate how these can be minimized by targeting outwash sediment instead (Fig. 6.1).

Ignoring potential complications, the basis for this approach is simple: (1) it relies on the fact that erosion on slopes is diffusive to a first order. Thus, diffusion of steep-sided unconsolidated landforms such as moraines will result in sediment moving down-slope causing these features to become increasingly blurred or subdued with time (Fig. 6.1)(e.g., Putkonen and Swanson, 2003), while diffusion of flat unconsolidated landforms such as outwash terraces will instead result in dispersal of surface sediment. Under diffusive-gravity driven erosion, planar surfaces are in a state of flux balance, and flat surfaces are in static equilibrium. If so, the sediment on outwash terraces are more likely to have remained continuously exposed relative to sediment on moraine crests, which are more likely to have been exhumed (Fig. 6.1b); (2) the outwash surface contains fluvial rounded sediment, their preservation indicates limited or negligible rock surface erosion since deposition (Fig. 6.2); and (3) outwash terraces can be linked to former moraine limits unambiguously. Other potential complications include post-depositional shielding by soil, loess, snow-cover and vegetation, and mixing of terrace sediment by biogenic or cryogenic processes (Fig. 6.1c). My results indicate that some of these processes are important, but the effects can be minimized by using detailed geologic observations and considered sampling strategies.

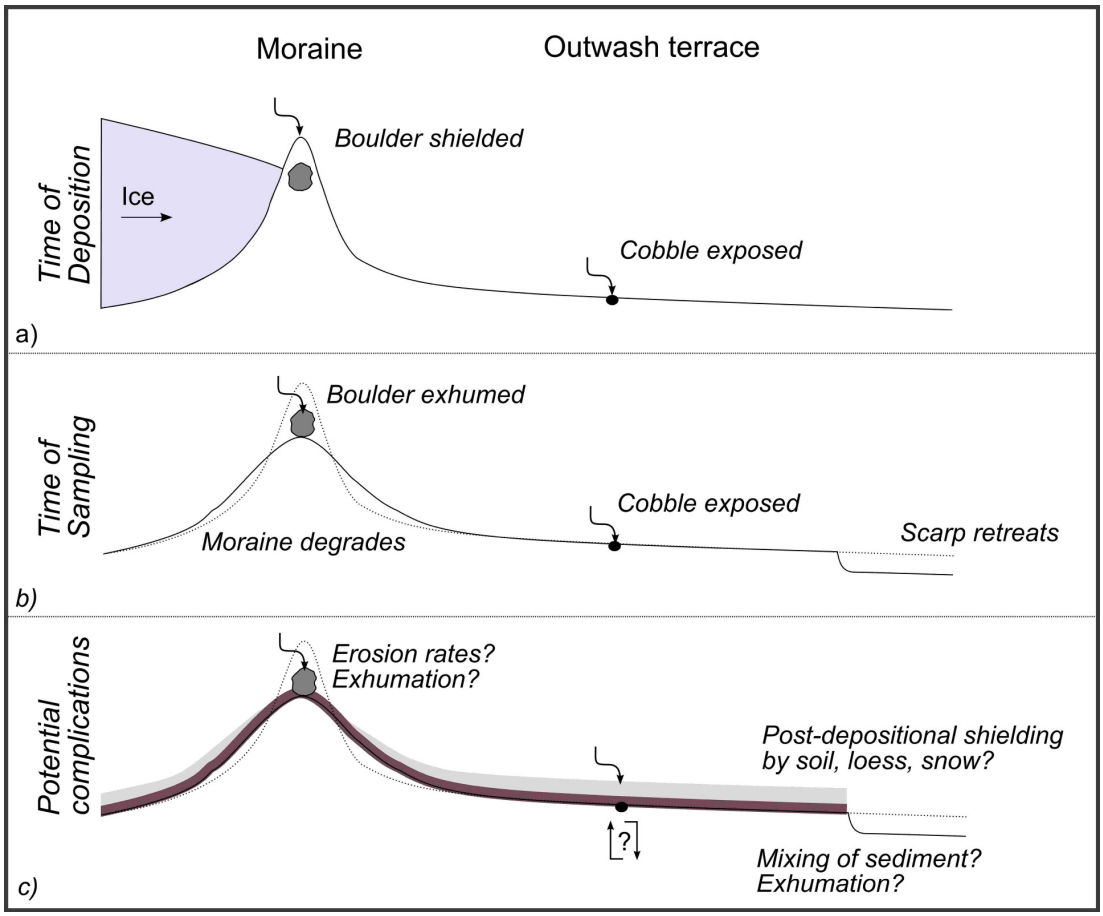

Figure 6.1. Cartoon of moraine and outwash diffusion

Cartoon showing the evolution of a moraine and outwash terrace between the (a) time of deposition and (b) time of sampling. The illustration suggests that moraine boulders are more susceptible to exhumation (cf. Putkonen and Swanson, 2003). The potential complications (c) for each surface are shown. The moraine boulders suffer mainly from exhumation and uncertainties with rock surface erosion; the outwash cobbles are more prone to post-depositional shielding by snow cover, soil, and mixing by bioturbation or cryoturbation processes. The geologic process lead to lower nuclide concentrations (Phillips et al., 1990). The arrows indicate the surface exposed to cosmic radiation.

6.2.2 Sampling strategies

The results of this study highlight the importance of an adaptive sampling strategy to obtain the best age estimate particularly for old glacial deposits. For deposits of LGM age, the traditional approach of using moraine boulders may be most



Figure 6.2. Ventifacts on fluvial cobble

Outwash cobble displaying fluvial form and clear aeolian erosion of its top surface. This indicates long-term exposure at the surface in the same position and allows estimation and correction for time-integrated erosion.

appropriate because erosion and exhumation of moraine boulders over this timescale are likely to be less severe.

6.2.2.1 Sample location

The stability of the outwash terraces varies considerably depending on the age and location of the surface. For example, a soil profile in the outermost Caracoles outwash terrace, which is protected from the dominant westerly winds by its location in the lee of the Meseta del Lago Buenos Aires (Fig. 6.3) shows ~50 centimeters soil inflation on top of imbricated outwash sediment (Fig. 6.4), and the surface is devoid of large pebbles and cobbles. Surface samples at this location are unlikely to provide

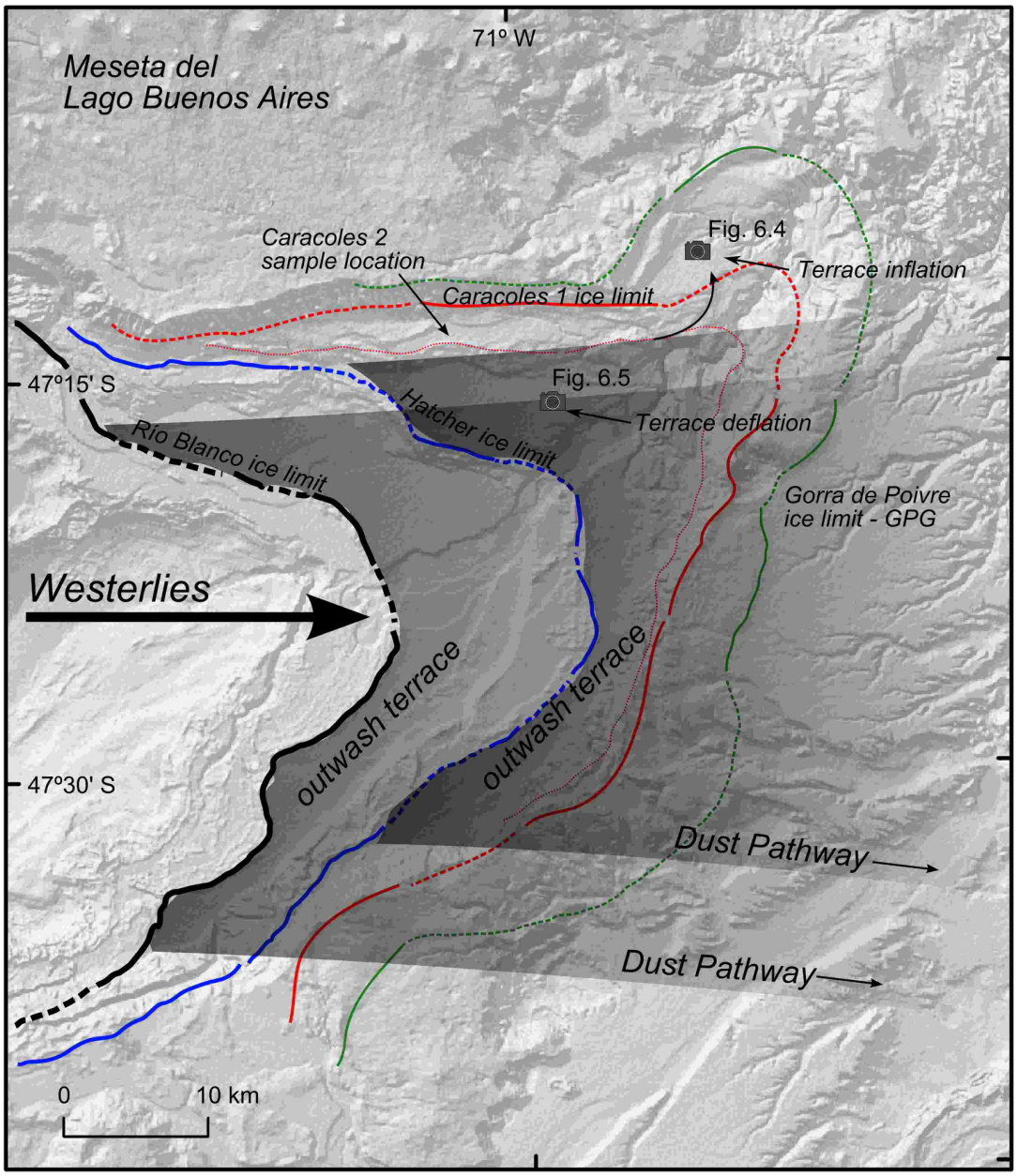

Figure 6.3. Dust pathway

Map showing the general pathway of dust from the Río Blanco and Hatcher outwash terraces based on the dominant westerly winds; this is the source of windblown dust responsible for aeolian erosion. The overlapping zones in the center of the valley are where aeolian erosion should be most severe, which is actually observed in the field. The samples from the Caracoles outwash terrace on the northern margin may have been relatively protected from subsequent aeolian erosion. The soil profile (Fig. 6.4) on the outer Caracoles outwash terrace is in the lee of the Meseta del Lago Buenos Aires, it shows clear evidence of soil inflation.

accurate exposure ages due to post-depositional shielding by soil. Meanwhile, the younger Caracoles and Hatcher outwash terrace surfaces dated in this study, which are fully exposed to the dominant westerly winds, support little or no soils and are devoid of features indicating inflation. In addition, the stability of these surfaces is further demonstrated by the presence of well-preserved braiding patterns that could only have formed during the original deposition of the surface, and by preserved imbricated terrace sediment as observed in soil profiles (Fig. 6.5). The geomorphic observations, lack of inflation and long-term stability, indicate that these surfaces are ideal for exposure age dating.

The potential for sediment mixing (bioturbation, cryoturbation) can be minimized by sampling at locations with little or weakly developed soil and a high density of larger clast sizes (large cobbles – small boulders). This situation often occurs close to the former ice limit where the depositional environment was of relatively high energy. At these locations, the sediment is often clast supported, which reduces the potential for sediment mixing. Further consideration should be given to the potential influx of older sediment; sources such as alluvial fans or drainage channels can be identified in the field and on satellite/aerial imagery, such sites must be avoided. Following the above criteria, the dating accuracy of old surfaces can be greatly improved.



Figure 6.4. Photo of soil inflation

Soil profile in the outer Caracoles outwash terrace (location shown on Fig. 6.3) showing soil inflation of top 50cm of profile. The soil is resting on imbricated outwash sediment which is indurated by pedogenic carbonate.



Figure 6.5. Photo of Hatcher soil profile

Soil profile in the Hatcher outwash terrace (location shown on Fig. 6.3) showing little inflation and soil formation.



Figure 6.6. Severe ventifacts on boulder

Severe ventifacts are often observed on moraine boulders and outwash cobbles. This boulder is located near Lago Argentina, 50˚ S.

The principal mechanism for rock surface erosion is by aeolian processes (i.e., sand-blasting; Fig. 6.6). My geologic observations indicate that aeolian erosion is episodic given the presence of rock varnish on ventifacts (Fig. 4.3b) and more intense towards the center of the valley. This occurs because active outwash terraces are the primary source of erosive windblown dust as shown more widely in Patagonia (Sugden et al., 2009), and these are most extensive in the center of the valley. In addition, wind speeds are generally higher in the center of wide valleys (e.g., Chock and Cochran, 2005). I find that outwash terraces on the northern margins of the valley are relatively protected from sand blasting erosion (lack of upwind sand sources), while still remaining exposed to the westerly winds. This is important because strong winds minimize the potential post-depositional burial of the surface by snow, soil,

loess, etc. Thus, it may be possible to reduce the impact of erosion by sampling from well-preserved surfaces on the margins of the valley (Fig. 6.3).

6.2.2.2 Sampling

If an ideal sample location is found, the most appropriate outwash surface sediment samples are large cobbles of resistant lithology (e.g., quartz, quartzite) that show evidence of long-term surface exposure, but not indicating rotation (e.g., desert varnish and/or ventifacts on the exposed surface, but not on the underside; Fig. 6.2). These can be cut at an appropriate thickness for analysis. Fig. 6.7 illustrates my sampling strategy and gives an approximate measure of confidence in a sample's representation of the original depositional surface, and thus my confidence in its exposure age to date the timing of the glacier advance.

The ideal surfaces are not often available but my results suggest that robust minimum ages can still be obtained from outwash sediment surfaces that are significantly older than the corresponding moraine boulder ages. At locations where surface instability is apparent, for example, where rotation of surface clasts is evident by ventifacts on all surfaces of the clast (e.g., Gorra de Poivre outwash terrace sediment; Chapter 5.2.2), targeted sampling can improve the exposure ages. In this situation, the smaller outwash surface sediment (diameter ~5-6cm) that are ventifacted on all surfaces provide the best results (e.g., Fig. 6.8). Their features indicate a long surface residence and they can be crushed and analyzed whole without having to assume an unknown orientation during the exposure history. Thereby uncertainties in the assessment of sample self-shielding can be largely avoided.

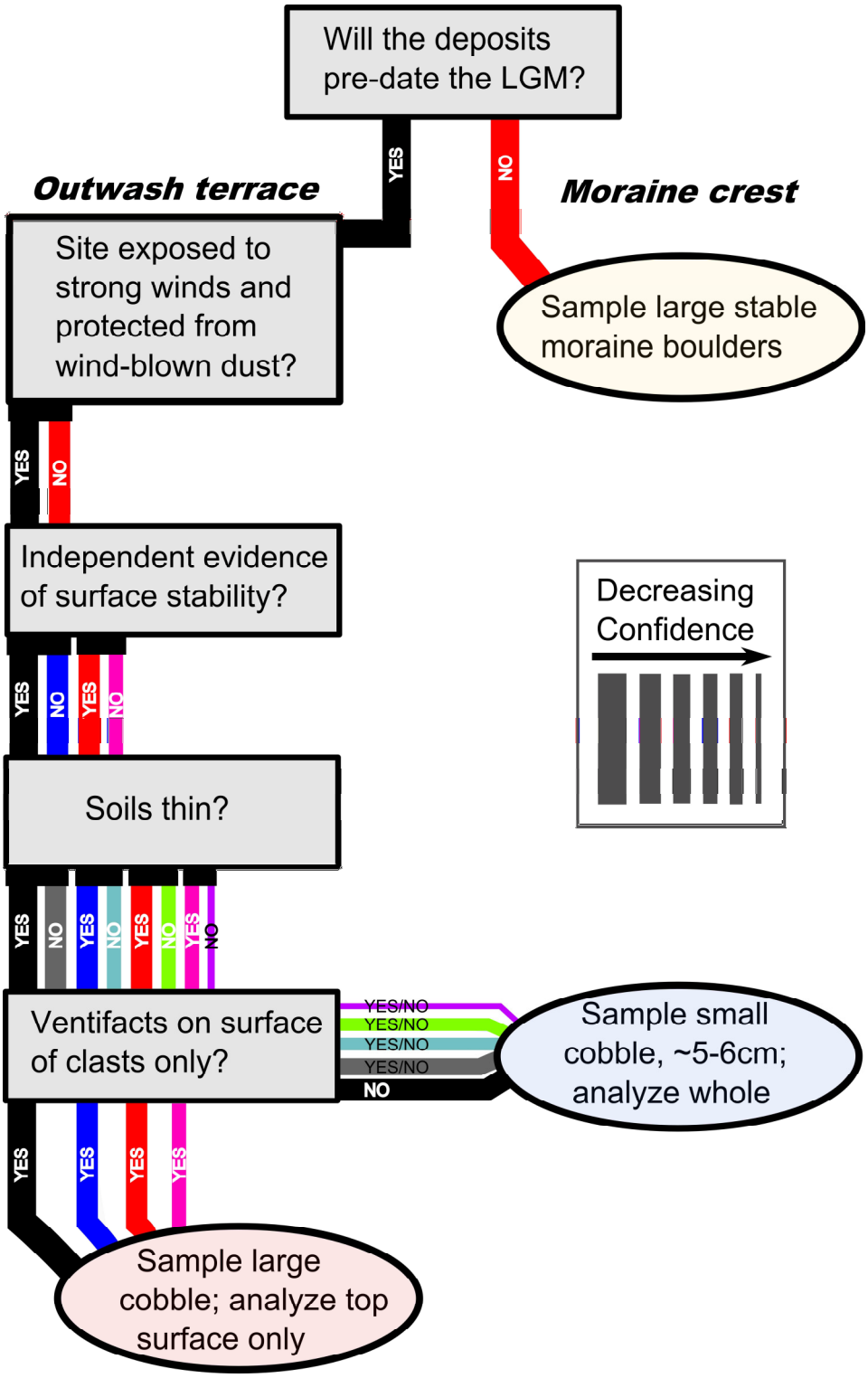

Figure 6.7. Sampling strategy and confidence

Flow chart illustrating my sampling strategy and my decreasing confidence in a sample as representative of the original surface based on a number of geomorphic observations. Thus it illustrates my decreasing confidence in its exposure age to date the timing of the glacial advance. This simplification is useful only as a general guide. In any case, depth profiles in the outwash terrace surface will significantly increase confidence as discussed in the text.



Figure 6.8. Ventifacts on surface cobble

Photo of a clast that is ventifacted on the top (left) and bottom (right) surfaces. A smaller clast like this can be crushed and analyzed whole. The presence of ventifacts on all sides is an indicator of vertical mixing but also of a long (continuous) surface exposure.

Generally, deep depth-profiles (> 1.5m) with several data points (> 6) add valuable constraints on the exposure age and erosion rate of the terrace surface, and inherited nuclide concentrations of the terrace sediment as well as allowing the assessment of vertical mixing of the sediment.

6.2.3 Summary

This work has demonstrated that old glacial deposits in central Argentine Patagonia can be more reliably dated by cosmogenic-nuclide surface exposure methods using outwash sediment rather than traditionally used moraine boulders. This is due to the long-term stability of outwash terrace surfaces in the region, and climatic conditions that favor continuous surface exposure of outwash sediment. I find that careful

sampling strategies that are adaptive to geomorphic and geologic field observations can greatly improve age estimates.

I have demonstrated in Chapter Four that moraine cobbles are useful for estimating moraine degradation rates, but not for dating moraine deposition. This is an important distinction to make. While the moraine cobble ages are often precise with less scatter, they are far from accurate, at least for the surfaces dated in this study. I suspect that this scenario is not unique. If moraine cobbles are sampled for exposure age dating (as they sometimes are when boulders are not available), I suggest a cautious approach to interpreting such data.

Summarizing, if cosmogenic nuclide inheritance is demonstrably low, the oldest outwash surface clasts provide good age estimates for the entire temporal range of the Patagonian glacial record. Where feasible, the surface cobble approach should be paired with depth-profiles to obtain additional constraints on terrace age, erosion rate and nuclide inheritance. I emphasize that this approach is not limited to Patagonia; it may prove useful in other semi-arid environments.

6.3 Glacial chronology

This study provides the first direct age-estimates for four distinct ice limits that span the entire temporal range of ice-contact landforms in the Lago Pueyrredón valley, central Patagonia; the results are summarized in Table 6.1 and Figures 6.9 and 6.10. These figures provide the reference frame for the remainder of this section. Data

discussed in Chapter Three resolves the LGM age of the Río Blanco moraines that were previously inferred to be Late-glacial to Holocene in age (Wenzens, 2005). I find the maximum ice extent occurred at ca. 27 – 25 ka, and subsequent readvances occurred at ca. 23 ka, ca. 19 ka, ca. 17.5 ka and with deglaciation following ca. 17.5. I find that both the maximum extent and the onset of deglaciation occurred broadly synchronously throughout Patagonia and with mountain glaciers globally (e.g., Denton et al., 1999a). Rapid deglaciation occurred at ca. 15 – 16 ka and was interrupted when glaciers stabilized during the Antarctic Cold Reversal. In Chapter Four I resolve the age of the penultimate glacial deposits in the Lago Pueyrredón valley which are represented by the Hatcher moraines and outwash terraces. I obtain an exposure age of ca. 260 ka for the Hatcher outwash terrace. This corresponds to Marine Isotope Stage (MIS or 'Stage') 8. In Chapter Five I resolve the likely age of the next oldest and most significant ice limit that is represented by the Caracoles 2 ice limit. This limit is situated within the Cañadón de Caracoles unit as originally mapped by Caldenius (1932). I obtain exposure ages of ca. 600 ka for the Caracoles 2 ice limit, which suggests it likely corresponds to MIS 16 as exposure ages provide minimum age-estimates. The Caracoles 1 ice limit is only known to be older than 780 ka based on reversely magnetized glacial sediment associated with this limit (Sylwan et al., 1991). Finally, I obtain age-estimates for the Gorra de Poivre outwash terrace, which is the oldest and most extensive glacial deposit in the valley. The deposit is the stratigraphic equivalent to the independently dated "Greatest Patagonian Glaciation" (Mercer, 1983) which marks the most extensive ice advance in Patagonia. My surface exposure age of ca. 1.2 Ma agrees within uncertainties with the independent $^{40}Ar/^{39}Ar$ constraint obtained from over- and underlying

basaltic lavas near Lago Buenos Aires (~47˚ S) and Río Gallegos (~52˚ S) at ca. 1.1 Ma (Singer et al., 2004).

Table 6.1. Summary of the glacial chronology at Lago Pueyrredón

	Moraine limit	Age (ka) ± 1σ (int)	± 1σ (ext)	MIS	Chronometer
Decreasing relative age	*Gorra de Poivre*	1210 ± 36	± 200	~32 – 40	cosmogenic ^{10}Be exposure age
	Cañadón de Caracoles 1	> 780		~22 - 32	paleomagnetic measurements*
	Cañadón de Caracoles 2	600 ± 20	± 85	~16	cosmogenic ^{10}Be exposure age
	Hatcher	261 ± 6.5	± 34	8	cosmogenic ^{10}Be exposure age
	Río Blanco	26.0 ± 1.0 to 17.4 ± 0.7	± 3.1 ± 2.2	2	cosmogenic ^{10}Be exposure age
	Columna	~16.0 – 18.0		2	cosmogenic ^{10}Be exposure age**

* by Sylwan et al. (1991)
**estimated based on minimum and maximum age-estimates (see Chapter 3).

The cosmogenic nuclide chronology is internally consistent and concurs with the stratigraphy; the outermost and oldest deposits give the oldest surface exposure ages, and subsequent less extensive and younger deposits give younger surface exposure ages. The chronology indicates that glacial sequences in the Lago Pueyrredón valley record more than one million years of terrestrial climate extremes in southern South America. The chronology may not be complete; careful mapping may reveal additional ice limits that are not resolved in this study. Based on the mapping and chronology presented, I highlight four key features of the chronology: (1) The oldest and most extensive glacial deposit in the valley precedes the global ice volume

maximum (< 800 ka) as observed in marine records; this early maximum advance has been identified elsewhere in Patagonia (e.g., Mercer, 1976; Singer et al., 2004); (2) there is an overall pattern of decreasing maximum ice extents

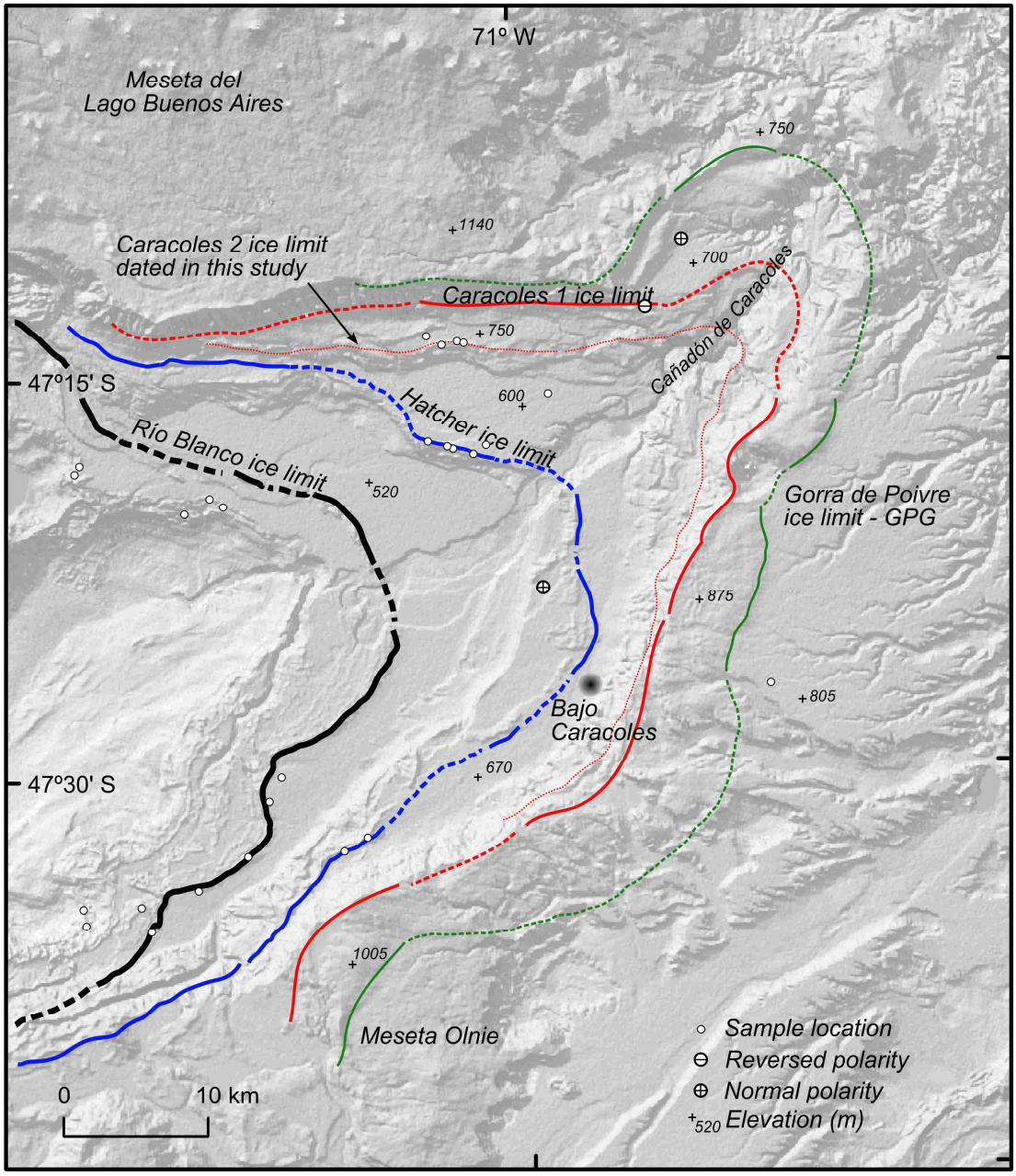

Figure 6.9. Ice limits in the Lago Pueyrredón valley

SRTM 90m DEM of the Lago Pueyrredón valley with the principal ice limits and sample locations marked. Magnetic polarity measurements are from Sylwan et al. (1991). GPG – Greatest Patagonian Glaciation.

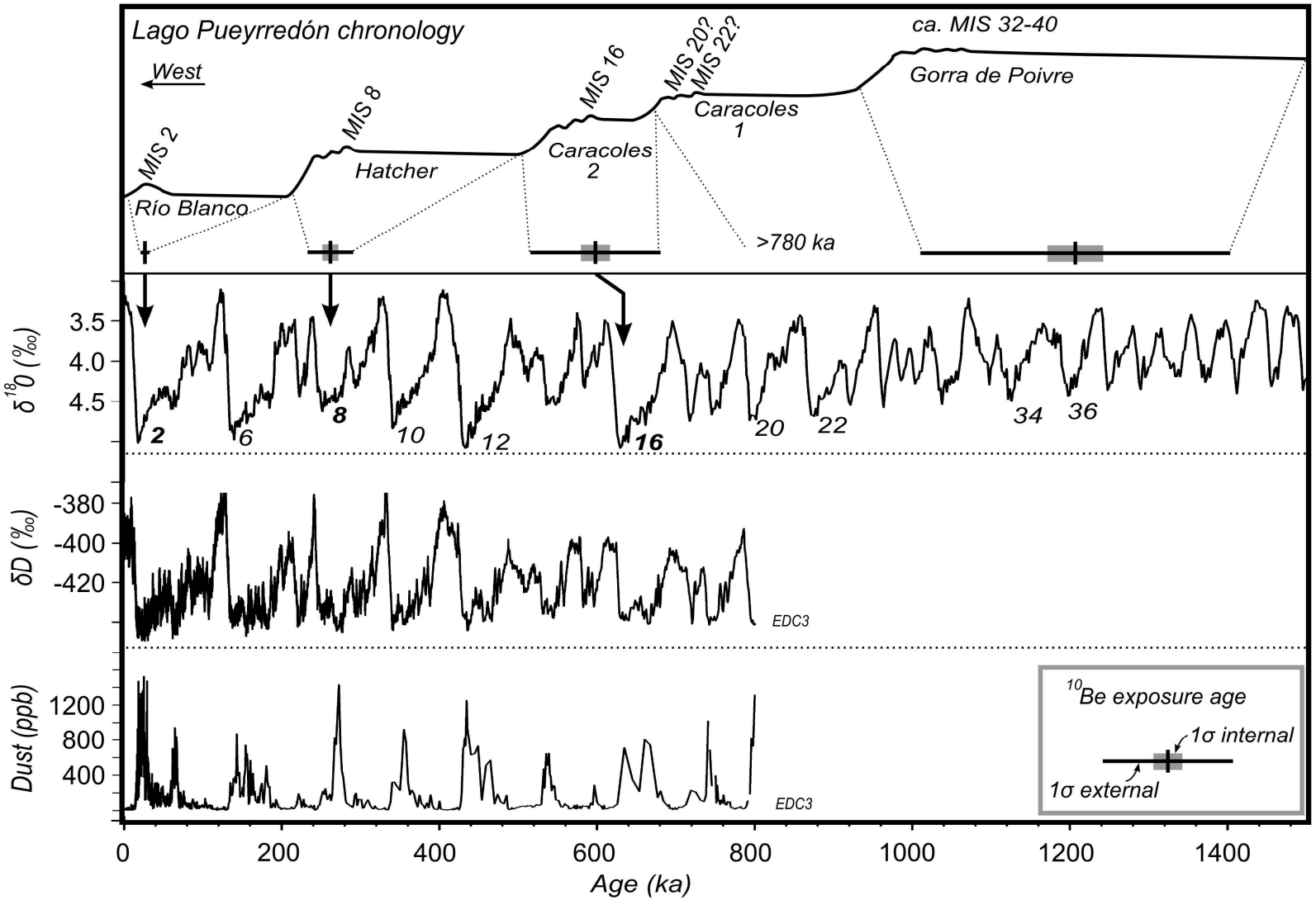

Figure 6.10. Lago Pueyrredón chronology vs. marine and ice core records

Figure 6.10. a) Cartoon of ice-limits in the Lago Pueyrredón valley (see Fig. 6.9) and interpreted age based on b) ^{10}Be exposure ages and my related glacial stage (arrow); c) The δ^{18}O marine record (Lisiecki and Raymo, 2005) is a proxy for global ice volumes (Shackleton and Opdyke, 1977) and selected Marine Isotope Stages (numbered). Bold numbers indicate the glacial stages identified in this study; d) The δD (Jouzel et al., 2007) and e) dust (Lambert et al., 2008) records from the EPICA Dome C ice core for the past 800 ka on the EDC3 timescale (Parrenin et al., 2007). The Caracoles 1 age constraint (> 780) is based on reversely magnetized sediments (Sylwan et al., 1991).

with each successive glaciation which bears no direct relationship to global ice volumes or Antarctic temperatures as observed in marine and ice core records, this pattern was recognized by Clapperton (1990) and Rabassa and Clapperton (1990); (3) the supposed MIS 16 advance of the Patagonian ice sheet is consistent with marine and ice core records that indicate this was a severe glacial stage; and (4) the preservation of glacial deposits dating to MIS 8 carries the implication that this glacial stage was bigger than Stages 6, 4 or 2. However, Stage 8 was not significant in terms of high northern hemisphere ice volumes or particularly low Antarctic temperatures.

6.3.1 Comparison to other Patagonian records

There are few particularly well-constrained ice limits in Patagonia that extend beyond MIS 2. The most extensive glacial deposits in Patagonia (i.e., marking the Greatest Patagonian Glaciation) are dated at ca. 1.1 Ma (Meglioli, 1992; Mercer, 1976; Singer et al., 2004; Ton-That et al., 1999). Throughout the rest of Patagonia, the dating of pre-MIS 2 ice limits is mainly restricted to broad limiting ages constrained by K-Ar or ^{40}Ar/^{39}Ar methods and by infinite radiocarbon ages (Coronato et al., 2004). The area with perhaps the best age control for Quaternary moraines is at Lago Buenos Aires, 46.5º S, Argentina. Here, at least six moraine

limits are known to be younger than 1,016 ka and older than 760 ka, and at least six moraine limits are known to be younger than 760 ka and older than 109 ka, based on $^{40}Ar/^{39}Ar$ ages of associated lava flows (Singer et al., 2004). The penultimate glacial limit at Lago Buenos Aires is constrained by a minimum $^{40}Ar/^{39}Ar$ age of 109 ka (Singer et al., 2004) and by cosmogenic ^{10}Be and ^{26}Al surface exposure ages on moraine boulders that give ages of ca. 140 – 150 ka, and thus indicate a MIS 6 glacial advance (Kaplan et al., 2005). The result is supported by $^{230}Th/U$ ages of soil carbonate formed in associated outwash gravels and ^{10}Be concentrations in moraine cobbles (see discussion Chapter 4.5.3).

There remains a possibility that part of the penultimate moraine system at Lago Buenos Aires (e.g., Moreno 2 and 3) may instead correlate to MIS 8, as is the case in the Lago Pueyrredón valley located immediately to the south. Based on my findings at Lago Pueyrredón, it may be possible that moraine boulder exposure ages underestimate the age of the deposit. In the case of Moreno 3, Kaplan et al. (2005) have already considered this a possibility given the older exposure ages obtained on this surface. This is important to resolve because it has implications for paleoclimate reconstructions and/or landscape evolution. For example, the preservation of Stage 6 in one valley and Stage 8 in a nearby valley could be completely random (Gibbons et al., 1984), or may reflect some difference in climate or geologic conditions. If they are both Stage 8 deposits, this may suggest either a climate driven effect that led to a more extensive Stage 8 advance at these latitudes, despite Stage 6 being the more significant glacial stage in terms of global ice volumes (Shackleton, 1987), or that significant erosion restricted the extent of subsequent advances. Re-dating the

deposits following an approach based on the outwash surface sediment would help to confirm the age assignment.

Across Patagonia, several other glacial deposits are known to pre-date the last glacial cycle based on limiting age constraints (Coronato et al., 2004). Many of the penultimate (i.e., Gotiglacial of Caldenius, 1932) deposits have been assigned to MIS 6 based on good minimum age constraints and geomorphic associations (Rabassa, 2008). However, it is possible that they could relate to earlier cold periods or be of composite origin (Clapperton, 1993; Rabassa, 2008).

In northern Patagonia, radiocarbon ages and pollen analysis led Denton et al. (1999b) to infer that the outermost Llanquihue advance in the Chilean Lake District may correspond to Stage 4. A Stage 4 advance is also inferred in the Strait of Magellan (Glacial Stage A) based on radiocarbon and amino acid racemization ages (Clapperton et al., 1995), and because dust peaks in Antarctic ice cores at this time have Strontium and Neodymium isotopic ratios that match glacial sediments in southernmost Patagonia, the inferred source (Sugden et al., 2009). In central Patagonia, no Stage 4 deposits are identified at Lago Buenos Aires (Kaplan et al., 2005) or Lago Pueyrredón; this suggests that the Stage 4 advance at these latitudes was probably less extensive than Stage 2.

Overall, the pattern of an early maximum ice-extent followed by generally decreasing ice-extents with each successive glaciation is observed throughout Patagonia and is not unique to the Lago Pueyrredón valley (Clapperton, 1990;

Clapperton, 1993; Coronato et al., 2004; Kaplan et al., 2009; Mercer, 1983; Singer et al., 2004).

6.3.2 Comparison to global glacier records

Glacial deposits associated with the LGM are found in most formerly glaciated regions of the world. Where chronologic constraints exist for older glacial deposits in other mountainous regions of the world, these often date to MIS 6. This suggests that in many areas, the Stage 6 advance was larger than Stages 4 or 2. Glacial deposits of this age are found, for example, in the Wind Rivers (Chadwick et al., 1997; Phillips et al., 1997), the Tetons (Licciardi and Pierce, 2008), and the Alaska Range (Begét and Keskinen, 2003) of North America; in the Mediterranean mountains (e.g., see Hughes et al., 2006); in the Himalayas of India (e.g., Owen et al., 2006), the Tianshan mountains of China (e.g., Zhao et al., 2009); and in the New Zealand Alps (e.g., Newnham et al., 2007).

Glacier deposits relating to MIS 8 have been identified at various locations globally, but only a few ice limits have remained preserved and have been dated to this stage, for example, in east Africa (Shanahan and Zreda, 2000). This probably reflects the removal of these deposits by larger glacier advances during Stages 6, 4 or 2. Thus, in general, the Stage 8 glacier advances in other mountainous regions of the world appear to have been smaller than Stages 6 or 2. In this context, my dating of the Hatcher moraines at Lago Pueyrredón to Stage 8, with the implication that this advance was larger than Stage 6, is uncharacteristic in terms of global glaciers. It

suggests some regional differences in climate may have persisted at this time in central Patagonia.

In other mountainous regions of the world, the most commonly dated ice limits that are older than MIS 6 (and thus more extensive) are dated to MIS 12 and MIS 16. Advances of this age have been dated, for example, in the Tianshan Mountains of China (e.g., Zhao et al., 2009) and the central Rocky Mountains (Chadwick et al., 1997; Hall and Jaworowski, 1999) of North America. In general, the most extensive deposits of the great northern hemisphere ice sheets are also thought to have been deposited at this time (Ehlers and Gibbard, 2003 and references therein). Thus, in terms of global glacier advances, Stage 12 and Stage 16 are often of the most extensive. In this context, my dating of a Caracoles ice limit to Stage 16 is consistent with extensive glacier advances globally at this time.

While the most extensive mountain glacier and ice sheet deposits are largely associated with Stage 12 and Stage 16, it is interesting to note that the most extensive advance of at least part of the Laurentide ice sheet in the central United States, may have been as early as 1.5 Ma at a time when ice is inferred to have diverted drainage of the Ohio river along an ice sheet margin (Granger et al., 2001). Subsequent advances are also inferred by river incision events at ca. 1.2 Ma, and aggradation events at 0.7-0.8 Ma at Mammoth Cave, Kentucky (Granger et al., 2001). These data support recent cosmogenic ^{10}Be and ^{26}Al burial dating of paleosols in tills in Missouri that indicate glacial advances at 1.25 Ma and 0.8 Ma (Balco and Rovey, 2008). The cause of this early maximum advance of the Laurentide ice sheet, despite

low global ice volumes as recorded in the marine isotope records (Shackleton et al., 1984; Shackleton and Opdyke, 1977), is unknown. It is, however, an interesting analogue to the Greatest Patagonian Glaciation at ca. 1.1 Ma.

6.3.3 Comparison to marine and ice-core records

The marine oxygen isotopic records are usually interpreted to reflect changes in global ice volume which primarily reflect the expansion and contraction of the great northern hemisphere ice sheets (Shackleton et al., 1984; Shackleton and Opdyke, 1977). These records indicate that maximum global ice volumes occurred over the past ca. 800 ka when the 100 ka (eccentricity) climate cycles prevailed. Prior to the Mid-Pleistocene Transition at ca. 900 ka, the 41 ka (obliquity) climate cycle dominated the marine record. The higher frequency climate cycles occur at lower amplitudes, indicating less severe ice ages in terms of global ice volume and temperature (Shackleton and Hall, 1989). The Greatest Patagonian Glaciation occurred during this time of high frequency, low amplitude climate changes and before maximum global ice volumes. Thus, there is no obvious causal link evident in the marine record that can explain the large expansion in Patagonia glaciers at ca. 1.1 Ma.

Shackleton (1987) identifies the glacial extremes of MIS 12 and MIS 16 in particular, followed by MIS 6 and MIS 2, as being the most significant in terms of global ice volume (MIS 12 and MIS 16 were ~15% greater than MIS 2) when compared to other glacial stages during the Brunhes Chron. The consequence of greater ice volumes is generally thought to be greater areal coverage of continental

ice sheets (i.e., a greater ice-extent) during these stages. Where chronometric ages are available, the most extensive deposits often date to Stage 12 or Stage 16 (e.g., section 6.3.2) and thus provide support for this idea. The marine records are complemented by ice core records that extend back to 800 ka at Dome C in Antarctica (EPICA community members, 2004). The ice cores record atmospheric parameters such as the concentration of greenhouse gases, temperature and aeolian dust concentrations. The deuterium record (proxy for ice surface temperature) from the EPICA Dome C ice core indicates that the amplitude of temperature changes was highest over the past four (100 ka) glacial cycles, and lowest during earlier glacial cycles when a higher proportion of each cycle was spent in the warm mode (Jouzel et al., 2007). Despite this lower amplitude, MIS 16 was one of the colder glacial stages at Dome C, which also corresponds to the lowest atmospheric CO_2 values ever found in an ice core (Luthi et al., 2008). Thus, Antarctic temperatures were near their lowest when global ice volumes were at or near their highest during Stage 16, this indicates that MIS 16 was probably a severe glacial stage. In this context, extensive Patagonian glaciers, such as those represented by the Caracoles 2 ice limit at Lago Pueyrredón, should be expected at this time.

The penultimate ice limit in the Lago Pueyrredón valley corresponds to MIS 8; this advance was more extensive than Stages 6 and 2, and possibly more extensive than Stages 14, 12 and 10 given that these deposits have not been found. This is surprising given that Stage 12 was also a severe glacial stage in terms of the marine and ice core records. It is possible that the deposits exist as part of the Caracoles unit, but simply have not yet been identified as such. The marine records indicate that Stage 8 was a

minor glacial stage in terms of global ice volumes, particularly compared against the relatively large glacial stages of MIS 6 and MIS 2 (Shackleton, 1987). Additionally, the temperature at Vostok (Petit et al., 1999) and Dome C (Jouzel et al., 2007) in Antarctica, and the sea-surface temperatures in the Atlantic sub-Antarctic zone (Becquey and Gersonde, 2003), were both warmer during Stage 8 than during these subsequent stages. However there is a peak in sea salt (ssNa) flux in the Dome C ice core during Stage 8, which may indicate extensive Antarctic sea-ice at this time (Wolff et al., 2006). In sum, there is no clear link with the ice core or marine records of global climate change that can at present easily explain the relatively large advance of the Lago Pueyrredón outlet glacier at this time.

6.3.4 Potential non-climatic influences on ice extent

The pattern of an early maximum ice extent followed by decreasing maximum ice extents with each subsequent glaciation is at odds with records of global ice volume and Southern Ocean and Antarctic temperatures. Thus, a non-climatic mechanism may be required to explain the pattern (Clapperton, 1990; Clapperton, 1993; Kaplan et al., 2009; Rabassa and Clapperton, 1990; Singer et al., 2004). Clapperton (1990) suggests two potential non-climatic causes: (1) tectonic subsidence reduced the ice accumulation area over time; or (2) progressive deepening of major valleys meant that successively larger volumes of ice were required to sustain glaciers of similar areal extent. Clapperton (1993) further suggests that (3) higher precipitation, velocities, ice flux and calving margins could have caused faster rates of erosion on the west side of the Andes compared to the drier east side. This may have caused preferential over-deepening of western fjords and increased efficiency of westward

drainage that may have led to less extensive eastern outlets through time as increasingly more ice discharged to the west.

Subsequent hypotheses build upon these principal ideas. For example, while there is little evidence to suggest tectonic subsidence occurred over the past 1 Ma, there is evidence for tectonic uplift (e.g., Ramos, 2005; Thomson, 2002). Singer et al. (2004) hypothesize that uplift of the Andes, caused by subduction of the Chile Rise spreading centre beneath the Lago Buenos Aires region (ca. 46.5º S; Ramos, 2005), may have culminated during the Quaternary period by 1.2 Ma; this allowed Patagonian glaciers, which are thought to be highly sensitive to changes of ELA (Hulton and Sugden, 1997), to expand to their greatest areal extent; the Greatest Patagonian Glaciation. Subsequently, glacial erosion progressively reduced the area of the ice accumulation zone, causing a corresponding increase in the ablation zone, and therefore shorter outlet glaciers during successive advances. Kaplan et al. (2009) further suggest that glacial modification of the landscape, specifically the development from non-glacial V- to glacial U-shape valleys, together with lowering of mass-accumulation areas, would strongly affect glacial dynamics, the mass balance profile and mass-flux during subsequent glaciations, especially for low-gradient outlet glaciers occupying low areas. Thus, they argue these factors may help to explain the pattern observed in Patagonia. Kaplan et al. (2009) also suggest that increasing westward drainage may not be an appropriate explanation because the trend is also observed on the western side of the Andes north of ca. 42º S where ice margins were land-based (Caldenius, 1932; Clapperton, 1993).

Non-climatic explanations for the pattern of decreasing maximum ice extent all invoke glacial erosion of the landscape to some extent. Glaciological models have demonstrated the importance of glacial erosion on development of longitudinal profiles in alpine landscapes (e.g., MacGregor et al., 2000; Oerlemans, 1984) and the effect on ice margin extent (e.g., Jamieson, 2008). MacGregor et al. (2000) suggest this 'self-defeating' mechanism may explain why older glacial deposits are often located down-valley of LGM deposits, despite the strength of the LGM in terms of the marine oxygen isotope record. Jamieson (2008) demonstrates this effect with a 3-D glaciological model coupled with a subglacial erosion model. Using an alpine topography and climate analogous to Patagonia, he finds that glacial erosion alone causes a reduction in ice-extent through time.

Thus, at Lago Pueyrredón, the preserved glacial deposits likely reflect both influences of climate and glacial modification of the landscape. The Caracoles 2 moraines were deposited during Stage 16, ~600 ka after the outermost Gorra de Poivre moraines at 1.2 Ma. There are 8 – 10 glacial stages evident in the marine records during the intervening period (Fig. 6.10); thus, glacial erosion had likely already significantly modified the landscape by this time. Therefore, despite being one of the most severe glacial stages, the Stage 16 deposits are not the most extensive in the valley. The Stage 8 advance was more extensive than advances associated with Stage 6, 4 and 2. Glacial erosion would favor this pattern of preservation; however, climate records do not.

6.4 Southern hemisphere westerlies

The southern hemisphere mid-latitude westerlies dominate the climate system in Patagonia. The extremely cold polar (Antarctic) and warm subtropical regions cause a steep pole-to-equator thermal gradient which is primarily responsible for the intensity of the southern westerlies and the associated Antarctic Circumpolar Current (Markgraf et al., 1992). Seasonally, the southern westerlies vary between 40º S and 50º S in winter and summer, respectively, over South America (Markgraf et al., 1992). This variation is controlled primarily by the Antarctic low pressure belt and sea-ice extent in the south, and the strength and position of the Southeast Pacific anticyclone in the north (Markgraf, 1989a; Pittock, 1978). Summer and winter storm-tracks are equally intense in the southern hemisphere, but in the winter the activity extends over a broader range of latitudes (Trenberth, 1991). These storm-tracks embedded in the southern westerlies provide the precipitation that feeds Patagonian glaciers. The fluctuation of Patagonian glaciers therefore reflects changes in temperature and precipitation, the latter of which is primarily governed by the southern westerlies. Well-dated glacial deposits are one proxy that can be used to infer the relative strength and position of the southern westerlies during glacial periods.

The behavior of the southern westerlies during the LGM is not well-understood with respect to their strength and latitudinal position, and is the focus of much research and debate (e.g., Heusser, 1989; Markgraf, 1989b). For example, many paleoclimate proxies have been interpreted to suggest an equatorward shift of the southern westerlies and the associated Antarctic Circumpolar Current by ca. 5º - 10º during

the LGM (Heusser, 1989), while others suggest a poleward shift (Markgraf, 1989b; Markgraf et al., 1992). Here, I limit a brief discussion to the empirical evidence in and around South America; for a detailed review of the evidence obtained from numerous paleoclimate proxies in the southern mid-latitudes, see Shulmeister et al. (2004). The two viewpoints are highlighted and I discuss some implications of recent findings.

Based on a synthesis of paleovegetation records, Markgraf et al. (1992) argue that the southern westerlies intensified during the LGM and became focused between 43º S and 50º S with less seasonal variations. The evidence to support this comes from several key sources. First, Magellanic Moorland vegetation, which can only exist under cool and extremely stormy conditions, expanded into lowland areas between 43º and 45º S (Villagran, 1988). Villagran (1988) interpret this to reflect the location of the core of the winter westerlies during the LGM. South of 50º S, the paleovegetation records indicate substantially drier conditions, although none of these records extend as far back as the LGM. North of 42º S, the occurrence of some Andean vegetation at lower elevations than today is interpreted to indicate an increase in effective moisture caused by ~4º C lower temperatures or increased precipitation (Markgraf, 1989b). Markgraf et al. (1989b) argue the increased precipitation could not be attributed to the southern westerlies because the presence of steppe taxa in the Chilean Lake District (ca. 42º S) further south indicates seasonal moisture stress. Instead, they suggest an increase in subtropical moisture that may relate to winter rain anomalies similar to the modern El Niño/Southern Oscillation events, or to a poleward shift of the subtropical high pressure ridge. Markgraf et al.

(1992) argue that the paleovegetation records are best explained by a poleward and equatorward migration of the northern and southern margins of the westerlies, respectively, and intensification of the westerlies between 43º and 50º S.

This interpretation is challenged by Heusser (1989) who argues, based on a range of paleoclimate proxies, that the westerlies and the oceanic polar front shifted northwards by ~5º latitude. This interpretation has been reiterated to explain increases in precipitation evident in paleoecological records north of 41º S at this time (e.g., Heusser et al., 1999; Moreno and Leon, 2003; Moreno et al., 1999). It also explains the expansion of glaciers at a more northerly location than would otherwise be possible (Clapperton, 1993; Denton et al., 1999b). A recent study of chironomids and the identification of Magellanic Moorland vegetation at 41º S both support cold and stormy conditions during the LGM (Massaferro et al., 2009; Moreno et al., 1999). Marine records off the coast of Chile at the same latitude (41º S) also support a northward migration of the westerlies based on the depletion of iron in terrigenous sediments which is used to infer an increase in coastal precipitation (in catchments with low Fe) during the LGM (Lamy et al., 2001; Lamy et al., 2004). Additionally, sea-surface temperatures indicate a clear "Antarctic" timing of sea-surface temperature changes that appear linked to an equatorward shift of the Antarctic Circumpolar Current and the southern westerlies by 4º – 5º (Kaiser et al., 2005; Lamy et al., 2004). Further north (33º S), increases in paleoproductivity are linked to a northward shift of the Antarctic Circumpolar Current which is thought to have brought nutrient rich waters to the area (Mohtadi and Hebbeln, 2004). In sum,

most terrestrial and marine records are interpreted to indicate a northward migration of the westerlies, or at least their northern margin, during the LGM.

In the Strait of Magellan of southernmost Patagonia (ca. 53º S), Sugden et al. (2009) find that the isotopic composition of dust in Antarctic ice cores matches that of glacial aged dust in the Magellan region. They argue that dust found in Antarctic ice cores during the last glacial period was blown from active glacial outwash plains in the Magellan region. Strong winds (4 – 8 m s^{-1}) are necessary to lift dust into the atmosphere (Bagnold, 1941). Given that outwash plain activity is highly seasonal and peak discharges of suspended sediment occur in the summer months as the bed of the glacier is flushed out (Swift et al., 2005), strong westerly winds must have blown across southernmost Patagonia during the summer months. This suggests that the summer storm-tracks during the LGM must have been located to the south. Meanwhile, the expansion of Patagonian glaciers at low latitudes and the paleovegetation and marine records indicate increased westerly precipitation to the north at the same time.

What appears to be required is greater seasonality during the LGM. For example, the summer westerlies may have shifted south towards the Magellan region (ca. 53º) where dry conditions, as indicated by paleovegetation records (Markgraf, 1989a; McCulloch and Davies, 2001), were enhanced by the growth of an ice sheet upwind, and the strong westerly winds blew dust from active outwash plains and on to Antarctica. During the winters, the westerly storm-tracks must have broadened and intensified and shifted further north as indicated by glacier, paleoecological and

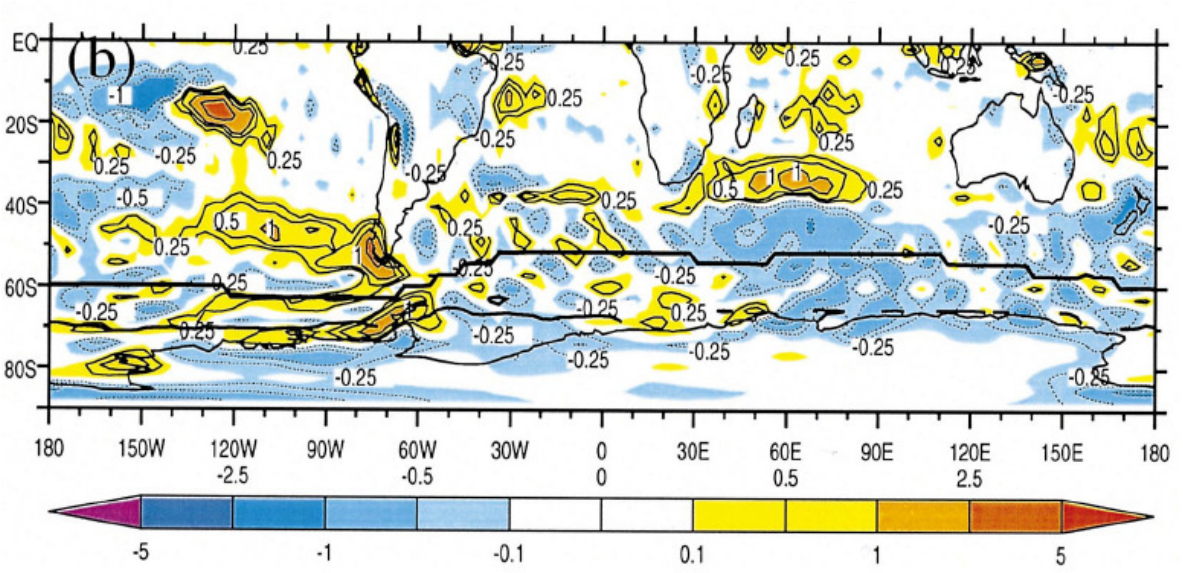

Figure 6.11. Difference in summer precipitation

The difference in summer precipitation (mm d^{-1}) between the LGM and present day conditions based on a global circulation model. The figure shows an intensification of the summer westerlies, particularly in southernmost Patagonia. The black lines indicate sea-ice extent at the LGM and present day [Figure 13 (Wyrwoll et al., 2000)].

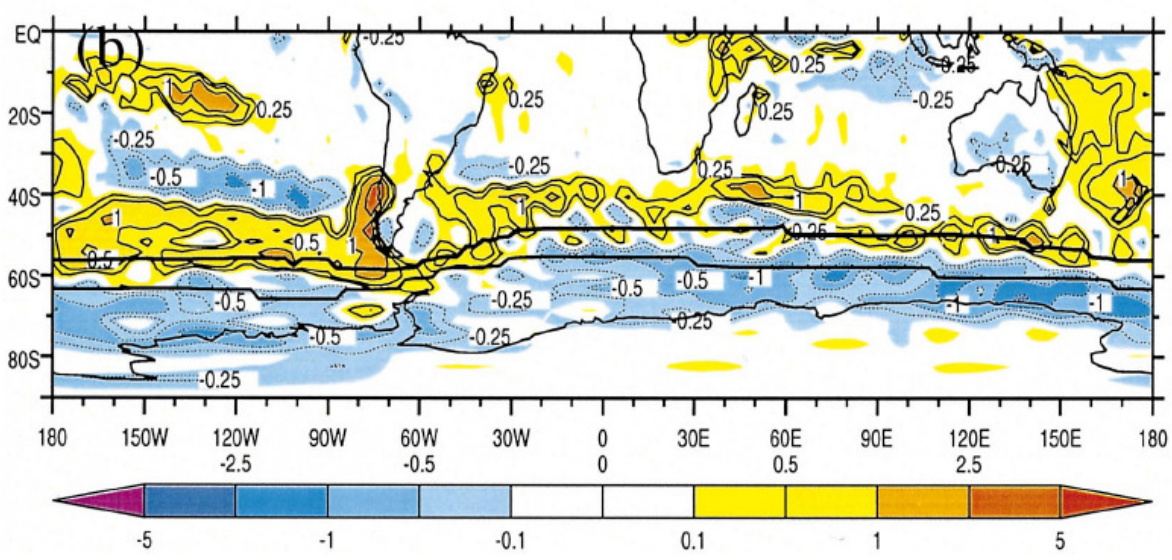

Figure 6.12. Difference in winter precipitation

The difference in winter precipitation (mm d^{-1}) between the LGM and present day conditions based on a global circulation model. The figure shows an intensification of the winter westerlies, particularly in NW Patagonia. The black lines indicate sea-ice extent at the LGM and present day [Figure 12 (Wyrwoll et al., 2000)].

marine records; this is broadly similar to the modern day configuration. This speculation is supported in part by some global circulation models. Wyrwoll et al. (2000) show that during the LGM, the southern westerlies shifted somewhat poleward, with summer storm-tracks increasing precipitation over southernmost Patagonia (Fig. 6.11), and the winter storm-tracks both intensified and widened their latitudinal range (Fig. 6.12).

Improving the chronology of Patagonian glacial deposits is central to understanding southern hemisphere climates and global climate changes. The chronology developed in this study provides some of the first terrestrial indicators of the strength and position of the southern westerlies that extends beyond the last glacial cycle. At Lago Pueyrredón, 47.5º S, the penultimate glacial advance is dated to MIS 8. In comparison to Stages 2 or 6, this was a relatively minor glacial stage (Fig. 6.13). The natural conclusion is that the southern westerlies were positioned differently at this time than during later glacial stages, and were likely centered near 47º S. This reorganization could reflect a different latitudinal shift in the westerlies that occurs during less extreme glacial periods, or perhaps a relative narrowing in the latitudinal range traversed by winter storm-tracks associated with the southern westerlies at this time. It is interesting to note the peak in sea salt flux (ssNa) in the Dome C ice core during Stage 8 (Fig. 6.13). High peaks in sea salt flux are interpreted to indicate increased winter Antarctic sea-ice extent (Wolff et al., 2006). Thus, sea-ice extent may have been greater during Stage 8, which would strongly affect the pole-to-equator thermal gradient, and the strength and position of the southern westerlies. However, somewhat warmer sea-surface temperatures are also indicated in the South

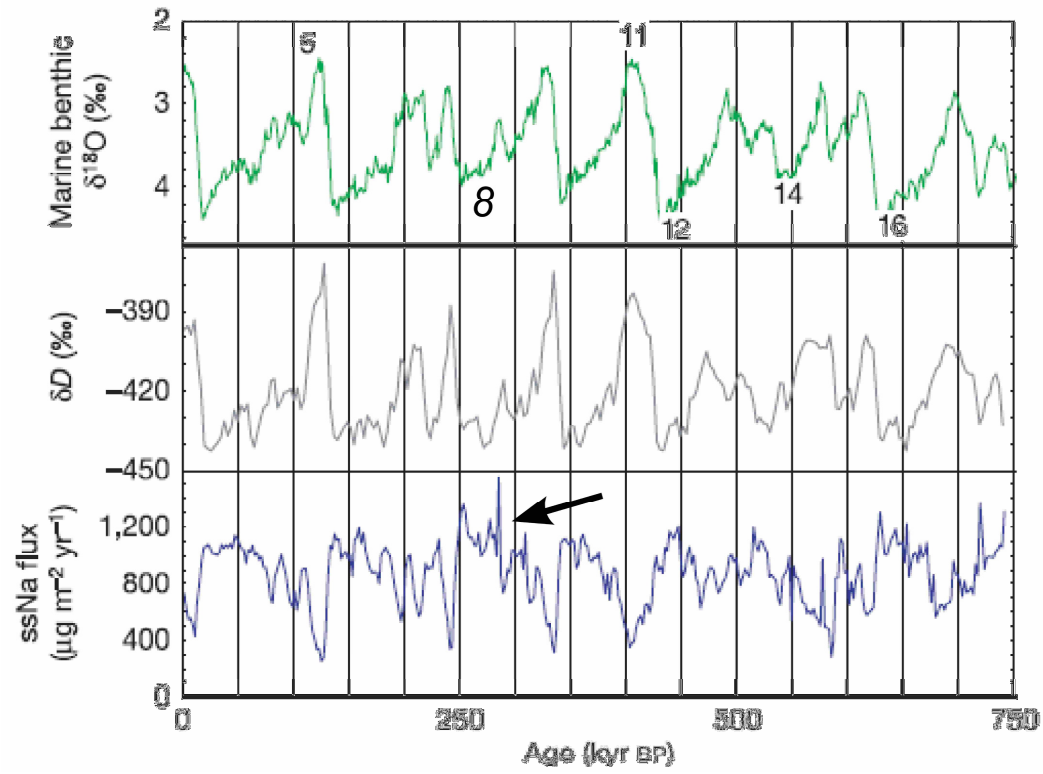

Figure 6.13. Comparison of deuterium, sea-salt and benthic $\delta^{18}O$

Figure showing the a) marine oxygen isotope record (Lisiecki and Raymo, 2005), b) Antarctic deuterium and c) sea salt flux from EPICA dome C (Wolff et al., 2006). The high ssNa flux is interpreted to indicate increased Antarctic sea-ice extent, there is a peak during MIS 8 (Figure modified after Wolff et al., 2006).

Atlantic at this time which appears inconsistent with these data (Becquey and Gersonde, 2003).

6.5 Dust in Antarctica

Antarctic ice cores indicate that windblown dust concentrations increased by more than 25 fold during the last glacial period (Lambert et al., 2008; Petit et al., 1990). The source of windblown dust has been isotopically fingerprinted to southern South America (Basile et al., 1997; Delmonte et al., 2004; Gaiero, 2007; Gaiero et al.,

2004; Grousset et al., 1992; Sugden et al., 2009). The peaks have been associated with, for example, increased aridity and wind speeds in source areas during glacial periods and exposure of the South American continental shelf due to sea level lowering (Petit et al., 1990). Recently, Sugden et al. (2009) identify a link between glacier activity in southernmost Patagonia and dust deposited in Antarctica during the last glacial period. Specifically, they find that glacial age dust in the Magellan region (ca. 53º S) of Patagonia is isotopically identical (Sr and Nd) to that found in the Dome C ice core. By comparing dust peaks to an independently dated sequence of glacial moraines, they find that peaks occur when glaciers were extensive and discharged sediment directly onto outwash plains, but not when they were less extensive and terminated in lakes. They infer that the active outwash plains of southernmost South America were a primary source of windblown dust that is found in Antarctic ice cores. Therefore, the glaciers act as an on/off switch for Antarctic dust deposition. The hypothesis explains why the decline in Antarctic dust concentrations occurs prior to the main phase of warming, sea-level rise and reduction in southern hemisphere sea-ice extent (Wolff et al., 2006).

If so, the Antarctic dust record could be considered a proxy for glacier fluctuations in southernmost Patagonia, at least over the last glacial cycle. By making the assumption that this relationship persists over multiple glacial cycles, the 800 ka record of Antarctic dust fluxes at Dome C could be considered a proxy for Patagonian glacier fluctuations. My dating of outwash terraces, while incomplete, indicates that Patagonian glaciers advanced during these older glacial stages.

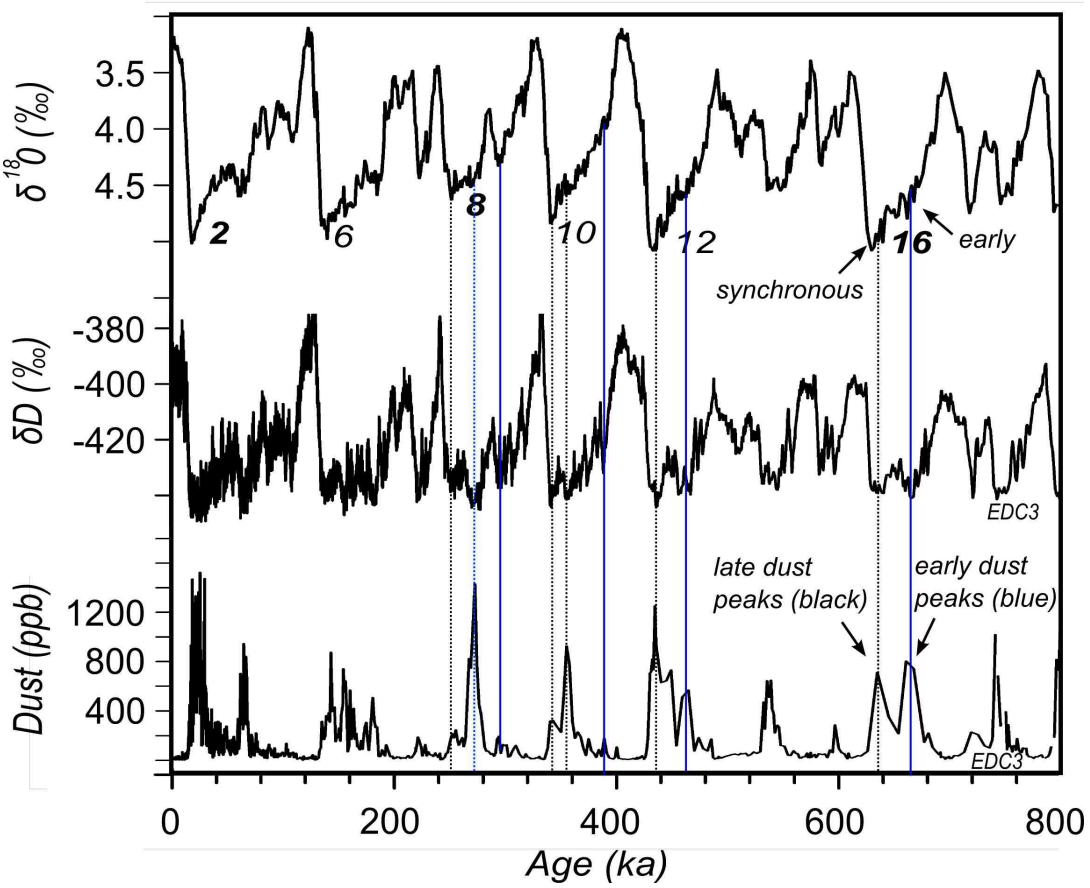

Figure 6.14. The timing of Antarctic dust peaks

The figure shows that early dust peaks in Antarctica mirror Antarctic temperature depressions, but there is no clear correlation with the 'global' ice volume record. I infer that as temperatures drop in Antarctica, so do southern hemisphere temperatures (e.g., Becquey and Gersonde, 2003; Lamy et al., 2004), this causes a widespread and rapid advance of Patagonian glaciers responding to westerly precipitation (cf. Hulton and Sugden, 1997); these deliver sediment to active outwash plains from which it is blown to Antarctica (cf. Sugden et al., 2009). This occurs prior to and synchronous to the maximum global ice volume. The $\delta^{18}O$ marine record (Lisiecki and Raymo, 2005) is inferred as a proxy for global ice volumes (Shackleton and Opdyke, 1977) and selected marine isotope stages are numbered. The bold indicates the glacial stages preserved at Lago Pueyrredón. The δD (Jouzel et al., 2007) and dust (Lambert et al., 2008) records from the EPICA Dome C ice core for the past 800 ka on the EDC3 timescale (Parrenin et al., 2007).

Considering the Antarctic dust record as a proxy for Patagonian glacier expansion helps to explain some peculiarities of the Antarctic dust record.

For example, there are distinct dust peaks at the onset of each glacial stage that mirror Antarctic temperature depressions, but precede the global ice volume maximum as recorded in marine sediments (Fig. 6.14). Several dust peaks also occur near to the global ice maximum and then rapidly diminish. The pattern occurs to varying degrees during each glacial cycle. This pattern can be explained by glacier activity in Patagonia. As Antarctica cools, so do temperatures in the southern mid-latitudes (Becquey and Gersonde, 2003; Kaiser et al., 2005; Lamy et al., 2004); the Patagonian glaciers, which are sensitive to changes in ELA (Hulton and Sugden, 1997), rapidly advance in response to increased snowfall from the westerlies. Thus, the initial dust peak coincides with expansion of the highly sensitive Patagonian ice sheet, which occurs prior to the maximum global ice volume of the (primarily) great northern hemisphere ice sheets (Shackleton and Opdyke, 1977). The subsequent dust peaks may reflect the waxing and waning of outlet glaciers (Sugden et al., 2009) or changes in wind direction or intensity.

If so, as the long-term glacial chronology across Argentine Patagonia improves, the isotopic composition of dust from sediment associated with each glacial stage could be assessed to determine potential source areas and thereby atmospheric circulation routes. The isotopic composition of Antarctic dust is similar during Stages 2, 4 and 6, but is somewhat less radiogenic during earlier glacial cycles (Delmonte et al., 2004). This could reflect the mixing of different source areas caused by changes in atmospheric circulation patterns during glacial periods, or complete removal (i.e., through erosion) of a particular source lithology (Delmonte et al., 2004). Analyzing the geochemical properties of glacial outwash sediment will help to refine our

knowledge of long-term atmospheric circulation in the southern hemisphere and the strength and position of the southern westerlies and this remains an avenue for future research.

6.6 Overall conclusions

This thesis has investigated the chronology of glacial deposits from a major outlet lobe of former Patagonian ice sheets in central Argentine Patagonia. In doing so, it has not only provided considerable detail about the timing of Quaternary glacial events in this valley, but it gives insight into the wider pattern of glaciation in the region and its relationship to global events. The principal conclusions are summarized below:

- This thesis has established a near complete glacial chronology for a single outlet lobe of the Patagonian ice sheet based on methodological advances in cosmogenic-nuclide surface exposure age dating.
- Cosmogenic ^{10}Be and ^{26}Al surface exposure ages and previous magnetic polarity measurements (Sylwan et al., 1991) provide ages or constraints on the timing of at least five major glacial sequences preserved in the landform record at Lago Pueyrredón. The names and ages are summarized in Table 6.1; in increasing stratigraphic age they correlate with Marine Isotope Stages 2, 8, ~16, > 20 and ~32 – 40.
- The preservation of the particular glacial sequences identified in this study, at present, bears no obvious relationship with the magnitude of global cooling

as evident in marine and ice core records. Thus, changes in local climate and landscape evolution must play a role in regulating the glacier's extent.

- I find that for younger (i.e., last glacial) moraines, well-constrained surface exposure ages can be derived from the common-practice of dating large boulders on the moraine surface.
- In contrast, for older (i.e., pre-LGM) sequences in the area, I demonstrate that the glacial outwash surface sediment, if carefully chosen, can provide more consistently accurate results than associated moraine boulders.

6.7 Further considerations and future research

This thesis is a first step in resolving the long-term glacial chronology across much of Argentine Patagonia. While having just scratched the surface, my direct dating of glacial deposits improves dating accuracy, and our understanding of long-term Patagonian climate and landscape change. We can begin to analyze some of these processes in greater detail than has previously been possible. As the long-term glacial chronology improves, we will be better placed to answer a range of important questions regarding, for example: (1) long-term climate in southern South America and its relation to global climate changes and ice age theories; (2) the evolution of the Patagonian landscape; (3) long-term changes in the atmospheric circulation routes of the southern hemisphere as recorded by the changing isotopic composition (i.e., changing of source areas) of Patagonian dust found in Antarctic ice cores; and (4) the contribution of Patagonian glaciers to sea-level changes. The development of

new glacial chronologies will provide crucial empirical constraints for coupled glaciological and global circulation models.

Thesis development

The following briefly summarizes the development of my project from the initial ideas to the work that ultimately led to this thesis. The purpose is to provide context to the project as a whole, and to detail some of the decisions I made that ultimately led to my work in the Lago Pueyrredón valley. Finally, it details some of my challenges and experiences in the field, the laboratory and at home during this time.

The project was first suggested to me by Mike Kaplan just after I completed the ice sheet modelling work associated with my MSc in GIS. Mike and Nick Hulton put the project together following on from their study of Quaternary moraines in Tierra del Fuego. I started my project in September 2005 at the same time that Mike Kaplan left Edinburgh and Tibor Dunai arrived. As a result, Tibor became my second supervisor.

The project itself was vague to begin with, we knew we wanted to try to date old moraine sequences in Patagonia, but we did not know exactly where or how. As such, I spent my first months looking at potential field sites in satellite imagery, making maps to take into the field, and generating funds to back the field programme.

The first field season, with Tibor and Anne-Sophie Meriaux, began in El Calafate, Argentina, just east of the South Patagonian Icefield. The programme for the first field season was to sample moraine cobbles and outwash terrace cobbles from each

moraine sequence at each of ~five field sites. The idea was to analyse a few samples from each site in order to determine an area to focus my attention on for the remainder of the project. We started east of Lago Argentino (50º S), then visited Lago Pueyrredón (47.5º S), Lago Buenos Aires (46.5º S), Esquel (43º S), Bariloche (42º S) and Mendoza (32º S). In the end we travelled over 12,000 kilometers across the length and breadth of Argentine Patagonia and had a truck dangerously overloaded with stones. Thankfully, Dr. Oscar Martínez from the *Universidad Nacional de la Patagonia* in Esquel was willing to store the stones and arrange shipment to the UK.

Back in Edinburgh, Steve Binnie taught me the beryllium chemistry. The process begins with a rock and ends with a beryllium oxide scum that is scraped off the inside walls of a quartz crucible to be pressed into a copper cathode target. The whole process is long and rather tedious (see Appendix A). It is nearly enough to bring you to tears when you lose a sample after all this work, which happened to me as I pressed one of my first targets…oops! However, it is satisfying to finally get results. The initial pilot samples were moraine cobbles. These were chosen because desert pavements are well-developed on moraine crests, and we though they may have armoured the surface after their initial formation. The first exposure ages were consistent but young. Interestingly, I got ages of about 50 – 60 thousand years at Lago Pueyrredón, equivalent in age to Marine Isotope Stage 4.

Going into the second field season, I was concerned about the moraine cobble ages. I just didn't believe the Stage 4 ages because the moraines of equivalent relative age

in the neighboring Lago Buenos Aires (LBA) valley were dated at ~150 ka based on moraine boulder exposure ages (Kaplan et al., 2005). I began to worry about the potential outcome of my project. I decided to integrate a back-up plan just in case my attempts to date the old outwash terraces failed (at this point I still had no data from the terraces). I knew that the moraine boulder approach worked reasonably well for the penultimate moraines at LBA. Therefore, for the second field season I decided to focus my work on the Lago Pueyrredón deposits because the environment is similar to LBA. I decided to sample the LGM moraines and the penultimate 'Stage 4' moraines using the moraine boulder approach. This way I knew I would have a solid chronology for my thesis, even if it was only for the LGM and penultimate glaciation. I returned with Nick Hulton and we set about sampling boulders and mapping the deposits throughout the valley.

The Lago Pueyrredón valley is remote with just a few 'estancias' (farms) and two small, windswept settlements. The valley is huge; just getting to moraines on the opposite side of the valley is an all-day affair, and finding farm tracks to access moraines was a challenge in itself. When Nick left, the boulder sampling increased in difficulty. The strong winds blew each chip I broke-off about 10 – 20 meters; this meant without taking my eye off the chip, I had to set my tools down, get off the boulder and walk ~20 meters to find the chip of rock. At one point, I simply could not work because physically I could hardly stand in one place let alone try to chip away at a boulder. It was then that I decided to return to a small quarry I had noticed dug into the outwash terrace the day before. I had already sampled the terrace surface during the first field season, but I saw an opportunity here to obtain a depth

profile. I spoke to Tibor on the satellite phone to get sampling advice. I then spent five hours in the wind and cold, plucking pebbles from the profile and becoming borderline hypothermic in the process; I wrote in my field notebook: "I hope its worth it!". Thankfully, it was (see Chapter Four). The remainder of the field trip was plagued by flat tyres (eight in total) which ultimately left me benighted in my truck, hitchhiking, and hanging out at more "Gomeria's" (tyre shops) than I care to remember.

Following the second field season, I started once again processing samples and generating funds to measure my samples. Nick and I applied for a NERC-CIAF beam-time only grant for AMS analyses. The application was successful and we secured funding for 50 AMS analyses. From this point forward I focused on measuring both the outwash terrace surface samples and the moraine boulders. The new data clarified the chronology and at this point the project really started to come together. This was fortunate for me because my home life at the time was in complete chaos following the arrival of my son Francis on 22nd May, 2007 and the subsequent renovation of our flat. I began writing finally in May 2008 and slowly but surely finished the remaining chapters of the thesis. The writing was interrupted by fieldwork in Peru, a short field visit to Lago Pueyrredón in concert with unrelated fieldwork in Chile, and several conferences at which I gave both oral and poster presentations.

The following summarizes an approximate timeline of the project.

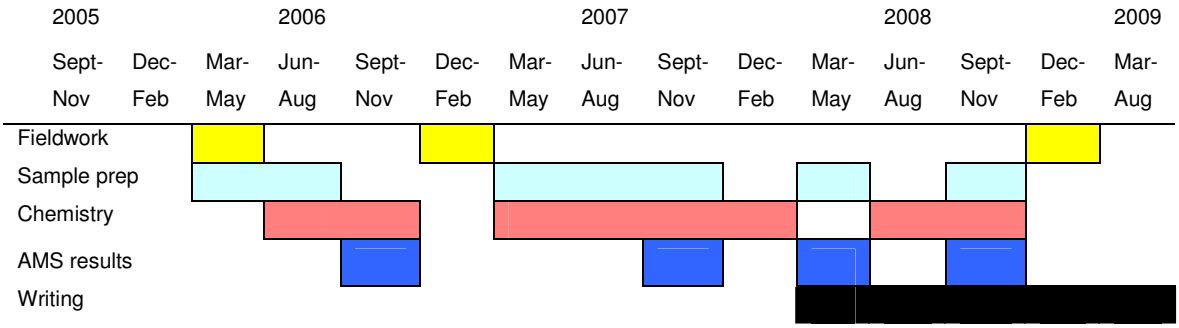

Appendix A Isotope extraction and measurement

A.1 Target preparation

This section describes the procedure used at the University of Edinburgh's Cosmogenic Isotope Laboratory to extract ^{10}Be and ^{26}Al from rocks. The procedure is similar to the methods employed at most other laboratories. This section summarizes the protocols developed by Binnie (2005) which in turn is an adaptation of the protocols of Kohl and Nishiizumi (1992), Bierman et al. (2002), Ivy-Ochs (1996) and with contributions from C. Fogwill, W. Phillips, H. Cockburn, and other lab users prior to 2005 (Binnie, 2005). This section is presented for completeness, and because it reflects some minor changes to the protocols mainly by S. Binnie and T. Dunai between 2006 and 2009 when the samples in this study were analyzed.

A.1.1 Quartz extraction

A.1.1.1 Physical separation

The first stage is the isolation of pure quartz from rock samples. To avoid large corrections for self-shielding, rock samples are, where necessary, trimmed with a diamond blade saw to a thickness of less than ~5 cm. A rock splitter is then used to reduce the sample to fragments of less than about 3 – 4 cm. The sample is then passed through a large jaw crusher and then is further reduced with a Fritsch P13 laboratory disk mill which can be tuned such that grains of approximately the desired size are discharged. The sample is then sieved dry to obtain the desired size fraction

of 250 – 710 μm. For most granite in the Lago Pueyrredón valley (~25% quartz), about 200 g of the 250 – 710 μm size fraction was sufficient to obtain approximately 30 – 40 g of pure quartz.

A.1.1.2 Junk etch

The next stage involves a series of 'junk etches' aimed at reducing non-quartz minerals. Up to 200 g of sample are placed in a 1 l bottle and are then rinsed several times with tap water to remove fine sediment and organic material. The bottle is then filled with 100 ml HCl (36% laboratory reagent grade) and 200 ml H_2SiF_6 (31% technical grade) and is placed on a shaker table (~170 rpm) for three to seven days. The HCl removes carbonates and helps to clean Al and Fe coatings from grains (Kohl and Nishiizumi, 1992) and the H_2SiF_6 helps to selectively dissolve non-quartz minerals (Bourlès, 1988); the result is a sample that is relatively enriched in quartz. The acid is drained and the sample rinsed in tap water. The processes is repeated until the acids no longer produce a significant reaction (i.e., when the acid solution remains clear). Most samples in this study required only one junk etch, however, some required up to five. The rinsed samples are dried in an oven at 60º C and bagged.

A.1.1.3 Quartz etch

The next stage is aimed at chemical isolation of quartz and removal of atmospheric (meteoric) ^{10}Be that may be adsorbed on the surface of the mineral grains (Kohl and Nishiizumi, 1992). Most silicate minerals dissolve relatively easily in HF compared to quartz; these can be removed by repeated etching in a dilute (2%) HF and (1%)

HNO_3 solution; this also etches the outer surface of the quartz grains and thereby removes atmospheric ^{10}Be. Up to 35 g of sample are placed in a 2.5 l bottle that is filled with ~ 2 l of 15 mΩ water, 50 ml of HF (40% GPR grade) and 30 ml HNO_3 (70% analytical reagent grade). The sample is then placed in a heated ultrasonic bath for up to 24 hours. This is repeated at least three times. 48% analytical reagent grade HF and 18.2 mΩ water are used for the 'final etch'. Following etching, the sample is rinsed in copious amounts of ultrapure water, dried in an oven and bagged. If mafic minerals survived the etching process, they are removed with a strong hand magnet, a Frantz magnetic separator, or they are physically removed. In any case, a further final etch is then performed. An approximate 30% reduction of initial quartz mass is normally sufficient to produce clean quartz separates with less than ~ 200 ppm Al.

A.1.2 Isotope extraction

The remaining procedures are aimed at extracting ^{10}Be and ^{26}Al from the quartz grains and purifying the BeO and Al_2O_3 targets ready for AMS analysis. The chemicals used in the following procedures are as follows: HF: 48% analytical reagent grade; HNO_3: 70% analytical reagent grade; HCl: 36% trace analysis grade; $HClO_4$: 70% analytical reagent grade; and NH_4OH: 35% trace analysis grade. All water used in the following procedures is ultrapure: 18.2mΩ.

A.1.2.1 Aluminium test strips

Prior to dissolution the purity of the quartz is checked by estimating the Al content of the sample. The quartz is considered sufficiently clean when the Al content is lower

than about 250 ppm. If the concentration is higher then further quartz etching is necessary. A semi quantitative determination can be obtained using a simple Al test strip (Merck Al^{3+} Aluminium Test is used). Approximately 1 g of sample (*m*) is added to an acid cleaned Savillex jar (the same jar is used throughout the following procedures) followed by ~20 ml of HF and 1 ml of HNO_3. The sample is placed on a hotplate at ~170º C until dissolved. The sample is taken up in 5 ml of 2% HNO3 and the acid addition is weighed (*L*). The Al test is performed on the solution following the instructions provided. This involves raising the pH of the solution to 13 by dropwise addition of the supplied reagent, the strip is then dipped in the solution for 1 second, the excess is shaken of, and 1 drop of a second supplied reagent is added to the strip. After 1 minute the color of the strip can be compared to a reference chart giving an estimate of the Al content (*A*). The total ppm in the sample (C_{Al}) can then be calculated as follows:

$$C_{Al}(ppm) = \frac{A * L}{m}$$

The remaining sample is discarded and the Savillex jar is thoroughly rinsed with ultrapure water and dried in the oven ready for dissolution.

A.1.2.2 Quartz dissolution

This procedure involves dissolving the sample and adding ^{9}Be and (in some cases) ^{27}Al carrier to the sample. The carrier is added because AMS measures isotope concentrations by measuring the ratio between two isotopes. Because ^{9}Be rarely occurs in quartz samples (Bierman et al., 2002), a known amount of ^{9}Be is added to

the sample as carrier to set the $^{10}Be/^{9}Be$ ratio. For the Lago Pueyrredón samples, about 250 μg of a standard solution was used for samples and blanks (see Table A.1). ^{27}Al is common in quartz samples so ^{27}Al carrier was added only to process blanks and to samples with low native ^{27}Al content as determined in Section A.1.2.1. Based on the estimated native ^{27}Al content of each sample, sufficient ^{27}Al carrier (Table A.1) was added to yield approximately 1.5 mg of ^{27}Al. One process blank is included with each batch of seven samples in order to estimate the amount of ^{10}Be and ^{26}Al atoms that are added during the post-etching stages of the sample preparation.

Table A.1. ^{9}Be and ^{27}Al carriers used

Carrier	Date of use	Lot #	Concentration (mg/l)	+/- (mg/l)	Density (g/ml)	Background ratio
Spectrosol Be carrier	before 17/4/07	70222943	1000	5.00	1.02	$\sim10^{-15}$
Scharlau Be carrier	18/4/07-28/05/08	78589	1000	5.00	1.02	$\sim10^{-15}$
Scharlau Be carrier	29/-5/08 - present	81145	1000	5.00	1.02	$\sim10^{-15}$
Fischer Al carrier	2006 – 4/09	90376613	1000 ppm	5.00	na	$\sim10^{-15}$
Fischer Al carrier	4/09 – present	0736322	1000 ppm	5.00	na	$\sim10^{-15}$

The samples are weighed as they are added to 180 ml Savillex jars. Ultrapure water is washed down the inside walls of the jars to weigh down quartz grains that tend to climb the walls due to static electricity. The samples are transferred to a fume cupboard and ^{9}Be and (where necessary) ^{27}Al carrier is added and the weights are recorded. The sample is then dissolved in concentrated HF and HNO_3 with an approximate sample mass to HF ratio of about 1:4; however complete dissolution of some samples requires ratios approaching 1:8. 100 ml of HF is added to the process blank. The hotplate is set to about 170º C and the samples are left to dissolve, this

can take between two and seven days to completely dissolve, with additional HF added when necessary. The samples are then evaporated to dryness.

A.1.2.3 Perchloric fuming

The residues are fumed in $HClO_4$ to convert insoluble fluorides to soluble perchlorates (Yokoyama et al., 1999). This helps to liberate aluminum from fluoride and to reduce boron levels (Binnie, 2005). Four 1 ml additions of $HClO_4$ are fumed on a hotplate at 190º C to 200º C, with each fume lasting approximately two hours until dry. The walls of the jar are then rinsed with ultrapure water and this is evaporated to dryness.

A.1.2.4 Aluminium aliquot

An aliquot of the dissolved sample is taken at this stage to measure the stable ^{27}Al content by ICP-OES. This is required for calculating the ^{26}Al concentration of the sample. The sample is taken into solution with 5 ml of HNO3, to which 35 ml of ultrapure water is added and the solution weighed (V_1). 1 ml of this solution is added to a 10 ml vial and the weight is recorded (V_2). The sample is returned to the hotplate to dry down. 9 ml of 2% HNO_3 is added to the vial and the total weight is recorded (V_3). The solution is then measured and the abundance of aluminum in the sample (X) is then calculated as follows (Binnie, 2005):

$$X(mg) = \frac{\left(C_1 V_3 / V_2\right) V_1}{1000}$$

where C_1 is the concentration of aluminum in the aliquot measured by ICP-OES (ppm), and V_1, V_2 and V_3 are the weights recorded above. The concentration of aluminum in the sample (C_0) can then be calculated as follows (Binnie, 2005):

$$C_0(ppm) = \frac{X * 1000}{m}$$

where m is the total sample mass.

A.1.2.5 Anion columns

The samples are then taken up in HCl and passed through anion exchange chromatography columns to remove Fe and other contaminants. The resin beads in the columns are treated with strong HCl which coats the surface of the beads with hydrogen cations. Because Fe forms a chloride anion in HCl, it is adsorbed to the resin beads while Al and Be are eluted (Binnie, 2004). A weak HCl solution desorbs the Fe anions which are then eluted.

The columns are preconditioned with ultrapure water and then 60 ml of 9 M HCl is added. Once eluted (into a waste bottle) the sample is added along with 40 ml of 9 M HCl with the elutant going back into the Savillex jar as it contains the Al and Be. 80 ml of 0.5 M HCl is then added with the elutant going into the waste bottle, this is followed by 60 ml of ultrapure water. The samples are put on the hotplate to dry down after addition of 50 ml of ultrapure water. The water addition helps to dilute the acid solution and prevent the samples from drying black.

A.1.2.6 Titanium precipitation

Titanium can interfere with AMS measurements by reducing or contaminating the beam current (Bierman et al., 2002). It can be removed by precipitation. The sample is taken up in 2 ml of concentrated HCl to which 18 ml of ultrapure water is added. The sample is transferred to a 50 ml centrifuge tube and the pH is adjusted to between 3.8 and 4.0 using drops of NH_4OH. The sample is vortexed and centrifuged for ten minutes. If Ti is present, it is in the precipitate. The supernatant contains the Be and Al which is decanted into a second centrifuge tube. The pH is then adjusted to between eight and nine (Al and Be precipitate at this pH) by addition of NH_4OH. The samples are left overnight to help reduce ^{10}B levels (cf. Ivy-Ochs, 1996). The samples are then centrifuged for ten minutes. Providing a precipitate is evident (containing the Al and Be), the supernatant is decanted into the waste tube. 5 ml of ultrapure water is then added to the samples, they are vortexed and centrifuged for ten minutes. The supernatant is decanted and the precipitate is taken up in 3 ml of 3 M HCl and transferred back to the Savillex jars and placed on the hotplate to dry down.

A.1.2.7 Cation columns

The cation exchange chromatography columns split the Al and Be fractions of the sample by desorbing Be and Al from resin beads at different HCl molarity. The columns are preconditioned with ultrapure water. With a waste bottle catching the elutant, 60 ml of 9 M HCl is added to the columns followed by 60 ml of 4.5 M HCl which in turn is followed by 60 ml of 1 M HCl. The sample, which was previously dissolved in 1 M HCl, is then loaded into the column and a further 60 ml of 1 M HCl is added incrementally. When this has passed through the columns, the Savillex jar

is placed under the columns to catch the Be which is eluted with the addition of 160 ml of 1 M HCl. The jar is removed and the waste bottle is replaced and 80 ml of 1 M HCl is added. Once eluted, a new bottle is placed under the column to catch the Al which is eluted with the addition of 80 ml of 1 M HCl. The waste bottle is returned and 60 ml of ultrapure water is added to the columns. The Savillex jars are returned to the hotplate and dried down and the Al fraction is capped and stored until the Be chemistry is complete.

A.1.2.8 Final perchloric fume

To help reduce boron levels in Be targets, a final fume in $HClO_4$ is performed. One milliliter of $HClO_4$ is added to the sample which is placed on the hotplate at 190º C to 200º C. Once dry, the walls of the Savillex jars are washed with ultrapure water which is then evaporated to dryness on the hotplate.

A.1.2.9 Hydroxide precipitation

The next stage produces Al and Be hydroxide gels through precipitation. The process also helps to purify the final targets. The samples are dissolved by adding 2 ml of 3 M HCl to which 5 ml of ultrapure water is added. The sample is transferred to a 15 ml centrifuge tube. The pH is adjusted to 9 for Be, and 8 for Al by addition of NH_4OH. The sample is vortexed and centrifuged for ten minutes. Providing a precipitate is observed (containing the Al or Be), the supernatant is decanted into a second 15 ml centrifuge tube. The sample is redissolved with 5 ml of ultrapure water and ~3 drops of 3 M HCl, and vortexed. The pH is then adjusted again to the correct range by addition of NH_4OH. The sample is vortexed and left to sit overnight to help

reduce boron levels. The sample is then centrifuged for ten minutes. If the precipitate is present, the supernatant is decanted and 5 ml of ultrapure water added to the sample; this is vortexed and centrifuged for five minutes and the rinse is then repeated.

A.1.2.10 Firing and target pressing

The next stage converts the Al and Be hydroxide gels into oxides that are mixed with metal powder and loaded into a copper cathode ready for AMS analysis. The samples are transferred to acid cleaned (weak HNO_3) 10 mm quartz crucibles and dried on an Al heating block at 90º C. One dry, quartz caps are placed on the crucibles and they are transferred to a preheated furnace (700º C) where they are converted to oxides. After about 45 minutes the samples are removed. The oxide weights are recorded. For Be, niobium powder is added with a BeO to Nb ratio of about 1:5. For Al, silver powder is added with an Al_2O_3 to Ag ratio of about 1:2. The sample is scraped off the walls of the quartz crucible with a quartz pestle and the oxide and metal is thoroughly mixed. The mixed sample is then added to an acid cleaned copper cathode and the target is pressed. The target is then ready for AMS analysis.

A.2 AMS analysis

This section provides a brief description of the SUERC accelerator mass spectrometer as described by Freeman et al. (2007), Schnabel et al. (2007) and Maden et al. (2007). Fig. A.1 shows the schematic layout of the NEC 5MV Pelletron

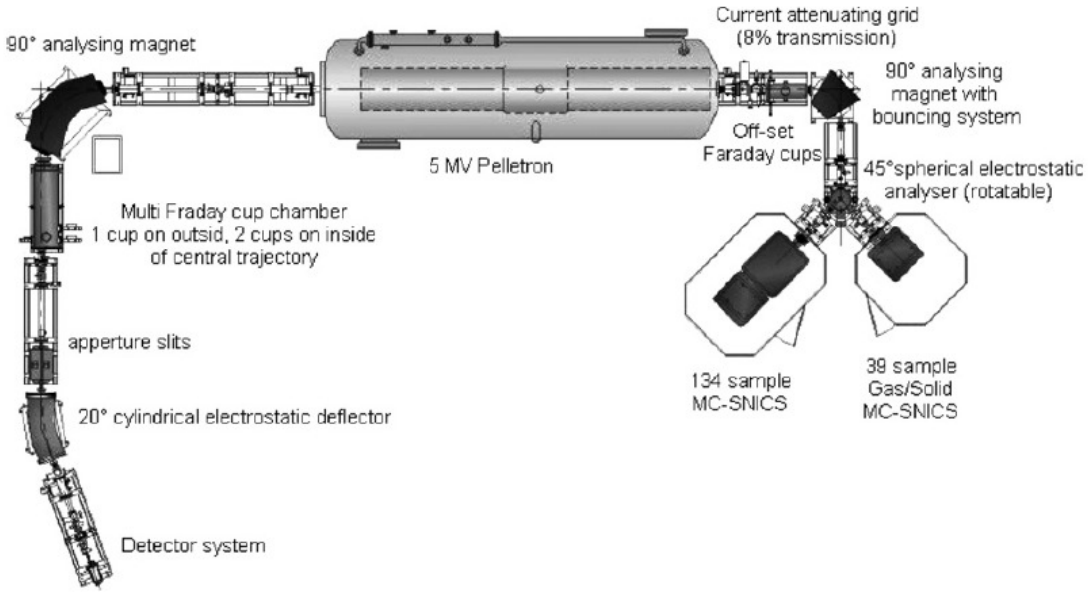

Figure A.1. Schematic layout of the SUERC AMS
(from Maden et al., 2007).

AMS used at SUERC. The target cathodes are loaded on a wheel with capacity for 134 cathodes. A 6 keV Cs^+ primary beam is used to sputter sample material in the cathode to produce negatively charged secondary ions. The negative ion beam ($^{10}Be^{16}O^-$ and $^{9}Be^{16}O^-$ [Be] and $^{26}Al^-$ and $^{27}Al^-$ [Al]) is accelerated towards the positively charged high voltage terminal of the 5MV Pelletron accelerator. Argon gas is used to break up molecules and strip their electrons producing $^{10}Be^{3+}$ and $^{9}Be^{3+}$ (Be) or $^{26}Al^{3+}$ and $^{27}Al^{3+}$ (Al). The now positively charged ions are repelled away from the high voltage terminal toward the 90º analyzing magnet which deflects the stable $^{9}Be^{3+}$ or $^{27}Al^{3+}$ ions towards Faraday cups where their abundance is determined based on electrical currents. The $^{10}Be^{3+}$ and $^{26}Al^{3+}$ pass through a cylindrical electrostatic deflector before entering the detector system where $^{10}Be^{3+}$ and $^{26}Al^{3+}$ are measured by a series of five anodes. For Be, the isobar $^{10}B^{3+}$ is suppressed with an absorber cell located in front of the detector. Two primary

standards (NIST-SRM4325:Be; Purdue Z92-0222: Al) and at least one secondary standard are run in groups of 11 cathodes for normalization.

A.3 Calculating ^{10}Be and ^{26}Al concentrations

The AMS facility returns the measured ^{10}Be/^{9}Be and ^{26}Al/^{27}Al ratios and 1σ uncertainties which then are converted to nuclide concentrations. The number of ^{10}Be and ^{26}Al atoms in a sample includes a small amount introduced during the chemical processing and from within the ^{9}Be and ^{27}Al (if used) carrier. The number of atoms introduced during the chemical processing can be approximated based on the ^{10}Be/^{9}Be and ^{26}Al/^{27}Al ratios of the procedural blanks, one of which is run with each batch of 7 – 8 samples. The atoms in the blank are then subtracted from those in the sample. The nuclide concentration (*Nc*) is calculated as follows (after Gosse and Phillips, 2001):

$$N_{c10_{Be}} = \frac{\left[R_{10/9(sample)} m_{c(sample)} \left(\frac{N_A}{A_{Be}}\right)\right] - \left[R_{10/9(blank)} m_{c(blank)} \left(\frac{N_A}{A_{Be}}\right)\right]}{m_{qtz}}$$

where $R_{10/9}$ is the ^{10}Be/^{9}Be ratio provided by the AMS facility, m_c is the mass of ^{9}Be carrier added, N_A is Avogadro's Number (6.02214179(30) x 10^{23} mole^{-1})[10], A_{Be} is the atomic weight of beryllium (9.01218)[11] and m_{qtz} is the mass of dissolved quartz (g). The calculation is the same for ^{26}Al, with m_c being the mass of stable ^{27}Al measured

[10] 2006 CODATA *recommended values* (http://physics.nist.gov/cgi-bin/cuu/Value?na)
[11] NIST Physical Reference Data
http://physics.nist.gov/PhysRefData/Handbook/Tables/berylliumtable1.htm

by ICP-OES, and substituting A_{Be} for A_{Al}, the atomic weight of aluminum (26.98154)[11]. The uncertainties are calculated by standard error propagation methods with typical AMS uncertainties being 2 – 3% for $^{10}Be/^{9}Be$ and $^{26}Al/^{27}Al$ and a conservative 2% ^{9}Be carrier mass addition and 5% ICP-OES (^{27}Al) uncertainty are used.

Appendix B Exposure age calculator

This section describes the use of the CRONUS-Earth community exposure age calculator. It describes (1) the necessary user-input, (2) how the reference production rates are derived, (3) the calculation method, assumptions and constants used in version 2.2, and (4) the output from the calculator. The full documentation for version 2.1 is provided by Balco et al. (2008). The updates for version 2.2, together with all MATLAB codes are available at the website (http://hess.ess.washington.edu/math/index.html). This section summarizes the work of Greg Balco (Balco et al., 2008).

B.1 Input

The calculator requires that users submit to a central server a spreadsheet containing the relevant data for calculating exposure ages. The input parameters and their relevance for the calculations are described below.

B.1.1 Location

The sample location is required to calculate spatial scaling factors for spallation production (S_{Xx}) and for calculating altitude dependent muon production rates. The latitude and longitude should be in decimal degree format and be referenced to the WGS 84 geoid. Altitudinal information can be entered as either elevation (m) above sea-level or as atmospheric pressure (hPa). If elevation is entered, the calculator

derives the atmospheric depth internally using the NCEP-NCAR reanalysis dataset[12] for sites with standard atmospheric conditions (i.e., locations outside of Antarctica; cf. Stone, 2000). This integrates 1000 mbar temperature fields and geographically variable mean sea-level pressure to account for regional variations in the height-pressure relationship. Alternatively, the user can enter atmospheric pressure independently. In this study I used both options as described in Chapter Four.

B.1.2 Sample thickness and density

The thickness of the measured sample (cm) and its density (g cm^{-3}) are required to scale spallogenic (S_{thick}) production with depth. Spallogenic production is taken to have exponential depth dependence with a single attenuation length of 160 g cm^{-2}. Production by muons within a sample is assumed to have linear depth dependence with a single attenuation length of 1500 g cm^{-2}. The muon production rate at the center of the sample is taken as the production rate throughout.

B.1.3 Shielding correction

The shielding correction (0-1; nondimensional) refers to the geometric scaling factor (S_G) that accounts for various obstructions blocking the full 2-pi horizon and thus cosmic-ray flux at a sample site. A separate calculator (skyline)[13] based on the model of Nishiizumi et al. (1989) is provided online to calculate the scaling factor for simple geometric obstructions. This scaling factor is not applied to muon production

[12] NCEP-NCAR reanalysis (www.cdc.noaa.gov/ncep_reanalysis/)
[13] http://hess.ess.washington.edu/math/general/skyline_input.php

rates because the effect of doing so is negligible. In this study, no such corrections are required.

B.1.4 Erosion rate

The independently determined rock surface erosion rate (cm a^{-1}) is required. In this study I base the erosion rate on geologic observations and quantitative estimates derived at a nearby location, and these are described in the following chapters.

B.1.5 Nuclide concentration

The measured nuclide concentration (at g^{-1}) in quartz and 1σ analytical uncertainties is required. These must be corrected for procedural blanks as described in Appendix A.3. ^{10}Be concentrations must be normalized to the 07KNSTD standardization of Nishiizumi et al. (2007) and ^{26}Al to the KNSTD standardization of Nishiizumi (2004). This can be done internally within the calculator by specifying the measurement standard material and ratio used by the AMS facility to normalize sample measurements. All ^{10}Be measurements made at SUERC that appear in this thesis were originally normalized to the NIST SRM-4325 Be standard material with a nominal ratio of 3.06×10^{-11}. The reported ^{10}Be concentrations in the data tables of this thesis, however, have been renormalized offline to the revised 07KNSTD standardization (nominal ratio 2.79×10^{-11}) using a conversion factor of 0.9130. In doing the conversion offline, both the ages and reported ^{10}Be concentrations are then based on the same ^{10}Be half-life. The ^{26}Al measurements are normalized to the

Purdue Z92-0222 Al standard material with a nominal $^{26}Al/^{27}Al$ ratio of 4.11×10^{-11} which agrees with the Al standard material of Nishiizumi (2004).

B.2 Reference production rates

The reference ^{10}Be and ^{26}Al production rates by muons are based entirely on muon-flux measurements and interaction cross-sections by Heisinger et al. (2002a; 2002b). The reference ^{10}Be and ^{26}Al spallation production rates for each of the five scaling models implemented is calculated from a geologic calibration dataset composed of previously published data (available as supplementary material; Balco et al., 2008). The calculator averages the ^{10}Be reference production rates obtained from each sample at a calibration site, and then averages the mean values from all calibration sites to obtain the ^{10}Be reference production rate, with the uncertainty being one standard deviation of the population. The ^{26}Al calibration sites are less geographically distributed, and because they share a similar production profile, they are calculated directly from the ^{10}Be reference production rate by multiplication of the $^{26}Al/^{10}Be$ ratio of 6.75 (see Table 2.1).

B.3 Exposure age calculation

With the relevant data submitted, the calculator solves the following equation numerically as described by Balco et al (2008):

$$N = S_{thick} S_G P_{ref,sp,Xx} \int_0^T S_{Xx}(t) \exp(-\lambda t) \exp\left(\frac{-\varepsilon t}{\Lambda_{sp}}\right) dt + P_\mu \int_0^T \exp(-\lambda t) \exp\left(\frac{-\varepsilon t - z/2}{\Lambda_\mu}\right) dt$$

where N is the nuclide concentration, S_{thick} is the scaling factor for sample thickness (nondimensional), S_G is a geometric scaling factor (nondimensional), $P_{ref,sp,Xx}$ is the reference spallation production rate (at g^{-1} a^{-1}) for the scaling model Xx [The calculator implements five different scaling models with abbreviations ($_{Xx}$): St= Lal(1991) /Stone(2000); De=Desilets et al. (2006); Du=Dunai(2001); Li=Lifton et al. (2005); Lm= Lal(1991) /Stone(2000)/ /Nishiizumi et al. (1989)], $S_{Xx}(t)$ is the scaling factor for scaling model Xx which may or may not be time (t) -dependent (nondimensional), λ is the radioactive decay constant for the particular cosmogenic nuclide [5.1×10^{-7} a^{-1} for ^{10}Be (Nishiizumi et al., 2007); 9.83×10^{-7} a^{-1} for ^{26}Al (Nishiizumi, 2004)], ε is the independently determined rock surface erosion rate (cm a^{-1}), Λ_{sp} is the effective attenuation length for spallogenic production (160 g cm^{-2}), P_μ is the surface production rate due to muons (at g^{-1} a^{-1}), z is the sample thickness, and Λ_μ is the effective attenuation length for production by muons (1500 g cm^{-2}).

The time-dependent scaling models all use the same magnetic field model which is a composite of three data sets: 1) A spherical harmonic field model for the period 0-7 ka (Korte and Constable, 2005), 2) a GAD with dipole moment for the period 7-12 ka (Yang et al., 2000), and 3) a GAD with dipole moment from the SINT800 record for the period 12-800 ka and a GAD with mean intensity of the SINT800 record extending beyond 800 ka (Guyodo and Valet, 1999).

The calculator scales production by muons separately but implements several simplifications. These simplifications have little effect on surface exposure ages because muon production is only significant at depth, or when erosion rates are very high; the latter case would not be suitable for exposure age dating. Production rates for fast muons and slow negative muons are not scaled separately, despite their different attenuation lengths. Instead, the depth-dependence is taken as exponential with a single attenuation length of 1500 g cm^{-2}. Production by fast muon interactions are calculated according to Heisinger et al. (2002b), and production by slow negative muons according to Heisinger et al. (2002a). Muon production rates are scaled for altitude following energy-dependent attenuation lengths from Boezio et al. (2000). Muon production rates are not scaled for magnetic field variations and thus are constant in space and time.

B.4 Output

The CRONUS-Earth exposure age calculator will be continually updated to maintain consistency with the most up-to-date practices and relevant constants and calibration datasets. Therefore, the version information for each component of the software that is used in a calculation is included in the output file. The data in this study were calculated using the following versions: wrapper script (v. 2.2); main calculator (v. 2.1); constants (v. 2.2); muons (v. 1.1).

The output file contains the following information which is independent of the five scaling models: 1) the calculated thickness scaling factor; 2) the user entered

shielding factor; 3) the calculated ^{10}Be and/or ^{26}Al muon production rate (at g^{-1} a^{-1}); 4) the calculated ^{10}Be and/or ^{26}Al 1σ internal uncertainty (i.e., analytical uncertainty).

The output file contains the following information which is dependent on the individual scaling model: 1) The calculated ^{10}Be and/or ^{26}Al exposure age; and 2) the calculated ^{10}Be and/or ^{26}Al 1σ external uncertainty (i.e., reflecting production rate and scaling uncertainties). In addition, for the constant production rate scaling model of Lal(1991) /Stone(2000), the spallation production rate is provided (at g^{-1} a^{-1}). For the time-dependent scaling models, a comparison of the time-varying production rate and cutoff rigidity is provided. If both ^{26}Al and ^{10}Be nuclide concentrations are submitted, the ^{26}Al/^{10}Be ratios are reported.

Appendix C Chapter Four supplementary material

C.1 Production rates

The time-averaged long term ^{10}Be and ^{26}Al production rates in the Lago Pueyrredón valley are higher than sites with standard atmospheric conditions because of an inferred low pressure anomaly during glacial times (cf. Ackert et al., 2003; Staiger et al., 2007). The anomaly is attributed to a northward shift of the Southern Westerlies (currently centered at ~50º S) and the associated circumpolar air pressure gradient of up to 5º – 10º based on marine (Howard and Prell, 1994), terrestrial (Heusser, 1983; Moreno et al., 1999) and glacier reconstructions (Hulton et al., 2002). Lower atmospheric pressure will result in an increased cosmic ray flux and a corresponding increase in production of ^{10}Be and ^{26}Al, which are produced primarily by neutron spallation reactions. The amount of increase, integrated over a full glacial-interglacial cycle, has been estimated at 5% and 11% near Lago Pueyrredón based on two independent studies. Ackert et al. (2003) measured ^{3}He concentrations in two ^{40}Ar/^{39}Ar dated lava flows at ~ 47º S (dated at 67.8 ka and 108.7 ka) and found the derived ^{3}He reference production rate was 11% higher than other published values. Staiger et al. (2007) modeled changes in the atmospheric density distribution during glaciations and its effect on terrestrial cosmogenic nuclide (spallation) production rates. They found an 8% increase in production rates near Lago Pueyrredón during glacial times. When tuned to a δ^{18}O temperature record and integrated over ~ 109 ka

(age of oldest ^{3}He calibration site of Ackert et al., 2003), their model indicates that long-term production rates are 5% higher. In this study, I increase production rates by 5% given that no local ^{10}Be calibration site is available, and cross-calibration of ^{10}Be or ^{26}Al with ^{3}He is not well established.

C.2 Depth-profile production rate

The production rate used for the depth-profile exposure model optimization (8.22 atoms ^{10}Be g^{-1} a^{-1}) was derived using the CRONUS-Earth exposure age calculator to maintain consistency with the other exposure ages presented in this study. This was achieved by using the geographic coordinates and air pressure for the surface near the depth-profile site (see Table 1 in text), negligible sample thickness (e.g., 0.000001cm) as sample parameters, and then introducing an artificial ^{10}Be concentration until an exposure age of 250 ka was obtained. Thus, the time-averaged production rate could then be derived from this artificial ^{10}Be concentration. The sensitivity of the production rate to the length of integration time was assessed: it varied less than 0.1% when, for comparison, a terrace age of 150 ka or 350 ka was assumed.

Appendix D Raw chemistry and AMS data

This Appendix details all the raw chemistry and AMS data relevant to all of the samples that were processed in relation to this thesis. It includes additional data that was part of the pilot study, but was not included in the writing of Chapter Three, Four or Five. All data relevant for calculating the exposure ages is included in these tables, and some general context is given. Table D1 gives the beryllium data including sample coordinates, total mass dissolved, etc. Table D2 gives the data specific to calculating the aluminium ages.

Table D.1. Beryllium data

Context	Lab ID	Sample ID	AMS ID	Latitude (dd)	Longitude (dd)	Alt (m)	Thick-ness (cm)	Lithology*	Boulder height (cm)	^{9}Be carrier [a] mass (µg)	Sample mass (g)	$^{10}Be/^{9}Be$[b]	σ ($^{10}Be/^{9}Be$)	% of standard	σ (% of standard)	avg. LE current	Be-10 concentration[b] (atoms/g)	σ Be-10 concentration[c] (atoms/g)	% error
Lago Pueyrredón																			
Gorra de Poivre outwash	**ASH-70**	BC06-84	b2947	-47.448013	-70.771220	811	3.0	Granitoid cobble OWT	NA	246.1	17.3231	2.949E-12	2.781E-14	9.64	0.091	2.84E-06	2.779E+06	6.195E+04	2.23%
	ASH-71	BC06-85	b2948	-47.448148	-70.771530	811	3.0	Qtz cobble OWT	NA	246.6	1.4703	2.811E-13	5.927E-15	0.92	0.019	2.83E-06	2.892E+06	9.379E+04	3.24%
	ASH-72	BC06-86	b2949	-47.448163	-70.771318	813	2.0	Qtz cobble OWT	NA	245.6	2.8949	1.744E-12	1.730E-14	5.70	0.057	2.22E-06	9.758E+06	2.210E+05	2.27%
	ASH-73	BC06-87	b2950	-47.448141	-70.771018	814	2.0	Qtz cobble OWT	NA	246.8	16.3597	8.409E-12	8.315E-14	27.48	0.272	2.82E-06	8.455E+06	1.892E+05	2.24%
moraine	**ASH-9**	BC06-109	b1223	-47.207128	-70.898857	869	3.5	Qtz cobble MC	NA	249.4	15.0840	8.421E-13	2.149E-14	2.75	0.070	2.85E-06	9.025E+05	3.028E+04	3.36%
	ASH-10	BC06-110	b1224	-47.207033	-70.897297	869	3.0	Qtz cobble MC	NA	252.8	15.0206	9.034E-13	2.313E-14	2.95	0.076	2.51E-06	9.881E+05	3.312E+04	3.35%
	ASH-11	BC06-111	b1225	-47.207068	-70.897109	870	3.0	Qtz cobble MC	NA	242.2	15.2958	9.407E-13	2.399E-14	3.07	0.078	2.80E-06	9.680E+05	3.237E+04	3.34%
	ASH-12	BC06-112	b1226	-47.206853	-70.896430	874	4.0	Qtz cobble MC	NA	244.2	15.0524	9.581E-13	2.472E-14	3.13	0.081	2.50E-06	1.011E+06	3.401E+04	3.37%
Caracoles 2 outwash	**ASH31**	BC07-54	b2044	-47.230133	-71.065167	765	2.5	Qtz cobble OWT	NA	247.0	18.9782	5.415E-12	9.432E-14	17.70	0.308	2.45E-06	4.697E+06	1.249E+05	2.66%
	ASH23	BC07-56	b1773	-47.229050	-71.065583	765	2.5	Qtz cobble OWT	NA	246.4	20.7016	6.720E-12	1.493E-13	21.96	0.490	1.60E-06	5.332E+06	1.598E+05	3.00%
	ASH24	BC07-57	b1774	-47.228433	-71.065750	760	3.0	Qtz cobble OWT	NA	246.1	19.9434	5.601E-12	1.315E-13	18.30	0.432	7.58E-07	4.606E+06	1.425E+05	3.09%
	ASH32	BC07-59	b2045	-47.229267	-71.066017	765	2.0	Qtz cobble OWT	NA	246.7	18.3588	4.671E-12	8.085E-14	15.27	0.264	2.84E-06	4.182E+06	1.110E+05	2.65%
younger moraine	**BC06-88**	BC06-88	b1209	-47.447353	-70.921677	705	3.5	Qtz cobble MC	NA	250.7	15.0152	3.280E-13	1.068E-14	1.07	0.035	1.76E-06	3.468E+05	1.430E+04	4.12%
	BC06-89	BC06-89	b1210	-47.447409	-70.921649	705	3.5	Qtz cobble MC	NA	253.9	15.0860	4.135E-13	9.859E-15	1.35	0.032	2.55E-06	4.459E+05	1.477E+04	3.31%
	BC06-90	BC06-90	b1211	-47.447472	-70.921733	705	3.5	Qtz cobble MC	NA	256.6	15.0274	3.972E-13	1.607E-14	1.30	0.053	7.58E-07	4.341E+05	2.067E+04	4.76%
	BC06-91	BC06-91	b1212	-47.447519	-70.921707	704	3.5	Qtz cobble MC	NA	252.0	15.6379	3.802E-13	1.179E-14	1.24	0.039	1.66E-06	3.910E+05	1.538E+04	3.93%
moraine	**ASH59**	BC07-35	b2083	-47.232267	-71.046533	775	3.0	Granite MC	130	247.8	17.8902	1.605E-12	3.205E-14	5.25	0.105	3.05E-06	1.477E+06	4.201E+04	2.84%
	ASH60	BC07-36	b2084	-47.234983	-71.056433	766	1.5	Granite MC	75	245.6	20.2027	2.040E-12	4.729E-14	6.67	0.155	2.26E-06	1.650E+06	5.076E+04	3.08%
	ASH38	BC07-37	b2054	-47.235333	-71.045550	762	1.0	Granite MC	95	245.9	7.6353	1.215E-12	2.839E-14	3.97	0.093	2.23E-06	2.580E+06	8.057E+04	3.12%
	ASH61	BC07-38	b2085	-47.233900	-71.039133	775	1.5	Granite MC	100	246.7	21.4400	3.144E-12	7.229E-14	10.28	0.236	2.60E-06	2.411E+06	7.369E+04	3.06%
	ASH62	BC07-39	b2086	-47.234217	-71.038117	769	2.5	Granite MC	60	246.6	20.1155	6.494E-12	1.427E-13	21.22	0.466	2.62E-06	5.312E+06	1.581E+05	2.98%
Hatcher outwash	**ASH22**	BC07-50	b1772	-47.266100	-70.964083	582	4.0	Qtz cobble OWT	NA	247.2	17.4325	2.296E-12	5.300E-14	7.50	0.174	1.37E-06	2.160E+06	6.649E+04	3.08%
	ASH40	BC07-51	b2056	-47.266117	-70.964183	582	2.0	Qtz cobble OWT	NA	244.5	19.7668	2.095E-12	3.810E-14	6.85	0.125	2.04E-06	1.718E+06	4.685E+04	2.73%
	ASH26	BC07-52	b2037	-47.266117	-70.964233	582	3.5	Qtz cobble OWT	NA	246.9	11.1850	1.198E-12	2.430E-14	3.92	0.079	1.07E-06	1.746E+06	5.040E+04	2.89%
	ASH41	BC07-53	b2057	-47.266100	-70.964150	583	2.5	Qtz cobble OWT	NA	246.5	20.1070	2.603E-12	4.235E-14	8.51	0.138	2.80E-06	2.119E+06	5.501E+04	2.60%
	ASH66	BC06-103	b2892	-47.299846	-71.036177	620	2.5	Qtz cobble OWT	NA	247.0	19.2727	2.069E-12	3.562E-14	6.76	0.116	3.71E-06	1.766E+06	4.677E+04	2.65%
	ASH67	BC06-104	b2893	-47.299817	-71.036223	622	2.0	Qtz cobble OWT	NA	245.3	25.1177	3.085E-12	6.199E-14	10.08	0.203	2.92E-06	2.009E+06	5.709E+04	2.84%
	ASH68	BC06-106	b2896	-47.299756	-71.036285	622	3.0	Qtz cobble OWT	NA	245.9	20.9424	2.145E-12	3.356E-14	7.01	0.110	2.17E-06	1.678E+06	4.275E+04	2.55%
depth-profile	**ASH49**	BC07-48a	b2068	-47.266267	-70.963200	583	3.0	Qtz pebbles n=41; 10cm	NA	244.5	21.6540	2.226E-12	5.226E-14	7.27	0.171	1.58E-06	1.654E+06	5.188E+04	3.14%
	ASH48	BC07-48b	b2067	-47.266267	-70.963200	583	3.5	Qtz pebbles n=14; 20cm	NA	245.0	27.4242	2.316E-12	5.420E-14	7.57	0.177	2.82E-06	1.363E+06	4.262E+04	3.13%
	ASH47	BC07-48c	b2066	-47.266267	-70.963200	583	3.5	Qtz pebbles n=10; 30cm	NA	246.8	39.0634	3.030E-12	6.116E-14	9.90	0.200	2.28E-06	1.265E+06	3.638E+04	2.88%
	ASH46	BC07-48d	b2063	-47.266267	-70.963200	583	4.0	Qtz pebbles n=18; 40cm	NA	247.1	46.1808	2.942E-12	6.850E-14	9.61	0.224	1.39E-06	1.040E+06	3.231E+04	3.11%
	ASH45	BC07-48e	b2062	-47.266267	-70.963200	583	4.0	Qtz pebbles n=37; 50cm	NA	235.7	58.1919	3.284E-12	6.637E-14	10.73	0.217	1.68E-06	8.793E+05	2.529E+04	2.88%
	ASH44	BC07-48f	b2061	-47.266267	-70.963200	583	4.0	Qtz pebbles n=19; 75cm	NA	245.7	61.5383	2.444E-12	5.681E-14	7.99	0.186	1.40E-06	6.170E+05	1.920E+04	3.11%
	ASH34	BC07-48g	b2048	-47.266267	-70.963200	583	3.5	Qtz pebbles n=49; 100cm	NA	245.7	59.4350	1.531E-12	2.772E-14	5.00	0.091	2.75E-06	4.183E+05	1.142E+04	2.73%
	ASH43	BC07-48h	b2060	-47.266267	-70.963200	583	3.0	Qtz pebbles n=44; 150cm	NA	244.4	63.8225	7.916E-13	1.687E-14	2.59	0.055	2.57E-06	2.022E+05	6.242E+03	3.09%
moraine	**ASH35**	BC07-1	b2049	-47.294617	-71.086500	680	2.0	Granite MC	95	246.7	19.6454	1.569E-12	2.385E-14	5.13	0.078	3.43E-06	1.303E+06	3.312E+04	2.54%
	ASH19	BC07-3	b1767	-47.298717	-71.057883	673	1.5	Granite MC	200	245.0	18.6180	1.625E-12	3.255E-14	5.31	0.107	2.07E-06	1.415E+06	4.051E+04	2.86%
	ASH27	BC07-4	b2038	-47.298783	-71.057600	678	2.0	Granite MC	100	245.3	20.4468	1.317E-12	3.147E-14	4.30	0.103	2.20E-06	1.044E+06	3.293E+04	3.15%
	ASH28	BC07-5	b2039	-47.540750	-71.150883	783	2.0	Granite MC	135	246.9	20.0563	1.199E-12	2.782E-14	3.92	0.091	2.60E-06	9.746E+05	3.025E+04	3.10%
	ASH63	BC06-98	b2087	-47.302469	-71.045467	653	5.0	Qtz cobble MC	NA	245.5	19.6917	5.285E-13	1.295E-14	1.73	0.042	2.88E-06	4.324E+05	1.398E+04	3.23%
	ASH57	BC06-99	b2080	-47.302462	-71.045533	652	3.0	Qtz cobble MC	NA	246.7	21.2545	6.093E-13	1.221E-14	1.99	0.040	3.00E-06	4.602E+05	1.346E+04	2.93%
	BC06-37	BC06-37	b1206	-47.533277	-71.143090	762	1.5	Qtz cobble MC	NA	274.5	15.0548	3.863E-13	1.576E-14	1.26	0.052	1.21E-06	4.515E+05	2.159E+04	4.78%

	BC06-42	BC06-42	b1207	-47.534048	-71.142937	763	4.5	Qtz cobble MC	NA	260.6	15.0285	5.143E-13	1.765E-14	1.68	0.058	1.06E-06	5.766E+05	2.386E+04	4.14%
	BC06-43	BC06-43	b1208	-47.534129	-71.143089	762	3.5	Qtz cobble MC	NA	252.4	15.5849	4.054E-13	1.162E-14	1.33	0.038	1.86E-06	4.203E+05	1.560E+04	3.71%
Río Blanco outwash	**ASH53**	BC06-32	b2074	-47.485633	-71.216942	564	3.5	Qtz cobble OWT	NA	245.7	24.1803	3.041E-13	7.201E-15	0.99	0.024	3.06E-06	1.956E+05	6.533E+03	3.34%
	ASH54	BC06-34	b2075	-47.486016	-71.217054	563	4.0	Qtz cobble OWT	NA	244.9	30.9418	3.993E-13	8.219E-15	1.31	0.027	3.09E-06	2.026E+05	6.147E+03	3.03%
	ASH55	BC06-35	b2078	-47.485867	-71.216613	564	4.0	Qtz cobble OWT	NA	246.6	24.7066	3.116E-13	7.392E-15	1.02	0.024	3.45E-06	1.971E+05	6.574E+03	3.34%
moraine	**ASH36**	BC07-7	b2050	-47.518609	-71.236114	564	2.5	Granite MC	225	240.8	20.9284	3.027E-13	6.982E-15	0.99	0.023	2.81E-06	2.198E+05	7.295E+03	3.32%
	ASH30	BC07-8	b2043	-47.556350	-71.262850	587	1.5	Granite MC	190	246.5	27.7948	4.683E-13	1.072E-14	1.53	0.035	2.56E-06	2.690E+05	8.495E+03	3.16%
	ASH18	BC07-12	b2036	-47.583983	-71.354783	665	1.5	Granite MC	310	246.2	24.1815	3.475E-13	8.166E-15	1.14	0.027	2.73E-06	2.266E+05	7.385E+03	3.26%
	ASH39	BC07-43	b2055	-47.507917	-71.245067	581	1.5	Granite MC	80	252.4	25.7394	3.501E-13	8.412E-15	1.14	0.028	2.57E-06	2.111E+05	7.058E+03	3.34%
	ASH51	BC06-27	b2072	-47.570083	-71.303506	643	3.0	Qtz cobble MC	NA	247.0	28.8330	3.506E-13	8.785E-15	1.15	0.029	2.77E-06	1.915E+05	6.527E+03	3.41%
	ASH52	BC06-29	b2073	-47.570307	-71.306062	647	4.0	Qtz cobble MC	NA	243.5	20.2262	1.611E-13	5.288E-15	0.53	0.017	2.92E-06	1.165E+05	5.221E+03	4.48%
	ASH56	BC07-9	b2079	-47.579567	-71.358183	709	3.0	Granite MC	95	246.1	27.0887	3.613E-13	8.352E-15	1.18	0.027	3.13E-06	2.096E+05	6.806E+03	3.25%
	ASH-75	BC07-16	b2953	-47.304100	-71.402900	620	1.0	Granite MC	100	246.0	26.0982	2.899E-13	5.906E-15	0.95	0.019	2.93E-06	1.681E+05	5.338E+03	3.18%
	ASH17	BC07-17	b1766	-47.308717	-71.404950	614	2.0	Granite MC	100	247.0	27.8613	2.708E-13	1.042E-14	0.88	0.034	1.17E-06	1.507E+05	7.085E+03	4.70%
	ASH20	BC07-18	b1770	-47.338017	-71.249017	570	2.0	Granite MC	140	246.3	27.9337	1.981E-13	7.232E-15	0.64	0.024	2.32E-06	1.069E+05	5.039E+03	4.71%
	ASH-76	BC07-20	b2954	-47.325917	-71.293767	565	2.0	Granite MC	75	245.6	31.3211	3.310E-13	6.377E-15	1.08	0.021	2.82E-06	1.613E+05	4.911E+03	3.04%
	ASH29	BC07-13	b2042	-47.452467	-71.711983	352	1.5	Granite Bedrock	75	246.1	30.9626	2.142E-13	9.458E-15	0.70	0.031	1.24E-06	1.061E+05	5.587E+03	5.26%
	ASH37	BC07-21	b2051	-47.336083	-71.283033	509	2.0	Metamorphic MC	95	246.0	28.5270	2.497E-13	8.465E-15	0.82	0.028	2.11E-06	1.344E+05	5.792E+03	4.31%
	ASH21	BC07-22A	b1771	-47.572567	-71.417083	544	1.5	Granite MC	250	244.9	28.8329	3.542E-13	1.251E-14	1.15	0.041	1.24E-06	1.916E+05	8.263E+03	4.31%
	ASH64	BC07-22B	b2090	-47.572567	-71.417083	544	1.5	Granite MC	250	235.3	31.7051	3.703E-13	1.040E-14	1.21	0.034	1.58E-06	1.787E+05	6.373E+03	3.57%
	ASH-74	BC07-23	b2951	-47.575800	-71.412600	541	3.5	Metamorphic MC	130	246.3	8.5658	1.178E-13	4.651E-15	0.39	0.015	2.17E-06	1.818E+05	1.060E+04	5.83%
Lago Buenos Aires																				
Moreno I	**LBA06-1**	LBA06-1	b1197	-46.564515	-70.885146	504	3.0	Qtz cobble MC	NA	212.3	14.6478	8.415E-13	2.175E-14	2.75	0.071	1.67E-06	8.006E+05	2.672E+04	3.34%
moraine	**LBA06-3**	LBA06-3	b1198	-46.564685	-70.885077	504	3.5	Qtz cobble MC	NA	215.3	11.6867	7.613E-13	2.089E-14	2.49	0.068	2.12E-06	9.194E+05	3.194E+04	3.47%
	LBA06-5	LBA06-5	b1199	-46.564909	-70.885027	503	3.0	Qtz cobble MC	NA	208.6	11.7794	6.399E-13	1.924E-14	2.09	0.063	1.63E-06	7.393E+05	2.747E+04	3.72%
	ASH-1	LBA06-6	b1214	-46.564931	-70.885037	503	4.0	Qtz cobble MC	NA	250.2	17.0105	8.446E-13	4.036E-14	2.76	0.132	3.98E-07	8.122E+05	4.314E+04	5.31%
	ASH-2	LBA06-7	b1215	-46.564883	-70.885049	504	3.0	Qtz cobble MC	NA	249.8	15.7023	9.013E-13	2.025E-14	2.95	0.066	2.40E-06	9.387E+05	2.906E+04	3.10%
Moreno III	**LBA06-14**	LBA06-14	b1200	-46.560768	-70.839621	516	4.0	Qtz cobble MC	NA	210.9	16.0426	8.920E-13	2.401E-14	2.92	0.079	1.93E-06	7.706E+05	2.635E+04	3.42%
moraine	**LBA06-15**	LBA06-15	b1201	-46.560710	-70.839502	517	3.5	Qtz cobble MC	NA	209.7	12.1107	5.079E-13	1.275E-14	1.66	0.042	2.29E-06	5.704E+05	1.904E+04	3.34%
	LBA06-16	LBA06-16	b1202	-46.560680	-70.839545	517	2.0	Qtz cobble MC	NA	209.4	12.1143	5.512E-13	1.637E-14	1.80	0.054	1.85E-06	6.194E+05	2.295E+04	3.70%
	ASH-3	LBA06-18	b1218	-46.560710	-70.839545	517	2.0	Qtz pebbles n=~30	NA	249.4	15.5142	5.324E-13	1.502E-14	1.74	0.049	2.82E-06	5.522E+05	2.013E+04	3.65%
Esquel																				
M2	**ASH-6**	ES06-25	b1221	-43.116604	-71.031160	765	3.5	Granite cobble MC	NA	247.7	15.6477	1.345E-13	5.587E-15	0.44	0.018	2.57E-06	1.228E+05	7.536E+03	6.14%
moraine	**ASH-13**	ES06-26	b1227	-43.116523	-71.031201	766	3.5	Granite cobble MC	NA	243.5	7.5552	8.344E-14	4.140E-15	0.27	0.014	2.90E-06	1.239E+05	1.098E+04	8.86%
	ASH-14	ES06-27	b1228	-43.116635	-71.031337	767	3.0	Granite cobble MC	NA	244.0	21.7248	1.542E-13	5.818E-15	0.50	0.019	2.72E-06	9.635E+04	5.275E+03	5.47%
M4	**ASH-4**	ES06-13	b1219	-43.153737	-70.987227	1184	3.5	Granite cobble MC	NA	247.2	15.4825	3.720E-13	1.385E-14	1.22	0.045	1.19E-06	3.772E+05	1.719E+04	4.56%
moraine	**ASH-5**	ES06-16	b1220	-43.152861	-70.986208	1193	4.0	Granite cobble MC	NA	248.6	13.1631	3.654E-13	1.081E-14	1.19	0.035	2.79E-06	4.380E+05	1.705E+04	3.89%
Calafate																				
M7	**ASH-7**	CA06-11		-50.338798	-71.470425	861	3.5	Qtz cobble MC	NA	252.9	15.4712	Be target lost during preparation								
M5	**ASH-15**	CA06-115	b1229	-50.187377	-71.179898	534	3.0	Qtz cobble MC	NA	244.5	15.0248	1.288E-12	3.273E-14	4.21	0.107	2.54E-06	1.373E+06	4.537E+04	3.31%
Process Blanks[d]																				
	LBA-Blank[B1]	LBA1,3,5-7	b1205	NA	NA	NA	NA	NA	NA	210.2	NA	1.505E-14	2.172E-15	0.05	0.007	1.96E-06				
	BC06-BLk[B1]	BC0637,42,43,88-91	b1213	NA	NA	NA	NA	NA	NA	252.3	NA	1.716E-14	2.617E-15	0.06	0.009	1.82E-06				
	ASH-8[B1]	ASH1-7	b1222	NA	NA	NA	NA	NA	NA	251.0	NA	1.820E-14	3.439E-15	0.06	0.011	1.45E-06				
	ASH-16[B1]	ASH9-15	b1230	NA	NA	NA	NA	NA	NA	242.5	NA	2.600E-14	2.415E-15	0.09	0.008	2.68E-06				
	ASH25[B2]	ASH17,19-24	b1776	NA	NA	NA	NA	NA	NA	246.4	NA	1.659E-14	2.237E-15	0.05	0.007	1.58E-06				
	ASH33[B2]	ASH26-32,18	b2047	NA	NA	NA	NA	NA	NA	244.4	NA	1.457E-14	1.656E-15	0.05	0.005	2.61E-06				
	ASH42[B2]	ASH34-41	b2059	NA	NA	NA	NA	NA	NA	245.8	NA	1.648E-14	2.073E-15	0.05	0.007	1.90E-06				
	ASH50[B2]	ASH43-49	b2069	NA	NA	NA	NA	NA	NA	247.1	NA	3.362E-14	3.363E-15	0.11	0.011	1.83E-06				
	ASH58[B2]	ASH51-57	b2081	NA	NA	NA	NA	NA	NA	245.3	NA	1.619E-14	1.894E-15	0.05	0.006	2.20E-06				
	ASH65[B2]	ASH59-64	b2091	NA	NA	NA	NA	NA	NA	248.2	NA	9.447E-15	1.376E-15	0.03	0.005	2.57E-06				
	ASH69[B2]	ASH66-68	b2897	NA	NA	NA	NA	NA	NA	244.7	NA	7.017E-15	1.096E-15	0.02	0.004	2.44E-06				
	ASH77[B3]	ASH70-76	b2955	NA	NA	NA	NA	NA	NA	245.1	NA	2.327E-14	1.755E-15	0.08	0.006	2.68E-06				

*MC – sampled from moraine crest. OWT – sampled from outwash terrace. n= number of pebbles included in amalgamation.

[a]The ^{9}Be carrier additions are corrected for the density of the carrier used, as listed in note d.

[b]Measurements are standardized to the NIST SRM-4325 standard material with a nominal ratio of $3.06E^{-11}$; note nuclide concentrations in data tables of thesis are normalized to 07KNSTD standards (Nishiizumi *et al.,* 2007) w/ conversion factor 0.9118.
[c]Nuclide concentrations uncertainty includes a 2% carrier addition uncertainty.
[d]Beryllium carriers used for samples/blanks listed above blank below: B1-Spectrosol (1000 mg/l), Lot#70222943, density 1.02; B2-Scharlau (1000 mg/l), density 1.02; B3-Scharlau (1000 mg/l), Batch#81145, density 1.02
In total 91 Be targets were prepared (79 samples, 12 blanks). Most appear in the thesis but some are not included. I hope to use the remaining data listed above in future publications.

Table D.2. Aluminum data

Context	Lab ID	Sample ID	AMS ID	^{27}Al carrier[a] mass (µg)	V1 (g)	V2 (g)	V3 (g)	Al-ICP results (ppm) (µg/g)	Al-27 content of Sample (mg)	^{26}Al/^{27}Al[b]	σ (^{26}Al/^{27}Al)	% of standard	σ (% of standard)	Avg. LE current	Al-26 nuclide concentration[b] (atoms/g)	σ A-26 nuclide concentration[c] (atoms/g)	% error
Lago Pueyrredón																	
Gorra de Poivre	**ASH-70**	BC06-84	a866	0.5117	42.5065	1.0589	10.2173	7.58	3.108893	3.824E-12	4.583E-14	9.30	0.111	4.25E-07	1.528E+07	7.877E+05	5.15%
outwash	**ASH-71**	BC06-85	a867	0.5119	42.4470	1.0593	10.2183	2.00	0.818911	1.440E-12	5.590E-14	3.50	0.136	1.68E-07	1.749E+07	1.136E+06	6.50%
	ASH-72	BC06-86	a870	0.5127	42.1347	1.0299	10.1263	2.13	0.882420	6.647E-12	1.567E-13	16.17	0.381	1.65E-07	4.502E+07	2.501E+06	5.55%
	ASH-73	BC06-87	a871	0.5114	42.9552	1.0598	10.1645	16.79	6.917172	4.262E-12	6.687E-14	10.37	0.163	5.58E-07	4.019E+07	2.108E+06	5.25%
moraine	**ASH-9**	BC06-109	a510	1.5275	42.2130	1.0687	26.7255	1.71	1.800671	1.909E-12	3.631E-14	4.64	0.088	4.99E-07	5.081E+06	2.721E+05	5.36%
	ASH-10	BC06-110	a511	1.5297	42.0139	1.0674	26.5179	1.63	1.700147	2.212E-12	4.383E-14	5.38	0.107	7.28E-07	5.585E+06	3.007E+05	5.38%
	ASH-11	BC06-111	a513	1.5191	42.3213	1.0627	26.4062	1.67	1.756385	2.286E-12	4.076E-14	5.56	0.099	4.91E-07	5.853E+06	3.110E+05	5.32%
	ASH-12	BC06-112	a514	1.5300	41.8000	1.0621	26.8075	2.00	2.113719	1.909E-12	4.398E-14	4.64	0.107	2.92E-07	5.978E+06	3.294E+05	5.51%
Caracoles 2	**ASH31**	BC07-54	a650	0	41.7625	1.0569	10.4416	3.54	1.460572	1.500E-11	3.333E-13	36.49	0.811	3.88E-07	2.575E+07	1.410E+06	5.47%
outwash	**ASH23**	BC07-56	a645	0	42.2835	1.0646	10.4520	8.78	3.644839	7.065E-12	1.588E-13	17.19	0.386	3.75E-07	2.776E+07	1.522E+06	5.48%
	ASH32	BC07-59	a651	0	41.5650	1.0538	10.4278	2.36	0.970676	1.926E-11	4.190E-13	46.87	1.020	4.81E-07	2.273E+07	1.240E+06	5.46%
younger moraine	**BC06-88**	BC06-88	a491	1.5426	27.8002	1.1777	25.3719	3.18	1.902351	7.139E-13	2.587E-14	1.74	0.063	2.45E-07	2.008E+06	1.247E+05	6.21%
	BC06-89	BC06-89	a492	1.5384	26.4961	1.1315	26.1213	7.03	4.301140	4.432E-13	1.715E-14	1.08	0.042	3.36E-07	2.810E+06	1.784E+05	6.35%
	BC06-90	BC06-90	a493	1.5303	27.8630	1.0903	25.9612	3.41	2.259429	9.985E-13	2.477E-14	2.43	0.060	3.68E-07	3.341E+06	1.871E+05	5.60%
	BC06-91	BC06-91	a496	1.5311	42.0323	1.0860	26.2319	1.98	2.012515	7.510E-13	2.013E-14	1.83	0.049	5.02E-07	2.147E+06	1.225E+05	5.70%
moraine	**ASH59**	BC07-35	a662	0	41.7134	1.0622	10.3978	9.49	3.875047	1.803E-12	4.781E-14	4.39	0.116	3.34E-07	8.713E+06	4.935E+05	5.66%
	ASH60	BC07-36	a663	0	41.6697	1.0598	10.4121	7.42	3.037657	2.892E-12	6.523E-14	7.04	0.159	5.61E-07	9.701E+06	5.324E+05	5.49%
	ASH38	BC07-37	a656	0	41.6426	1.0622	10.4474	3.94	1.613749	2.908E-12	6.496E-14	7.08	0.158	2.91E-07	1.371E+07	7.514E+05	5.48%
	ASH61	BC07-38	a664	0	42.1496	1.0650	10.4161	15.78	6.505130	2.177E-12	4.958E-14	5.30	0.121	5.41E-07	1.474E+07	8.103E+05	5.50%
	ASH62	BC07-39	a667	0	41.9107	1.0599	10.4087	7.36	3.029245	7.896E-12	1.743E-13	19.21	0.424	3.42E-07	2.654E+07	1.451E+06	5.47%
Hatcher	**ASH22**	BC07-50	a642	0	41.9413	1.0721	10.4650	9.05	3.705053	2.638E-12	7.049E-14	6.42	0.172	2.04E-07	1.251E+07	7.096E+05	5.67%
outwash	**ASH40**	BC07-51	a657	0	41.7218	1.0589	10.4119	4.44	1.821466	5.045E-12	1.131E-13	12.28	0.275	5.24E-07	1.037E+07	5.687E+05	5.48%
	ASH41	BC07-53	a658	0	41.6579	1.0609	10.4100	0.93	0.380151	3.044E-11	1.220E-12	74.06	2.970	3.16E-08	1.284E+07	8.233E+05	6.41%
moraine	**ASH35**	BC07-1	a655	0	41.8059	1.0631	10.5091	2.45	1.012500	7.476E-12	2.664E-13	18.19	0.648	2.05E-08	8.596E+06	5.281E+05	6.14%
	ASH19	BC07-3	a641	0	41.7095	1.0713	10.4915	4.57	1.866713	4.267E-12	1.256E-13	10.38	0.306	8.35E-08	9.545E+06	5.541E+05	5.81%
	ASH27	BC07-4	a647	0	42.2600	1.0585	10.4516	6.22	2.595445	2.175E-12	4.475E-14	5.29	0.109	4.65E-07	6.154E+06	3.333E+05	5.42%
	ASH28	BC07-5	a649	0	42.2690	1.0568	10.4725	4.80	2.010577	2.595E-12	5.948E-14	6.31	0.145	4.29E-07	5.798E+06	3.194E+05	5.51%
	BC06-37	BC06-37	a487	0	41.6426	1.0622	10.4474	3.94	1.613749	1.135E-12	3.378E-14	2.76	0.082	2.26E-07	2.691E+06	1.572E+05	5.84%
	BC06-42	BC06-42	a488	1.0309	27.2752	1.0991	25.2062	2.04	1.273430	1.640E-12	3.828E-14	3.99	0.093	2.55E-07	3.091E+06	1.712E+05	5.54%
	BC06-43	BC06-43	a489	1.5427	26.5051	1.1186	26.0033	3.33	2.054528	8.827E-13	2.044E-14	2.15	0.050	4.78E-07	2.587E+06	1.432E+05	5.53%
Lago Buenos Aires																	
Moreno I	**LBA06-1**	LBA06-1	a475	0	41.9098	1.0374	25.3318	0.51	0.521922	3.554E-12	6.915E-14	8.65	0.168	2.71E-07	2.821E+06	1.517E+05	5.38%
moraine	**ASH-1**	LBA06-6	a498	1.5396	38.3415	1.0224	27.0011	66.26	67.098233	1.007E-13	6.616E-15	0.25	0.016	5.08E-07	8.861E+06	7.322E+05	8.26%
	ASH-2	LBA06-7	a500	1.5261	41.6556	1.0419	26.2325	1.50	1.572351	2.359E-12	3.628E-14	5.74	0.088	4.31E-07	5.263E+06	2.758E+05	5.24%
Moreno III	**LBA06-14**	LBA06-14	a479	0	41.6125	1.0500	26.3308	0.43	0.448711	5.953E-12	1.018E-13	14.48	0.248	3.04E-07	3.711E+06	1.964E+05	5.29%
moraine	**ASH-3**	LBA06-18	a501	1.5809	41.5860	1.0403	26.6578	2.04	2.177027	1.023E-12	2.219E-14	2.49	0.054	4.71E-07	3.194E+06	1.746E+05	5.47%
Esquel																	
M2 moraine	**ASH-6**	ES06-25	a505	0	42.1632	1.0453	26.4081	8.56	9.120044	8.316E-14	5.769E-15	0.20	0.014	6.77E-07	1.073E+06	9.257E+04	8.63%
	ASH-13	ES06-26	a515	0	42.2902	1.0737	26.5139	1.47	1.536290	1.575E-13	7.278E-15	0.38	0.018	5.07E-07	7.042E+05	4.881E+04	6.93%
	ASH-14	ES06-27	a517	0	41.6646	1.0639	26.8087	3.00	3.148229	1.767E-13	1.006E-14	0.43	0.025	2.97E-07	5.678E+05	4.333E+04	7.63%
M4 - moraine	**ASH-4**	ES06-13	a502	0	34.9491	1.0185	26.7321	19.18	17.597725	1.257E-13	7.712E-15	0.31	0.019	4.72E-07	3.181E+06	2.525E+05	7.94%
	ASH-5	ES06-16	a504	0	36.9685	1.0200	27.1129	7.10	6.980524	2.708E-13	1.283E-14	0.66	0.031	3.61E-07	3.195E+06	2.208E+05	6.91%
Calafate																	
M7	**ASH-7**	CA06-11	a506	1.5351	41.8394	1.0454	26.6485	1.55	1.653132	9.851E-12	1.930E-13	23.97	0.470	6.09E-07	2.349E+07	1.262E+06	5.37%
M5	**ASH-15**	CA06-115	a518	0	41.7925	1.0548	26.7651	0.66	0.702699	4.387E-12	8.699E-14	10.67	0.212	4.37E-07	4.575E+06	2.464E+05	5.39%
Process Blanks																	
	ASH25	ASH17,19-24	a646	1.6343	41.9831	1.0616	10.4819	3.88	1.608368	2.606E-15	1.165E-15	0.01	0.003	3.70E-07			
	ASH33	ASH26-32,18	a652	1.5642	41.8880	1.0574	10.6430	3.60	1.517808	5.868E-15	1.694E-15	0.01	0.004	4.52E-07			
	ASH42	ASH34-41	a661	1.2786	41.5585	1.0597	10.4257	2.88	1.177537	3.802E-15	1.700E-15	0.01	0.004	2.45E-07			

ASH65	ASH59-64	a668	1.6266	41.9840	1.0628	10.3928	4.00	1.642195	3.243E-15	1.226E-15	0.01	0.003	4.32E-07
LBA-Blank	LBA1,14	a485	1.5356	41.6536	1.0430	26.3371	1.10	1.156988	3.432E-15	1.144E-15	0.01	0.003	5.82E-07
BC06-BLk	BC0637,42,43,88-91	a497	1.5333	41.2652	1.0856	26.8819	1.43	1.462861	4.993E-15	1.765E-15	0.01	0.004	3.63E-07
ASH-8	ASH1-7	a509	1.5331	41.7280	1.0528	26.5128	1.24	1.306856	4.797E-15	1.446E-15	0.01	0.004	4.39E-07
ASH-16	ASH9-15	a519	1.5336	41.6900	1.0557	26.7046	1.21	1.273139	2.794E-15	9.878E-16	0.01	0.002	4.91E-07
ASH77	ASH70-76	a872	1.6159	43.2546	1.0666	10.2210	3.96	1.641418	1.666E-14	3.268E-15	0.04	0.008	2.79E-07

[a] ^{27}Al carrier used: Fischer (1000 ppm), Lot# 90376613.
[b]Measurements are standardized to the Purdue Z92-0222 Al standard material with a nominal ratio of $4.11E^{-11}$, which agrees with the standards of Nishiizumi (2004).
[c]Nuclide concentration uncertainty includes a 5% icp measurement uncertainty.

In total 51 Al targets were prepared (42 samples, 9 blanks). Most appear in the thesis but some are not included. I hope to use the remaining data listed above in future publications.

References

Ackert, R.P. et al., 2008. Patagonian glacier response during the late glacial-holocene transition. Science, 321(5887): 392-395.

Ackert, R.P. and Mukhopadhyay, S., 2005. Constraining landform erosion and ages from surface exposure age distributions on old Patagonian moraines. Geochimica et Cosmochimica Acta, 69(10): A162.

Ackert, R.P., Singer, B.S., Guillou, H., Kaplan, M.R. and Kurz, M.D., 2003. Long-term cosmogenic He-3 production rates from Ar-40/Ar-39 and K-Ar dated Patagonian lava flows at 47 degrees S. Earth and Planetary Science Letters, 210(1-2): 119-136.

Alley, R.B., 2000. The Younger Dryas cold interval as viewed from central Greenland. Quaternary Science Reviews, 19(1-5): 213-226.

Anderson, R.S., Repka, J.L. and Dick, G.S., 1996. Explicit treatment of inheritance in dating depositional surfaces using in situ Be-10 and Al-26. Geology, 24(1): 47-51.

Andrews, J.T. and Smithson, B.B., 1966. Till Fabrics of Cross-Valley Moraines of North-Central Baffin Island Northwest Territories Canada. Geological Society of America Bulletin, 77(3): 271-&.

Ariztegui, D., Bianchi, M.M., Masaferro, J., Lafargue, E. and Niessen, F., 1997. Interhemispheric synchrony of late-glacial climatic instability as recorded in proglacial Lake Mascardi, Argentina. Journal of Quaternary Science, 12(4): 333-338.

Bagnold, R.A., 1941. The Physics of Blown Sand and Desert Dunes. Chapman Hall, London, p.265 pp.

Balco, G. et al., 2009. Regional beryllium-10 production rate calibration for late-glacial northeastern North America. Quaternary Geochronology, 4(2): 93-107.

Balco, G. and Rovey, C.W., 2008. An Isochron Method for Cosmogenic-Nuclide Dating of Buried Soils and Sediments. American Journal of Science, 308(10): 1083-1114.

Balco, G., Stone, J.O., Lifton, N.A. and Dunai, T.J., 2008. A complete and easily accessible means of calculating surface exposure ages or erosion rates from Be-10 and Al-26 measurements. Quaternary Geochronology, 3(3): 174-195.

Basile, I. et al., 1997. Patagonian origin of glacial dust deposited in East Antarctica (Vostok and Dome C) during glacial stages 2, 4 and 6. Earth and Planetary Science Letters, 146(3-4): 573-589.

Becquey, S. and Gersonde, R., 2003. A 0.55-Ma paleotemperature record from the Subantarctic zone: Implications for Antarctic Circumpolar Current development. Paleoceanography, 18(1).

Begét, J.E. and Keskinen, M.J., 2003. Trace-element geochemistry of individual glass shards of the Old Crow tephra and the age of the Delta glaciation, central Alaska. Quaternary Research, 60(1): 63-69.

Bell, C.M., 2008. Punctuated drainage of an ice-dammed quaternary lake in southern South America. Geografiska Annaler Series a-Physical Geography, 90A(1): 1-17.

Bender, M. et al., 1994. Climate Correlations between Greenland and Antarctica During the Past 100,000 Years. Nature, 372(6507): 663-666.

Benn, D.I. and Clapperton, C.M., 2000. Glacial sediment-landform associations and paleoclimate during the last glaciation, Strait of Magellan, Chile. Quaternary Research, 54(1): 13-23.

Bennett, K.D., Haberle, S.G. and Lumley, S.H., 2000. The last glacial-Holocene transition in southern Chile. Science, 290(5490): 325-328.

Benson, L. et al., 2004. The probable importance of snow and sediment shielding on cosmogenic ages of north-central Colorado Pinedale and pre-Pinedale moraines. Quaternary Science Reviews, 23(1-2): 193-206.

Bentley, M.J., 1997. Relative and radiocarbon chronology of two former glaciers in the Chilean Lake District. Journal of Quaternary Science, 12(1): 25-33.

Berger, A.L., 1978. Long-Term Variations of Daily Insolation and Quaternary Climatic Changes. Journal of the Atmospheric Sciences, 35(12): 2362-2367.

Bevington, P. and Robinson, K., 2003. Data Reduction and Error Analysis for the Physical Sciences, McGraw-Hill, New York.

Bierman, P.R. et al., 2002. Rates and timing of earth surface processes from in situ-produced cosmogenic Be-10, Beryllium: Mineralogy, Petrology, And Geochemistry. Reviews In Mineralogy & Geochemistry. Mineralogical Soc America, Washington, pp. 147-205.

Bierman, P.R., Marsella, K.A., Patterson, C., Davis, P.T. and Caffee, M., 1999. Mid-Pleistocene cosmogenic minimum-age limits for pre-Wisconsinan glacial surfaces in southwestern Minnesota and southern Baffin island: a multiple nuclide approach. Geomorphology, 27(1-2): 25-39.

Binnie, S.A., 2004. Deriving basin-wide denudation rates from cosmogenic radionuclides, San Bernardino Mountains, California. PhD Thesis, University of Edinburgh, Edinburgh, 332 pp.

Binnie, S.A., 2005. Edinburgh University Cosmogenic Laboratory Protocols, Al/Be Target Preparation, unpublished.

Blunier, T. et al., 1998. Asynchrony of Antarctic and Greenland climate change during the last glacial period. Nature, 394(6695): 739-743.

Bockheim, J., Coronato, A., Rabassa, J., Ercolano, B. and Ponce, J., in press. Relict sand wedges in southern Patagonia and their stratigraphic and paleo-environmental significance. Quaternary Science Reviews, In Press, Corrected Proof.

Boezio, M. et al., 2000. Measurement of the flux of atmospheric muons with the CAPRICE94 apparatus. Physical Review D, 62(3).

Bourlès, D.L., 1988. Etude de la géochimie de l'isotope cosmogénique 10Be et de son isotope stable 9Be en milieu océanique. Application à la datation des sédiments marins., Paris-sud Centre d'Orsay, PhD thesis.

Briner, J.P., Kaufman, D.S., Manley, W.E., Finkel, R.C. and Caffee, M.W., 2005. Cosmogenic exposure dating of late Pleistocene moraine stabilization in Alaska. Geological Society Of America Bulletin, 117(7-8): 1108-1120.

Brocard, G.Y., van der Beek, P.A., Bourles, D.L., Siame, L.L. and Mugnier, J.L., 2003. Long-term fluvial incision rates and postglacial river relaxation time in

the French Western Alps from Be-10 dating of alluvial terraces with assessment of inheritance, soil development and wind ablation effects. Earth and Planetary Science Letters, 209(1-2): 197-214.

Broecker, W.S. and Denton, G.H., 1989. The Role Of Ocean-Atmosphere Reorganizations In Glacial Cycles. Geochimica Et Cosmochimica Acta, 53(10): 2465-2501.

Brown, E.T. et al., 1995. Evidence for Muon-Induced Production of Be-10 in near-Surface Rocks from the Congo. Geophysical Research Letters, 22(6): 703-706.

Brown, E.T., Brook, E.J., Raisbeck, G.M., Yiou, F. and Kurz, M.D., 1992. Effective Attenuation Lengths of Cosmic-Rays Producing Be-10 and Al-26 in Quartz - Implications for Exposure Age Dating. Geophysical Research Letters, 19(4): 369-372.

Brown, L.L., Singer, B.S. and Gorring, M.L., 2004. Paleomagnetism and Ar-40/Ar-39 chronology of lavas from Meseta del Lago Buenos Aires, Patagonia. Geochemistry Geophysics Geosystems, 5.

Bujalesky, G.G., Heusser, C.J., Coronato, A.M., Roig, C.E. and Rabassa, J.O., 1997. Pleistocene glaciolacustrine sedimentation at Lago Fagnano, Andes of Tierra del Fuego, southernmost South America. Quaternary Science Reviews, 16(7): 767-778.

Caldenius, C.R.C., 1932. Las glaciaciones cuaternarias en la Patagonia y Tierra del Fuego : una investigación regional, estratigráfica y geocronológica : una comparación con la escala geocronológica sueca : with an English summary. Data 17 fr. Stockholms högskolas Geokronol. institutet.;. [Stockholms högskola], Stockholm, 164 p., 42 p. of plates (some folded) pp.

Chadwick, O.A., Hall, R.D. and Phillips, F.M., 1997. Chronology of Pleistocene glacial advances in the central Rocky Mountains. Geological Society of America Bulletin, 109(11): 1443-1452.

Chock, G.Y.K. and Cochran, L., 2005. Modeling of topographic wind speed effects in Hawaii. Journal of Wind Engineering and Industrial Aerodynamics, 93(8): 623-638.

Chorley, R.J., Schumm, S.A. and Sugden, D.E., 1984. Geomorphology, Methuen, London, New-York, 605pp. pp.

Clapperton, C.M., 1990. Quaternary Glaciations in the Southern-Hemisphere - an Overview. Quaternary Science Reviews, 9(2-3): 299-304.

Clapperton, C.M., 1993. Quaternary Geology and Geomorphology of South America, 1. Elsevier Science Publishers B. V., Amsterdam, 779 pp.

Clapperton, C.M., Sugden, D.E., Kaufman, D.S. and McCulloch, R.D., 1995. The Last Glaciation in Central Magellan-Strait, Southernmost Chile. Quaternary Research, 44(2): 133-148.

Clark, P.U. et al., 2009. The Last Glacial Maximum. Science, 325(5941): 710-714.

Coronato, A., Coronato, F., Mazzoni, E. and Vázquez, M., 2008. The Physical Geography of Patagonia and Tierra del Fuego. In: J. Rabassa (Editor), The Late Cenozoic of Patagonia and Tierra del Fuego. Developments in Quaternary Science. Elsevier, London, pp. 13 - 55.

Coronato, A., Martinez, O. and Rabassa, J., 2004. Glaciations in Argentine Patagonia, southern South America In: J. Ehlers and P.L. Gibbard (Editors),

Quaternary Glaciations – Extent and Chronology, Part III. Developments in quaternary science 2. Elsevier, London, pp. 49-67.

Darwin, C., 1842. On the distribution of erratic boulders and on the contemporaneous unstratified deposits of South America. Transactions Geological Society London, 2nd Series, 6: 415-431.

de Geer, G., 1927. Late Glacial clay varves in Argentina, measured by Dr. Carl Caldenius, dated and connected with solar curve through the Swedish timescale. Geografiska Annaler, 9: 1-8.

Delmonte, B. et al., 2004. Comparing the Epica and Vostok dust records during the last 220,000 years: stratigraphical correlation and provenance in glacial periods. Earth-Science Reviews, 66(1-2): 63-87.

Denton, G.H. et al., 1999a. Interhemispheric linkage of paleoclimate during the last glaciation. Geografiska Annaler Series A-Physical Geography, 81A(2): 107-153.

Denton, G.H. et al., 1999b. Geomorphology, stratigraphy, and radiocarbon chronology of Llanquihue drift in the area of the southern Lake District, Seno Reloncavi, and Isla Grande de Chiloe, Chile. Geografiska Annaler Series a-Physical Geography, 81A(2): 167-229.

Desilets, D. and Zreda, M., 2003. Spatial and temporal distribution of secondary cosmic-ray nucleon intensities and applications to in situ cosmogenic dating. Earth and Planetary Science Letters, 206(1-2): 21-42.

Desilets, D., Zreda, M. and Prabu, T., 2006. Extended scaling factors for in situ cosmogenic nuclides: New measurements at low latitude. Earth and Planetary Science Letters, 246(3-4): 265-276.

Douglass, D.C. et al., 2005. Evidence of early Holocene glacial advances in southern South America from cosmogenic surface-exposure dating. Geology, 33(3): 237-240.

Douglass, D.C., Singer, B.S., Kaplan, M.R., Mickelson, D.M. and Caffee, M.W., 2006. Cosmogenic nuclide surface exposure dating of boulders on last-glacial and late-glacial moraines, Lago Buenos Aires, Argentina: Interpretive strategies and paleoclimate implications. Quaternary Geochronology, 1(1): 43-58.

Dunai, T.J., 2000. Scaling factors for production rates of in situ produced cosmogenic nuclides: a critical reevaluation. Earth And Planetary Science Letters, 176(1): 157-169.

Dunai, T.J., 2001. Influence of secular variation of the geomagnetic field on production rates of in situ produced cosmogenic nuclides. Earth and Planetary Science Letters, 193(1-2): 197-212.

Dunai, T.J. and Stuart, F.M., Reporting of cosmogenic nuclide data for exposure age and erosion rate determinations. Quaternary Geochronology, In Press, Corrected Proof.

Dunai, T.J. and Team, a., 2005. CRONUS-EU - Cosmic ray produced nuclide systematics - The European contribution. Geochimica Et Cosmochimica Acta, 69(10): A165-A165.

Dunne, J., Elmore, D. and Muzikar, P., 1999. Scaling factors for the rates of production of cosmogenic nuclides for geometric shielding and attenuation at depth on sloped surfaces. Geomorphology, 27(1-2): 3-11.

Ehlers, J. and Gibbard, P.L., 2003. Extent and chronology of glaciations. Quaternary Science Reviews, 22(15-17): 1561-1568.

Fabel, D. et al., 2002. Landscape preservation under Fennoscandian ice sheets determined from in situ produced Be-10 and Al-26. Earth and Planetary Science Letters, 201(2): 397-406.

Fairbanks, R.G. et al., 2005. Radiocarbon calibration curve spanning 0 to 50,000 years BP based on paired Th-230/U-234/U-238 and C-14 dates on pristine corals. Quaternary Science Reviews, 24(16-17): 1781-1796.

Farber, D.L., Hancock, G.S., Finkel, R.C. and Rodbell, D.T., 2005. The age and extent of tropical alpine glaciation in the Cordillera Blanca, Peru. Journal of Quaternary Science, 20(7-8): 759-776.

Farber, D.L., Meriaux, A.S. and Finkel, R.C., 2008. Attenuation length for fast nucleon production of Be-10 derived from near-surface production profiles. Earth and Planetary Science Letters, 274(3-4): 295-300.

Feruglio, E., 1944. Estudios geologicos y glaciologicos en la region del Lago Argentino (Patagonia) (Expedición Alberto M. De Agostini 1930-31). Cordoba, 255 p. illus., plates, ports., maps, plans. pp.

Feruglio, E., 1950. Descripción geológica de la Patagonia. Impr. y Casa Editora "Coni", Buenos Aires, 3 v. illus., maps (part fold., part col.) diagrs., profiles (part fold.) tables (part fold.) 28 cm. pp.

Fidalgo, F. and Riggi, J.C., 1965. Los rodados patagónicos en la Meseta del Guenguel y alrededores (Santa Cruz). Asociación Geológica Argentina, Revista, 25: 430-443.

Fleck, R.J., Nairn, A.E.M., Peterson, D.N. and Mercer, J.H., 1972. Chronology Of Late Pliocene And Early Pleistocene Glacial And Magnetic Events In Southern Argentina. Earth And Planetary Science Letters, 16(1): 15-&.

Flint, R.F. and Fidalgo, F., 1964. Glacial Geology Of The East Flank Of The Argentine Andes Between Latitude 39-Degrees-10's And Latitude 41-Degrees-20's. Geological Society of America Bulletin, 75(4): 335.

Flint, T.F. and Fidalgo, F., 1969. Glacial Drift In Eastern Argentine Andes Between Latitude 41 Degrees 10's And Latitude 43 Degrees 10]S. Geological Society Of America Bulletin, 80(6): 1043-&.

Fogwill, C.J. and Kubik, P.W., 2005. A glacial stage spanning the Antarctic Cold Reversal in Torres del Paine (51 degrees S), Chile, based on preliminary cosmogenic exposure ages. Geografiska Annaler Series A-Physical Geography, 87A(2): 403-408.

Freeman, S. et al., 2007. The SUERC AMS laboratory after 3 years. Nuclear Instruments & Methods in Physics Research Section B-Beam Interactions with Materials and Atoms, 259(1): 66-70.

Freeman, S. et al., 2004. Initial measurements with the SUERC accelerator mass spectrometer. Nuclear Instruments & Methods in Physics Research Section B-Beam Interactions with Materials and Atoms, 223: 195-198.

Gaiero, D.M., 2007. Dust provenance in Antarctic ice during glacial periods: From where in southern South America? Geophysical Research Letters, 34.

Gaiero, D.M., Depetris, P.J., Probst, J.L., Bidart, S.M. and Leleyter, L., 2004. The signature of river- and wind-borne materials exported from Patagonia to the southern latitudes: a view from REEs and implications for paleoclimatic interpretations. Earth And Planetary Science Letters, 219(3-4): 357-376.

Gibbons, A.B., Megeath, J.D. and Pierce, K.L., 1984. Probability of Moraine Survival in a Succession of Glacial Advances. Geology, 12(6): 327-330.

Gillespie, A.R. and Bierman, P.R., 1995. Precision of terrestrial exposure ages and erosion rates estimated from analysis of cosmogenic isotopes produced in situ. Journal of Geophysical Research-Solid Earth, 100(B12): 24637-24649.

Glasser, N.F., Harrison, S., Ivy-Ochs, S., Duller, G.A.T. and Kubik, P.W., 2006. Evidence from the Rio Bayo valley on the extent of the North Patagonian Icefield during the Late Pleistocene-Holocene transition. Quaternary Research, 65(1): 70-77.

Glasser, N.F., Jansson, K.N., Harrison, S. and Kleman, J., 2008. The glacial geomorphology and Pleistocene history of South America between 38 degrees S and 56 degrees S. Quaternary Science Reviews, 27(3-4): 365-390.

Gorring, M., Singer, B., Gowers, J. and Kay, S.M., 2003. Plio-Pleistocene basalts from the Meseta del Lago Buenos Aires, Argentina: evidence for asthenosphere-lithosphere interactions during slab window magmatism. Chemical Geology, 193(3-4): 215-235.

Gosse, J.C. and Phillips, F.M., 2001. Terrestrial in situ cosmogenic nuclides: theory and application. Quaternary Science Reviews, 20(14): 1475-1560.

Granger, D.E., Fabel, D. and Palmer, A.N., 2001. Pliocene-Pleistocene incision of the Green River, Kentucky, determined from radioactive decay of cosmogenic Al-26 and Be-10 in Mammoth Cave sediments. Geological Society of America Bulletin, 113(7): 825-836.

Granger, D.E., Kirchner, J.W. and Finkel, R.C., 1997. Quaternary downcutting rate of the New River, Virginia, measured from differential decay of cosmogenic Al-26 and Be-10 in cave-deposited alluvium. Geology, 25(2): 107-110.

Granger, D.E. and Smith, A.L., 2000. Dating buried sediments using radioactive decay and muogenic production of Al-26 and Be-10. Nuclear Instruments & Methods in Physics Research Section B-Beam Interactions with Materials and Atoms, 172: 822-826.

Grousset, F.E. et al., 1992. Antarctic (Dome C) Ice-Core Dust at 18 Ky Bp - Isotopic Constraints on Origins. Earth and Planetary Science Letters, 111(1): 175-182.

Guillou, H. and Singer, B., 1997. Combined unspiked K-Ar and $^{40}Ar/^{39}Ar$ dating of Late Quaternary lavas, EOS Transactions of the American Geophysical Union, 78, Fall Meeting, pp. 771.

Guyodo, Y. and Valet, J.P., 1999. Global changes in intensity of the Earth's magnetic field during the past 800 kyr. Nature, 399(6733): 249-252.

Hajdas, I., Bonani, G., Moreno, P.I. and Ariztegui, D., 2003. Precise radiocarbon dating of late-glacial cooling in mid-latitude South America. Quaternary Research, 59(1): 70-78.

Hall, R.D. and Jaworowski, C., 1999. Reinterpretation of the Cedar Ridge section, Wind River Range, Wyoming: Implications for the glacial chronology of the Rocky Mountains. Geological Society of America Bulletin, 111(8): 1233-1249.

Hallet, B. and Putkonen, J., 1994. Surface Dating Of Dynamic Landforms - Young Boulders On Aging Moraines. Science, 265(5174): 937-940.

Hancock, G.S., Anderson, R.S., Chadwick, O.A. and Finkel, R.C., 1999. Dating fluvial terraces with Be-10 and Al-26 profiles: application to the Wind River, Wyoming. Geomorphology, 27(1-2): 41-60.

Hays, J.D., Imbrie, J. and Shackleton, N.J., 1976. Variations In Earths Orbit - Pacemaker Of Ice Ages. Science, 194(4270): 1121-1132.

Hein, A.S. et al., 2009. Middle Pleistocene glaciation in Patagonia dated by cosmogenic nuclide measurements on outwash gravels. Earth and Planetary Science Letters: doi:10.1016/j.epsl.2009.06.026.

Heisinger, B. et al., 2002a. Production of selected cosmogenic radionuclides by muons: 2. Capture of negative muons. Earth and Planetary Science Letters, 200(3-4): PII S0012-821X(02)00641-6.

Heisinger, B. et al., 2002b. Production of selected cosmogenic radionuclides by muons 1. Fast muons. Earth and Planetary Science Letters, 200(3-4): PII S0012-821X(02)00640-4.

Heusser, C.J., 1983. Quaternary Pollen Record from Laguna-De-Tagua-Tagua, Chile. Science, 219(4591): 1429-1432.

Heusser, C.J., 1989. Southern Westerlies During The Last Glacial Maximum. Quaternary Research, 31(3): 423-425.

Heusser, C.J., Heusser, L.E. and Lowell, T.V., 1999. Paleoecology of the southern Chilean Lake District-Isla Grande de Chiloe during middle-late Llanquihue glaciation and deglaciation. Geografiska Annaler Series a-Physical Geography, 81A(2): 231-284.

Hoganson, J.W. and Ashworth, A.C., 1992. Fossil Beetle Evidence for Climatic-Change 18,000-10,000 Years BP in South-Central Chile. Quaternary Research, 37(1): 101-116.

Howard, W.R. and Prell, W.L., 1994. Late Quaternary Caco3 Production and Preservation in the Southern-Ocean - Implications for Oceanic and Atmospheric Carbon Cycling. Paleoceanography, 9(3): 453-482.

Hubbard, A., Hein, A.S., Kaplan, M.R., Hulton, N.R.J. and Glasser, N., 2005. A modelling reconstruction of the last glacial maximum ice sheet and its deglaciation in the vicinity of the Northern Patagonian Icefield, South America. Geografiska Annaler Series A-Physical Geography, 87A(2): 375-391.

Hubbard, A.L., 1997. Modelling climate, topography and palaeoglacier fluctuations in the Chilean Andes. Earth Surface Processes and Landforms, 22(1): 79-92.

Hughes, P.D., Woodward, J.C. and Gibbard, P.L., 2006. Quaternary glacial history of the Mediterranean mountains. Progress in Physical Geography, 30(3): 334-364.

Hulton, N. and Sugden, D., 1997. Dynamics of mountain ice caps during glacial cycles: the case of Patagonia. Annals of Glaciology, Vol 24, 1997, 24: 81-89.

Hulton, N.R.J., Purves, R.S., McCulloch, R.D., Sugden, D.E. and Bentley, M.J., 2002. The Last Glacial Maximum and deglaciation in southern South America. Quaternary Science Reviews, 21(1-3): 233-241.

Hulton, N.R.J., Sugden, D.E. and Purves, R.S., 2003. Comment on: 'The Last Glacial Maximum and deglaciation in southern South America' - Authors response to the comment by G. Wenzens. Quaternary Science Reviews, 22(5-7): 755-757.

Huybers, P., 2006. Early Pleistocene glacial cycles and the integrated summer insolation forcing. Science, 313(5786): 508-511.

Huybers, P. and Denton, G., 2008. Antarctic temperature at orbital timescales controlled by local summer duration. Nature Geoscience, 1(11): 787-792.

Inbar, M., Ostera, H.A., Parica, C.A., Remesal, M.B. and Salani, F.M., 1995. Environmental Assessment of 1991 Hudson Volcano Eruption Ashfall Effects on Southern Patagonia Region, Argentina. Environmental Geology, 25(2): 119-125.

Ivy-Ochs, S., 1996. The dating of rock surfaces using in situ produced ^{10}Be, ^{26}Al and ^{36}Cl, with examples from Antarctica and the Swiss Alps, unpublished PhD thesis, ETH Zurich, 196 pp.

Jamieson, S.S.R., 2008. Modelling Landscape Evolution Under Ice Sheets. PhD Thesis, University of Edinburgh, Edinburgh, 255 pp.

Jouzel, J. et al., 2007. Orbital and millennial Antarctic climate variability over the past 800,000 years. Science, 317(5839): 793-796.

Kaiser, J., Lamy, F. and Hebbeln, D., 2005. A 70-kyr sea surface temperature record off southern Chile (Ocean Drilling Program Site 1233). Paleoceanography, 20(4).

Kaplan, M.R., Ackert, R.P., Singer, B.S., Douglass, D.C. and Kurz, M.D., 2004. Cosmogenic nuclide chronology of millennial-scale glacial advances during O-isotope stage 2 in Patagonia. Geological Society Of America Bulletin, 116(3-4): 308-321.

Kaplan, M.R. et al., 2007. Cosmogenic nuclide measurements in southernmost South America and implications for landscape change. Geomorphology, 87(4): 284-301.

Kaplan, M.R., Douglass, D.C., Singer, B.S. and Caffee, M.W., 2005. Cosmogenic nuclide chronology of pre-last glacial maximum moraines at Lago Buenos Aires, 46 degrees S, Argentina. Quaternary Research, 63(3): 301-315.

Kaplan, M.R. et al., 2008a. Southern Patagonian glacial chronology for the Last Glacial period and implications for Southern Ocean climate. Quaternary Science Reviews, 27(3-4): 284-294.

Kaplan, M.R., Hein, A.S., Hubbard, A. and Lax, S.M., 2009. Can glacial erosion limit the extent of glaciation? Geomorphology, 103(2): 172-179.

Kaplan, M.R., Moreno, P.I. and Rojas, M., 2008b. Glacial dynamics in southernmost South America during Marine Isotope Stage 5e to the Younger Dryas chron: a brief review with a focus on cosmogenic nuclide measurements. Journal of Quaternary Science, 23(6-7): 649-658.

Kaplan, M.R., Singer, B.S., Douglass, D.C., Ackert, R.P. and Caffee, M.W., 2006. Comment on: Cosmogenic nuclide chronology of pre-last glacial maximum moraines at Lago Buenos Aires, 46 degrees S, Argentina (Quaternary Research 63/3, 2005, 301-315) - Reply. Quaternary Research, 66(2): 367-369.

Karner, D.B. and Muller, R.A., 2000. Paleoclimate - A causality problem for Milankovitch. Science, 288(5474): 2143-2144.

Kohl, C.P. and Nishiizumi, K., 1992. Chemical Isolation of Quartz for Measurement of Insitu-Produced Cosmogenic Nuclides. Geochimica et Cosmochimica Acta, 56(9): 3583-3587.

Korte, M. and Constable, C.G., 2005. The geomagnetic dipole moment over the last 7000 years - new results from a global model. Earth and Planetary Science Letters, 236(1-2): 348-358.

Lagabrielle, Y. et al., 2004. Neogene to Quaternary tectonic evolution of the Patagonian Andes at the latitude of the Chile Triple Junction. Tectonophysics, 385(1-4): 211-241.

Lal, D., 1991. Cosmic-Ray Labeling Of Erosion Surfaces - Insitu Nuclide Production-Rates And Erosion Models. Earth And Planetary Science Letters, 104(2-4): 424-439.

Lal, D. and Peters, B., 1967. Cosmic ray produced radioactivity on the earth. In: K. Sitte (Editor), Handbuch der Physik. Springer, Berlin, pp. pp. 551-612.

Lambert, F. et al., 2008. Dust-climate couplings over the past 800,000 years from the EPICA Dome C ice core. Nature, 452(7187): 616-619.

Lamy, F., Hebbeln, D., Rohl, U. and Wefer, G., 2001. Holocene rainfall variability in southern Chile: a marine record of latitudinal shifts of the Southern Westerlies. Earth and Planetary Science Letters, 185(3-4): 369-382.

Lamy, F. et al., 2004. Antarctic timing of surface water changes off Chile and Patagonian ice sheet response. Science, 304(5679): 1959-1962.

Langel, R.A. et al., 1988. Definitive Igrf Models for 1945, 1950, 1955, and 1960. Journal of Geomagnetism and Geoelectricity, 40(6): 645-702.

Leya, I., Lange, H.J., Neumann, S., Wieler, R. and Michel, R., 2000. The production of cosmogenic nuclides in stony meteoroids by galactic cosmic-ray particles. Meteoritics & Planetary Science, 35(2): 259-286.

Licciardi, J.M. and Pierce, K.L., 2008. Cosmogenic exposure-age chronologies of Pinedale and Bull Lake glaciations in greater Yellowstone and the Teton Range, USA. Quaternary Science Reviews, 27(7-8): 814-831.

Lifton, N.A. et al., 2005. Addressing solar modulation and long-term uncertainties in scaling secondary cosmic rays for in situ cosmogenic nuclide applications. Earth and Planetary Science Letters, 239: 140-161.

Lingenfelter, R.E., 1963. Production of Carbon-14 by Cosmic-Ray Neutrons. Reviews of Geophysics, 1(1): 35-55.

Lisiecki, L.E. and Raymo, M.E., 2005. A Pliocene-Pleistocene stack of 57 globally distributed benthic delta O-18 records. Paleoceanography, 20(1).

Lowell, T.V. et al., 1995. Interhemispheric Correlation of Late Pleistocene Glacial Events. Science, 269(5230): 1541-1549.

Lumley, S.H. and Switsur, R., 1993. Late Quaternary Chronology of the Taitao Peninsula, Southern Chile. Journal of Quaternary Science, 8(2): 161-165.

Luthi, D. et al., 2008. High-resolution carbon dioxide concentration record 650,000-800,000 years before present. Nature, 453(7193): 379-382.

MacGregor, K.R., Anderson, R.S., Anderson, S.P. and Waddington, E.D., 2000. Numerical simulations of glacial-valley longitudinal profile evolution. Geology, 28(11): 1031-1034.

Maden, C. et al., 2007. SUERC AMS ion detection. Nuclear Instruments & Methods in Physics Research Section B-Beam Interactions with Materials and Atoms, 259(1): 131-139.

Malagnino, E., 1995. The discovery of the oldest extra-Andean glaciation in the Lago Buenos Aires Basin, Argentina. In: J. Rabassa and M. Salemme (Editors), Quaternary of South America and Antarctic Peninsula. A.A. Balkema, Rotterdam, pp. 69-83.

Marden, C.J. and Clapperton, C.M., 1995. Fluctuations of the South Patagonian Ice-Field During the Last Glaciation and the Holocene. Journal of Quaternary Science, 10(3): 197-209.

Markgraf, V., 1989a. Paleoclimates in Central and South-America since 18,000 Bp Based on Pollen and Lake-Level Records. Quaternary Science Reviews, 8(1): 1-24.

Markgraf, V., 1989b. Southern Westerlies During The Last Glacial Maximum - Reply. Quaternary Research, 31(3): 426-432.

Markgraf, V., Dodson, J.R., Kershaw, A.P., McGlone, M.S. and Nicholls, N., 1992. Evolution of late Pleistocene and Holocene climates in the circum-South Pacific land areas. Climate Dynamics, 6(3-4): 193-211.

Martínez, O. and Coronato, A., 2008. The Late Cenozoic Fluvial Deposits of Argentine Patagonia. In: J. Rabassa (Editor), The Late Cenozoic of Patagonia and Tierra del Fuego. Developments in Quaternary Science. Elsevier, London, pp. 205-226.

Martinson, D.G. et al., 1987. Age Dating and the Orbital Theory of the Ice Ages - Development of a High-Resolution-0 to 300,000-Year Chronostratigraphy. Quaternary Research, 27(1): 1-29.

Masarik, J. and Beer, J., 1999. Simulation of particle fluxes and cosmogenic nuclide production in the Earth's atmosphere. Journal of Geophysical Research-Atmospheres, 104(D10): 12099-12111.

Masarik, J. and Reedy, R.C., 1995. Terrestrial cosmogenic-nuclide production systematics calculated from numerical simulations. Earth and Planetary Science Letters, 136(3-4): 381-395.

Masarik, J. and Wieler, R., 2003. Production rates of cosmogenic nuclides in boulders. Earth and Planetary Science Letters, 216(1-2): 201-208.

Massaferro, J. and Brooks, S.J., 2002. Response of chironomids to Late Quaternary environmental change in the Taitao Peninsula, southern Chile. Journal of Quaternary Science, 17(2): 101-111.

Massaferro, J.I., Moreno, P.I., Denton, G.H., Vandergoes, M. and Dieffenbacher-Krall, A., 2009. Chironomid and pollen evidence for climate fluctuations during the Last Glacial Termination in NW Patagonia. Quaternary Science Reviews, 28(5-6): 517-525.

McCulloch, R.D. et al., 2000. Climatic inferences from glacial and palaeoecological evidence at the last glacial termination, southern South America. Journal Of Quaternary Science, 15(4): 409-417.

McCulloch, R.D. and Davies, S.J., 2001. Late-glacial and Holocene palaeoenvironmental change in the central Strait of Magellan, southern Patagonia. Palaeogeography Palaeoclimatology Palaeoecology, 173(3-4): 143-173.

McCulloch, R.D., Fogwill, C.J., Sugden, D.E., Bentley, M.J. and Kubik, P.W., 2005. Chronology of the last glaciation in central Strait of Magellan and Bahia Inutil, southernmost South America. Geografiska Annaler Series A-Physical Geography, 87A(2): 289-312.

Meglioli, A., 1992. Glacial geology and chronology of southernmost Patagonia and Tierra del Fuego, Argentina and Chile, Lehigh University, Bethlehem, 298 pp.

Mercer, J.H., 1969. Glaciation In Southern Argentina More Than 2 Million Years Ago. Science, 164(3881): 823-&.

Mercer, J.H., 1976. Glacial History Of Southernmost South-America. Quaternary Research, 6(2): 125-166.

Mercer, J.H., 1982. Holocene glacier variations in southern South America. Striae, 18: 35-40.

Mercer, J.H., 1983. Cenozoic Glaciation In The Southern-Hemisphere. Annual Review Of Earth And Planetary Sciences, 11: 99-132.

Mercer, J.H. and Sutter, J.F., 1982. Late Miocene Earliest Pliocene Glaciation In Southern Argentina - Implications For Global Icesheet History. Palaeogeography Palaeoclimatology Palaeoecology, 38(3-4): 185-206.

Millar, S.W.S., 2006. Processes dominating macro-fabric generation in periglacial colluvium. Catena, 67(1): 79-87.

Mohtadi, M. and Hebbeln, D., 2004. Mechanisms and variations of the paleoproductivity off northern Chile (24 degrees S-33 degrees S) during the last 40,000 years. Paleoceanography, 19(2).

Moreno, P.I. et al., 2009. Renewed glacial activity during the Antarctic cold reversal and persistence of cold conditions until 11.5 ka in southwestern Patagonia. Geology, 37(4): 375-378.

Moreno, P.I. and Leon, A.L., 2003. Abrupt vegetation changes during the last glacial to Holocene transition in mid-latitude South America. Journal of Quaternary Science, 18(8): 787-800.

Moreno, P.I., Lowell, T.V., Jacobson, G.L. and Denton, G.H., 1999. Abrupt vegetation and climate changes during the last glacial maximum and last termination in the Chilean Lake District: A case study from Canal de la Puntilla (41 degrees s). Geografiska Annaler Series a-Physical Geography, 81A(2): 285-311.

Mörner, N.A. and Sylwan, C., 1989. Magnetostratigraphy of the Patagonian moraine sequence at Lago Buenos Aires. Journal of South American Earth Sciences, 2(4): 385-389.

Mudelsee, M. and Schulz, M., 1997. The Mid-Pleistocene climate transition: onset of 100 ka cycle lags ice volume build-up by 280 ka. Earth and Planetary Science Letters, 151(1-2): 117-123.

Newnham, R.M., Vandergoes, M.J., Hendyc, C.H., Lowe, D.J. and Preusser, F., 2007. A terrestrial palynological record for the last two glacial cycles from southwestern New Zealand. Quaternary Science Reviews, 26(3-4): 517-535.

Nishiizumi, K., 2004. Preparation of Al-26 AMS standards. Nuclear Instruments & Methods in Physics Research Section B, 223-24: 388-392.

Nishiizumi, K., Finkel, R.C., Klein, J. and Kohl, C.P., 1996. Cosmogenic production of Be-7 and Be-10 in water targets. Journal of Geophysical Research-Solid Earth, 101(B10): 22225-22232.

Nishiizumi, K. et al., 2007. Absolute calibration of Be-10 AMS standards. Nuclear Instruments & Methods in Physics Research Section B, 258(2): 403-413.

Nishiizumi, K. et al., 1991. Cosmic-Ray Produced Be-10 and Al-26 in Antarctic Rocks - Exposure and Erosion History. Earth and Planetary Science Letters, 104(2-4): 440-454.

Nishiizumi, K. et al., 1989. Cosmic-Ray Production-Rates of Be-10 and Al-26 in Quartz from Glacially Polished Rocks. Journal of Geophysical Research-Solid Earth and Planets, 94(B12): 17907-17915.

Oerlemans, J., 1984. Numerical experiments on large-scale glacial erosion. Zeitschrift für Gletscherkunde und Glazialgeologie, 20: 107–126.

Owen, L.A., Caffee, M.W., Bovard, K.R., Finkel, R.C. and Sharma, M.C., 2006. Terrestrial cosmogenic nuclide surface exposure dating of the oldest glacial successions in the Himalayan orogen: Ladakh Range, northern India. Geological Society Of America Bulletin, 118(3-4): 383-392.

Parrenin, F. et al., 2007. The EDC3 chronology for the EPICA dome C ice core. Climate of the Past, 3(3): 485-497.

Petit, J.R. et al., 1999. Climate and atmospheric history of the past 420,000 years from the Vostok ice core, Antarctica. Nature, 399(6735): 429-436.

Petit, J.R. et al., 1990. Palaeoclimatological and Chronological Implications of the Vostok Core Dust Record. Nature, 343(6253): 56-58.

Phillips, F.M. et al., 1997. Cosmogenic Cl-36 and Be-10 ages of Quaternary glacial and fluvial deposits of the Wind River Range, Wyoming. Geological Society of America Bulletin, 109(11): 1453-1463.

Phillips, F.M. et al., 1990. Cosmogenic Chlorine-36 Chronology for Glacial Deposits at Bloody Canyon, Eastern Sierra-Nevada. Science, 248(4962): 1529-1532.

Phillips, R.J., Sharp, W.D., Singer, B.S. and Douglass, D.C., 2006. Utilising U-series disequilibria of calcic soils to constrain the surface age of Quaternary deposits: A comparison with 10Be, 26 Al age data from Patagonian glacial moraines. Geochimica et Cosmochimica Acta, 70(18-supplement 1): A491.

Pigati, J.S. and Lifton, N.A., 2004. Geomagnetic effects on time-integrated cosmogenic nuclide production with emphasis on in situ C-14 and Be-10. Earth and Planetary Science Letters, 226(1-2): 193-205.

Pittock, A.B., 1978. Climatic change and variability : a Southern perspective. Cambridge University Press, Cambridge ; New York, 455 pp.

Porter, S.C., 1981. Pleistocene Glaciation in the Southern Lake District of Chile. Quaternary Research, 16(3): 263-292.

Prohaska, F., 1976. The climate of Argentina, Paraguay and Uruguay. In: S. W (Editor), Climates of Central and South America. World Survey of Climatology. Elsevier, Amsterdam, pp. 13-112.

Putkonen, J., Connolly, J. and Orloff, T., 2008. Landscape evolution degrades the geologic signature of past glaciations. Geomorphology, 97(1-2): 208-217.

Putkonen, J. and O'Neal, M., 2006. Degradation of unconsolidated Quaternary landforms in the western North America. Geomorphology, 75(3-4): 408-419.

Putkonen, J. and Swanson, T., 2003. Accuracy of cosmogenic ages for moraines. Quaternary Research, 59(2): 255-261.

Putnam, A., submitted. In situ cosmogenic Be-10 production rate from the Southern Alps, New Zealand. Quaternary Geochronology.

Rabassa, J., 1999. Cuaternario de la Cordillera Patagónica y Tierra del Fuego. In: M.J. Haller (Editor), Geología Argentina. Anales SEGEMAR, Buenos Aires.

Rabassa, J., 2008. Late Cenozoic Glaciations in Patagonia and Tierra del Fuego. In: J. Rabassa (Editor), The Late Cenozoic of Patagonia and Tierra del Fuego. Developments in Quaternary Science. Elsevier, Amsterdam; Boston [Mass.]; Oxford, UK, pp. 151-204.

Rabassa, J. and Clapperton, C.M., 1990. Quaternary Glaciations Of The Southern Andes. Quaternary Science Reviews, 9(2-3): 153-174.

Rabassa, J. and Coronato, A., in press. Glaciations in Patagonia and Tierra del Fuego during the Ensenadan Stage/Age (Early Pleistocene-earliest Middle Pleistocene). Quaternary International, In Press, Corrected Proof: doi:10.1016/j.quaint.2009.06.019

Rabassa, J. et al., 2000. Quaternary of Tierra del Fuego, Southernmost South America: an updated review. Quaternary International, 68: 217-240.

Rabassa, J., Coronato, A.M. and Salemme, M., 2005. Chronology of the Late Cenozoic Patagonian and their correlation with biostratigraphic glaciations units of the Pampean region (Argentina). Journal Of South American Earth Sciences, 20(1-2): 81-103.

Rabassa, J. and Evenson, E.B., 1996. Reinterpretación de la estratigrafía glaciaria de la región de San Carlos de Bariloche. XIII Congreso Geológico Argentino, Actas, 4: 327.

Rabassa, J., Evenson, E.B. and Stephens, S.A., 1986. Nuevas evidencias del englazamiento Plioceno-Pleistoceno inferior en los Andes Patagónicos Septentrionales: Cerro Tronador, Río Negro. Asociación Geológica Argentina, Revista, 41: 405-409.

Ramos, V.A., 2005. Seismic ridge subduction and topography: Foreland deformation in the Patagonian Andes. Tectonophysics, 399(1-4): 73-86.

Ramos, V.A. and Kay, S.M., 1992. Southern Patagonian Plateau Basalts And Deformation - Backarc Testimony Of Ridge Collisions. Tectonophysics, 205(1-3): 261-282.

Reedy, R.C., Arnold, J.R. and Lal, D., 1983. Cosmic-Ray Record in Solar-System Matter. Science, 219(4581): 127-135.

Repka, J.L., Anderson, R.S. and Finkel, R.C., 1997. Cosmogenic dating of fluvial terraces, Fremont River, Utah. Earth and Planetary Science Letters, 152(1-4): 59-73.

Schaefer, J.M., 2005. The CRONUS-Earth (Cosmic-Ray prOduced NUdide systematics on earth) initiative. Geochimica et Cosmochimica Acta, 69(10): A167-A167.

Schaefer, J.M. et al., 2006. Near-synchronous interhemispheric termination of the last glacial maximum in mid-latitudes. Science, 312(5779): 1510-1513.

Schäfer, J.M. et al., 2008. Cosmogenic beryllium-10 and neon-21 dating of late Pleistocene glaciations in Nyalam, monsoonal Himalayas. Quaternary Science Reviews, 27(3-4): 295-311.

Schellmann, G., 1998. Jungkänozoische Landschafts-gesschichte Patagoniens (Argentinien). Andine Vorlandvergletscherungen, Talentwicklung und marine Terrasen. Essener Geographische Arbeiten, 29: 1-218.

Schildgen, T., Dethier, D.P., Bierman, P. and Caffee, M., 2002. Al-26 and Be-10 dating of late Pleistocene and Holocene fill terraces: A record of fluvial deposition and incision, Colorado Front Range. Earth Surface Processes and Landforms, 27(7): 773-787.

Schlieder, G., 1989. Glacial Geology of the Northern Patagonian Andes between lakes Aluminé and Lácar, Unpublished Ph.D. Thesis, Lehigh University, Bethlehem, Pennsylvania, USA.

Schnabel, C. et al., 2007. Inter-comparison in Be-10 analysis starting from pre-purified quartz. Nuclear Instruments & Methods in Physics Research Section B-Beam Interactions with Materials and Atoms, 259(1): 571-575.

Shackleton, N.J., 1987. Oxygen Isotopes, Ice Volume and Sea-Level. Quaternary Science Reviews, 6(3-4): 183-190.

Shackleton, N.J. et al., 1984. Oxygen Isotope Calibration of the Onset of Ice-Rafting and History of Glaciation in the North-Atlantic Region. Nature, 307(5952): 620-623.

Shackleton, N.J., Berger, A. and Peltier, W.R., 1990. An Alternative Astronomical Calibration of the Lower Pleistocene Timescale Based on Odp Site 677. Transactions of the Royal Society of Edinburgh-Earth Sciences, 81: 251-261.

Shackleton, N.J. and Hall, M.A., 1989. Stable isotope history of the Pleistocene at ODP Site 677. In: K. Becker and H. Sakai, et al. (Editors), Proceedings of the Ocean Drilling Program, Scientific Results, College Station, TX (Ocean Drilling Programm), pp. 295-316.

Shackleton, N.J. and Opdyke, N.D., 1977. Oxygen Isotope and Paleomagnetic Evidence for Early Northern Hemisphere Glaciation. Nature, 270(5634): 216-219.

Shanahan, T.M. and Zreda, M., 2000. Chronology of quaternary glaciations in East Africa. Earth and Planetary Science Letters, 177(1-2): 23-42.

Shulmeister, J. et al., 2004. The Southern Hemisphere westerlies in the Australasian sector over the last glacial cycle: a synthesis. Quaternary International, 118: 23-53.

Singer, B.S., Ackert, R.P. and Guillou, H., 2004. Ar-40/Ar-19 and K-Ar chronology of Pleistocene glaciations in Patagonia. Geological Society of America Bulletin, 116(3-4): 434-450.

Singer, B.S. and Pringle, M.S., 1996. Age and duration of the Matuyama-Brunhes geomagnetic polarity reversal from Ar-40/Ar-39 incremental heating analyses of lavas. Earth and Planetary Science Letters, 139(1-2): 47-61.

Small, E.E., Anderson, R.S., Repka, J.L. and Finkel, R., 1997. Erosion rates of alpine bedrock summit surfaces deduced from in situ Be-10 and Al-26. Earth and Planetary Science Letters, 150(3-4): 413-425.

Smith, J.A., Finkel, R.C., Farber, D.L., Rodbell, D.T. and Seltzer, G.O., 2005. Moraine preservation and boulder erosion in the tropical Andes: interpreting old surface exposure ages in glaciated valleys. Journal Of Quaternary Science, 20(7-8): 735-758.

Staiger, J. et al., 2007. Atmospheric scaling of cosmogenic nuclide production: Climate effect. Journal of Geophysical Research-Solid Earth, 112(B2).

Stone, J.O., 2000. Air pressure and cosmogenic isotope production. Journal Of Geophysical Research-Solid Earth, 105(B10): 23753-23759.

Strelin, J.A., 1995. New evidence on the relationships between the oldest extra-andean glaciations in the Río Santa Cruz area. In: J. Rabassa and M. Salemme (Editors), Quaternary of South America and Antarctic Peninsula. Balkema, Rotterdam, pp. 105-116.

Strelin, J.A. and Denton, G., 2005. Strelin and G. Denton, Las Morenas de Puerto Bandera, Lago Argentino, Actas XVI Congreso Geológico Argentino, La Plata.

Strelin, J.A. and Malagnino, E., 2009. Charles Darwin and the oldest glacial events in Patagonia: the erratic blocks of the Río Santa Cruz valley. Revista de la Asociación Geológica Argentina, 64(1): 101 - 108.

Strelin, J.A. and Malagnino, E.C., 2000. Late-glacial history of Lago Argentino, Argentina, and age of the Puerto Bandera moraines. Quaternary Research, 54(3): 339-347.

Strelin, J.A., Re, G., Keller, R. and Malagnino, E., 1999. New evidence concerning the Plio-Pleistocene landscape evolution of southern Santa Cruz region. Journal Of South American Earth Sciences, 12(3): 333-341.

Suárez, M. and De La Cruz, R., 2001. Jurassic to miocene K-Ar dates from eastern central Patagonian Cordillera plutons, Chile (45 degrees-48 degrees S). Geological Magazine, 138(1): 53-66.

Sugden, D.E. et al., 2005. Late-glacial glacier events in southernmost South America: A blend of 'northern'and 'southern' hemispheric climatic signals? Geografiska Annaler Series A-Physical Geography, 87A(2): 273-288.

Sugden, D.E., McCulloch, R.D., Bory, A. and Hein, A.S., 2009. Influence of Patagonian glaciers on Antarctic dust deposition during the last glacial period. Nature Geoscience, d.o.i. (10.1038/NGEO474).

Swift, D.A., Nienow, P.W., Hoey, T.B. and Mair, D.W.F., 2005. Seasonal evolution of runoff from Haut Glacier d'Arolla, Switzerland and implications for glacial geomorphic processes. Journal of Hydrology, 309(1-4): 133-148.

Sylwan, C., 1989. Paleomagnetism, paleoclimate, and chronology of Late Cenozoic deposits in southern Argentina, Meddelanden Stockholms Universitets Geologiska Inst., Nr. PhD Thesis, Stockholm, 110 pp.

Sylwan, C., Beraza, L. and Caselli, A., 1991. Magnetoestratigrafia de la secuencia morenica en el valle del Lago Pueyrredon, provincia de Santa Cruz. Asociacion Geologica Argentina, Rev., XLVI(3-4): 235-238.

Thomson, S.N., 2002. Late Cenozoic geomorphic and tectonic evolution of the Patagonian Andes between latitudes 42 degrees S and 46 degrees S: An appraisal based on fission-track results from the transpressional intra-arc Liquine-Ofqui fault zone. Geological Society Of America Bulletin, 114(9): 1159-1173.

Ton-That, T., Singer, B., Mörner, N. and Rabassa, J., 1999. Datación de lavas basalticas por 40Ar/39Ar geología glacial de la region del lago Buenos Aires, provincia de Santa Cruz, Argentina. Revisita de la Asociación Geológica Argentina, 54: 333-352.

Trenberth, K.E., 1991. Storm Tracks in the Southern-Hemisphere. Journal of the Atmospheric Sciences, 48(19): 2159-2178.

Trombotto, D., 2008. Geocryology of Southern South America. In: J. Rabassa (Editor), The late Cenozoic of Patagonia and Tierra del Fuego. Developments in Quaternary Sciences. Elsevier, Amsterdam; Boston [Mass.]; Oxford, UK.

Turner, K.J., Fogwill, C.J., McCulloch, R.D. and Sugden, D.E., 2005. Deglaciation of the eastern flank of the North Patagonian Icefield and associated continental-scale lake diversions. Geografiska Annaler Series a-Physical Geography, 87A(2): 363-374.

Vermeesch, P., 2007. CosmoCalc: An Excel add-in for cosmogenic nuclide calculations. Geochemistry Geophysics Geosystems, 8.

Villagran, C., 1988. Expansion of Magellanic Moorland During the Late Pleistocene - Palynological Evidence from Northern Isla De Chiloe, Chile. Quaternary Research, 30(3): 304-314.

Washburn, A.L., 1980. Permafrost Features as Evidence of Climatic-Change. Earth-Science Reviews, 15(4): 327-402.

Wenzens, G., 1999. Fluctuations of outlet and valley glaciers in the southern Andes (Argentina) during the past 13,000 years. Quaternary Research, 51(3): 238-247.

Wenzens, G., 2000. Pliocene Piedmont glaciation in the Rio Shehuen Valley, Southeast Patagonia, Argentina. Arctic Antarctic And Alpine Research, 32(1): 46-54.

Wenzens, G., 2002. The influence of tectonically derived relief and climate on the extent of the last Glaciation east of the Patagonian ice fields (Argentina, Chile). Tectonophysics, 345(1-4): 329-344.

Wenzens, G., 2005. Glacier advances east of the Southern Andes between the Last Glacial Maximum and 5,000 BP compared with lake terraces of the endorrheic Lago Cardiel (49 degrees S, Patagonia, Argentina). Zeitschrift Für Geomorphologie, 49(4): 433-454.

Wenzens, G., 2006a. Comment on: Cosmogenic nuclide chronology of pre-last glacial maximum moraines at Lago Buenos Aires, 46 degrees S, Argentina (Quaternary Research 63/3, 2005, 301-315). Quaternary Research, 66(2): 364-366.

Wenzens, G., 2006b. Terminal moraines, outwash plains, and lake terraces in the vicinity of Lago Cardiel (49º S; Patagonia, Argentina) - Evidence for miocene andean foreland glaciations. Arctic Antarctic and Alpine Research, 38(2): 276-291.

Wolff, E.W. et al., 2006. Southern Ocean sea-ice extent, productivity and iron flux over the past eight glacial cycles. Nature, 440(7083): 491-496.

Wunsch, C., 2004. Quantitative estimate of the Milankovitch-forced contribution to observed Quaternary climate change. Quaternary Science Reviews, 23(9-10): 1001-1012.

Wyrwoll, K.H., Dong, B.W. and Valdes, P., 2000. On the position of southern hemisphere westerlies at the Last Glacial Maximum: an outline of AGCM simulation results and evaluation of their implications. Quaternary Science Reviews, 19(9): 881-898.

Yang, S., Odah, H. and Shaw, J., 2000. Variations in the geomagnetic dipole moment over the last 12 000 years. Geophysical Journal International, 140(1): 158-162.

Yokoyama, T., Makishima, A. and Nakamura, E., 1999. Evaluation of the coprecipitation of incompatible trace elements with fluoride during silicate rock dissolution by acid digestion. Chemical Geology, 157(3-4): 175-187.

Zech, R., Kull, C., Kubik, P.W. and Veit, H., 2007a. Exposure dating of late glacial and pre-LGM moraines in the Cordon de Dona Rosa, Northern/Central Chile (similar to 31 degrees S). Climate of the Past, 3(1): 1-14.

Zech, R., Kull, C., Kubik, P.W. and Veit, H., 2007b. LGM and Late Glacial glacier advances in the Cordillera Real and Cochabamba (Bolivia) deduced from 10Be surface exposure dating. Climate of the Past, 3(4): 623-635.

Zentmire, K.N., Gosse, J., Baker, C., McDonald, E. and Wells, S., 1999. The problem of inheritance when dating alluvial fans and terraces with TCN: Insight from the Matanuska Glacier. GSA Abstracts and Programs, 31.

Zhao, J.D., Liu, S.Y., He, Y.Q. and Song, Y.G., 2009. Quaternary glacial chronology of the Ateaoyinake River Valley, Tianshan Mountains, China. Geomorphology, 103(2): 276-284.

Zreda, M.G. and Phillips, F.M., 1995. Insights into alpine moraine development from cosmogenic Cl-36 buildup dating. Geomorphology, 14(2): 149-156.

Zreda, M.G., Phillips, F.M. and Elmore, D., 1994. Cosmogenic Cl-36 Accumulation in Unstable Landforms .2. Simulations and Measurements on Eroding Moraines. Water Resources Research, 30(11): 3127-3136.